Crystal Growth and Characterization of Cerium- and Ytterbium-based Quantum Critical Materials

Dissertation
zur Erlangung des Doktorgrades
der Naturwissenschaften

vorgelegt beim Fachbereich Physik
der Goethe-Universität in Frankfurt am Main

von
Kristin Kliemt
aus Freital

Frankfurt 2018

D30

Vom Fachbereich Physik
der Goethe-Universität Frankfurt am Main
als Dissertation angenommen.

Dekan:	Prof. Dr. Owe Philipsen
Erstgutachter:	Prof. Dr. Cornelius Krellner
Zweitgutachter:	Prof. Dr. Michael Lang
Drittgutachter:	Prof. Dr. Peter Gille (LMU München)
Datum der Disputation:	19.06.2018

Abstract

Nowadays, superconductivity, magnetism and quantum criticality are main research fields in solid-state physics. In this thesis, the investigated quantum critical compounds are the series $YbNi_4(P_{1-x}As_x)_2$ exhibiting a ferromagnetic quantum critical point (FM QCP) at $x \approx 0.1$, the compound $YbRh_2Si_2$ exhibiting a field induced QCP for $B_{crit} \approx 60\,mT$ ($B \perp c$), and the series $Ce(Ru_{1-x}Fe_x)PO$ with a QCP at $x \approx 0.86$.

The **$YbNi_4P_2$** single crystals have been grown by two different methods. The Bridgman method yielded single crystals with a mass up to 10 mg. The large single crystals obtained by the Czochralski method grew up to a mass of 1800 mg. The compound contains ytterbium and phosphorous with a high vapour pressure at high temperature and the high-melting element nickel. Initially, the high reactivity of the melt with the tendency to attack the crucible material impeded the prereaction. The following conditions were found to be suitable (i) the crucible setup consisting of a boron nitride inner and a niobium outer crucible, (ii) a Yb-P-Ni stacking of the elements in the crucible, and (iii) a maximum temperature of 900°C. Furthermore, a homogenization and cleaning of the obtained precursor is necessary. The application of an argon pressure of 20 bar in the growth chamber was key to slow down the evaporation of P and Yb and to achieve stable growth conditions. A seed holder with an appropriate heat diffusion rate was designed and a well oriented crystal was used for the single crystal growth by the Czochralski method from a levitating melt utilizing a Ni-rich flux. We have demonstrated that the high-temperature metal-flux technique can be used to grow large single crystals of materials with volatile elements. Furthermore, the Czochralski method was applied to grow single crystals in the substitution series **$YbNi_4(P_{1-x}As_x)_2$** for $x = 0.1, 0.12, 0.15, 0.2, 0.4, 0.6, 0.8$ and 1.0. Electrical transport measurements on $YbNi_4P_2$ down to 20 mK confirmed a sharp transition into the FM state at $T_C = 150\,mK$. Additionally, the resistivity ratio, the best indicator for the high sample purity, was improved from previous $RRR = 16$ to $RRR = 60$ for $j \parallel c$. Due to the high sample purity, the resolution in the transport measurements enabled the investigation of Lifshitz transitions in this compound by H. Pfau and coworkers. In particular, their cummulated occurence at low fields is extraordinary. In the $YbNi_4(P_{1-x}As_x)_2$ substition series, Fermi liquid behaviour was observed below $T = 2\,K$ in the specific heat as well in the electrical resistivity for $x \geq 0.6$. The anisotropy of the resistivity in $YbNi_4P_2$ turns into isotropic behaviour in $YbNi_4As_2$, and the resistivity Kondo maximum shifts to lower temperatures upon approaching the quantum critical concentration. The heat capacity data down to $T = 350\,mK$, shows critical behaviour on the non-magnetic side of the QCP up to $x = 0.2$ identical to that of $YbNi_4P_2$. Measurements of the magnetization showed that the effective magnetic moment decreases from $\mu^c_{\text{eff}} = (4.82 \pm 0.02)\,\mu_B$ at the phosphorous side to $\mu^c_{\text{eff}} = (4.52 \pm 0.02)\,\mu_B$ at the arsenic side, which hints a reduction of the Yb valence. The third missing crystal electric field level E_3, was worked out in collaboration with Z. Hüsges from neutron scattering and heat capacity data. Pure phase $LuNi_4P_2$, synthesized within this thesis, was used as a non-magnetic reference in this specific heat capacity measurements. The suggested levels are $E_1 = 8.5\,meV$, $E_2 = 12.5\,meV$ and $E_3 \approx 25\,meV$. This could be confirmed in high-field magnetization measurements. For a further improvement of the level scheme, nuclear magnetic resonance measurements on large single crystals have been started by H. Yasuoka, H. Tou and coworkers. Angle resolved photoemission spectroscopy (ARPES) experiments on $YbNi_4P_2$ performed in collaboration with D.V. Vyalikh and coworkers show coincidence with a former band structure calculation by H. Rosner, where mainly nickel states contribute to the density of states near the Fermi level. In collaboration with Z. Hüsges, S. Lucas and O. Stockert using samples with masses up to 1800 mg, antiferromagnetic (AFM) fluctuations far above the Curie temperature could be detected by inelastic neutron scattering, which is in good agreement with the non-occurence of an electron spin resonance (ESR) in earlier measurements by J. Sichelschmidt.

The best studied material close to an AFM QCP **$\mathbf{YbRh_2Si_2}$**, was grown from indium flux by a modified Bridgman method. A large number of single crystals have been grown, which vary in shape and size suitable for variable demands. On thin $YbRh_2Si_2$ single crystals, J. Saunders and coworkers confirmed the superconducting transition at $T_c \approx 2\,\text{mK}$ by measuring the thermal noise. On thin $YbRh_2Si_2$ single crystal platelets, a meander structure is prepared using the focused ion beam technique (FIB) by M. Brando and coworkers for low current resistivity measurements at millikelvin temperatures. On large $YbRh_2Si_2$ single crystals, D.V. Vyalikh and coworkers found the "small" Fermi surface by Compton scattering at room temperature. Due to its low lying Néel temperature, its small ordered moment and the absence of single crystals suitable for neutron scattering, the magnetic structure of $YbRh_2Si_2$ is still unknown. With our new large single crystals, magnetization measurements at low temperatures (M. Brando and coworkers) as well as microwave spectroscopy at low temperatures and low fields that were unaccessible until now (M. Scheffler and coworkers) have been started. Single crystals of $YbRh_2Si_2$ which allowed for the preparation of a large flat polished surface were investigated by C. Wetli, M. Fiebig and H. Kroha using time-resolved THz spectroscopy to unravel the dynamics of the Kondo state.

In the series **$\mathbf{Ce(Ru_{1-x}Fe_x)PO}$**, single crystals with $x = 0, 0.44, 0.77, 0.86$ and 1.0 were grown successfully from tin flux. The nature of the QCP that occurs at $x \approx 0.86$, was under debate. Here, AFM order in the vicinity of this QCP was confirmed by magnetization measurements.

We have characterized single crystals of **$\mathbf{SmRh_2Si_2}$, $\mathbf{GdRh_2Si_2}$, $\mathbf{GdIr_2Si_2}$, $\mathbf{HoRh_2Si_2}$ and $\mathbf{HoIr_2Si_2}$** which were grown from indium flux using a Bridgman-type method. The investigation of the magnetic structure by neutron scattering of compounds containing Sm, Gd and Ho is hindered due to their large absorption cross-section for neutrons. Nevertheless, the detailed study of the bulk magnetization of $GdRh_2Si_2$ enabled us to determine its magnetic structure by combining resonant inelastic x-ray scattering (RIXS) with VSM measurements and comparing the latter with the data predicted by a mean-field model. As a follow up, within this framework the rotation of the AFM order parameter driven by an external rotating field was traced by ESR. ARPES revealed two-dimensional electron states at the Si-terminated surface of $GdRh_2Si_2$. These Dirac and Shockley surface states exhibit itinerant magnetism and their spin splitting arises from a strong exchange interaction with the ordered Gd 4f moments. The surface states in $HoRh_2Si_2$ are affected by the electromagnetic exchange interaction (RKKY) as well as by the spin-orbit coupling. The study revealed that the temperature can be used as a tuning parameter for the surface magnetism as the temperature dependent changes in the moment orientation in the bulk are reflected in the surface properties. ARPES studies revealed that for Sm ions in $SmRh_2Si_2$, the electronic properties of bulk and surface are rather similar and the Sm ions behave slightly mixed valent in both cases with a mean valence of about 2.94 at $T = 10\,\text{K}$. Our resistivity and heat capacity data exclude the presence of the Kondo effect in this compound. The electronic surface states of the LnT_2Si_2 compounds were investigated by ARPES in collaboration with D.V. Vyalikh and coworkers.

Contents

List of Figures

List of Tables

List of Abbreviations

ACT alternating current transport option

AFM antiferromagnetic

AFM QCP antiferromagnetic quantum critical point

ARPES angle resolved photoemission spectroscopy

CEF crystal electric field

DOS density of states

DTA differential thermal analysis

EDX energy-dispersive x-ray spectroscopy

EPMA electron probe microscopy analysis

ESR electron spin resonance

FIB focused ion beam

FL Fermi liquid

FM ferromagnetic

FM QCP ferromagnetic quantum critical point

FS Fermi surface

HC heat capacity

HFML High Field Magnet Laboratory Nijmegen, Netherlands

HTP high-temperature phase

HZB Helmholtz Zentrum Berlin

HZDR Helmholtz Zentrum Dresden-Rossendorf

ILL Institute Laue Langevin Grenoble

INS inelastic neutron scattering

Ln lanthanide

LT Lifshitz transition

LTP low-temperature phase

MLZ Maier-Leibnitz Zentrum, Technische Universität München

MPI CPfS Max-Planck-Institut für chemische Physik fester Stoffe Dresden

μSR muon spin resonance

NMR nuclear magnetic resonance

PPMS physical property measurement system

PSI Paul Scherrer Institut, Villigen, Schweiz

PXRD powder x-ray diffraction

QCP quantum critical point

QPT quantum phase transition

RIXS resonant inelastic x-ray scattering

RKKY Ruderman-Kittel-Kasuya-Yosida

SDW spin density wave

SEM scanning electron microscopy

STM scanning tunneling microscopy

TG thermogravimetry

VSM vibrational sample magnetometer

XMCD x-ray magnetic circular dichroism

Introduction

Nowadays, phenomena like magnetism, superconductivity or quantum criticality meet strong interest among solid state physicists who study their origin and fundamental properties from the experimental and theoretical point of view. Materials showing strong correlations are of special interest. In these materials, the electron-electron interactions play a major role and affect the physical properties of the systems. The work on strongly correlated electron systems always comprises the search for materials which enable the understanding of fundamental phenomena with potential for future applications. Many intermetallic systems that contain lanthanide (Ln) elements are strongly correlated systems in which the magnetic properties are determined by the local nature of the $4f$ electrons. For instance, this class of compounds contains hard magnetic materials [1, 2], diluted and dense Kondo systems [3, 4], Kondo insulators [5, 6], valence fluctuating systems [7, 8], heavy-fermion systems and heavy-fermion superconductors [9–11], systems exhibiting no Fermi liquid (FL) behaviour at low temperatures [12] and quantum critical materials [13, 14]. Ln compounds offer the opportunity to investigate a large variety of physical phenomena. Several competing mechanisms are present, such as the Ruderman-Kittel-Kasuya-Yosida (RKKY) interaction which leads to an alignment of magnetic spins yielding an antiferromagnetic (AFM) or a ferromagnetic (FM) ground state, the Kondo interaction which is the screening of the magnetic moments by the conduction electrons and the effects of the crystal electric field (CEF) splitting. The theoretical treatment of Ln compounds, which contain a large number of electrons and in which the different interactions have to be taken into account, is elaborate, if even possible.

In solid state physics, the study of phase transitions is one of the main topics. Two categories of phase transitions can be distinguished. At a first order phase transition, the system shifts discontinuously, for example upon changing its state for increasing temperature from a solid to a liquid. The first derivative of its free energy jumps at the phase transition. In contrast, at a second order phase transition, the system shifts continuously which is, for example, the case at a magnetic phase transition upon lowering the temperature where the second derivative of the free energy is discontinuous. Upon shifting the system towards a second order phase transition, fluctuations of the order parameter grow which extend over the entire system. These are called "critical fluctuations" at the critical point. While classical physics gouverns the fluctuations that evolve by approaching a non-zero temperature phase transition, the fluctuations become quantum mechanical in nature at a zero temperature quantum phase transition (QPT). Near a quantum critical point (QCP) the characteristic energy of the quantum fluctuations becomes larger than the thermal fluctuation energy of k_BT. The influence of an existing QCP on the physical properties of a system can already be observed at non-zero temperatures. The FL behaviour of the system changes into non-FL behaviour when approaching the QCP. It is believed that in many systems, the arising unusual metallic states act as precursors for the development of superconductivity.

At a QPT, different microscopic systems exhibit the same scaling behaviour. They show scale invariance in space and time of the critical fluctuations extending over a wide region in the phase diagram. Thus, the fascinating property of a phase transition is that different materials show universality in their behaviour at this phase transition and can be described by the same theory which is scale invariant. The existence of a QCP is connected to a diverging Grüneisen parameter. Its nature can be characterized by comparison with the predicted power law behaviour of the volume thermal expansion and the specific heat in the frame of the spin density wave (SDW) scenario [15]. A second scenario, which was proposed for systems where no SDW order is found directly at the QCP, is the Kondo-breakdown scenario [16, 17]. For this scenario, ω/T scaling of the dynamic susceptibility $\chi(\vec{q}, \omega, T)$ is predicted [18, 19] which is not expected in the SDW theory.

The search for compounds where quantum criticality emerges often starts with the search for compounds with low lying ordering temperatures. If a tuning parameter for a particular system exists, which at a certain value allows to suppress the magnetic order down to lowest temperatures, this point is called a QCP. Pressure, magnetic field or the substitution of elements can act as such tuning parameters. Quantum critical behaviour was not only found in intermetallic compounds such as $YbRh_2Si_2$ [20], $CeCu_2Si_2$ [21], $CeIn_3$ [22] or $CeCu_{6-x}Au_x$ [23], but was also studied in oxides such as $Er_2Ti_2O_7$ [24] and organic compounds [25]. In the past, mainly the suppression of AFM order resulting in an antiferromagnetic quantum critical point (AFM QCP) has been investigated, that is due to the fact that the FM order is not stable all the way down to lowest temperatures. Instead, for many FM materials the second order phase transition into the magnetically ordered state turns into a transition of first order or a different ordered phase forms [26]. In the recent past, only few compounds close to a ferromagnetic quantum critical point (FM QCP) have been identified and attracted considerable attention. One of the rare examples, where the existence of a FM QCP was confirmed is $YbNi_4(P_{1-x}As_x)_2$ at $x \approx 0.1$.

The aim of this work is to prepare and characterize compounds that allow the study of physical phenomena near a QCP. While the low temperature properties of different Ce compounds have been investigated intensively in the past, only few Yb (which is the hole analogon of Ce) compounds were studied. One reason for this imbalance is the difficulty in the preparation of Yb compounds due to the high vapour pressure of this element. Therefore, one focus of this work is the single-crystal growth and the characterization of Yb compounds. Nowadays, measurement techniques facilitate the investigation of quantum-critical compounds down to sub-millikelvin temperatures and the quest for high-quality single crystals is of extended interest.

This thesis is organized as follows: In Chapter 1 the basic concepts and experimental techniques concerning single crystal growth and structural and chemical characterization are presented. Furthermore, a summary of the previously known physical properties of Ln-based compounds together with a description of the applied methods for their characterization is given. The crystal growth and characterization of $YbNi_4P_2$, which is a system close to a FM QCP is described in Chapter 2. The results on $YbRh_2Si_2$, which has become established in the past as a canonical example for a system close to an AFM QCP, are presented in Chapter 3. The series $Ce(Ru_{1-x}Fe_x)PO$ where the existence of a FM QCP was proposed recently is investigated in Chapter 4. Chapter 5 is dedicated to the preparation and characterization of magnetic materials showing no Kondo effect for which the occurence of electronic surface states was predicted by band structure calculations. The aim here is to study the influence of the bulk magnetic properties on these states. In the past, the band structure of different $4f$ and $5f$ materials was studied by angle resolved photoemission spectroscopy (ARPES) [27] and we contribute to this field by providing high-quality single crystals of Sm, Gd and Ho based $\mathrm{LnT_2Si_2}$ (T = Rh, Ir) compounds. At first, in chapters 2 to 5 an introduction to the respective compound is given followed by a summary of the specific results. The details can be found in the main part of each chapter.

1

Basic concepts and experimental techniques

1.1 Crystal growth

The following sections, provide an overview about the relevant aspects concerning the crystal-growth experiments performed in this thesis. A general introduction into the field of crystal growth is given in [28]. Working with phase diagrams as collected in [29] is indispensable especially when growing crystals from an off-stoichiometric solution (flux). The temperature dependent vapour pressure of the elements, summarized in [30], has to be considered when performing crystal-growth experiments using highly-volatile elements.

1.1.1 Nucleation and crystal growth

The thermodynamic potential which can be used to describe a system in a crystal growth experiment is the Gibbs free energy

$$G = H - TS = F + PV, \qquad dG = -SdT + Vdp + \sum_i \mu_i dn_i, \tag{1.1}$$

with the enthalpy $H = U + PV$, the Helmholtz free energy $F = U - TS$, the temperature T, the entropy S, the volume V, the pressure p, the chemical potential μ and the mole number n of the i-th component. U is the internal energy. For constant temperature, pressure and number of particles, the Gibbs free energy is constant, $dG = 0$. This is the case, when two phases, such as liquid and solid coexist in the thermodynamic equilibrium during a phase transition. Under equilibrium conditions, crystal growth is impossible. The driving force for crystallization is the difference in the chemical potential $\Delta\mu$ of the liquid and the solid phase. The growth rate depends directly on $\Delta\mu$ while ΔT is the associated undercooling. At low temperatures, the solid phase has a lower Gibbs energy than the liquid phase and is formed upon cooling. By cooling down a melt of a certain composition several cases have to be distinguished. (i) The melt solidifies as a stoichiometric phase of the identic stochiometry (congruent solidification). (ii) The melt solidifies with an eutectic composition. (iii) The system cools down meeting a miscibility gap where no thermodynamically stable composition exists as a solid. In this peritectic case, a part of the melt solidifies and the composition of the remaining liquid shifts towards the eutectic.

Nucleation can take place in a liquid at surfaces such as the wall of the container, at the seed crystal, or at impurities (heterogeneous nucleation) or away from any surface (homogeneous nucleation). In a homogeneous nucleation process, no surface is present to support the formation of the initial nucleus. Here, during the nucleation, the change of the Gibbs free energy composes of the (negative) volume energy $\Delta G_v \propto r^3$ of the nucleus with radius r and the (positive) energy that is necessary to form the surface $\Delta G_s \propto r^2$. A critical size r^* can be deduced for the three dimensional case according to $\Delta G_{\text{nucleus}} = \Delta G_v + \Delta G_s$ and $\Delta G'_{\text{nucleus}}(r) = 0$. For $r > r^*$ the free energy of the system decreases when a nucleus grows. A nucleus will be formed and will grow further at/above the critical radius r^*. Small nuclei with $r < r^*$ will be dissolved again by the melt. In the Bridgman growth experiments, Sec. 1.2.3, heterogeneous nucleation at the crucible wall as well as homogeneous nucleation in the flux can take place while in Czochralski growth experiments, Sec. 1.2.4, only heterogeneous nucleation at the inserted seed occurs. While in the Bridgman-type flux-growth experiments sometimes up to 100 small single crystals are formed in a random manner, the Czochralski experiments yield one large single crystal due to the availability of the seed crystal. In these experiments, the output can be highly deterministic. To induce crystal growth, the supersaturation or undercooling of the melt is required. In a small temperature region below the melting point of the solid it is possible to decrease the temperature of the (metastable) melt without the occurence of a crystallization (Ostwald-Miers region). During the crystal growth process, which is accompagnied by a first order phase transition latent heat is released upon formation of the new crystal lattice. To provide suitable growth conditions not only a material transport towards the growing crystal but also a heat and a flux transport away from the growth front have to be supported. A molecular model proposed by Kossel and Stranski [31, 32] states the following: Consider a flat lattice plane, where atoms get attached on and are dissolved from frequently. The possibility that an atom stays attached to this surface is low. In the crystal growth process this is the slowest step which determines the growth velocity. Ones a first atom stays attached to the surface permanently, the subsequent completion of the lattice plane is fast. Due to this mechanism, the crystal reproduces its morphology with flat faces. Faces with the lowest growth velocity are those with the largest energy of the nucleus formation on the respective surface. They determine the habitus of the (ideal) single crystal in the sense that fast growing faces die out.

According to the general definition which includes quasicrystals, a single crystal is a set of atoms which generates sharp reflections in a scattering experiment. The lattice of an ideal single crystal (excluding quasicrystals) is formed by a periodic repetition of a set of atoms which are part of the unit cell. The unit cell is fully described by the lattice vectors and the angles inbetween. In this thesis, crystals from Bridgman or box-furnace experiments with a minimum edge length of 1 mm are referred to as single crystals, conglomerates of smaller ones as polycrystals. By Czochralski growth, large samples can be obtained. These are referred to as single crystal if more than 80% of the sample belongs to one single crystal grain with a misalignment below 1° determined by Laue analysis. Otherwise, the sample is called polycrystalline. The aim of the crystal growth experiments is not only to obtain large single crystals but also to minimize the emerging crystal defects.

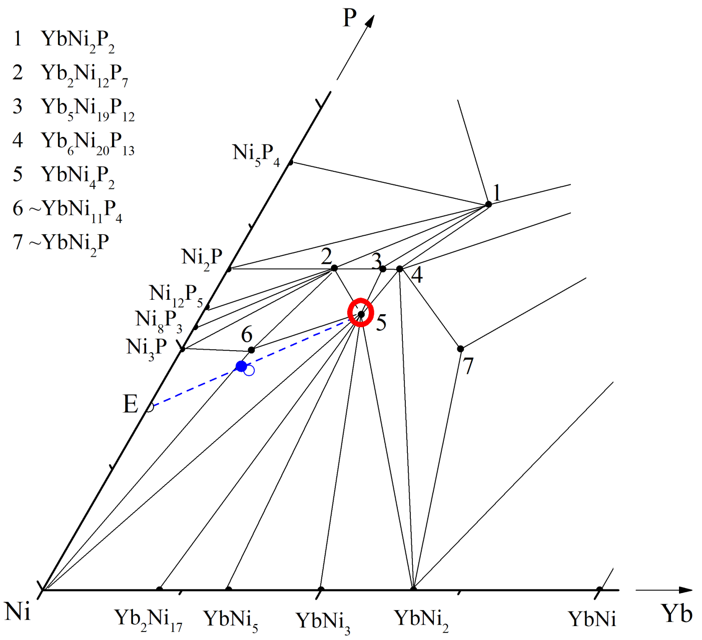

Figure 1.1: Yb-Ni-P phase diagram, isothermal section at 870 K (after Kuz'ma *et al.* [33]). The black circles indicate stable phases at 870 K. The blue solid circle marks the composition from which $YbNi_4P_2$ was grown in the frame of this thesis. The solidus and liquidus temperatures, associated with the binary border systems are summarized in [29]. The eutectic of the composition $Ni_{81}P_{19}$ is labelled by "E". The dashed blue line indicates the path of the crystallization in the growth experiments.

1.1.2 Ternary intermetallic compounds and phase diagrams

In contrast to binary intermetallic systems where the phase diagrams are known in many cases, only for some of the three-component systems isothermal sections of the respective phase diagram are reported. As an exemplary system, the Yb-Ni-P phase diagram is discussed here. For this system, an isothermal section at 870 K of a phase diagram was reported bei Kuz'ma *et al.* [33] which is depicted in Fig. 1.1. In samples, used in their study which were annealed in closed ampoules at 870 K, there exist 12 binary and 7 ternary known stable phases besides the elements. In an isothermal section, several triangular regions are marked (thin solid black lines). The corners of these three-phase triangles show the three coexisting phases in samples with a total composition located inside the respective triangle. It is not known which are the congruently melting compounds among the reported ternary phases but it is known from preliminary work that $YbNi_4P_2$ which is marked by a red circle in the phase diagram is an incongruently melting compound. It was found that this phase can be grown from an off-stoichiometric composition in a closed Ta crucible using the eutectic with the composition of Ni-Ni_3P as the flux [14]. It turned out that it is also possible to use the same starting composition for the growth from a levitating melt using the Czochralski method. The starting composition corresponds to an $YbNi_4P_2$: $Ni_{81}P_{19}$ ratio of 1:1 and is marked by a blue solid circle in Fig. 1.1. The open circle marks a composition from which $YbNi_4P_2$ can also be grown [14]. In growth experiments using the marked compositions (blue circles) with $T > 1100\,°C$ and $p = 20\,bar$, the resulting phases were $YbNi_4P_2$, Ni_3P and Ni while $YbNi_{11}P_4$ (phase 6) did not occur.

The liquidus line of a binary system corresponds to a liquidus surface in a ternary phase diagram and the binary solidus line to a surface of all solidus points in the ternary diagram. In such a phase diagram, the coexistence of two solid phases in the melt appears as an eutectic line corresponding to an eutectic point in a binary diagram. A ternary eutectic is a distinct temperature point in the phase diagram where three solid phases coexist with the ternary eutectic liquid. Such a ternary eutectic has a low melting point and is thus an excellent flux to grow the neigbouring phases from. For the Yb-Ni-P phase diagram, the surfaces of all liquidus and that of all solidus points are unknown. The starting composition used in our experiments is in the liquid state above $T = 1285\,°\mathrm{C}$. Upon cooling between 1285 °C and $T_E = 875°\mathrm{C}$ [34] no other phases than $\mathrm{YbNi_4P_2}$ and the Ni-$\mathrm{Ni_3P}$ eutectic form.

1.2 Crystal growth methods

In this section, the different crystal growth methods that were used in this work are introduced in general. An overview about the methods which were applied to grow the different compounds, is shown in Tab. 1.1. A more detailed description of the growth conditions can be found in the section for each compound separately in the following chapters.

1.2.1 Ln-compounds: Crystal growth from flux

Growing crystals of Yb compounds containing transition metals (like Fe, Ni, Rh or Ru) means dealing with the high vapour pressure of the first and the high melting temperature of the latter. For the crystal growth of Ln compounds therefore often a flux method at high temperatures is applied. By using a flux it is possible to solve the high-melting elements as well as the elements with low boiling points and obtain a melt with a moderate vapour pressure which is suitable for the growth. A good overview about the use of metallic fluxes is given in [35–37]. In the past, the flux method has been successfully applied for the growth of Ln compounds using indium, tin or lithium as flux [37–41]. In some cases, the use of a solvent leads to the formation of unwanted phases, in this regard the use of a self-flux can be more successful. Even when using a flux, the growth temperature often exceeds 1200°C. Due to the highly volatile and reactive constituents the growth usually is performed in a closed niobium or tantalum crucible. Another attempt is the application of inert gas pressure during the growth. Due to its high reactivity, reports on the growth of phosphorous containing bulk single crystals are rare. Binary phosphides have been grown by a liquid-encapsulated Czochralski method (InP [42],[43]), by chemical vapour phase transport ($\mathrm{CuP_2}$ [44]) or under high pressure ($\mathrm{CoP_3}$ [45]). Ternary phosphides have been grown in a closed crucible from tin flux ($\mathrm{LnRu_2P_2}$[37, 46]) or by applying the Bridgman method in combination with the accelerated crucible rotation technique (ACRT) ($\mathrm{ZnGeP_2}$ [47]). After a growth experiment from flux, the flux has to be removed either by etching, by centrifugation or by pulling the crystal out of the flux in case of the Czochralski method.

1.2.2 Synthesis and crystal growth in a box furnace

Sample synthesis, prereactions and crystal growth experiments were performed in a box furnace in air (Nabertherm L5/G19, Nabertherm L5/S) or in a box furnace where a protective Ar atmosphere is available (Linn). In both devices, temperatures up to 1100°C can

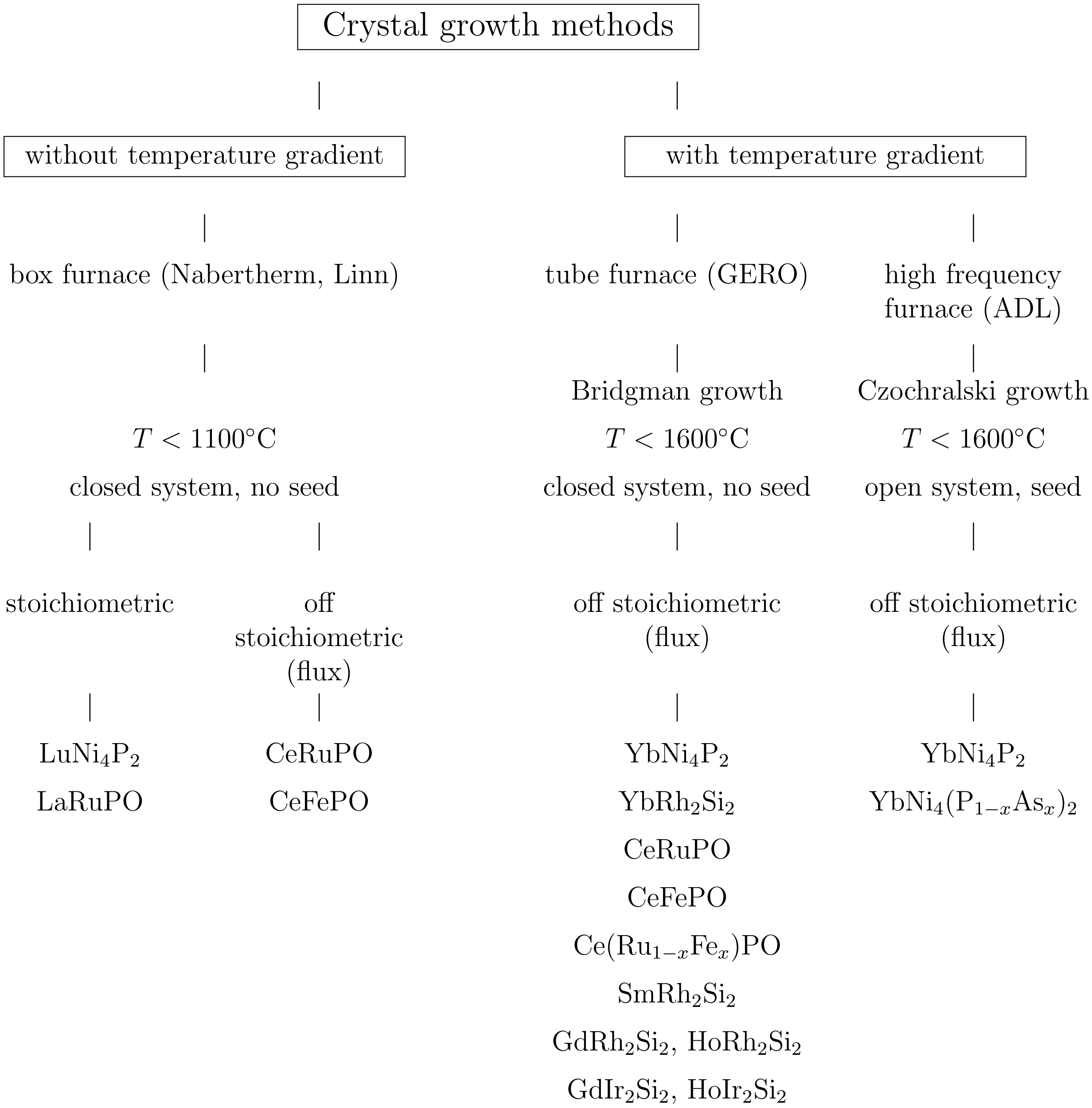

Table 1.1: Overview about the crystal growth methods applied in the experiments.

be achieved. Usually the experiments are performed using quartz ampoules as crucible material. In cases where the occurrence of a high pressure during the experiments due to the evaporation of the educts is expected, it is crucial to use niobium or tantalum as the crucible material. The use of quartz ampoules in these cases would lead to the explosion of the ampoule. The use of metallic crucibles requires the application of a protective atmosphere. In a box furnace, the temperature gradient is small and cannot be influenced therefore in many cases the obtained single crystals are small since nucleation starts in the crucible at different places at the same time. The use of a seed usually is not possible in such experiments since it is dissolved by the melt.

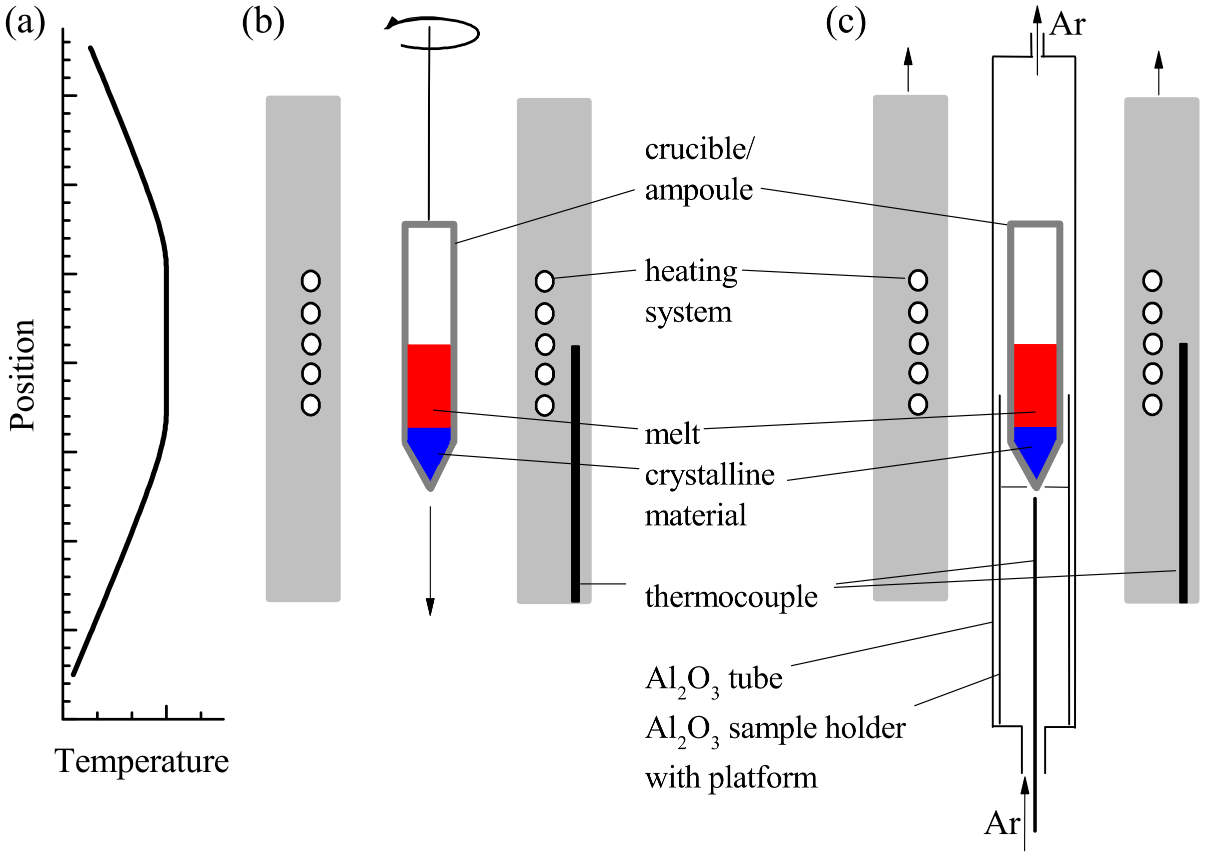

Figure 1.2: Bridgman technique: The sample is moved through a temperature gradient (a) by lowering the ampoule (b) (after [28]). The setup used in this work is depicted in (c).

1.2.3 Bridgman technique

The Bridgman technique often is used to grow single crystals of congruent melting materials. In the conventional Bridgman technique, shown in Fig. 1.2 (a, b), the crystallization of a sample is controlled by moving an ampoule which contains the molten educts through a temperature gradient. The ampoule is moved from the hotter to the colder zone of a tubular furnace. During cooling, a growth front between melt and solid forms, where the crystallization takes place. The disadvantage of this method is the direct contact of the material with the crucible which causes strain and defects in the grown single crystal.

In this work, a modified Bridgman method was applied for the growth experiments of $\mathrm{YbNi_4P_2}$, $\mathrm{LnRh_2Si_2}$ and the series $\mathrm{CeRu}_{1-x}\mathrm{Fe}_x\mathrm{PO}$ in a vertical resistive furnace (GERO HTRV70250/18) in which a maximum temperature of 1600°C was used. A typical temperature-time profile is shown in Fig. 3.2. In our experiments, the crucible is placed on a sample holder which remains on a fixed position, Fig. 1.2 (c). To achieve crystallization, the furnace is moved upwards. This setup is advantageous since the furnace is decoupled from the sample holder and the sample does not experience vibrations due to the motion of the furnace. A flow of argon through the growth tube was present (≈ 150 ml/min) in the experiments which prevented oxidation of metallic crucibles and provided an additional cooling at the bottom of the crucible. The ternary and quarternary materials do not melt congruently, therefore flux growth was performed. For $\mathrm{YbNi_4P_2}$ a Ni-P self-flux, for the $\mathrm{LnRh_2Si_2}$ compounds an indium flux and for the series $\mathrm{CeRu}_{1-x}\mathrm{Fe}_x\mathrm{PO}$ tin flux was used. In an ideal growth experiment, solidification should start at the coldest point, the tip at bottom. Afterwards, the crystal should grow from the tip. Ideally, this should prevent further nucleation in the crucible. But in the experiments the formation of many small crystals was observed. An explanation for this could be the constitutional undercooling of the melt. An improvement of the mixing of the melt e.g. by rotating the crucible could prevent the undercooling. In these experiments it is not possible to use a seed in the present set up since the cooling at the lower part of the crucible is not strong enough to avoid that the seed is dissolved by the melt. A disadvantage of this method is that, like in box furnace experiments, the growth can not be directly observed since it is performed in a closed crucible (closed system).

1.2.4 Czochralski technique

The Czochralski method was applied to grow large single crystals of the $\mathrm{YbNi_4(P}_{1-x}\mathrm{As}_x)_2$ series from an off-stoichiometric solution (self-flux). The growth experiments were performed in a commercial ADL (Arthur D. Little) growth chamber including pulling heads equipped with a high-frequency generator (Hüttinger) that provides a maximum power of about 30 kW. The maximum temperature was $\approx$ 1600°C during the homogenization period. The temperature was measured with an IRCON pyrometer. In our setup, Fig. 1.3, it is possible to grow single crystals from a levitating melt. The melt levitates in a magnetic-field gradient established by a high-frequency field and enhanced by the special shape of a Hukin-type crucible. Due to the high vapour pressure of the educts Yb, P, As, an argon pressure of 20 bar was applied. Usually, the growth experiments consisted of several steps: the preparation of the precursor, the homogenization and the growth. The preparation of the precursor was done in a box furnace. Here, the process was optimized such that the reaction was performed at comparably low temperatures ($\approx$ 900°C) to avoid the reaction with the crucible material. The prereacted material consisting of nickel phosphides, ytterbium phosphides and ternary Yb-Ni-P compounds subsequently was placed in the crucible of the high-frequency furnace and homogenized by increasing and reducing the power up to 10 times. By observing the melt directly through the window of the growth chamber it is possible to see whether the material is solid or liquid. For each composition, the liquidus and solidus temperature can be determined as shown in Fig. 2.7. The seeding was usually done at a temperature $\approx$ 50°C

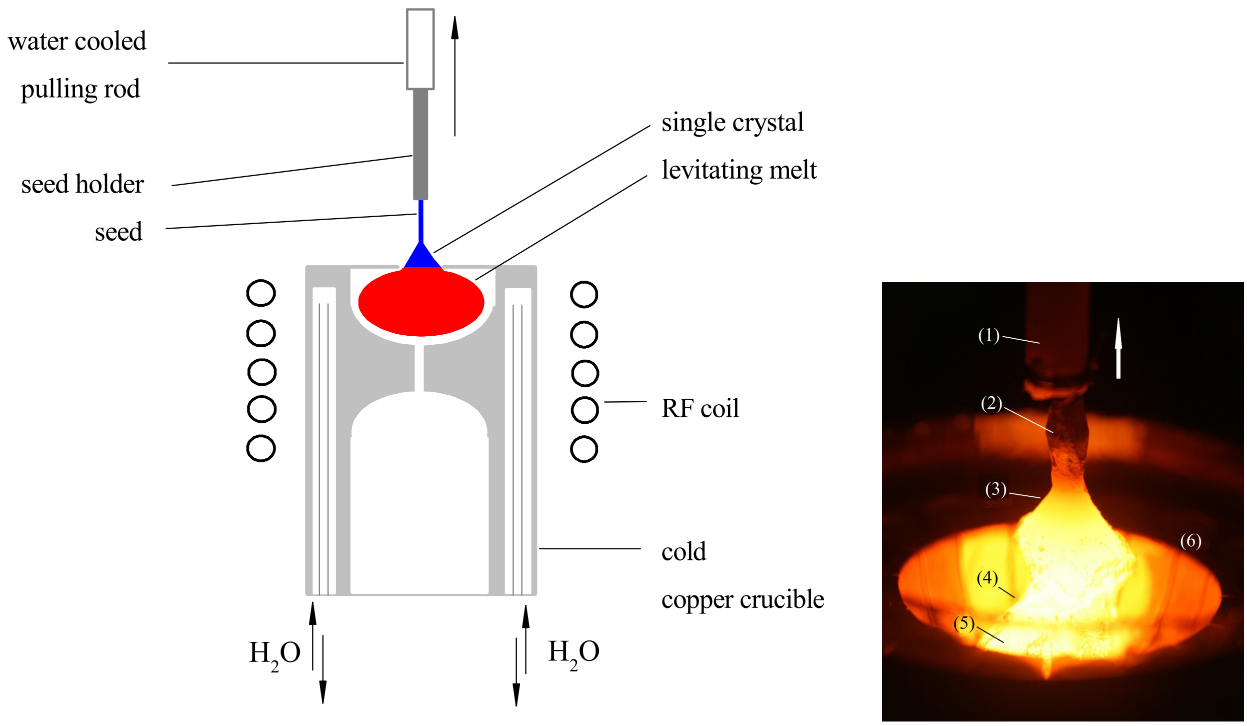

Figure 1.3: Czochralski technique. *Left:* Schematic drawing of the setup for the Czochralski growth experiments. *Right:* Czochralski growth from the levitating melt: The $YbNi_4(P_{1-x}As_x)_2$ crystals were grown from a levitating melt. The arrow marks the pulling direction of the seed (2) in the seed holder (1). The meniscus (4) marks the border between the grown sample (3) and melt (5) levitating in a cold copper crucible (6). Figure (under CCA 3.0 licence) taken from [48].

above the liquidus temperature. A pulling rate of about 0.2 mm/h was chosen which leads to a duration of 3-4 days for one growth.

This method in the present setup has several outstanding advantages compared to the other methods described above: (1) It is possible to use a seed, (2) the orientation of the crystal to grow can be predetermined by using a seed which is cut in a certain orientation, (3) the process can be directly observed and influenced in situ (open system) (4) the growth can be performed from a levitating melt which supports the growth of pure crystals and (5) the single crystal is pulled out of the flux and is separated from the flux in situ. An elaborate centrifugation step is not needed.

1.3 Structural and chemical characterization

In this section, the methods are described which were applied for the structural and chemical characterization of the materials. The crystal structure was confirmed by powder x-ray diffraction (PXRD), Sec.1.3. The chemical composition was analyzed by energy-dispersive x-ray spectroscopy (EDX) described in Sec. 1.3 and the orientation of the single crystals was determined by x-ray Laue backscattering as shown in Sec. 1.3.

Powder x-ray diffractometry

In a three-dimensional crystal, the atoms of the crystal lattice form parallel lattice planes with distance d. The angle between an incident monochromatic x-ray beam with wavelength λ and a lattice plane is denoted by θ. Bragg's Law states, that constructive interference occurs, if the condition $n\lambda = 2d \sin\theta$ is fulfilled for any integer n. Powder diffraction patterns contain several characteristic information about the structure of a crystalline material: From the angle under which the reflection in the pattern occurs one can calculate the lattice parameters and determine the possible crystal system. The reflection intensity is connected to the structure factor of the atoms in the unit cell. The reflection broadening can be used to estimate crystallite size, and the background in the pattern contains information about the fraction of the amorphous phase. Each reflection in a powder diffraction pattern of a material belongs to a set of lattice planes indicated by the Miller indices (hkl).

In this work, PXRD was done to confirm the growth of crystals with the desired structure, to exclude the formation of impurity phases and to determine the lattice constants. The powder diffraction patterns were recorded on a diffractometer with Bragg-Brentano geometry (Bruker AXS D8, reflection) or on a Guinier diffractometer (Seifert, transmission) at room temperature. The characteristic x-rays used for measurements were the lines of copper $\mathrm{K}_{\alpha_1} = 0.1540598\,\mathrm{nm}$ and $\mathrm{K}_{\alpha_2} = 0.1544426\,\mathrm{nm}$ (Bruker AXS D8) and of molybdaenum $\mathrm{K}_{\alpha_1} = 0.709300\,\mathrm{nm}$ and $\mathrm{K}_{\alpha_2} = 0.713590\,\mathrm{nm}$ (Guinier). The K_β line was filtered off by a nickel foil. The reflection positions were refined with GSAS (General Structure Analysis System [49]).

Scanning electron microscopy (SEM) and energy-dispersive x-ray spectroscopy (EDX)

By scanning electron microscopy (SEM) an image of the surface of a sample can be created while by EDX the elemental composition of the surface can be determined. The sample is scanned by an electron beam which is emitted by a heated tungsten cathode. Between this primary beam and the sample surface several interactions take place. The elastically back scattered electrons and the inelastically scattered secondary electrons are used for imaging. In the obtained images from polished surfaces, a phase contrast can be seen since the scattering cross section of the elastically back scattered electrons is the higher the higher the atomic number of an element. The chemical analysis of a sample is done analyzing the energy spectrum of the emitted characteristic x-rays. In this work, a scanning electron microscope, Zeiss DSM 940 A, with an additional energy dispersive detector (EDX, EDAX® Ametek GmbH) was used. All measurements were performed with an accelerating voltage of 30 kV. The precision of the chemical-composition analysis is about 1-3 atomic percent and depends on the atomic number.

Laue backscattering method

The Laue method is used to determine the orientation of a single crystal relative to an x-ray or neutron beam. Addionally, the shapes of the obtained reflections give information on the crystallinity of the single crystal. Scattering processes are described in the momentum space. The wave vector of the incident beam is denoted by $\vec{k_0}$, and of the reflected beam by $\vec{k}$. The incident beam is scattered by the lattice planes of the crystal. The Laue condition for constructive interference $\vec{G}_{hkl} = \vec{k} - \vec{k_0}$ has to be fulfilled, which means, that the scattering vector $\vec{k} - \vec{k_0}$ has to be equal to a vector of the reciprocal lattice. For a periodic arrangement of atom groups the vectors $\vec{G} = h\vec{g}_1 + k\vec{g}_2 + l\vec{g}_3$ of the reciprocal lattice are determined by $e^{i\vec{R}\vec{G}} = 1$ with the vector $\vec{R}$ of the direct lattice. Each point in a Laue pattern corresponds to a set of lattice planes denominated by the Miller indices (hkl).

In this work, Laue patterns were recorded using an x-ray equipment "Micro 91" (Müller) with tungsten anode. The 12 keV electrons produced a beam consisting of Bremsstrahlung with a beam diameter of about 0.5 mm. The time of exposure of the image plates to the x-ray beam was between 3 to 15 min for each measurement. The analysis of the images was done with the software "Orient Express" [50].

Some of the large single crystals of the $\mathrm{YbNi_4(P_{1-x}As_x)_2}$ series have been investigated by O. Stockert (Max-Planck-Institut für chemische Physik fester Stoffe Dresden (MPI CPfS)) using neutron Laue backscattering. The respective measurements have been performed at the Institute Laue Langevin Grenoble (ILL). The advantage of using neutrons is that their penetration depth into the material is in the cm range while with x-rays it is only possible to investigate some μm below the surface. With a pinhole diameter determining the incident neutron beam of 6 mm and a distance between film and crystal of 5 cm it is not possible to detect small misaligned grains. The Laue pattern obtained by this method show sharp Laue spots if the main part of the crystal belongs to the same grain.

1.4 Properties of lanthanide compounds

The elements of the Ln series in the periodic table are characterized by an increasing number n of electrons in the $4f$ shell for increasing atomic number accompagnied by a decrease in their radii (Ln contraction). This phenomenon is caused by the increasing nuclear charge which leads to an attractive force on the electrons of the outer shells. These elements have the electronic configuration $[\mathrm{Xe}]4f^n5d6s^2$ and give their $5d$ and $6s$ valence electrons to the conduction band when they are part of a solid. In most of the Ln compounds investigated in this work, the valence of the Ln ion is near 3+ which leads to an odd number of unpaired spins such that these compounds are magnetic. The investigated compounds in this thesis are the Ce and Yb based Kondo-lattice systems $\mathrm{YbNi_4P_2}$, $\mathrm{YbRh_2Si_2}$ and CeRuPO which are presented in Chapters 2, 3 and 4. Their magnetic moments are screened by the conduction electrons (Kondo effect) which leads to very low ordering temperatures - in the Yb compounds of only several millikelvins. The magnetic interaction, the RKKY interaction, between the local magnetic moments is indirect and mediated by the conduction electrons [51–53]. The low lying antiferromagnetic or ferromagnetic ordering temperatures of these compounds allow for tuning them to an (AFM or FM) QCP using a control parameter like pressure, magnetic field or doping (chemical pressure). Furthermore, Sm, Gd and Ho compounds of the $\mathrm{LnT_2Si_2}$ (T = Rh, Ir) structure which do not show the Kondo effect are characterized in this thesis (Chapter 5).

1.4.1 Crystal electric field and Kondo effect

In the temperature range $T = 2 - 300\,\mathrm{K}$, the CEF as well as the Kondo effect influence many of the investigated quantities like magnetization, electrical resistivity or specific heat capacity. We therefore give a brief overview on these topics.

Ground state of ions in a crystal electric field

The orbitals of a Ln ion with different orbital angular momentum $\hat{\vec{L}}$ and different energies couple to the spin $\hat{\vec{S}}$ of the ion. The spin-orbit coupling yields a total angular momentum $\hat{\vec{J}} = (\hat{J}_x, \hat{J}_y, \hat{J}_z)$ with the quantum number J which takes values according to $|L-S| \leq J \leq L+S$. The splitting energy between levels of different J is of the order of $\Delta E^{SO} \approx 100\,\text{meV}$. The degeneracy of a J multiplet is $2J+1$. For a Ce^{3+} ion, for instance, the splitting between the ground state multiplet ($J = 5/2$) and the first excited multiplet level ($J = 7/2$) is $\approx 300\,\text{meV}$ [54], while this energy difference is smaller for a Sm^{3+} ion ($\approx 134\,\text{meV}$) [55]. In the solid, the Ln atoms give their valence electrons to the conduction band and can be considered as ions. They are surrounded by neighbouring ions which cause an electrostatic potential at the site of each Ln ion. Since in general this potential is not spherical symmetric it leads to an anisotropy in the magnetic properties of the respective compound. In the presence of this CEF, the degeneracy of each J multiplet is lifted and the energy difference between the CEF levels is $\Delta E^{CEF} \approx 10\,\text{meV}$. This is much smaller than ΔE^{SO} since the wave functions of the $4f$ electrons are spatially less extended than the more extended wavefunctions of the $5d$ and $6s$ valence electrons. The combination of quantum numbers L, S that minimizes the energy and belongs to the ground state can be found by applying Hund's rules, see Tab. 1.2. Kramers theorem which states that for an odd number of electrons in the $4f$ shell the ground state is at least two-fold degenerate (doublet state) is applicable for e.g. Ce^{3+} and Yb^{3+}. Ce^{3+} ($4f^1$ configuration) and Yb^{3+} ($4f^{13}$ configuration) are socalled "Kramers ions" due to their odd number of electrons. In the presence of an applied magnetic field, the degeneracy of the ground-state doublet is lifted. The splitting energies for laboratory magnetic fields of about 10 T are about one order of magnitude smaller than the CEF splitting. How the CEF acts on the charge distribution of the $4f$ wave function in cubic or tetragonal environments was calculated for different Ln ions and is illustrated in [56]. An introduction to the topic of the crystal electric field effects can be found in [54, 55]. The theoretical description of the CEF effect usually is done using the Stevens-operator formalism [57] but for a real solid it is not possible to calculate the splitting energies caused by the CEF without using experimental input. The crystal electric field causes an anisotropy of the charge distribution in the solid and effects on different measured quantities can be found.

The splitting of the J multiplet in the presence of the CEF is small ($10\,\text{meV} \approx 100\,\text{K}$) and therefore usually the full effective magnetic moment of the J multiplet is obtained at elevated temperatures. The effective magnetic moment can be calculated according to

$$\mu_{\text{eff}}^{\text{theo}} = g_J\sqrt{J(J+1)}\mu_{\text{B}}, \quad g_J \quad = \quad 1 + \frac{J(J+1) + S(S+1) - L(L+1)}{2J(J+1)} \tag{1.2}$$

and determined experimentally from the slope of the linear fit to the inverse magnetic susceptibility for temperatures higher than 200 K. Below, CEF effects have strong influence on the magnetization.

Dilute Kondo systems

Dilute Kondo systems show a characteristic behaviour of the electrical resisitivity. In these systems, the magnetic moments are impurities in the crystal, with stochastic occurrence of low concentration in the host material. The effect was studied experimentally in noble

Ln^{3+}	shell	S	L	J	d	g_J	$\mu_{\mathrm{eff}}^{\mathrm{theo}}$ $[\mu_{\mathrm{B}}]$
Ce^{3+}	$4f^1$	5/2	5	5/2	6 fold	6/7	2.54
Sm^{3+}	$4f^5$	5/2	5	5/2	6 fold	2/7	0.85
Gd^{3+}	$4f^7$	7/2	0	7/2	8 fold	2	7.94
Ho^{3+}	$4f^{10}$	2	6	8	17 fold	5/4	10.6
Yb^{3+}	$4f^{13}$	1/2	3	7/2	8 fold	8/7	4.53

Table 1.2: Configuration of the $4f$ shell for selected Ln^{3+} ions, S, L, J quantum numbers of the state with minimal energy according to Hund's rules and degeneracy d of the J multiplet $(2J+1)$. The effective magnetic moment was calculated according to Eqn. 1.2 where g_J is the Landé factor.

metals, in which magnetic impurities were introduced [3]. In these systems, the spins of the conduction electrons interact with the magnetic moment of the impurity by spin-flip scattering. This gives an additional contribution to the specific electrical resistivity, and leads to a logarithmic increase of the resistivity at low temperatures. Jun Kondo deduced in fundamental work [58], that the electrical resistivity shows a minimum and increases logarithmically at lower temperatures. He treated the spin-flip scattering on magnetic impurities by pertubation theory and found in each order logarithmic divergencies, which had to be renormalized. In metals with magnetic impurities, he expected the behaviour of the resistivity to be

$$\rho(T) = aT^5 + c\rho_0 - c\rho_1 \ln T, \tag{1.3}$$

where c is the concentration of the magnetic impurities, ρ_0 is the residual resistivity and ρ_1 is a positive constant. The aT^5 term includes the phonon contribution of the lattice, while an additional contribution taking into account the e-e scattering was not included into the model. This leads to a minimum in the resistivity at the Kondo temperature

$$T_K = \left(\frac{c\rho_1}{5a}\right)^{\frac{1}{5}} \tag{1.4}$$

and a logarithmic increase of the resistivity for temperatures below T_K. The Kondo temperature T_K, is the energy difference between the Kondo singlet and triplet state

$$\Delta E = k_B T_K.$$

The specific heat capacity of a dilute Kondo system was derived by Schotte and Schotte [59]. The Kondo temperature T_K, can be determined from the entropy S and is twice the temperature when S of the two level system consisting of the spin singlet and spin triplet states has the value

$$S|_{\frac{1}{2}T_K} = \frac{1}{2} k_B \ln 2.$$

Kondo-lattice systems

The Kondo-lattice effect has been reported in many compounds where Ce or Yb act as scattering centers. In contrast to dilute systems where the Kondo screening acts on single impurities (”single ion” effect), the system forms a Kondo lattice if the magnetic moments are arranged periodically [60]. $CeAl_3$ was the first system where this effect was studied [61, 62]. The crossover from a dilute Kondo system to a Kondo-lattice system was investigated by electrical transport measurements in the series $Ce_xLa_{1-x}Cu_6$ by Sumiyama *et al.* [63]. For low Ce concentrations the system behaves like a dilute Kondo system and turns into a Kondo-lattice system for high Ce content. When lowering the temperature, the electrical resistivity of a Kondo-lattice system decreases, runs through a minimum, increases, and after reaching the maximum, it drops down rapidly. The shape of the peak varies from material to material and depends on the crystal orientation. The coherent Kondo scattering leads to an enhanced density of states (DOS) at the Fermi level $D(E_F)$. This can be quantified as an effective mass m^* of the charge carriers which founded the terminology ”heavy-fermion systems”.

The Kondo-lattice temperature T_K^*, usually is determined from the entropy in analogy to the single ion Kondo temperature T_K. T_K^*, is twice the temperature when the entropy S of the two niveau system consisting of the spin singlet and spin triplet states has the value

$$S|_{\frac{1}{2}T_K^*} = \frac{1}{2}\, k_B \ln 2.$$

The entropy S can be obtained from the magnetic part of the specific heat $C_{\text{mag}}(T)$ via

$$S = \int \frac{C_{\text{mag}}}{T}\,\mathrm{dT}.$$

Furthermore, the width at half maximum of the enhanced density of states at the Fermi level (Abrikosov-Suhl resonance) is connected to the Kondo temperature T_K^* [64].
In the solid, the CEF is present. At low temperatures due to the Kondo effect, the lowest lying CEF doublet state hybridizes with the spin of a conduction electron. It splits up to a singlet ground state and a triplet state with higher energy. The singlet ground state is non-magnetic.

1.4.2 Ruderman-Kittel-Kasuya-Yosida (RKKY) and Kondo interactions

Localized magnetic moments in a lattice interact with each other indirectly via conduction electrons. This interaction, was first described by Ruderman and Kittel, Kasuya and Yosida [51–53]. It is therefore called RKKY interaction and leads to a magnetically ordered state. If the ground state presents FM or AFM order depends on the distance between the magnetic moments R_{12} and the Fermi wave vector k_F. The interaction energy is

$$J_{\text{RKKY}}(x) = \frac{1}{x^4}(x\cos x - \sin x), \tag{1.5}$$

with $x = 2k_FR_{12}$. Sebastian Doniach suggested the following theoretical approach for a 1D system [65]: In intermetallic rare earth compounds RKKY and Kondo interaction are competing interactions. The binding energy of a Kondo singlet is

$$W_K(J) \propto \frac{1}{D(E_F)} e^{-\frac{1}{D(E_F)J}} \tag{1.6}$$

and that of the RKKY antiferromagnetic state is

$$W_{AF}(J) \propto CJ^2 D(E_F), \tag{1.7}$$

where $D(E_F)$ is the density of states at the Fermi level of the conduction electrons and C is a dimensionless constant depending on details of the band structure. Which of both interaction dominates, depends on the exchange coupling J between the magnetic moments and the conduction electrons. Sometimes J is called hybridization strength. The relevant energies were compared by S. Doniach with each other for a one-dimensional Kondo lattice using the model of the linear chain. Doniach assumed that $D(E_F)$ is constant. He also identified a critical value J_C of the hybridization strength J where both interactions are equal. For the critical hybridization strength J_C quantum critical behaviour is proposed to occur. In real systems, J as well as $D(E_F)$ are material properties and can be varied by a control parameter r like magnetic field, hydrostatic or chemically induced pressure. Doniachs proposal can be directly adapted to real systems only if $D(E_F)$ stays constant.

Chemically induced pressure

Physical properties of compounds are frequently studied under applied hydrostatic pressure. Alternatively, the lattice parameters can be changed by substitution of elements (chemical pressure). The application of pressure can have a large influence on the ground state of the respective compound. Hydrostatic pressure or the application of positive chemical pressure by a substitution of atoms by smaller ones yields a compression of the lattice. This leads to the suppression of a magnetic order in Ce compounds by stabilizing the non-magnetic Ce^{4+} but to the enhancement of the magnetism in Yb compounds by stabilization of the magnetic Yb^{3+} state.

In this work, the effect of substitution has been investigated in several series of compounds. In the series $Ce(Ru_{1-x}Fe_x)PO$, the FM order was suppressed by substituting Ru by the smaller Fe. In the substitution series $YbNi_4(P_{1-x}As_x)_2$ phosphorous is replaced by the larger arsenic and thus, the system can be tuned towards the FM QCP. In $YbRh_2Si_2$, Rh can be replaced by the larger Ir to tune the system towards the AFM QCP. It has been found in the past that a substitution of 6% of the Rh atoms by Ir yields a volume increase which leads to the suppression of the magnetism in this compound [66]. The contrary can be achieved by Co substitution. The substitution of 7% of the Rh atoms by Co yields a volume decrease leading to the stabilization of the AFM order [67]. For $x = 0.27$ in $Yb(Rh_{1-x}Co_x)_2Si_2$ ferromagnetism appears [68] and the evolution of the magnetism upon doping in the complete system was studied by Klingner *et al.* [69].

1.4.3 Experimental investigations of electronic correlations

An introduction into the basics of the topics which are summarized below can be found in standard textbooks [70–73]. In the past, several models have been proposed to describe the transport and thermodynamic properties of metals. In the frame of the Drude model, electrons are treated as non-interacting point charges obeying the Maxwell-Boltzmann distribution. This model is suited to describe transport properties of metals. The electronic transport properties of metals are determined by the electrons near the Fermi level since only these electrons can become thermally excited. To model the specific heat, the Pauli principle has to be taken into account by including the Fermi-Dirac statistics additionally.

For non interacting free fermions in a cube, the density of states depends on the energy by

$$D(E) = 2\frac{V}{4\pi^2}\left(\frac{2m}{\hbar^2}\right)^{\frac{3}{2}}\sqrt{E},$$

where m is the fermion mass, and V the volume of the cube. The Fermi energy is

$$E_F = \frac{\hbar^2}{2m}(3\pi^2 n_e)^{\frac{2}{3}},$$

with the density of electrons n_e. The density of states at the Fermi level

$$D(E_F) = \frac{V}{\pi^2\hbar^2}\left(3\pi^2 n_e\right)^{\frac{1}{3}} m \tag{1.8}$$

is proportional to the mass of the fermions.

If the electrons exist in a periodic potential like in the potential caused by the atoms in a solid, the DOS at the Fermi level is modified compared to that given by a free-electron model. To account for the periodic potential, an additional pertubation was included by Bloch resulting in the "nearly free electron model". He proposed that electrons, described as "Bloch waves", exist in energy bands and have a renormalized mass m^*. In real metals strong interactions, like the Coulomb interaction, between the electrons exist. These interactions, have been included in the phenomenological Landau-Fermi liquid theory resulting in a modification of the electronic bands [74].

Specific heat

For $T \ll \Theta$, the specific heat of metals is given by

$$C(T) = \gamma_0 T + \beta T^3. \tag{1.9}$$

The Sommerfeld coefficient

$$\gamma_0 = \frac{\pi^2}{3} D(E_F) k_B^2, \tag{1.10}$$

with the DOS at the Fermi level $D(E_F)$ is characterizing the electron contribution, and

$$\beta = \frac{12\pi^4 Rs}{5\Theta^3} \tag{1.11}$$

characterizes the phonon contribution according to the Debye-model, where Θ is the Debye temperature and s the number of atoms per formula unit [75]. The electronic and the phononic contribution can be separated by plotting C/T as a function of T^2. In metals showing weak correlation effects, values of γ_0 between 0.6 and $3\,\mathrm{mJ/(molK^2)}$ are found experimentally. In Kondo lattice systems, C/T increases, when the temperature goes to zero. Experimentally, values for γ_0 between 1000 and $2000\,\mathrm{mJ/(molK^2)}$ are found. The Sommerfeld coefficient γ_0 is proportional to the effective mass m^* of the electrons (cf. Eqn. 1.8). with the charge carrier density n_e. The charge carrier density n_e can be obtained experimentally by Hall effect measurements. By experimental methods, values that are found for the effective mass are up to 2000 times larger than the mass of a free electron.

Resistivity

In the frame of the single-electron approximation one considers an electron in the periodic potential of all lattice atoms. The electrons are described by the Bloch functions which are solutions of the stationary Schrödinger equation

$$\psi_k(\vec{r}) = u_k(\vec{r}) \cdot e^{i\vec{k}\vec{r}}, \tag{1.12}$$

where $e^{i\vec{k}\vec{r}}$ are the plane waves and $u_k(\vec{r})$ is a modulation function with the periodicity of the lattice. In a perfect crystal with zero temperature, the potential of the lattice is perfectly periodic and time independent. An electron would stay in the state $\psi_k(\vec{r})$ forever and the resistivity is zero. In a real crystal with finite temperature, the electrons are scattered by phonons $\rho_{\mathrm{ph}}(\mathrm{T})$, crystal defects ρ_0, electron-electron interactions $\rho_{\mathrm{ee}}(\mathrm{T})$, and on magnetic centers $\rho_{\mathrm{mag}}(\mathrm{T})$ (Kondo scattering).

In metals with weak electron-electron interaction, the main contributions to the scattering of the electrons are caused by crystal defects and phonons. Therefore the resistivity can be written according to Mathiessen‘s rule as

$$\rho(T) = \rho_0 + \rho_{\mathrm{ph}}(T). \tag{1.13}$$

Crystal defects are point defects, like impurities on regular lattice or interstitial sites, dislocations of the crystal lattice, like line or screw dislocations, and lattice defects like grain boundaries and stacking faults. Their contribution to the resistivity ρ_0 still exists and can be observed at zero temperature when other contributions are negligible. The phonon contribution to the resistivity is expressed by the Bloch-Grüneisen relation

$$\rho_{\mathrm{ph}}(T) = \mathcal{A}_{ph} \left(\frac{T}{\Theta_D}\right)^5 \int\limits_0^{\frac{\Theta_D}{T}} \frac{x^5}{(e^x - 1)(1 - e^{-x})} dx, \tag{1.14}$$

where $\mathcal{A}_{ph}$ is a material dependent constant and Θ_D is the Debye temperature. For high temperatures $T \gg \Theta_D$, the resistivity is proportional to T and in the low temperature limit $T \ll \Theta_D$ the resistivity runs with T^5.

In the frame of the phenomenological Landau-Fermi liquid theory [74], the excitations of the electron gas in a metal are described as excitations of quasiparticles in a corresponding FL. These quasiparticles have the same spin and the same charge as the electrons but a different effective mass m^*. The effective mass is proportional to the DOS at the Fermi level in the original Fermi gas. Predicted by the Landau FL theory, the electron-electron scattering yields an additional contribution

$$\rho_{\mathrm{ee}}(T) = AT^2, \tag{1.15}$$

to the resistivity, where A is a material specific constant. Approaching zero temperature, when the T^5 contribution of the phonons becomes small, the T^2-behaviour is observable. This T^2 dependence of the resistivity stems from the scattering of the heavy fermions off the FL [60, 71]. In particular, in heavy-fermion compounds, these interactions play a significant role, due to the enlarged effective mass m^*, taking into account the fact, that $A \propto (m^*)^2$.

Kadowaki-Woods ratio

In 1986, Kadowaki and Woods observed experimentally [76], that for heavy-fermion systems the ratio of the resistivity coefficient A according to Eqn. 1.15 and the Sommerfeld coefficient of the electronic specific heat γ_0 according to Eqn. 1.10 at zero temperature (with the exception of UBe$_{13}$) takes a universal value of

$$\frac{A}{\gamma_0^2} \approx 10\ \mu\Omega\mathrm{cmK^2mol^2J^{-2}} \tag{1.16}$$

without providing a theoretical model. This ratio is one order of magnitude larger than that of for common d-band metals. Recently, Jacko *et al.* gave a generalized explanation for a large number of compounds including heavy-fermion systems, UBe$_{13}$ as well as d-band metals by rewriting the ratio according to

$$\frac{A}{\gamma_0^2} = \frac{81}{4\pi\hbar k_\mathrm{B}^2 \mathrm{e}^2} \frac{1}{\xi^2 n D_0^2 \langle v_{0x}^2 \rangle} \tag{1.17}$$

with the calculated quantities: model parameter ξ, electron density n, DOS of the bare system D_0 and the square of the Fermi velocity $\langle v_{0x}^2 \rangle$ with respect to the bare electron mass averaged over the Fermi surface [77].

Curie-Weiss law

In general, the magnetization $\vec{\mathcal{M}} := \vec{M}/V$ is defined as magnetic moment $\vec{M}$ per volume V. In an external field $\vec{H}$, the magnetic moments of an ideal paramagnetic sample align in the direction of the field. In a real material, the magnetic induction $\vec{B}$ is given by $\vec{B} = \mu_0(\vec{H} + \vec{\mathcal{M}})$. For small external magnetic fields H, the magnetization $\mathcal{M} = \chi_\mathrm{Vol} H + \cdots$ is proportional to H. The proportionality factor χ_Vol is called magnetic susceptibility. In anisotropic solids, χ_Vol depends on the orientation of the crystal and in general $\vec{\mathcal{M}}$ is not parallel to $\vec{H}$. For the paramagnetic contribution to the volume susceptibility of localized electrons, the relation

$$\chi_\mathrm{Vol}(T) = \frac{N}{V} \frac{\mu_0 J(J+1)(g_J \mu_B)^2}{3 k_B T} \tag{1.18}$$

with the Landé g-factor

$$g_J = 1 + \frac{J(J+1) + S(S+1) - L(L+1)}{2J(J+1)} \tag{1.19}$$

can be derived for small fields and high temperatures [78]. In this equation, J is the quantum number for the total angular momentum of the electrons, N is the number of independent atoms in the volume V, μ_0 is the vacuum permeability, μ_B is the Bohr magneton, k_B is the Boltzmann constant, and T the temperature. In a paramagnetic solid, the susceptibility exhibits Curie-Weiss behaviour:

$$\chi_{\text{mol}}(T) = \underbrace{N_A \frac{\mu_0 \mu_{\text{eff}}^2}{3k_B}}_{=:C_{\text{mol}}} \frac{1}{T - \theta_{\text{W}}}. \tag{1.20}$$

The inverse susceptibility is

$$\chi_{\text{mol}}^{-1}(T) = \frac{T - \theta_{\text{W}}}{C_{\text{mol}}} = -\frac{\theta_{\text{W}}}{C_{\text{mol}}} + \frac{1}{C_{\text{mol}}} T, \tag{1.21}$$

with the Weiss temperature θ_{W}. Experimentally, the effective magnetic moment μ_{eff} of the Ln^{3+} ions in e.g. LnRh_2Si_2, LnIr_2Si_2 or in YbNi_4P_2 can be obtained from the measurement of the temperature dependent magnetization. From the slope of the linear fit of the inverse molar susceptibility $d\chi_{\text{mol}}^{-1}/dT = 1/C_{\text{mol}}$ the Curie constant C_{mol} can be determined. The effective magnetic moment and the Weiss temperature can be determined according to

$$\mu_{\text{eff}} = \sqrt{\frac{3k_B}{\mu_0 N_A} C_{\text{mol}}} \quad \text{and} \quad \chi_{\text{mol}}^{-1}(T = 0) = -\frac{\theta_{\text{W}}}{C_{\text{mol}}}. \tag{1.22}$$

Pauli susceptibility

In the frame of the nearly free electron model, not only the Sommerfeld coefficient γ_0, Eqn. 1.10, but also the temperature independent magnetic susceptibility χ_0 depends on the DOS at the Fermi level

$$\chi_0 = \mu_0 \mu_B^2 D(E_F) \tag{1.23}$$

with the vacuum permeability μ_0 and the Bohr magneton μ_B.

Susceptibility in Kondo-lattice systems

At high temperatures, Kondo lattice compounds exhibit Curie-Weiss behaviour due to their localized $4f$ moments. In the intermediate temperature regime, the CEF affects the susceptibility. Additionally, the moments become screened by the conduction electrons (Kondo effect). The susceptibility flattens and becomes constant for $T \ll T_K^*$ with a value χ_0 for $T \to 0$. Assuming that the $4f$ moments are completely screened, the remaining susceptibility is the Pauli susceptibility χ_0 of heavy fermionic quasiparticles. It can be predicted using Eqn. (1.10) and Eqn. (1.23) and the deviation from the nearly-free electron-behaviour can be quantified by the Sommerfeld-Wilson ratio.

Sommerfeld-Wilson ratio

The ratio of the susceptibility in the limit $T = 0$ and the Sommerfeld coefficient γ_0 is called Sommerfeld-Wilson ratio

$$W = \frac{\pi^2 k_B^2}{3\mu_0 \mu_B} \frac{\chi_0}{\gamma_0}, \tag{1.24}$$

that is a value which characterizes a material. By definition, for free electrons $W = 1$, in real heavy-fermion systems W takes values between 2 and 5 [79].

1.5 Quantum criticality

Effects of quantum criticality can be observed at finite temperatures in systems where a second order phase transition occurs at zero temperature. Historically, the study of critical phenomena started in the context of classical phase transitions. We therefore shortly introduce classical phase transitions in the first part of this section. We move on to quantum phase transitions and describe two scenarios for magnetic quantum critical points in the last part.

1.5.1 Classical phase transitions and critical exponents

At a classical phase transition, a macroscopic system in the thermodynamic equilibrium changes its state. A first classification of general types of transition between phases of matter was introduced by Ehrenfest. He provided a classification of phase transitions on the basis of jumps in derivatives of the free energy function $F(T, V, ...)$. At a first order phase transition, a discontinuity in one of the first derivatives of the free energy occurs. It is called a "discontinuous" phase transition and is accompagnied by a release of latent heat. At a second order phase transition, the first derivative is continuous and a discontinuity occurs in the second derivative of the free energy. Second order phase transitions are called "continuous" phase transitions. While at a discontinuous phase transition the order parameter disappears suddenly, its change is continuous at a continuous phase transition. For a specific system with a fixed composition, at a certain pressure and in a certain field, the point of the phase transition is called "critical point". Landau introduced a theory to describe second order phase transitions and extended it further by including fluctuations of an order parameter ϕ [80]. Near the critical point, fluctuations of the order parameter with the coherence or spacial correlation length ξ occur. At the critical point, these fluctuations are called "critical fluctuations" and diverge as

$$\xi \propto |t|^{-\nu} \quad \text{with} \quad t = (T - T_c)/T_c \tag{1.25}$$

where t is the reduced temperature, and ν the critical exponent of the correlation length ξ. Additionally, there are temporal fluctuations of the order parameter characterized by the correlation time ξ_τ which diverges as

$$\xi_\tau \propto \xi^z \propto |t|^{-\nu z}. \tag{1.26}$$

Here, z is the dynamical exponent [81]. Near the critical point, fluctuations occur on all scales of length and time - the system behaves "scale-invariant".

In the vicinity of a second order phase transition, physical quantities show characteristic power law behaviour in measured properties like the order parameter ϕ, the susceptibility χ with respect to an order parameter or the specific heat C according to

$$\phi \propto |t|^\beta, \quad \chi := \frac{\partial \phi}{\partial r} \propto |t|^{-\gamma} \quad \text{and} \quad C \propto |t|^{-\alpha} \tag{1.27}$$

where r is a control parameter. At the critical temperature T_c, the Greens function $G(x) := \langle \phi(0) \cdot \phi(x) \rangle$, fulfills

$$G(x) \propto x^{-(d-2+\eta)}. \tag{1.28}$$

universality class	model	physical system	ϕ	β	γ
$d = 2$, $n = 1$	2D Ising	adsorbed layers	surface density	0.125	1.75
$d = 2$, $n = 2$	2D XY	liquid ^{4}He films	suprafluid phase amplitude	0.2...	2.2...
$d = 2$, $n = 3$	2D Heisenberg	–	magnetization	0.28...	3
$d = 3$, $n = 1$	3D Ising	uniaxial ferromagnets	magnetization	0.3...	1.25
$d = 3$, $n = 2$	3D XY	layered ferromagnets	magnetization	0.33...	1.22...
$d = 3$, $n = 3$	3D Heisenberg	isotropic ferromagnets	magnetization	0.57...	1.4...

Table 1.3: Universality classes, characterized by is the spatial dimension of the ordering system d and the dimension of the order parameter n, and critical exponents for classical phase transitions after Wilson [82].

Here, d is the dimension of the ordering system and η is a further critical exponent. In the 1970s, Wilson introduced critical exponents for the behaviour of physical quantities at an arbitrary second order phase transition [82]. He stated that two systems belonging to the same universality class will have the same critical exponents. Some examples of universality classes (defined by the dimension of the system d and dimension of the order parameter n) are given in Tab. 1.3.

Between the critical exponents $\alpha, \beta, \gamma, \eta, \nu$ and the dimension d of the ordering system the relations

$$\alpha = 2 - d\,\nu, \quad \gamma = \nu\,(2 - \eta), \quad \beta = \nu\,\frac{d - 2 + \eta}{2} \tag{1.29}$$

hold [83].

1.5.2 Quantum criticality and scaling behaviour

Classical phase transitions, exhibit divergence of the coherence length ξ and time ξ_τ of the order parameter ϕ. Upon approaching the transition, ϕ fluctuates coherently over increasing distances and time scales meaning that there exists a characteristic frequency for order-parameter fluctuations ω_ϕ with $\omega_\phi \to 0$ at the phase transition [84]. At a finite-temperature phase transition the nature of the fluctuations is classical in the sense that $\hbar\omega_\phi \ll k_B T_c$. The fluctuations become quantum mechanical in nature at a QPT where $T_c = 0$. At a QCP, the characteristic energy of the quantum fluctuations becomes larger than the thermal fluctuation energy

$$\hbar\omega_\phi \gg k_B T_c. \tag{1.30}$$

Fig. 1.4 shows a schematic phase diagram near a QCP. By tuning a system through a QPT its transition temperature into an ordered state is shifted to zero and the QCP is reached at a critical value r_c of the control parameter r. In experiments this can be realized by a control parameter r like pressure, field or doping. At classical critical points, the critical

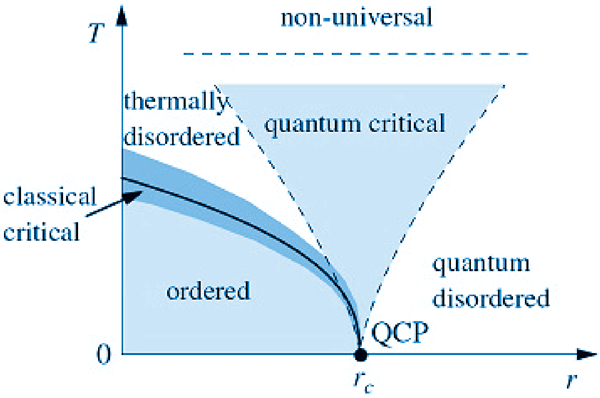

Figure 1.4: Schematic $T - r$ phase diagram for temperatures T and values r of a tuning parameter near a QCP after [85]. The solid line indicates the boundary between ordered and disordered phases. The dashed lines mark the boundaries of the quantum critical region.

fluctuations are limited to a narrow region around the phase transition. In contrast, the influence of a quantum critical point on the physical properties can be observed over a wide range of temperature above the QCP. Therefore, the effect of quantum criticality is also relevant and observable in different physical quantities at finite temperatures. Near a QCP several physical quantities like the specific heat $C(T)$, the linear thermal expansion $\alpha(T)$ or the electrical resistivity $\rho(T)$ exhibit power-law behaviour.

At a QPT, different microscopic systems exhibit the same scaling behaviour. They show scale invariance in space and time of the critical fluctuations extending over a wide region in the phase diagram. The fascinating property of a phase transition is that different materials show universality in their behaviour and can be described by the same theory. In contrast to classical phase transitions, at a QPT the dynamics (the existence of temporal fluctuations of the order parameter) also affects the critical thermodynamic properties and therefore a larger number of universality classes can be expected. To account for this fact, the effective dimensionality for a system near a QPT is extended to $d_{\text{eff}} = d + z$ [84].

The FL behaviour of the system changes into non-FL behaviour when approaching the QCP. It is believed that in many systems the arising unusual metallic states act as precursors for the development of superconductivity.

Commonly, the exponents are obtained from fits to the data. For instance, the temperature dependence of the resistivity is fitted to the model form $\rho(T) = \rho_0 + AT^{\kappa}$ in a certain temperature range $T_{\text{min}} < T < T_{\text{max}}$. Such fits are believed to be reliable if (i) the exponent depends only weakly on T_{min} and T_{max}, (ii) the fit extends over more than one decade in T, and (iii) a plot of $\rho(T)$ as a function of T^{κ} looks linear [84]. At low temperatures, the resistivity of a FL obeys

$$\rho(T) \propto T^2. \tag{1.31}$$

In the neighbourhood of a QCP, a different behaviour of the resistivity

$$\rho(T) \propto T^{\kappa} \quad \text{with} \quad \kappa < 2 \tag{1.32}$$

was observed. Even unconventional power-law behaviour in the magnetic susceptibility

$$\chi(T) \propto -\ln T \;\text{ or }\; \frac{1}{T^{\gamma}} \quad \text{with} \quad \gamma < 1 \tag{1.33}$$

and in the specific heat

$$\frac{C_p}{T} \propto -\ln T \;\text{ or }\; \frac{1}{T^{\alpha}} \quad \text{with} \quad \alpha < 1 \tag{1.34}$$

were found [86, 87]. This non-FL behaviour occurs above the QCP in the quantum critical region shown in Fig. 1.4. Reaching the QCP, the Grüneisen ratio

$$\Gamma(T) := \frac{\beta(T)}{C_p(T)} = -\frac{1}{V_m T}\frac{(\partial S/\partial p)_T}{(\partial S/\partial T)_p} \propto \frac{1}{T^{\lambda}} = \frac{1}{T^{1/\nu z}} \tag{1.35}$$

diverges for $T \to 0$ at any QCP with the critical exponent $\lambda > 0$. Eqn. 1.35 is valid for a pressure as well as a field-tuned QCP [15]. Here,

$$\beta(T) = \frac{1}{V} \cdot \frac{\partial V}{\partial T}\bigg|_p = -\frac{1}{V} \cdot \frac{\partial S}{\partial p}\bigg|_T \tag{1.36}$$

is the volume thermal expansion and

$$C_p(T) = \frac{T}{N} \cdot \frac{\partial S}{\partial T}\bigg|_p \tag{1.37}$$

the molar specific heat at constant pressure with the entropy S and the molar volume $V_m = V/N$. By the critical exponent λ the existence of a QCP can be checked and the QCP can be characterized.

1.5.3 Theoretical approaches

Today, two scenarios for what happens during a magnetic QPT are under discussion, the spin-density wave scenario and the Kondo-breakdown scenario.

Spin-density wave scenario

A widely accepted scenario is the formation of a SDW. A SDW is an itinerant magnetic ground state of metals. In this state, the density of the spins of the conduction electrons is spatially modulated. In general, the wave length of the SDW is incommensurable with respect to the atomic lattice. The SDW is a property of the ground state of a system but not an excitation like a magnon. According to Hertz, Millis and Moriya [81, 88, 89], in the heavy Fermi-liquid a SDW might form. The order parameter of the SDW exhibits critical fluctuations while the heavy quasiparticles stay intact. Zhu *et al.* explicitly derived exponents of the power-law behaviour of the Grüneisen ratio for the SDW scenario near a QCP [15]. The critical exponents derived for the description of SDW metals are summarized in Tab. 1.4 and compared to real systems in Tab. 1.5. In $\mathrm{CeNi_2Ge_2}$, for instance, a QCP with $\lambda = 1$ is observed, which can be explained with a three dimensional spin-density-wave model [90].

	AFM $d = 2$ $z = 2$	AFM $d = 3$ $z = 2$	FM $d = 2$ $z = 3$	FM $d = 3$ $z = 3$	FL $d = 3$
$\beta_{cr} \propto$	$\ln \ln \frac{1}{T}$	$T^{1/2}$	$\ln \frac{1}{T}$	$T^{1/3}$	const.
$C_{cr} \propto$	$T \ln \frac{1}{T}$	$-T^{3/2}$	$T^{2/3}$	$T \ln \frac{1}{T}$	const.
$\Gamma_{r,cr} \propto$	$\frac{\ln\ln\frac{1}{T}}{T\ln\frac{1}{T}}$	$-T^{-1}$	$T^{-2/3}\ln\frac{1}{T}$	$\left(T^{2/3}\ln\frac{1}{T}\right)^{-1}$	const.
$\rho(T) \propto$	–	$T^{3/2}$	–	–	T^2

Table 1.4: Critical exponents: Results for a model which is suitable to describe a SDW metal in the quantum critical regime $T \gg |r|^{z/2}$ deduced by Zhu et al. [15]. Here, r is the control parameter and measures the distance to the QCP, d is the dimension of the ordering system. The dynamical exponent z decribes an AFM metal with $z = 2$ and a FM metal $z = 3$. The critical exponent for the electrical resistivity was derived by Moriya and Takimoto [91].

system	model	$\beta_{cr} \propto$	$C_{cr} \propto T^{-\alpha}$	$\Gamma_{cr} \propto T^{-1/\nu z}$	$\rho_{cr} \propto T^{\kappa}$	ref.
$CeCu_2(Si_{1-x}Ge_x)_2$	SDW	–	–	–	$T^{1 \cdots 2}$	[92, 93]
$Ce_{1-x}La_xRu_2Si_2$		–	$T^{1/2}$	–	$T^{1.5}$	[94]
$CeNi_2Ge_2$		$T^{1/2}$	$T^{3/2}$	T^{-1}	$T^{1.2 \cdots 1.5}$	[90]
$CeIn_{3-x}Sn_x$		$T^{1/2}$	T	$T^{-(1.1\pm0.1)}$	–	[95]
$CeCu_{6-x}Au_x$	Kondo break-down	–	$T\ln(T_0/T)$	–	T	[12, 96]
						[19]
$YbRh_2(Si_{1-x}Ge_x)_2$		T	$T^{-1/3}$	$T^{-(0.7\pm0.1)}$	T	[96, 97]
$CeCu_{6-x}Ag_x$		$T\ln(T_0/T)$	$T\ln(T_0/T)$	$< T^{-1}$	–	[95]
$YbNi_4(P_{1-x}As_x)_2$	?	$T^{0.36}$	$T^{0.57}$	$T^{-(0.22\pm0.04)}$	$T^{1 \cdots 1.2}$	[14]

Table 1.5: Materials and critical exponents. The tuning parameter is the composition x.

Kondo-breakdown scenario

Materials like $CeCu_{1-x}Au_x$ and $YbRh_2Si_2$ cannot be described by a SDW scenario [96]. This led to the development of a new approach which is known as "Kondo breakdown" or "Kondo destruction" scenario. Near a QPT, critical fluctuations arise and it is believed that these fluctuations cause a destruction of the Kondo state. In this picture, the Fermi surface looses its f-electron character upon crossing the QCP [98]. Several mechanisms have been proposed for different types of fluctuations.

- A locally quantum critical scenario where local fluctuations of the magnetization become divergent was proposed by Coleman and Si *et al.* [16, 17]. During a QPT, the local fluctuations of the magnetic order parameter couple to the nearly localized heavy quasiparticles. If these fluctuations become critical they might destroy the heavy Fermi liquid at the QCP. In $YbRh_2(Si_{1-x}Ge_x)_2$, a QCP with $\lambda \approx 0.7$ was found, which is not compatible with the itinerant SDW theory. Such a critical exponent is qualitatively consistent with the locally quantum critical picture [90]. Evidences of a Kondo destroying QCP in $YbRh_2Si_2$ were summarized recently by Steglich *et al.* [99]. For this scenario, ω/T scaling of the dynamic susceptibility $\chi(\vec{q}, \omega, T)$ with the magnetic wave vector $\vec{q}$ as a direct consenquence of the development of critical fluctuations connected to the breakdown of the Fermi surface (FS) is predicted [18, 19, 100]. This scaling is not expected in the SDW theory.

- The occurence of an abrupt change of the Fermi surface (Fermi volume collapse) caused by Fermi surface fluctuations which destroy the Kondo singlet state was proposed by Vojta *et al.* [101].

- A scenario of critical quasiparticles characterized by a diverging effective mass and a singular quasiparticle interaction generated by order-parameter fluctuations of a SDW instability was proposed by Wölfle, Abrahams and Schmalian [102–104].

1.5.4 Quantum critical compounds and $YbNi_4P_2$

Some quantum critical materials where the critical exponents for the volume thermal expansion β, the specific heat C, the Grüneisen parameter Γ and the resistivity ρ were determined are listed in Tab. 1.5. For these materials, it was possible to determine whether the SDW or the Kondo-breadown scenario occurs at the QCP. The table additionally includes the exponents determined in the case of the FM $YbNi_4P_2$ for which none of these scenarios has proven to be valid.

The quantum critical ferromagnet $YbNi_4P_2$

In $YbNi_4(P_{1-x}As_x)_2$, $x \approx 0.1$ a FM QCP was found. Samples with $x = 0.08$ show that the dimensionless Grüneisen ratio diverges as $\Gamma(T) \propto T^{-0.22\pm0.04} \propto T^{-\lambda} = T^{-1/\nu z}$ which indicates the existence of a QCP at $x_c \approx 0.1$ [14]. The exponent $1/\nu z = 0.22$ rules out an itinerant SDW scenario in $YbNi_4(P_{1-x}As_x)_2$ because it leads to $\nu z \approx 5$, which is much larger than for itinerant FM systems ($\nu = 1/2$, $z = 3$). Until now, it is not possible to deduce an appropriate characterization of the QCP which occurs in $YbNi_4(P_{1-x}As_x)_2$ for $x \approx 0.1$ from existing theories [26].

Our recent study [105], sheds light on the question whether the Fermi surface looses its f-electron character upon crossing the QCP. In the unsubstituted system, Lifshitz transitions occur at low fields which means that the f-electrons are incorporated in the Fermi surface and that the magnetically ordered side of the QCP is a heavy Fermi liquid. This observation excludes a Kondo-breakdown scenario for the FM QCP. The occurrence of a FM QCP in heavy-fermion metals, like $\mathrm{YbNi_4(P_{1-x}As_x)_2}$, $x \approx 0.1$ is not understood so far since this type of instability should apparently not exist in itinerant metallic materials [106].

1.6 Characterization of physical properties

In this section, the methods are described which were applied for the characterization of the physical properties of the materials. The physical properties were investigated using the commercial measurement options of a Quantum Design physical property measurement system (PPMS). The setup and sample preparation is described below for heat capacity, four-point resistivity and magnetization measurements.

Specific heat capacity

Heat capacity measurements were performed using the heat capacity (HC) option of the PPMS. The measuring procedure consisted of two runs. The first step was the addenda measurement were the heat capacity of the sample platform together with the attached Apiezon N grease was determined. Secondly, the sample was attached to the platform and the heat capacity of the sample was measured by a relaxation method using the two-tau model and taking the addenda measurement into account. To increase the accuracy of the measurement, at each temperature set point three decay curves were measured applying a heat pulse of 2%. The specific heat capacity is a bulk property and with this option not only single crystals were measured but also polycrystalline material which was pressed into a pellet shape prior to the measurement. The sample weight should be between 3 to 5 mg. The largest extension of the single crystal or pellet was 3 mm.

Electrical transport

For resistivity measurements on samples with low resistivity, the four-point-geometry is used to minimize the uncertainty on the measurement results due to the wires and contacts. The samples were contacted on four points and connected with a platinum wire to the puck, which is part of the resistivity measurement unit of a commercial PPMS (alternating current transport option (ACT)). The platinum wire is 25 μm in diameter and is connected at one end with the sample by silver based electrically conductive adhesive while the other end is soldered using tin on top of the puck. A piece of cigarette paper prevents direct contact of the sample with the puck. The sample is fixed on the puck with Apiezon N, to provide thermal contact and protect the wires and contacts against breaking, when mounting the sample. A constant current flows from point $\mathrm{I_+}$ to $\mathrm{I_-}$ and the voltage is measured between the contacts $\mathrm{U_+}$ and $\mathrm{U_-}$ which are located between the current contacts. In figure 2.13, a sample with contacts on a puck prepared for a resistivity measurement is shown.

Resistivity measurements are used to study the anisotropy of materials. The crystal is oriented by Laue method and the positions of the two voltage contacts are in one line parallel to a defined crystal axis with a distance l of about 1 mm. The best suitable crystal shape is long and thin. With this geometry, other current contributions are minimized.

The residual resistivity ρ_0 depends on the concentration of the crystal defects therefore measurements of the resistivity can be used to characterize the quality of a sample. For metallic samples the residual resistivity ratio $RRR = \rho(300\,\mathrm{K})/\rho(\mathrm{T} \to 0)$ is usually used. In this work, all resistivity measurements with the ACT option of the PPMS were done down to a temperature of 1.8 K. The resistivity ratio $RR_{1.8K} = \rho(300\,\mathrm{K})/\rho(1.8\,\mathrm{K})$ was determined for several samples to compare the crystal quality. The larger the value of $\mathrm{RR}_{1.8\,\mathrm{K}}$ for a sample is, the smaller the defect contribution and the better is the crystal quality. Note that for the materials which exhibit a phase transition below 1.8 K the RRR value usually can differ significantly from the value of $\mathrm{RR}_{1.8\,\mathrm{K}}$.

Magnetization

The magnetic moment of a sample was measured, using the vibrational sample magnetometer (VSM) option of the PPMS. The measurement of the magnetic moment is done by oscillating the sample near a pickup coil inducing a time-dependent voltage $V = d\Phi/dt = (d\Phi/dz)(dz/dt)$. Here, Φ is the magnetic flux enclosed by the pickup coil, z the vertical position of the sample with respect to the coil, and t the time. For a sample position, that oscillates sinusodially, the voltage is given by $V = 2\pi fCmA\sin(2\pi ft)$, with the frequency of the oscillation f, a coupling constant C, the DC magnetic moment of the sample m and the amplitude of the oscillation A. During the magnetic moment measurements, the amplitude of the induced voltage is determined [107].

In this work, the VSM option was used to determine the anisotropic magnetic properties of the single crystals. Additionally, it was used to estimate the content of included flux in the single crystals. This was possible since the flux had a magnetic constituent (like in the case of the Ni-$\mathrm{Ni_3P}$ flux where Ni is magnetic at room temperature) or becomes superconducting (like in the case of In flux with $T_c = 3.4\,\mathrm{K}$). The determination of the purity of the crystals concerning the flux content is necessary, since many measurement methods require pure (flux free) crystals. To prepare a crystal for a VSM measurement the sample was oriented by Laue method and subsequently fixed with GE-varnish on a quartz paddle. In the PPMS, the external field H is applied in vertical direction which means parallel to the longest extension of the sample holder. The sample oscillated with an amplitude A of 2 or 4 mm and a frequency f of 20 or 40 Hz.

1.7 Angle resolved photoemission spectroscopy

In the past, several Ln-containing compounds turned out to develop surface states which have been examined by spectroscopic techniques like ARPES. Surface electronic states were theoretically predicted by I. Tamm (1932) and later on by W. Shockley (1939) and have been observed for the first time in 1975 on the Cu(111) surface by P.O. Gartland and B.J. Slagsvold [108]. The intrinsic property of surface states is that they are located in the projected bulk band gap where bulk states are prohibited to exist. They therefore must necessarily possess 2D character which is a fundamental fact well known in the condensed matter community. For $\mathrm{LnT_2Si_2}$ systems, the Shockley state at the M-point was discovered for instance in $\mathrm{YbRh_2Si_2}$ [109] and $\mathrm{YbCo_2Si_2}$ [110]. The Dirac-cone state is a resonance surface state.

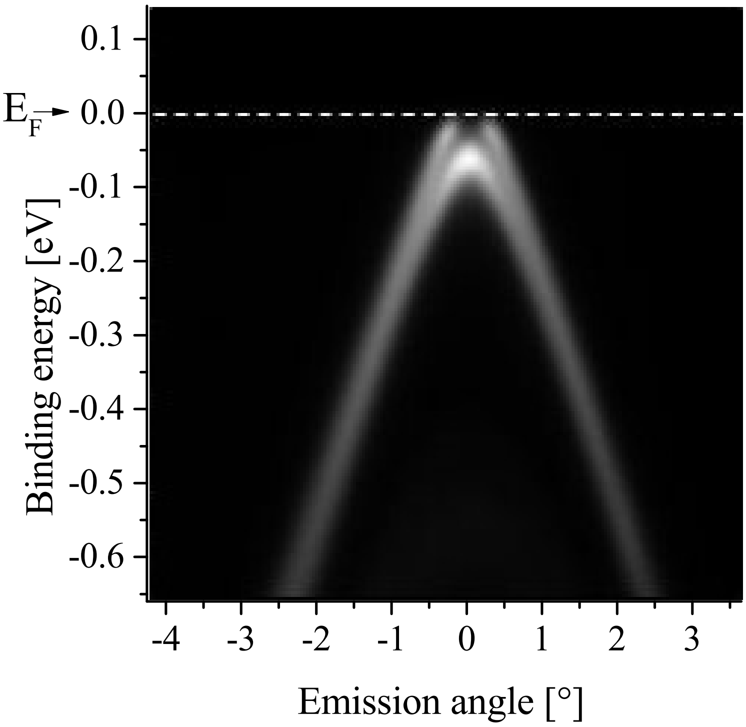

Figure 1.5: ARPES: Splitting of a surface state at the Γ point in $GdRh_2Si_2$ below the Néel temperature. The data where collected at the SIS beamline at the Swiss Light Source (SLS), PSI together with D. Vyalikh (San Sebastian).

Resonance surface states are states degenerate in energy with bulk states. In real space, resonance surface states are localized in several surface atomic layers distinguishing them from bulk states. The Dirac-cone state was studied for instance in graphene [111], $EuRh_2Si_2$ [112] or in URu_2Si_2 [113].

Photoelectron spectroscopy is a technique which utilizes the photoelectric effect. By ARPES the energy as well as the momentum of the electrons in the solid can be obtained. With this method, the band structure of a material can be determined experimentally. The measurement is performed while the sample and the detector are kept under ultra-high vacuum (10^{-10} bar) to minimize the contamination of the sample surface. The single crystal is cleaved right before the measurement in ultra-high vacuum and the sample surface allows for the collection of data during about 6 h at maximum, afterwards the contamination of the surface by adhesive atoms becomes too high. Due to this contamination, the sample has to be changed frequently and the method is very sample consuming. The compounds LnT_2Si_2 which crystallize in the $ThCr_2Si_2$-type structure ($I4/mmm$) exhibit an alternating stacking of atomic layers where the Ln atoms are separated from each other by Si-Rh-Si trilayers. It turned out in the past that materials of this structure-type are excellent candidates to by studied by ARPES since they can be cleaved easily due to their layered structure. The sample quality is directly reflected in the quality of the obtained data. Sharp electronic bands can be resolved only for single crystals of high purity and excellent crystallinity. For the $LnRh_2Si_2$ single crystals obtained by the high-temperature flux growth the Laue pattern Fig. 5.1 show extremely sharp spots indicating a high crystallinity of the single crystals which also reflects in the sharp bands visible in the ARPES spectra. In the frame of this work, single crystals of $SmRh_2Si_2$ [114], $GdRh_2Si_2$ [115] and $HoRh_2Si_2$ [116] were grown which allowed for their investigation by ARPES. The ARPES spectrum in Fig. 1.5, nicely shows the splitting of a surface state below the Néel temperature at the Γ point in $GdRh_2Si_2$. This picture shows the pure data and remarkably, besides the sharp electronic bands, there is an extremely low background contribution below the Fermi energy E_F which prooves the high crystallinity of our single crystals.

2

$\mathbf{YbNi_4P_2}$ and $\mathbf{YbNi_4(P_{1-x}As_x)_2}$, $(x = 0.1 - 1.0)$

2.1 Introduction to a system close to a ferromagnetic quantum critical point

The crystallographic structure of $YbNi_4P_2$ was reported by Chikhrij *et al.* about 30 years ago: The compound crystallizes in the tetragonal $ZrFe_4Si_2$ structure type ($P4_2/mnm$) in which, as shown in Fig. 2.1, the Yb atoms are located in channels of edge-connected Ni tetrahedral chains [117]. The first characterization of its high-temperature magnetic properties was done by Chikhrij *et al.*[119] and later by Deputier *et al.* [120] and the authors confirmed magnetic Yb^{3+} ions and no magnetic contribution of the Ni_4P_2 sublattice.

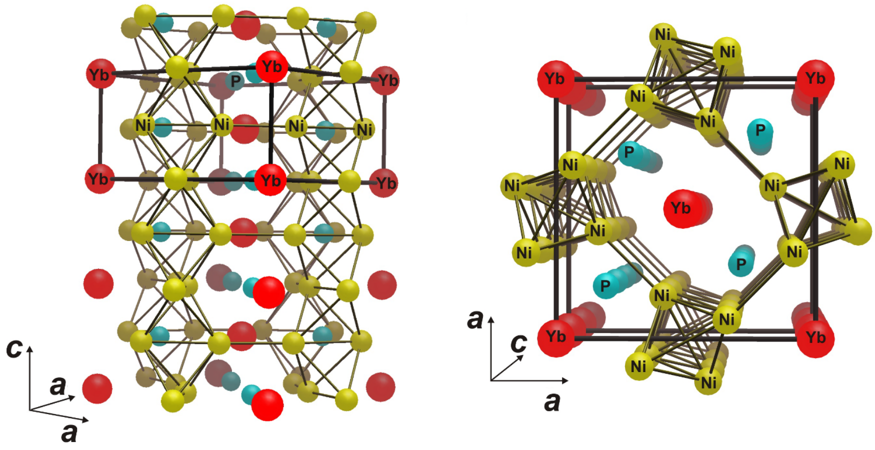

Figure 2.1: Tetragonal crystal structure of $YbNi_4P_2$. *Left:* View perpendicular to the c-direction. Neighbouring Yb chains are shifted towards each other by half a unit cell. *Right:* View along the crystallographic c-direction. Chains of Yb atoms are located in channels between P and Ni-tetraedra chains after [118].

In 2011, single-phase polycrystalline $YbNi_4P_2$ samples were prepared by Krellner *et al.* [121] and an extended study of its physical properties became possible. Additionally, from uncorrelated band structure calculations, two main issues were inferred: Firstly, the three main Fermi surfaces have predominantly 1D character. Secondly, spin-polarized calculations demonstrate the absence of Ni-related magnetism in $\mathrm{YbNi_4P_2}$, although Ni_{3d} states provide the main contributions to the density of states at the Fermi energy E_F. The Kondo temperature $T_\mathrm{K} \approx 8\,\mathrm{K}$ was estimated by means of the entropy, which was calculated from the specific heat data. The FM nature of the phase transition was one of the main results, since most known Kondo lattices order antiferromagnetically. The temperature of the phase transition $T_C = 0.17\,\mathrm{K}$ was the lowest-lying T_C ever observed among metallic correlated systems until that time.

The first successful single crystal growth was reported by Krellner and Geibel [118] and the examination of the magnetic anisotropy of $\mathrm{YbNi_4P_2}$ was performed in detail down to 1.8 K. A much higher polarized moment at 1.8 K was found for magnetic field along the c direction than for field in an in-plane direction. From the investigations of the magnetic properties the c axis of the tetragonal unit cell was deduced to be the magnetic easy direction. The magnetic properties were further studied by nuclear magnetic resonance (NMR) [122, 123] and muon spin resonance (μSR) [124]. Inelastic neutron scattering on powder was performed to investigate the CEF splitting and ferromagnetic fluctuations [125, 126]. The field dependence of the magnetization $M(B)$ for field $B \parallel c$ and $B \perp c$ was estimated by integration of the field dependence of the ac susceptibility $\chi'(B)$ measured at 0.03 K [127]. The estimated $M(B)$ shows a small FM hystereses for $B \perp c$. Due to the small ordered moment it was not possible to resolve the FM hystereses in a magnetization measurement until now. As $\mathrm{YbNi_4P_2}$ was the first clean example of FM quantum criticality [121], it was proposed to tune the system towards the non-magnetic side of the QCP by substitution of P by the larger As which is equal to the application of negative chemical pressure. QPTs are of current interest in solid state physics and $\mathrm{YbNi_4P_2}$ is one of the rare examples of compounds that allow the investigation of a FM QCP. Low-temperature measurements of Steppke *et al.* indicate the existence of a FM QCP in the $\mathrm{YbNi_4(P_{1-x}As_x)_2}$ substitution series for $x \approx 0.1$ [14]. Additionally, the re-examination of the pure compound yielded a $T_C = 0.15\,\mathrm{K}$ for $\mathrm{YbNi_4P_2}$ single crystals. The magnetic order and the spin dynamics across the QCP recently was investigated by μSR [128]. The critical fluctuations were found to be very slow in the pure compound and become even slower when approaching the QCP. These findings support the presence of a clean FM QCP in this system.

For further investigation of this intriguing phenomenon, large and high quality single crystals of the pure compound $\mathrm{YbNi_4P_2}$ as well as of single crystals in the substitution series $\mathrm{YbNi_4(P_{1-x}As_x)_2}$ are essential.

2.2 Summary of the results and outlook

The $\mathrm{YbNi_4P_2}$ single crystals have been grown by two different methods. The Bridgman method yielded single crystals with a mass of 10 mg at maximum. The single crystals which were obtained by the Czochralski method grew up to a mass of 1800 mg. Several obstacles were passed over when the process for the growth of large $\mathrm{YbNi_4P_2}$ single crystals was developed. The compound contains elements of high vapour pressure, namely ytterbium and phosphorous, in combination with the high melting element nickel. Additionally, the prereaction was impeded by the high reactivity of the melt with the tendency to attack the crucible material. It was key to find suitable conditions for this step. The conditions found by optimizing the process enabled us to grow large single crystals by the Czochralski method from a levitating melt utilizing a Ni-rich flux. We have shown that the high-temperature metal-flux technique can be used to grow large single crystals of materials with volatile elements. Furthermore, the Czochralski method was applied to grow single crystals in the substitution series $\mathrm{YbNi_4(P_{1-x}As_x)_2}$ for $x = 0.1, 0.12, 0.15, 0.2, 0.4, 0.6, 0.8$ and 1.0. By analyzing the chemical composition of the samples using EDX we found that the arsenic distribution in the samples is homogeneous. The characterization of their structure by PXRD showed that the increase of the arsenic content in the substitution series caused the unit cell to enlarge as expected. The crystallinity of the samples was investigated by Laue-Method using two different radiations, namely x-rays and neutrons. While x-rays penetrate only several μm into the sample, the neutron-penetration depth is several cm. Therefore, x-ray Laue is sensitive to the surface and neutron Laue probes the bulk. By combining both techniques, single crystals were identified where the misalignment in the lattice is below the detection limits of about 0.5 degree. These single crystals were cut and prepared to further characterize their physical properties down to lowest temperatures.

Our single crystals of pure and arsenic substituted $\mathrm{YbNi_4P_2}$ have been further characterized by electrical transport, heat capacity and magnetization measurements. Electrical transport measurements were performed in collaboration with M. Brando and coworkers and S. Friedemann and coworkers down to lowest temperatures (20 mK) and showed, besides a sharp transition into the ferromagnetic state at $T_C = 150\,\mathrm{mK}$, a resistivity ratio of $RRR = 60$ for $j \parallel c$. The resistivity as well as the magnetization exhibit a strong anisotropy parallel and perpendicular to the crystallographic c-direction which is consistent with previous results [14, 118] and supports the assumption of a one-dimensional electronic structure. Due to the high sample purity the anomalies observed in transport measurements appear much more pronounced in comparison to measurements on previous samples. This enabled H. Pfau and coworkers to investigate the Lifshitz transitions that occur in this compound [105]. Upon these transitions the topology of the Fermi surface changes which yields signatures in electrical transport and thermodynamic data. By their analysis information on the topology of the Fermi surface can be obtained. Our large single crystals facilitate ultrasound studies which are currently performed by Y.Tsui and coworkers in the group of M. Lang in Frankfurt. The first analysis of the data yielded that the Lifshitz transitions in $\mathrm{YbNi_4P_2}$ can also be detected by ultrasound.

We studied the arsenic substituted samples in more detail to localize the region of occuring non-FL behaviour in the phase diagram. Electrical transport measurements on single crystals of the $\mathrm{YbNi_4(P_{1-x}As_x)_2}$ series show that the pronounced anisotropy in the electrical resistivity of $\mathrm{YbNi_4P_2}$ turns into an almost isotropic behaviour in the case of $\mathrm{YbNi_4As_2}$. For arsenic concentrations up to $x = 0.4$, the Kondo scattering causes a pronounced drop in the resistivity below $T = 50\,\mathrm{K}$. Additionally, CEF effects occur at high temperatures. For high arsenic concentrations, the Kondo scattering is reduced and the transport properties are dominated mainly by CEF effects. Low temperature electrical transport measurements on single crystals near the quantum critical arsenic content $x \approx 0.1$ as well as pressure studies on a single crystal with $x = 0.12$ have been started by S. Friedemann and coworkers to further investigate the physics around the FM QCP. The heat capacity was measured down to $T = 350\,\mathrm{mK}$ in collaboration with J. Banda (MPI CPfS): For low arsenic concentrations, the specific heat capacity divided by temperature C/T increases strongly at low temperatures indicating the presence of strong electronic correlations. The samples with $x \leq 0.2$ show a divergence of C/T leading to strongly enhanced Sommerfeld coefficients of $\gamma_0 > 1000\,\mathrm{mJmol^{-1}K^{-2}}$. For high arsenic concentrations, C/T becomes constant with en-

hanced Sommerfeld coefficients $\gamma_0 = 158\,\mathrm{mJmol^{-1}K^{-2}}$ for $x = 0.8$ and $\gamma_0 = 96\,\mathrm{mJmol^{-1}K^{-2}}$ for $x = 1.0$ showing FL behaviour below $T \approx 5\,\mathrm{K}$. The effective magnetic moment was determined in the substitution series from the inverse magnetic susceptibility. We found that the effective magnetic moment $\mu^c_{\mathrm{eff}} = (4.82 \pm 0.02)\,\mu_{\mathrm{B}}$ of the free Yb^{3+} ion ($\mu^{calc}_{\mathrm{eff}} = 4.53\mu_B$) in the pure phosphorous compound is slightly reduced to $\mu^c_{\mathrm{eff}} = (4.52 \pm 0.02)\,\mu_{\mathrm{B}}$ for the pure arsenic compound which hints to a reduction of the Yb valence. While the change in μ_{eff} is small, we found a large change in the Weiss temperature from $\Theta^c_W = (-17 \pm 2)\,\mathrm{K}$, $\Theta^a_W = (-37 \pm 3)\,\mathrm{K}$ for $x = 0$ to $\Theta^c_W = (-113 \pm 1)\,\mathrm{K}$, $\Theta^a_W = (-180 \pm 3)\,\mathrm{K}$ for $x = 1$. The angular dependence of the susceptibility $\chi(\phi)$ of $\mathrm{YbNi_4P_2}$ above $2\,\mathrm{K}$ in different external fields was studied in collaboration with M. Baenitz (MPI CPfS). While the anisotropy upon rotation about the (001) axis was below the detection limit, an anisotropy in $\chi(\phi)$ was found when rotating about the (100) axis.
Phase pure samples of $\mathrm{LuNi_4P_2}$ have been synthesized and were characterized in the frame of this work. These samples have been used as a non-magnetic reference compound in specific heat capacity measurements.

In collaboration with different groups, several experiments have been started using our new single crystals. From the high temperature part of the magnetic specific heat capacity of $\mathrm{YbNi_4P_2}$ it became possible to estimate the missing third CEF level E_3. The combination of the neutron [126] and heat capacity data suggests a level scheme of $E_1 = 8.5\,\mathrm{meV}$, $E_2 = 12.5\,\mathrm{meV}$ and $E_3 \approx 25\,\mathrm{meV}$ which was worked out in collaboration with Z. Hüsges [129]. The determined CEF scheme was obtained by an elaborate fitting procedure and is connected to large error bars. Therefore a further refinement is appreciated. Additional experimental input can be obtained by single crystal NMR. In the tetragonal compound $\mathrm{YbNi_4P_2}$, the environment of the Yb atoms is orthorhombic and NMR is one method by which the local anisotropy of the Yb atoms in their orthorhombic environment can be studied. NMR experiments on large single crystals have been started by H. Yasuoka, H. Tou and coworkers [130]. Good agreement was already found by comparing the calculated magnetization according to the estimated CEF scheme with high-field magnetization data in collaboration with T. Förster and M. Brando.

At the beginning of this work, $\mathrm{YbNi_4P_2}$ single crystals have been investigated by J. Sichelschmidt by electron spin resonance (ESR) down to $T = 2.9\,\mathrm{K}$ using X-band frequency ($9.4\,\mathrm{GHz}$). In contrast to the expectation that the observation of an ESR resonance is possible in Kondo lattice systems if ferromagnetic fluctuations are present [131], surprisingly no ESR resonance was detectable. Later, the new samples with masses up to 1800 mg facilitated first single crystal inelastic neutron scattering (INS) experiments carried out in collaboration with Z. Hüsges, S. Lucas and O. Stockert. The experiments showed that antiferromagnetic fluctuations occur already far above the Curie temperature $T_C = 0.15\,\mathrm{K}$.

First ARPES experiments on $\mathrm{YbNi_4P_2}$ performed in collaboration with D.V. Vyalikh and coworkers showed that mainly nickel states contribute to the DOS near the Fermi level. Further ARPES studies have been started to get more insight into its electronic structure.

With the new generation of single crystals it now becomes possible to investigate the physics of the FM QCP in arsenic substituted $\mathrm{YbNi_4P_2}$ in more detail. This will provide experimental data which might enable us to improve the understanding of ferromagnetic quantum criticality in Kondo-lattice systems.

2.3 Crystal growth of $YbNi_4P_2$

Preliminary work: Bridgman growth experiments

$YbNi_4P_2$ single crystals were grown by a modified Bridgman method from a Ni-P self-flux for the first time in 2012 [118]. In the mean time, the growth procedure has been optimized and several physical properties of this compound have been investigated. A detailed description of the growth parameters was reported in [132, 133] and is summarized in this section. The differential thermal analysis (DTA) was done using a simultaneous thermal analysis device (STA 449 C, Netzsch), which allows simultaneous thermogravimetry (TG) and DTA. For the Bridgman growth, the tantalum crucible was put under a flow of argon in a vertical resistive furnace (GERO HTRV70250/18) in which a maximum temperature of 1350°C was used in our experiment. During the growth, the temperature was measured in situ at the bottom of the tantalum crucible by a Pt/Rh thermocouple of type B. The sealed tantalum crucible was slowly heated up to 700° C with a rate of 30 K/h to allow a slow reaction of phosphorous with the other elements and to 1350°C with a rate of 50 K/h. The melt was held at this temperature for 1 h to ensure homogenization and then cooled by slow moving of the whole furnace with 0.88 to 3.4 mm/h leading to a cooling rate in the range of $0.5 - 4$ K/h down to 1000°C, while the position of the crucible stayed fixed. With this setup, we were able to cool the sample without vibrations resulting from the movement which is different from the conventional Bridgman process where the sample is moved from the hotter to the colder zone. After the growth, the $YbNi_4P_2$ single crystals were embedded in the Ni-Ni_3P eutectic. A typical growth result (cut image) with the $YbNi_4P_2$ single crystals embedded in the flux is shown in Fig. 2.3. Since the flux can not be removed by acids without solving the crystals, the use of a centrifuge (Christ UJ1) was necessary to separate the crystals from the flux. In preparation of the centrifugation process, the sample was cut using a spark erosion device and placed above some glassy carbon pieces and a graphite sieve in a fused silica ampoule. The ampoule was heated in a box furnace up to 1100°C, held at this temperature for one hour and then within a few seconds moved into a centrifuge. The flux with the eutectic temperature of $\approx$ 870°C was spun off. Afterwards, the remaining crystals could be easily separated from each other manually. The long, rod shaped single crystals are presented in Fig. 2.3.

2.3.1 Experimental details of the Czochralski growth experiments

High-purity starting materials Yb ingot (99.9%, Strem Chemicals), Ni slugs (99.995%, Alfa Aesar), red P pieces (99.999%, Mining & Chemical Products Ltd.) were used. The reagents, namely ytterbium and phosphorous, are air sensitive. The preparation of these reagents was done in a glove box filled with purified argon. The stoichiometric composition of the elements was weighed in together with $Ni_{81}P_{19}$ (eutectic composition) as flux resulting in a molar sample to flux ratio of 1:1. The total mass of each growth charge was 15 g. The elements were filled in a boron nitride crucible ($V = 30$ ml) for the preparation of the precursor for the Czochralski growth. The inner crucible was put in an outer crucible made of tantalum which was sealed under Ar using arc-melting. The prereaction was performed in a Linn furnace at $T_{max} = 950$°C under protective Ar atmosphere at ambient pressure. The Czochralski growth experiment was performed in a commercial ADL (Arthur D. Little) growth device

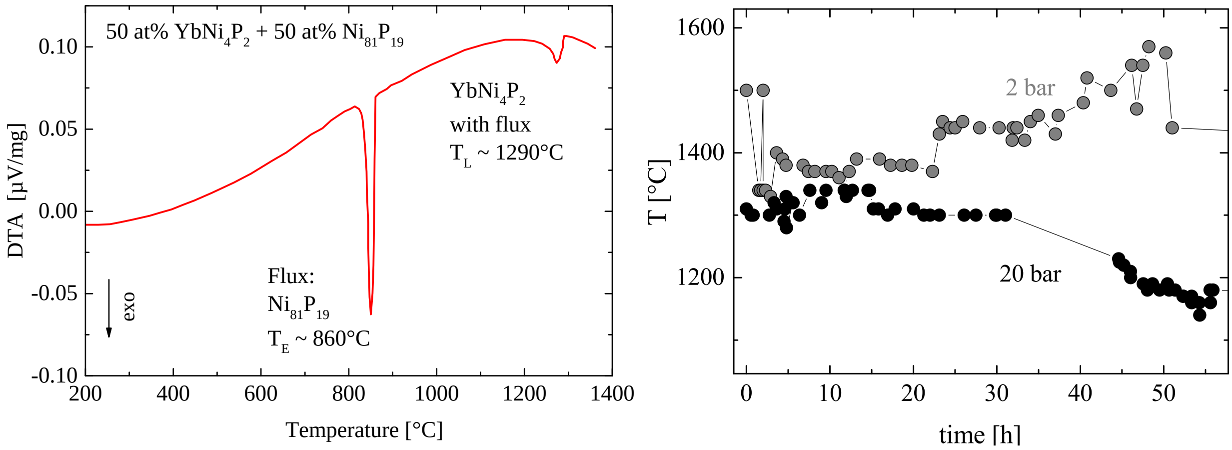

Figure 2.2: *Left:* The DTA signal recorded during cooling shows a dip at the liquidus temperature of the starting charge $T_\mathrm{L} \approx 1290°\mathrm{C}$ marking the onset of the crystallization of $YbNi_4P_2$. A second dip occurs at the eutectic temperature $T_\mathrm{E} \approx 860°\mathrm{C}$. The data were recorded by C. Krellner. Figure taken from [133] by courtesy of Elsevier. *Right:* Development of the melt temperature versus time where an Ar over pressure of either 2 bar (grey symbols) or 20 bar (black symbols) was applied in the growth chamber. Only in the second case stable growth conditions could be established which made a controlled crystal growth possible.

equipped with a high-frequency generator (Hüttinger) that provides a maximum power of about 30 kW. The temperature was measured with an IRCON pyrometer. The crystal structure was characterized by PXRD on crushed single crystals, using Cu-K_α radiation. The chemical composition was measured by EDX. The orientation of the single crystals was determined using a Laue camera with X-ray radiation from a tungsten anode. Four-point resistivity and magnetization measurements were performed using the PPMS.

2.3.2 Self-flux method

A complete ternary phase diagram of Yb-Ni-P compounds at high temperatures does not exist, but an isothermal section (T = 870 K) of this phase diagram was determined by Kuz'ma et al. [33]. Several stable ternary phases exist in the vicinity of $YbNi_4P_2$. In previous work, the decomposition of $YbNi_4P_2$ above 1500°C at ambient pressure was observed [121]. Therefore, one expects that the crystal growth of the stoichiometric compound by floating-zone or the Czochralski method not to be successful. The binary Ni-P phase diagram shows a low-melting eutectic, $Ni_{81}P_{19}$ [134]. A detailed investigation identified $Ni_{80.4}P_{19.6}$ as the eutectic composition with the eutectic temperature $T_\mathrm{E} = 875°\mathrm{C}$ [34]. We have used this eutectic as a self-flux in one series of experiments utilizing a Bridgman and in an other series the Czochralski technique to grow $YbNi_4P_2$ single crystals. One further problem is that the Yb-Ni-P melt exhibits a high reactivity with other materials leading to lack of inert crucible material. For the determination of the crystallization temperature of $YbNi_4P_2$ in $Ni_{81}P_{19}$ simultaneous TG and DTA have been performed in preliminary work by C. Krellner before starting the growth experiments. 555 mg of prereacted material consisting of 50 at% $YbNi_4P_2$ and 50 at% $Ni_{81}P_{19}$ was put in an open alumina crucible and heated with 10 K/min in an Ar flow. The weight loss after 3 heat/cool cycles was $\Delta m/m \approx 0.05$ and the signals of all three runs were reproducible. The DTA curve presented in Fig. 2.2 shows the third

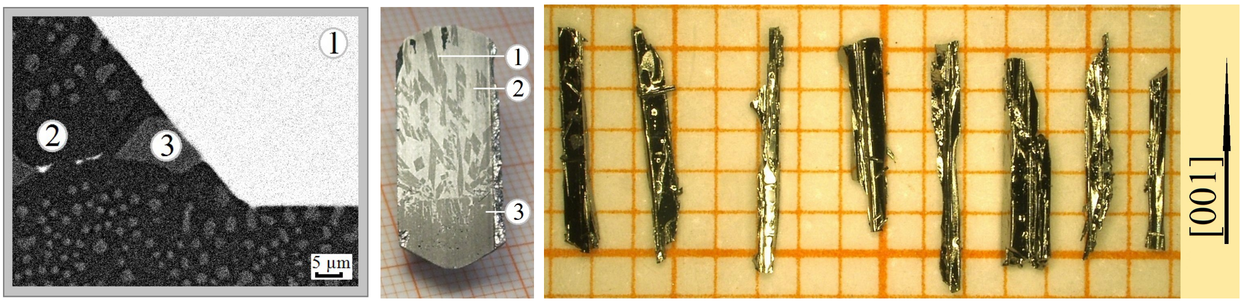

Figure 2.3: Bridgman growth: *Left:* The secondary electron image of the cut through the sample shows $YbNi_4P_2$ crystals (1) in a matrix of Ni_3P (2) and Ni (3). *Middle:* The $YbNi_4P_2$ single crystals (1) are enclosed in the Ni-P flux (2). A polycrystalline part of $YbNi_4P_2$ (3) formed at the bottom of the crucible. This axial cut through the ingot shows the distribution of phases that is expected from a directional solidification experiment according to the Bridgman technique. The ratio of the polycrystalline part and the part where the single crystals are surrounded by flux varied between different growth experiments. *Right:* Single crystals on mm grid after the centrifugation procedure. The crystals grow preferentially along the [001]-direction. Figures taken from [133] by courtesy of Elsevier.

cooling process. During heating, the melting signal of the eutectic appears at 870°C. The melting signal of the 142-compound is located at ≈ 1340°C and relatively weak. The high melting temperature of the transition metal Ni (1455°C) in combination with the starting sublimation of red P at low temperature (416°C) and its high reactivity additionally to the low boiling point (1196°C) and high vapour pressure of Yb necessitates the preparation of a precursor.

2.3.3 Czochralski growth from a levitating melt

In the past, the successful single crystal growth of cerium compounds in the same high frequency furnace that we used has been reported [135–137]. $YbNi_4P_2$ single crystals were grown from a levitating melt applying the Czochralski method using the same sample to flux ratio of 1:1 that was used in the Bridgman experiments described above. The composition is marked by a solid blue circle in Fig. 1.1. A precursor was prepared using a boron nitride crucible, welded inside a tantalum crucible using an argon arc furnace and were prereacted in a box furnace under argon atmosphere subsequently. The precusor was prepared from the elements and consisted of nickel phosphides, ytterbium phosphides and ternary Yb-Ni-P compounds. The Czochralski growth experiment was started by melting the precursor material in a cold copper crucible (Hukin-type) with a radio-frequency induction coil applying a power of 12 kW at maximum. The precursor was homogenized due to the strong stirring of the levitating melt within several minutes. The power was set in a way that the temperature of the melt was above the liquidus temperature at about 1400°C. The melt was kept at this temperature for 15 min to ensure complete homogenization. For the first Czochralski growth, we used an $YbNi_4P_2$ seed prepared from a Bridgman-grown crystal. In the following experiments, oriented seeds prepared from the first Czochralski experiment were used. The seed was lowered into the melt and the generator power was adjusted carefully after dipping. As soon as the process run stable after dipping, the seed was pulled upwards along its crystallographic [001]-direction with a pulling rate of 0.2 mm/h. Within the process time

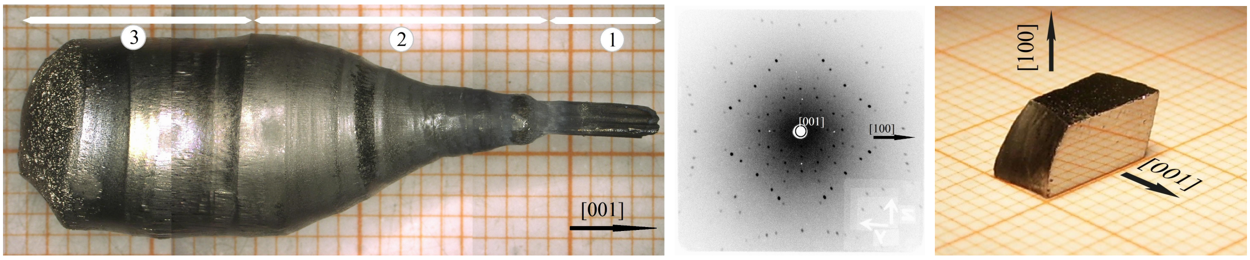

Figure 2.4: *Left:* Single crystal grown by the Czochralski method (Optical microscope image). An oriented seed (1) was used to grow an $YbNi_2P_2$ single crystal (2). The growth was terminated with a faster growth velocity which leads to an enhanced occurence of flux inclusions in the lower part of the sample (3). *Middle:* The Laue pattern of the [001]-direction of a sample prepared by Czochralski growth shows the four-fold symmetry. The good crystal quality is indicated by the sharp Laue reflections. *Right:* Single crystal sample cut for a magnetization measurement. Figures taken from [133] by courtesy of Elsevier.

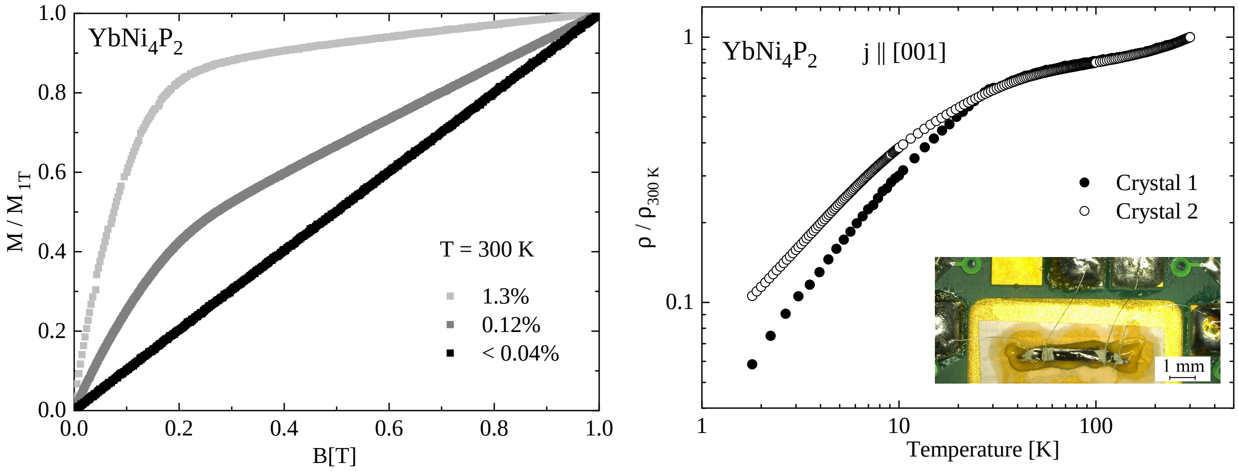

Figure 2.5: *Left:* Measured magnetization $M(B)$ normalized to $M(B = 1\,\mathrm{T})$ measured at $T = 300\,\mathrm{K}$ on crystals with a different amount of flux inclusions. These flux inclusions contain elementary Ni (given in weight percentage). The magnetic moment of $YbNi_4P_2$ depends linearly on B and is small at low fields. Below $\approx 0.1\,\mathrm{T}$ the measured moment is dominated by the contribution from the Ni inclusions. The black curve shows $M(B)$ measured on a crystal with a content of elementary Ni which is below the detection limit of this method. *Right:* Measured resistivity $\rho(\mathrm{T})$ normalized to the resistivity at $T = 300\,\mathrm{K}$. $RR_{1.8\mathrm{K}} = 17$ was determined for crystal 1 which was grown by the Czochralski method (closed symbols). For a crystal grown by the Bridgman method, crystal 2, we determined $RR_{1.8\mathrm{K}} = 9$ (open symbols). In the inset, a needle shaped crystal connected to the sample platform in four-point-geometry with platinum wire contacts prepared for a resistivity measurement is shown. Figures taken from [133] by courtesy of Elsevier.

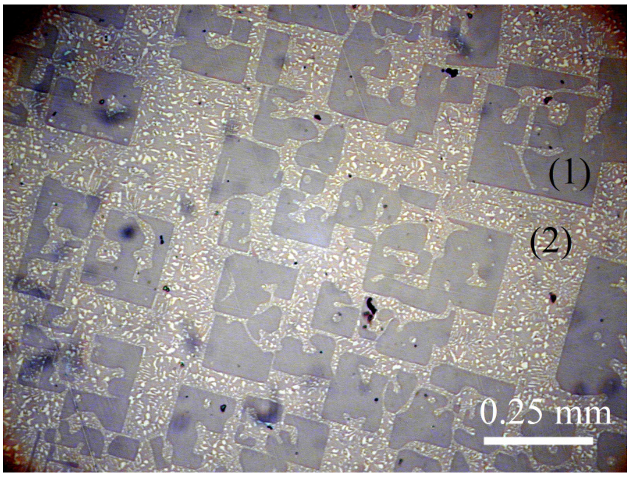

Figure 2.6: Polarization microscopy: $YbNi_4P_2$ (1) in Ni-Ni_3P flux (2). Here, a cut through the flux containing part (3) of the sample, shown in Fig. 2.4, is depicted.

of 30 h the total power reduction was about 30% during the experiment. To achieve an inclusion free sample, a low growth rate and a long process time of several days was necessary. First experiments applying an argon pressure of 2 bar led to considerable evaporation of phosphorous from the melt and therefore to a shift of the stoichiometry which made the crystal growth unstable. This evaporation of phosphorous from the melt was slowed down by applying an argon pressure of 20 bar in the growth chamber leading to stable growth conditions. Fig. 2.4 shows a typical growth result.

2.3.4 Comparison of the growth results

Structural and chemical characterization

PXRD measurements confirmed the tetragonal $ZrFe_4Si_2$ structure type ($P4_2/mnm$) with lattice parameters $a = 7.0560(3)$ Å and $c = 3.5876(5)$ Å, which are in agreement with the data published for polycrystalline samples [33]. EDX microprobe analysis of the crystals grown by the two different methods, revealed the stoichiometry of the 142-compound within an error of 2 at%. The single crystals additionally were analyzed with electron probe microscopy analysis (EPMA). The cut through a Bridgman growth sample showed that $YbNi_4P_2$ single crystals were embedded in the Ni-Ni_3P eutectic (Fig. 2.3). The high quality of the single crystals is evident from sharp Laue backscattering spots shown in Fig. 2.4. These samples sometimes exhibit inclusions of the eutectic. Besides the paramagnetic [138] Ni_3P phase, the eutectic flux also contains inclusions of magnetic Ni.

Magnetization and electrical transport

The grown $YbNi_4P_2$ crystals can contain flux inclusions consisting of the eutectic mixture of Ni_3P and Ni with the phase fractions of approximately 3:1 according to the lever rule. While Ni causes a ferromagnetic contribution to the magnetization of the sample, Ni_3P is paramagnetic. To estimate the residual Ni content, magnetic measurements were performed, Fig. 2.5. With this very sensitive method, the purest crystals concerning the flux content can be identified since the contribution of nickel to the measured moment is large and reaches 90% of the saturation at low fields $B \approx 0.1\,\mathrm{T}$. We utilized the fact that the contribution of the Yb moments increases linearly, and is therefore small at lower fields. As shown in Fig. 2.5, electrical transport measurements on $YbNi_4P_2$ single crystals with current along the [001]-direction were performed to compare the crystal quality of samples from different batches by means of the resistivity ratio $RR_{1.8\mathrm{K}} := \rho(300\mathrm{K})/\rho(1.8\mathrm{K})$.

Crystals grown by Bridgman method

The $YbNi_4P_2$ single crystals grown by the Bridgman method exhibit naturally grown faces. The rod-shaped crystals grow preferentially along the [001]-direction, whereas the tetragonal plane is bounded by {110} faces. The dimensions of the largest crystals were 0.8mm × 0.9mm × 6mm. During the growth, the melt attacked all tested crucible materials (Al_2O_3, glassy carbon, graphite, tantalum) leading to a contamination of the melt. The analysis by carrier gas hot extraction of a polycrystalline sample performed by G. Auffermann (MPI CPfS Dresden) showed that the crystals grown in a graphite crucible contain up to $1\,wt\%$ carbon. The crystals grown by the Bridgman method sometimes contain inclusions of residual flux consisting of the Ni-Ni_3P eutectic. This content of flux was estimated by magnetic measurements to be $0 - 1\,\mathrm{wt\%}$. The largest Ni-free single crystals have a mass of about 10 mg. We performed electrical-transport measurements with current parallel to the crystallographic [001]-direction and determined $RR_{1.8\mathrm{K}} = 9$ for the best crystals from the Bridgman growth experiments for current along the [001]-direction.

Crystals grown by Czochralski method

Several experiments were done, summarized in Tab. 2.1, to modify and optimize the growth process such that it became possible to grow large single crystals of $YbNi_4P_2$. Fig. 2.4 shows an example of a successful Czochralski growth from a levitating melt with a diameter of $9 - 10\,\mathrm{mm}$ and a total length of $14 - 15\,\mathrm{mm}$. The upper part of the sample (region 2) is about 9 mm long and consists of $YbNi_4P_2$. The mass of this single crystal part is about 1.8 g. In the lower part of the sample, $YbNi_4P_2$ contains an increasing amount of flux inclusions (region 3). The single crystal seeds that were used have been oriented and all samples were pulled out of the melt along the [001]-direction. A Laue image of a Czochralski grown single crystal is shown in Fig. 2.4. Flux inclusion consisting of the Ni-Ni_3P eutectic have been observed in the lower part of the grown sample. These also occur in the upper part at grain boundaries in samples that contain more than one grain. This content of flux was estimated by magnetic measurements to be $0 - 0.04\,\mathrm{wt\%}$. Fig. 2.4 shows a typical sample prepared for a magnetization measurement. We performed electrical transport measurements with current parallel to the crystallographic [001]-direction and determined $RR_{1.8\mathrm{K}} = 17$ for the best crystals from the Czochralski growth experiments. We found that with the crucible-free Czochralski method it is possible to grow large, inclusion-free single crystals with a higher residual resistivity ratio. The good quality of the samples became apparent since it was possible to observe quantum oscillations in the torque and the magnetoresistance measured on the samples in fields above 20 T as demonstrated in Fig. 2.15 [139].

exp. No.	crucible	result	p(Ar) [bar]	seed	remarks
021	C	proof of principle*	5	Ni	growth from crucible
025	C	no melt/levitation	5	Ni	carbide formation ?
026	C	first levitation*, PC	5	W	strong evaporation
027	C	PC	5	W	strong evaporation
028	Al_2O_3	evap. reduced*, PC	20*	019	impurity layer on melt
029	BN*	less impure melt surface*, PC	20	028	much larger grains
030	BN	no melt/levitation	20	029	PR stacking unsuitable
031	BN	PR failed	-	-	leaky crucible
032	BN	no melt/levitation	20	029	PR at 1350°C
033	BN	stable levitation*, PC sample	20	029	PR at 950°C *, rotation, seed holder failed
034	BN	PC, larger grains	20	029	rotation
035	BN	PC, few/large grains *	20	029	no rotation*
036	BN	PC, few/large grains	20	029	no rot., imp. layer on melt
037	BN	PC, few/large grains	20	029	no rot., imp. layer on melt
038	BN	one large grain + one small	20	029	additional cleaning step*, surface of melt very pure
039	BN	SC *	20	038	add. cleaning
040	BN	SC	20	038	add. cleaning
041	BN	SC	20	040	add. cleaning

Table 2.1: $YbNi_4P_2$ Czochralski growth experiments from the levitating melt. The prereaction (PR) has been performed using different crucible materials: carbon (C), aluminum oxide (Al_2O_3) or boron nitride (BN). The maximum temperature during the PR was 950°C if not specified else. While in the first experiments polycrystalline (PC) samples have been obtained, the last experiments yielded single crystals (SC). For a definition see Sec. 1.1.1. Main changes and key results are marked by an asterisk.

2.4 Crystal growth of $\mathbf{YbNi_4(P_{1-x}As_x)_2}$, $(x = 0.1 - 1.0)$

Preliminary work

In the past, samples of the substitution series $YbNi_4(P_{1-x}As_x)_2$ with As-contents up to $x = 0.13$ have been investigated and the material was studied close to the ferromagnetic QCP [14]. These samples, which were examined in preliminary work, had been grown by a modified Bridgman method which yields thin needle shaped single crystals as shown in Fig. 2.3. Until now, the physical properties of the compounds in the substitution series $YbNi_4(P_{1-x}As_x)_2$ and the respective T-x phase diagram are unexplored for higher As concentration in particular due to a lack of samples with $x > 0.13$. To observe the emergence of Fermi liquid behaviour in the system, samples with these higher As concentrations are required. For our study, the samples in the substituion series were grown by the Czochralski method based on the procedure which was used to grow the unsubstituted compound $YbNi_4P_2$ [133]. Using seeds from the new crystal generation, we have grown single crystals of the substituted compound $YbNi_4(P_{1-x}As_x)_2$ with $x \neq 0$.

2.4.1 Experimental details

High purity starting materials Yb ingot (99.9%, Strem Chemicals), Ni slugs (99.995%, Alfa Aesar), red P pieces (99.999%, Mining & Chemical Products Ltd.), black As pieces (99.9999%, MaTeck) were used. The experiments have been performed using the same parameters as for the growth of the pure phosphorous compound (cf. section 2.3.1). For the growth of the single crystals in the substituion series P was partially replaced by As.

2.4.2 Crystal growth from self-flux

The growth of the compounds in the substitution series $YbNi_4(P_{1-x}As_x)_2$ was performed in analogy to the growth of $YbNi_4P_2$ by Czochralski method [133]. We explored how the growth conditions change due to the addition of arsenic as a fourth element. A quarternary phase diagram of Yb-Ni-As-P compounds does not exist. An isothermal section ($T = 870\,\mathrm{K}$) of the Yb-Ni-P phase diagram [33] as well as binary Ni-P [34] and Ni-As [29] phase diagrams can be found in the literature. In the style of preliminary work [14, 133], the crystal growth in the substitution series is performed from a Ni-P, Ni-P-As or Ni-As self-flux. The binary phase diagrams show low melting eutectics, $Ni_{80.4}P_{19.6}$, with $T_E = 875°\mathrm{C}$ [34] and $Ni_{76.6}P_{23.4}$, with $T_E = 897°\mathrm{C}$ [29]. Since the fraction of the pnictogen as well as the eutectic temperatures in both eutectics are similar, we assumed to work near a Ni-P-As eutectic if we use the Ni-P eutectic as a self-flux and replace P partially by As depending on the desired stoichiometry of the substituted compound. The element combination of the high melting transition metal Ni ($T_L = 1455°\mathrm{C}$) with non metallic red P (sublimation at 416°C) and the toxic As (sublimation at 614°C) as well as of Yb having a low boiling point (1196°C) and a high vapour pressure necessitates the preparation of a precursor in a closed Nb crucible.

Prereaction

The preparation of the precursor is performed in an inner crucible to avoid alloying of the metallic melt with the Nb crucible. In preliminary work it was found that Al_2O_3 and C are attacked by the melt and BN is the most inert crucible material up to a temperature of 950°C. We therefore used BN as the material for the inner crucible. The Nb crucible with the inner BN crucible containing the elements was welded using an argon arc furnace. The preparation of the precursor for the Czochralski growth is performed in three steps. (i) To avoid the contamination of the melt with the crucible material BN, the reaction of P, As with Yb and Ni was performed at comparatively low temperatures. For all compositions, the closed Nb crucible was slowly heated up to 700°C with a rate of 30 K/h and up to T^1_{max} with a rate of 50 K/h. The maximum temperatures T^1_{max} for this process were reduced for higher As contents and are listed in Tab. 2.2. This prereaction was done in a box furnace under argon atmosphere. Since As is highly toxic, a bowl with iron powder was placed inside the furnace to act as an arsenic absorber in case of a leakage of a Nb crucible. After this first reaction, an inhomogeneous precursor was obtained which contained several binary, ternary and quarternary phases.

No.	x_{nom}	T^1_{max} [°C]	T^2_{max} [°C]	x_{seed}
042	0.1	950	1400	0
044	0.1	950	1400	0
045	0.12	920	1420	0
046	0.15	920	1450	0
043	0.2	920	1420	0
047	0.2	920	1420	0.2
048	0.4	850	1550	0.2
049	0.6	850	1550	0.2
050	0.8	850	1400	0.2
051	1.0	850	1350	0

Table 2.2: Maximum temperatures of $YbNi_4(P_{1-x}As_x)_2$ for different x (nominal values) during the prereaction. T^1_{max} was used during the prereaction in the box furnace and T^2_{max} was reached during the homogenization in the high frequency furnace. In the last column, the As concentration of the seeds is listed.

(ii) The complete charge was removed from the BN crucible and placed in the cold copper crucible of the high frequency furnace. The homogenization of the precursor as a levitating melt was done under an Ar pressure of 20 bar. To complete the prereaction and to ensure homogenization the precursor for each composition was heated 15-20 times upon oscillating its temperature between 900°C and T^2_{max}. This step was always finished when the reflective surface of the melt was visible and the thin layer of oxides or high melting phases at the surface of the melt slipped down to the bottom of the molten drop-shaped precursor. (iii) In preliminary studies it turned out that the seeding is hindered by a layer consisting of high-melting impurities. We therefore removed the impurity layer mechanically and subsequently by rinsing in ethanol. These three steps, prereaction, homogenization and cleaning, altogether caused a weight loss of 1-2% of the precursor.

Czochralski growth from a levitating melt

The Yb-Ni-P/As melt exhibits a high reactivity with other materials leading to lack of inert crucible material which makes the growth from a levitating melt indispensable. The purified precursor was put in a cold copper crucible (Hukin-type). The Czochralski growth experiment was started by melting the precursor with a radio-frequency induction coil applying a power of 14 kW at maximum. After several minutes the precursor was homogenized due to the strong stirring of the levitating melt and the seeding was started. The temperature where the seeding was done was chosen ≈ 50°C above the liquidus temperature T_L. For the seeding a single crystal seed prepared by a preliminary Czochralski growth experiment was used. The As concentrations of the seeds used in the growth experiments are shown in Tab. 2.2. The solidus and liquidus temperatures of the melts were determined pyrometrically for all experiments and are shown in Fig. 2.7. The single crystal seeds were carefully oriented along their crystallographic [001]-direction by Laue method in advance. In all growth experiments, as soon as the process runs stable after dipping, the seed was pulled upwards parallel to its [001]-direction. During the experiments, the total power reduction was about 30% within the process time of ≈ 50 h. All samples were grown in the same manner by starting the growth with a pulling rate of ≈ 0.3 mm/h and reducing the speed of the pulling rod after 24 h to 0.15 mm/h. In a flux-growth process such low growth rates are essential to achieve inclusion-free samples. After pulling the crystal ≈ 12 mm with the low pulling rate, the process was terminated by pulling faster (≈ 10 mm/h) to separate the sample from the residual melt.

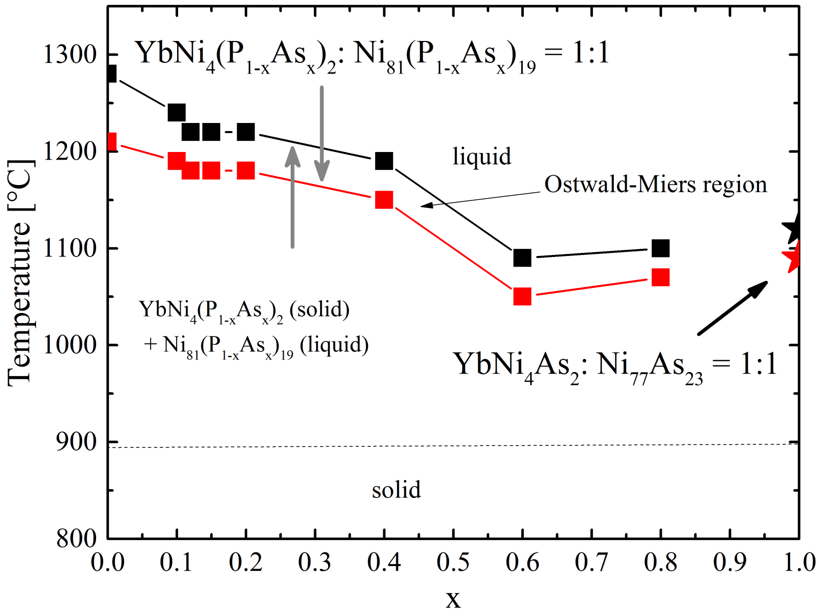

Figure 2.7: The solidus temperatures T_s (red squares) and the liquidus temperatures T_L (black squares) were measured pyrometrically during cooling (heating) during the homogenization step and mark the solidification (melting) of $YbNi_4(P_{1-x}As_x)_2$ in flux for different As concentrations x. The temperature where the seeding was done was set ≈ 50°C above T_L.

The evaporation of phosphorous, arsenic and ytterbium from the melt was slowed down by applying an argon pressure of 20 bar in the growth chamber leading to stable growth conditions. Fig. 2.8 shows typical growth results.

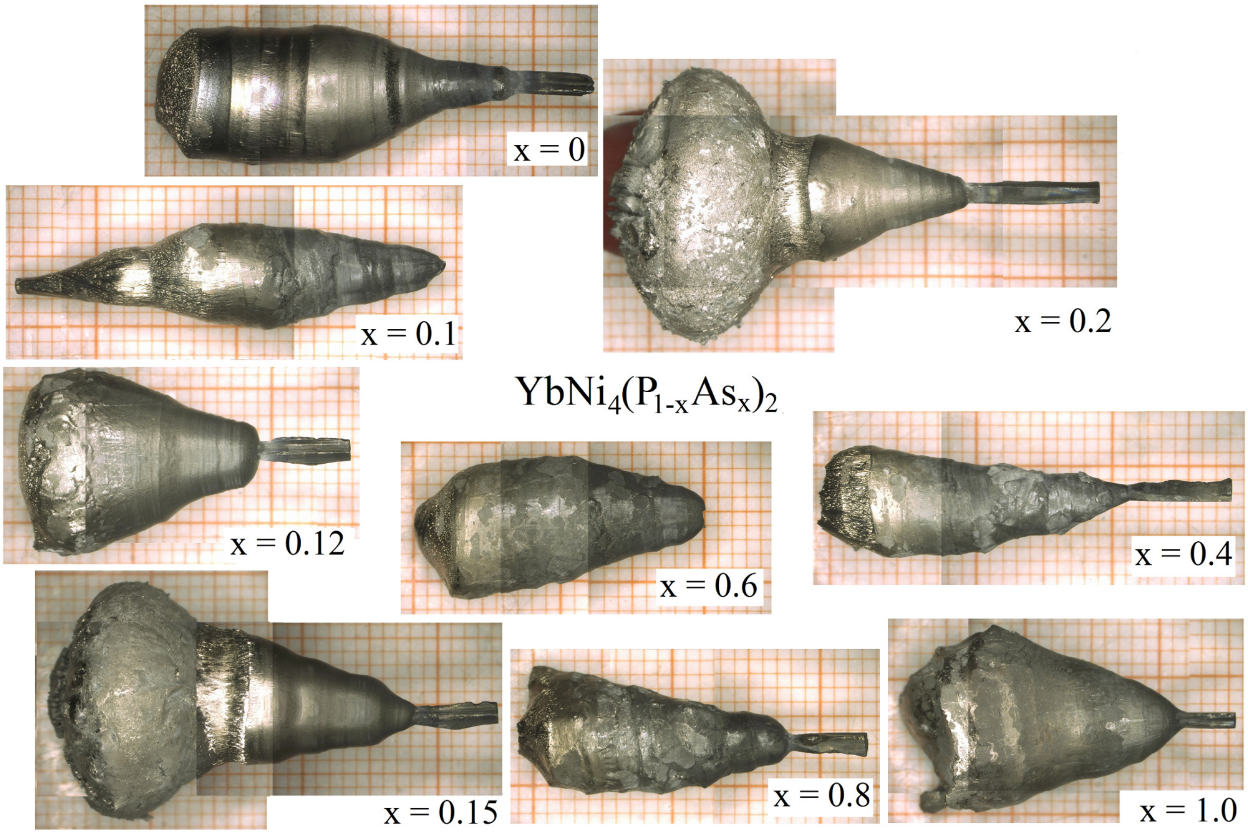

Figure 2.8: Resulting $YbNi_4(P_{1-x}As_x)_2$ single crystals. The samples with $x = 0.15$ and $x = 0.2$ have not been separated from the residual melt. Due to a generator shut down caused by a failure in the cooling water supply the residual melt solidified quickly at the end of the growth process.

2.4.3 Structural and chemical characterization

The analysis of the single crystals regarding the As concentration was performed by EDX for all samples in the same manner. Exemplarily, the analysis of a single crystal with a nominal As concentration of 20% is shown in Fig. 2.9. The growth of the sample with $x = 0.2$ was performed using an unsubstituted $YbNi_4P_2$ single crystal as the seed. The strong stirring of the levitating melt is advantageous since it supports not only the homogenization, namely the transport of the dopant but also the heat flux in the melt. It is known that low growth velocities are necessary to obtain crystals without flux inclusions. The distribution coefficient of As in the system $\kappa = c_l^{\mathrm{As}}/c_s^{\mathrm{As}}$ with the concentrations of As in the melt c_l^{As} and in the solid c_s^{As}, respectively, is not known and does not necessarily have to be exactly one [28]. A deviation from $\kappa = 1$ would lead to the enrichment or depletion of As in the melt and an inhomogeneous As distribution in the grown crystal. The As distribution in the single crystal, containing 20% As nominally, was investigated by EDX, and showed that the initial

As:P ratio of the melt of 1:4 can be found all over in our sample except at the first part which is connected to the seed. The seed consisted of $YbNi_4P_2$ ($x = 0$) and over a length of about 2.5 mm the crystal structure included more and more As and the lattice adapted to the new lattice constants. The analysis along radial lines (Cut A,B) and an axial line (Cut C) on polished surfaces shown in Fig. 2.9, yields a homogeneous As concentration from the center to the surface of the crystal. A similar analysis was performed on all grown single crystals. A part of each $YbNi_4(P_{1-x}As_x)_2$ sample was investigated by PXRD and the measurements confirmed the $P4_2/mnm$ tetragonal structure in the whole substitution series. The lattice parameters are summarized in Tab. 2.3 and Fig. 2.11. The structure refinement using the General Structure Analysis System (GSAS) [49, 140] yields an enlargement of the unit cell with increasing As content as expected. Both lattice constants $l_i(x)$ increase linearly with x leading to an enlargement of the unit cell volume $V_{\mathrm{YbNi4As2}} = 1.09\,V_{\mathrm{YbNi4P2}}$. The normalization of the data to the lattice constants of $YbNi_4P_2$ shows that the lattice constant a increases by $\approx 2\,\%$ while the increase is larger for the lattice constant c ($\approx 4.5\,\%$).

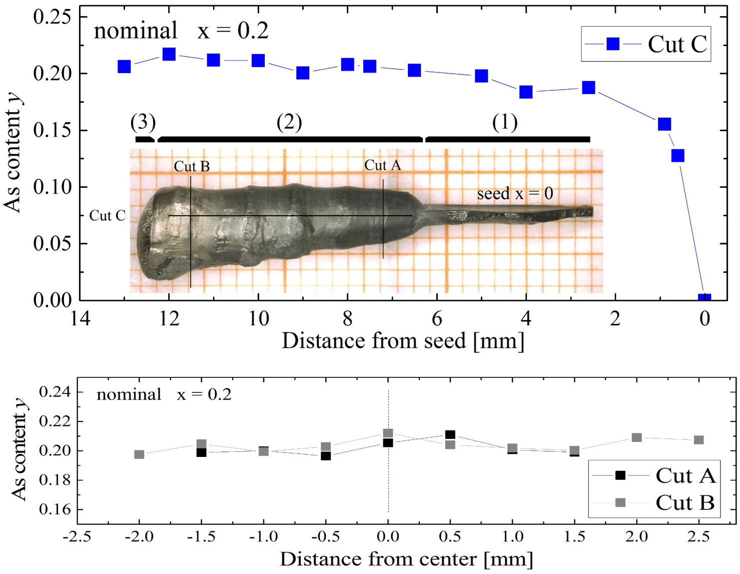

Figure 2.9: *Upper panel:* The as-grown sample with the nominal composition of $YbNi_4(P_{0.8}As_{0.2})_2$ is shown in the inset. The single crystal seed (1) consisted of $YbNi_4P_2$ and was oriented along the [001]-direction. The determination of the As content which was determined using EDX of region (2) of the grown sample is shown in the main figure. The growth was terminated with a faster growth velocity leading to the incorporation of flux in part (3) of the sample. The figure shows the As content along the axial cut C.; *Lower panel:* The real As content y in the grown sample along two radial lines, A and B in dependence of the distance from the center of the sample. Figure (under CCA 3.0 licence) taken from [48].

The orientation of the single crystals was determined using the Laue method. Conventional x-ray Laue devices use radiation from, for instance, a tungsten anode for this examination. The penetration depth of this radiation is typically only few μm for metallic samples which hinders the investigation of large single crystals. Additionally the beam diameter is only of $\approx$ 0.5 mm in width and usually large surfaces have to be investigated point by point. Besides x-rays we therefore also used neutrons to check the crystallinity of the single crystals. The neutron beam has a penetration depth in the cm range and a beam

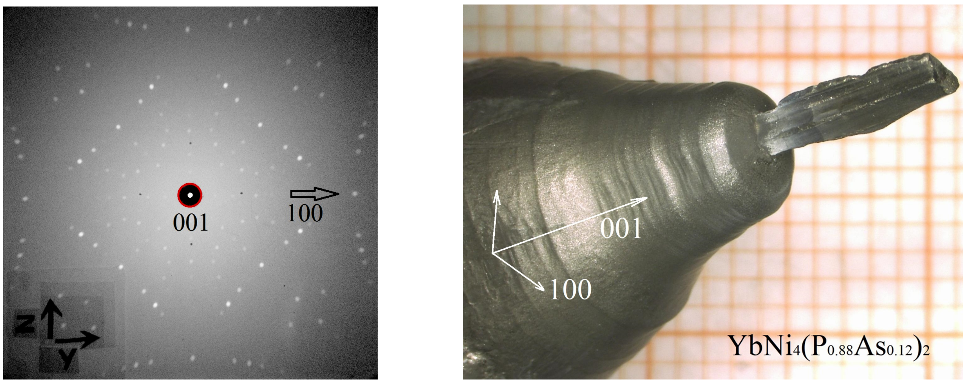

Figure 2.10: *Left:* X-ray Laue pattern of an $YbNi_4P_2$ single crystal oriented along the crystallographic [001] direction. *Right:* As grown $YbNi_4(P_{0.88}As_{0.12})_2$ single crystal. The single crystals develop natural {110} faces.

diameter (determined by the respective pinhole) of ≈ 6 mm. That means that the whole bulk of large samples interacts with the beam at the same time. In case that the sample exhibits grain boundaries and multiple single crystal grains, this shows up in the respective Laue pattern as demonstrated in the right panel Fig. 2.12. The sample, that was investigated here had an even surface, started to develop faces and did not show any signs of an intrinsic misalignment from its outer shape. All x-ray Laue pattern taken from this sample showed sharp Laue reflections. The investigation by neutron Laue backscattering yielded that there are at least two single crystal grains in the sample and that the misalignment between the grains is about 1-2%. An open question is, if it would be possible to detect such small misaligned by optical methods, like e.g. polarization microscopy, to avoid expensive neutron Laue investigations.

2.5 Synthesis and characterization of $LuNi_4P_2$

$LuNi_4P_2$ was prepared in a polycrystalline form as a non-magnetic reference compound for $YbNi_4P_2$ and the substitution series.

Phase pure polycrystalline $LuNi_4P_2$ was prepared in three steps according to [142] and [143]. A stoichiometric mixture of lutetium pieces (99.9%, Strem Chemicals), nickel powder (99.99%, ChemPur GmbH) and phosphorous pieces (99.999%, Mining & Chemical Products Ltd.) was sealed in an evacuated fused silica ampoule and prereacted at 800°C in a muffle furnace for three days. Afterwards, the sample was melted and homogenized in an arc furnace under argon atmosphere (purity 99.999%), grinded and pressed into pellets. The pellets again were sealed in an evacuated fused silica ampoule and annealed in a muffle furnace at 800°C for three days.

Powder x-ray diffraction measurements confirmed the $P4_2/mnm$ tetragonal structure with lattice parameters $a = 7.047(6)$ Å and $c = 3.583(4)$ Å, which is in agreement with the data published for polycrystalline samples [142].

x_{nominal}	x_{EDX}	a [Å]	c [Å]	V[Å^3]	λ [Å]	Reference
0	0	7.0565(2)	3.5877(1)	178.65		[121]
0	0	7.0560(3)	3.5876(5)	178.63	1.5418	[133]
0	0	7.0585(1)	3.5888(2)	178.80(4)	0.71069	this work
0.1	0.13	7.0706(2)	3.6010(7)	180.03(1)	0.71069	this work
0.2	0.2	7.0803(5)	3.6131(2)	181.13	1.5418	[48]
0.2	0.2	7.0838(2)	3.6145(3)	181.37(9)	0.71069	this work
0.4	0.4	7.1182(4)	3.6512(1)	185.00(5)	0.71069	this work
0.6	0.58	7.1500(8)	3.6889(2)	188.59(2)	0.71069	this work
0.8	0.79	7.1797(5)	3.7243(1)	191.98(3)	0.71069	this work
1	1	7.2035(1)	3.7513(6)	194.66(0)	0.71069	this work
1	-	7.216(4)	3.756(2)	195.61		[141]

Table 2.3: Lattice parameters a, c and the volume V of the unit cell of $YbNi_4(P_{1-x}As_x)_2$ were determined from x-ray powder data recorded by using the characteristic lines of Cu or Mo-radiation of wavelength λ.

Heat capacity and electrical resistivity

The specific heat of the reference compound was measured using exactly the same parameters like for the measurement of $YbNi_4P_2$. The specific heat capacity $C(T)$ of $LuNi_4P_2$ from 2 - 200 K is presented in Fig. 2.17. For $T > 200$ K, $C(T)$ approaches the classical Dulong-Petit limit of $7 \cdot 3\,R \approx 175\,\text{Jmol}^{-1}\text{K}^{-1}$. Below 10 K, $C(T)$ of $LuNi_4P_2$ can be described by $C/T = \gamma_0 + \beta T^2$ which is shown in the inset of the figure. The Sommerfeld coefficient is $\gamma_0 = 15.6\,\text{mJmol}^{-1}\text{K}^{-2}$ and from the slope $\beta = 0.183\,\text{mJmol}^{-1}\text{K}^{-4}$ of the linear fit a Debye temperature of $\Theta_D = 420.5$ K was determined. The electrical resistivity $\rho(T)$ of $LuNi_4P_2$, grey curve in Fig. 2.16, shows the behaviour of a normal metal between 1.8 and 300 K.

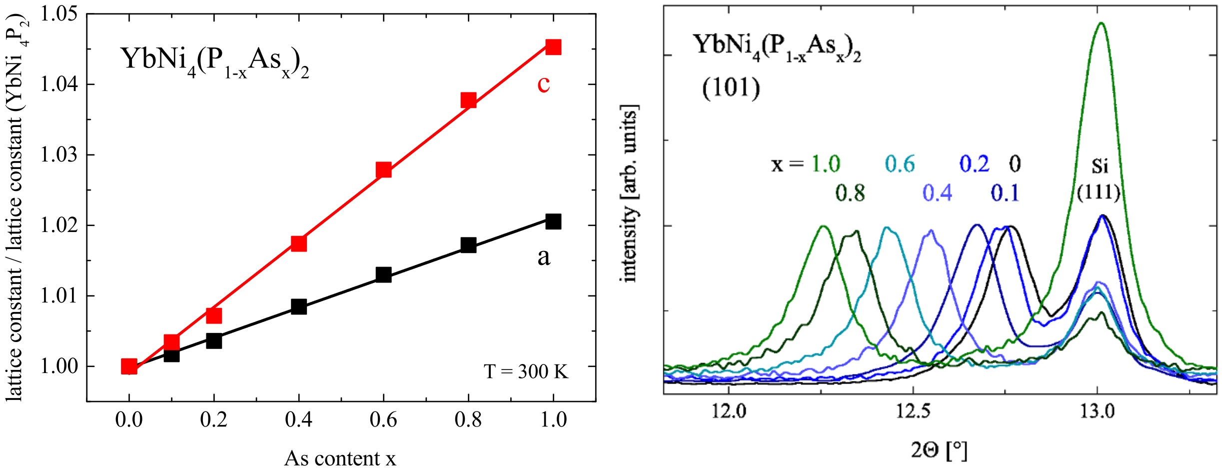

Figure 2.11: *Left:* Normalized lattice parameters of $YbNi_4(P_{1-x}As_x)_2$ determined by Rietveld refinement. The size of each point exceeds the statistical error. *Right:* X-ray powder diffraction data of the (1 0 1) reflection measured at 300 K with various substitution levels. The enlargement of the unit cell for increasing x is obvious from the shift of the reflection to smaller angles. Silicon was used as standard and position of the Si (1 1 1) reflection is shown for comparison.

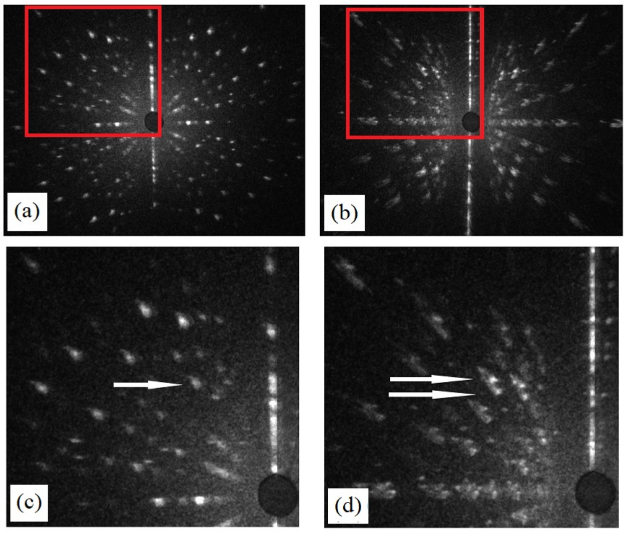

Figure 2.12: Neutron Laue backscattering images with incident beam parallel to the [110]-direction; (a) $YbNi_4P_2$. (b) $YbNi_4(P_{1-x}As_x)_2$, $x = 0.2$. (c) In the enlarged red box marked in Fig. (a) sharp Laue reflections are visible. (d) In the enlarged red box marked in Fig. (b) each Laue reflection splits up indicating the existence of at least two large single crystal grains in the sample. The Laue pattern were recorded at the ILL by O. Stockert (MPI CPfS).

2.6 Characterization of physical properties

2.6.1 $YbNi_4P_2$: Electrical resistivity

$YbNi_4P_2$ was found to be a Kondo lattice system with a Kondo temperature of $T_K \approx 8$ K revealed from specific heat measurements on powder samples. The occurence of coherent Kondo scattering was observed in the resistivity which steeply decreases below 20 K [121]. Resistivity measurements from $2-300$ K on small Bridgman grown $YbNi_4P_2$ single crystals show an anisotropy between the $j \parallel c$ and the $j \perp c$-direction [118]. A further measurement on single crystals gave absolute values at 300 K of 90 $\mu\Omega$cm for $j \parallel c$ and 160 $\mu\Omega$cm for $j \perp c$-direction [14]. Until now, all reported resistivity measurements on single crystals were performed on crystals grown by the Bridgman method. This method yields thin needle shaped crystals of about $2-3$ mm along the [001]$-$direction and of $0.5-0.7$ mm in the perpendicular extension.

Here, we have investigated the electrical transport properties down to 1.8 K of single crystal samples which were cut from one large crystal [48]. This single crystal had a conical shape with a diameter of $3-9$ mm and a length of 14 mm. It belongs to a new generation of single crystals grown by the Czochralski method from a levitating melt [133]. From this crystal, samples for the electrical transport measurement were cut using a spark erosion device. The samples had initial dimensions of $\approx 3\,\text{mm} \times 0.5\,\text{mm} \times 0.15\,\text{mm}$ and were oriented along the crystallographic main symmetry directions [100], [110] and [001]. Electrical transport measurements were performed between 1.8 and 300 K using the ACT option of a commercial PPMS (Quantum Design).

For a tetragonal material Ohm‘s law reads

$$\vec{j} = \begin{pmatrix} \sigma_a & & \\ & \sigma_a & \\ & & \sigma_c \end{pmatrix} \vec{E}, \qquad \rho = \frac{1}{\sigma} \tag{2.1}$$

with σ_a being the isotropic conductivity in the basal plane and σ_c the conductivity along the c direction for the electrical field $\vec{E}$. The coordinates are chosen such that the z axis is oriented along the crystallographic c-direction. Our Czochralski-grown $YbNi_4P_2$ single crystals reproduce the temperature dependence of the reported data as shown in the main part of Fig. 2.13 and with them it is also possible to resolve the temperature dependence of the resistivity ρ_{100} and ρ_{110} of the in-plane directions. As expected according to Eqn. 2.1, the resistivity is isotropic in the $a-a$ plane. We determined the absolute values at room temperature applying

$$\rho(T) = \frac{ab}{lI} U(T) \tag{2.2}$$

with the width a, the thickness b of the sample, the contact distance l and the applied constant current I and measured voltage U. For $j \parallel 001$ we determined the resistivity $\rho_{001}(300\,\text{K}) = 60\,\mu\Omega$cm, for $j \perp 001$ we found $\rho_{110}(300\,\text{K}) = 70\,\mu\Omega$cm. The absolute value determined for the [100]-direction agrees with that of the [110]-direction. For comparison, the resistivity of the non-magnetic reference $LuNi_4P_2$ was measured and is shown in the inset of Fig. 2.13. For the determination of the absolute values, the measurement device (U, I) as well as the geometry of the samples (a, b, l) have to be considered as sources for uncertainties. In the resistivity measurement, the main contribution to the uncertainty comes from the geometry factors $\Delta a/a \simeq 3\%$, $\Delta b/b \simeq 3\%$ and $\Delta l/l \simeq 1\%$. The uncertainty of the voltage $\Delta U/U$ is between 1% and 3% for different temperatures. The uncertainty of the current [144] with $\Delta I/I \simeq 5 \cdot 10^{-4}\%$ is negligible.

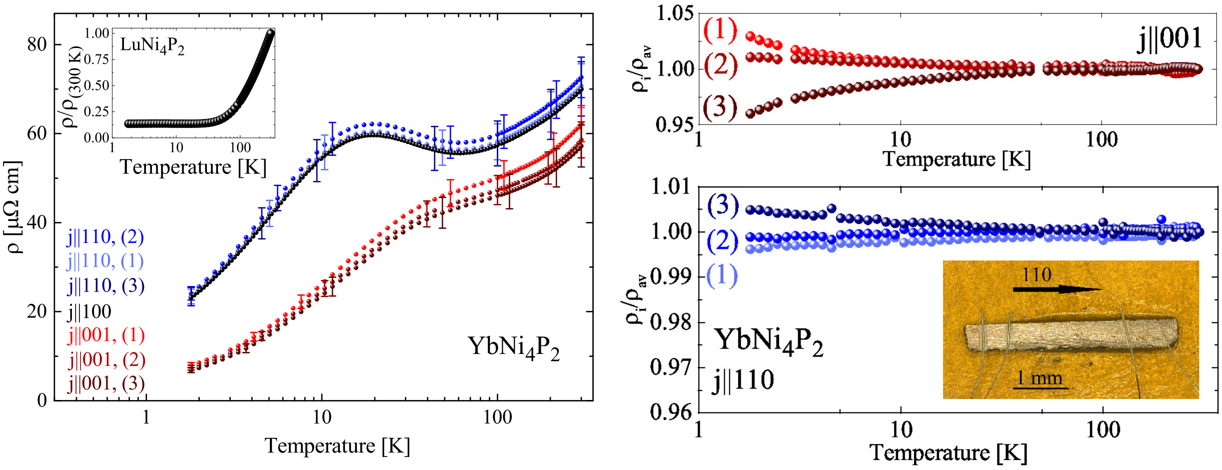

Figure 2.13: *Left:* Electrical resistivity ρ as a function of temperature from 1.8 K to 300 K measured with current j perpendicular ($j \parallel 100$ and $j \parallel 110$) and parallel to the crystallographic c-axis. The inset shows the electrical resistivity measured on a polycrystalline sample of $LuNi_4P_2$. The resistivity ratio was determined to be $\rho_{\mathrm{poly}}(300\,\mathrm{K})/\rho_{\mathrm{poly}}(1.8\,\mathrm{K}) = 7.4$. *Right:* Ratio of the normalized electrical resistivity ρ_i of measurement i divided by the average resistivity ρ_{av} for the respective current direction as a function of temperature. The samples were thinned down in two steps from 0.15 (i=1, curve (1)) to 0.09 mm (i=3, curve (3)). In the inset, an oriented sample with the four platinum wire contacts prepared for the measurement is shown. Figure (under CCA 3.0 licence) taken from [48].

The aim of our optimization of the crystal growth process is to minimize the crystal defects. Indispensable is the use of high-purity starting materials. The contamination of the melt by crucible materials has to be avoided. Low growth rates avoid flux inclusions. Adjusting the temperature during the growth experiment to the lowest possible value reduces the evaporation of the elements and therefore a shift in the stoichiometry. At lowest temperatures, the scattering on crystal defects is the only contribution to the resistivity. Therefore, the resistivity ratio $RR_{1.8\,\mathrm{K}} = \rho(300\,\mathrm{K})/\rho(1.8\,\mathrm{K})$ is an indicator for the amount of crystal defects.

For six different samples, which were cut from the same single crystal, different $RR^{001}_{1.8\,\mathrm{K}}$ values between 11 and 17 were found. For the purest sample, we determined the absolute resistivity value to be $\rho_{001}(1.8\,\mathrm{K}) = 3.5\,\mu\Omega\mathrm{cm}$. In the other case, if the current is perpendicular to the c-direction, $RR^{110}_{1.8\,\mathrm{K}}$ and $RR^{100}_{1.8\,\mathrm{K}}$, respectively, spread less for the six examined samples. The values are between 3.00 and 3.07. The absolute value is $\rho_{110}(1.8\,\mathrm{K}) = 22.8\,\mu\Omega\mathrm{cm}$. The large variation in $RR^{001}_{1.8\,\mathrm{K}}$ can be caused by a misalignment of the four contacts for the current and voltage measurement. During the growth small-angle grain boundaries can evolve in a single crystal. They lead to the distorsion of the lattice and enhance the residual resistivity. A further analysis by Laue method is required to clarify the origin of the variation of $RR^{001}_{1.8\,\mathrm{K}}$.

Sample No.	RRR $j\|\|a$	RRR $j\|\|c$	$RR_{4.5\,\mathrm{K}}$ $j\|\|a$	$RR_{4.5\,\mathrm{K}}$ $j\|\|c$
040-2-6	11.5	60	-	-
040-2-6-4	-	39	-	-
041-st1	-	-	1.8	4.3
041-st2	10.5	-	1.8	4.3

Table 2.4: RRR and $RR_{4.5\,\mathrm{K}}$ with $j||a$ and $j||c$ determined for selected samples cut from Czochralski grown single crystals (040 and 041).

A common technique to improve the crystallinity of materials is annealing. An experiment at 800°C in an inert atmosphere for 5 days yields an increase of 25% of $RR^{001}_{1.8\,\mathrm{K}}$. Due to the large anisotropy for the different current directions, it is not clear if this improvement is the result of the annealing procedure or was caused by a slight misalignment of the contacts during the resistivity measurement. For further annealing studies with different parameters, well cut samples with a precise orientation are necessary. We investigated the influence of grinding and polishing to the residual resistivity ratio. Two samples cut from the single crystal were oriented along the [110] and the [001]-direction. They were thinned down in two steps from 0.15 to 0.09 mm and the respective temperature dependence of the resistivity ρ_1, ρ_2, ρ_3 (curves (1-3)) was measured and is shown on the left hand side of Fig. 2.13. We determined from our data for each current direction the ratio $\rho_i/\rho_{\mathrm{av}}$ with $\rho_{\mathrm{av}} = (\rho_1 \cdot \rho_2 \cdot \rho_3)^{1/3}$ to investigate if our polishing procedure causes stress and strain in the samples and therefore influences the sample quality. The right part of Fig. 2.13 shows that $RR_{1.8\,\mathrm{K}}$ slightly varies between the different thicknesses labelled by (1), (2), (3). For the current parallel to the c-direction, the polishing reduces the value of $\rho_{001}(1.8\,\mathrm{K})$. For the perpendicular direction, the opposite effect occurs. This result might be caused by the anisotropy of $\mathrm{RR}_{1.8\,\mathrm{K}}$. In the thinner sample the ideal current flow without a perpendicular component is approached. That means that the current is confined to the [001] or the [110]-direction and the respective perpendicular current component is reduced upon thinning down the sample. For the [001]-direction ρ_i becomes smaller for increasing i leading to a larger $RR_{1.8\,\mathrm{K}}$ and for the [110]-direction ρ_i becomes larger leading to a smaller $RR_{1.8\,\mathrm{K}}$ value. This investigation also demonstrates that the polishing procedure itself seems not to enlarge the number of crystal defects.

Low-temperature characterization

The low-temperature characterization is presented in Fig. 2.14 and Tab. 2.4. The electrical resistivity of Czochralski grown single crystals demonstrates their high purity. For $j \parallel c$ we obtained $RRR = 39$ (sample $040-2-6-4$) which is much larger than the value $RRR = 16$ obtained for previous Bridgman grown samples [14]. In Fig. 2.14, (b), the low-temperature data for $j \parallel c$ are shown. The precision of the measurement was improved by performing the measurement on a micro-structured single crystal. The micro-structuring was done using the FIB technique, see for an example Fig. 3.5 on page 83.

Additionally, the electrical resistivity has been investigated in field by S. Friedemann (University of Bristol). Fig. 2.15 shows that quantum oscillations in the magnetoresistance

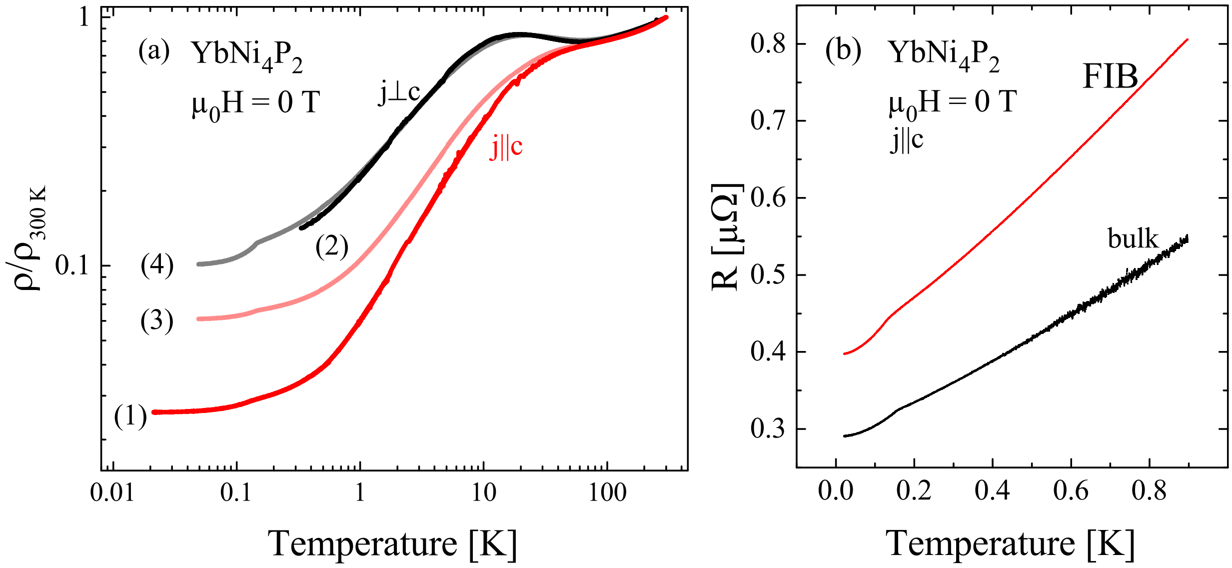

Figure 2.14: YbNi$_4$P$_2$ (a) Normalized electrical resistivity $\rho(T)/\rho(300\,\mathrm{K})$ as a function of temperature measured with $j \parallel c$ (red) and $j \perp c$ (black). Curves (1) and (2) show the resistivity measured on Czochralski grown samples (040, 041). The light red curve (3) and the grey curve (4) show the data published in [14] for comparison. In (b) the resistivity measured on a FIB micro-structured sample (red) and a not micro-structured bulk single crystal (black) in the low temperature region is depicted. The ferromagnetic phase transition is indicated by a kink in the curve at $T_C = 150\,\mathrm{mK}$. The measurements have been performed by S. Friedemann (Bristol) and S. Hamann (MPI CPfS).

have been observed above ≈ 15 T. Oscillation up to a frequency of 1.6 kT were detected. Higher oscillations frequencies (≈ 6 kT) corresponding to larger Fermi surfaces are expected to exist [145]. The further optimatization of the crystal growth is necessary since these frequencies can only be observed in purer samples. Nevertheless, the first derivative of the resistance dρ/dB (lower panel) clearly shows more pronounced kinks in the data obtained from the Czochralski-grown single crystal (red curve) in comparison to the data obtained from the Bridgman-grown single crystal (grey curve). The Czochralski-grown single crystals enabled us to resolve signatures of possible Lifshitz transitions in the magnetoresistance at $T \approx 0.4\,\mathrm{K}$ (see Sec. 2.6.8 and [105]). The fields at which the transitions occur are indicated by vertical dashed lines in Fig. 2.15.

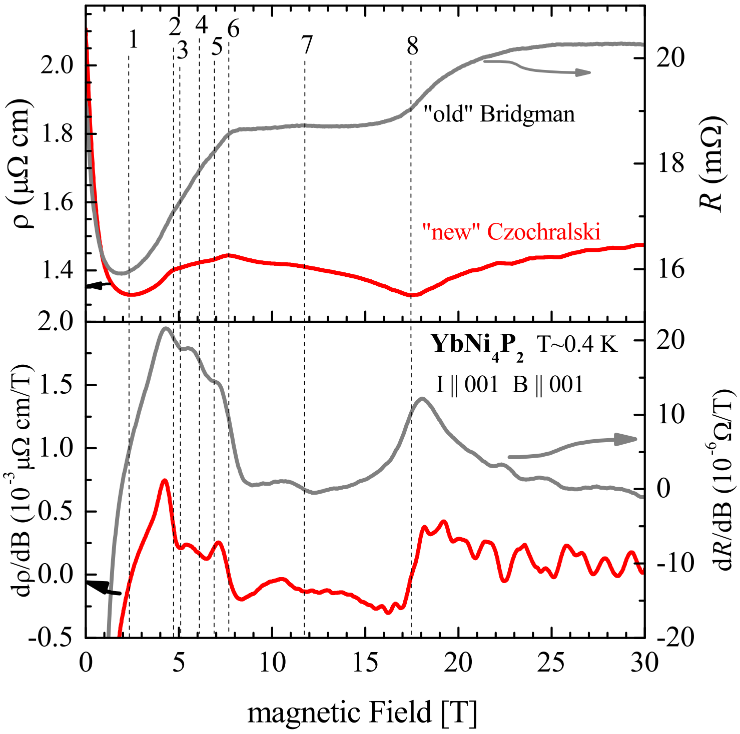

Figure 2.15: Comparison between the magnetoresistance of Bridgman (batch 63524 C. Krellner, MPI CPfS) and Czochralski grown (sample $040-2-6$, this work) single crystals. The low temperature measurements have been performed by S. Friedemann (Bristol).

2.6.2 $\mathbf{YbNi_4(P_{1-x}As_x)_2}$: Electrical resistivity

In the past, samples of the substitution series $YbNi_4(P_{1-x}As_x)_2$ with As-contents up to $x = 0.13$ have been investigated and the material was studied close to the FM QCP [14]. Until now, the $T - x$ phase diagram is incomplete due to a lack of samples with $x > 0.13$. To observe the emergence of Fermi liquid behaviour in the system, samples with higher As concentrations are required.

In this section, we present the characterization of the electrical resistivity of our arsenic substituted samples between 1.8 K and 300 K. The results are presented in Fig. 2.16. In the upper row, the normalized electrical resistivity $\rho/\rho(300\,\mathrm{K})$ is shown as a function of temperature measured with current parallel to the crystallographic a-axis, $j \parallel 100$ (a), and parallel to the c-axis, $j \parallel 001$ (b). For $j \parallel 100$ a clear maximum in the resistivity appears for $x \leq 0.2$ which broadens for higher arsenic concentrations. The grey curve shows the electrical resistivity $\rho^{\mathrm{Lu}}(T)$ measured on a polycrystalline sample of the non-magnetic reference compound $LuNi_4P_2$ [48] to estimate the phonon contribution to the resistivity. In the logarithmic plot of the difference data

$$\rho_{\mathrm{mag}} = \frac{\rho(\mathrm{YbNi_4P_2})}{\rho(\mathrm{YbNi_4P_2}, 300\,\mathrm{K})} - \frac{\rho(\mathrm{LuNi_4P_2})}{\rho(\mathrm{LuNi_4P_2}, 300\,\mathrm{K})} \tag{2.3}$$

a broad maximum at T_K^{ρ} can be traced which appears for all arsenic concentrations and both crystallographic directions. We give no absolute values for the difference data since the polycrystalline non-magnetic reference has a lower RRR than the single crystalline samples and the difference becomes negative.

x	$A^{j\|a}$ [$\mu\Omega$cm/K^2]	$T^{\rho}_{\rm fit}$ [K]	$A^{j\|c}$ [$\mu\Omega$cm/K^2]	$T^{\rho}_{\rm fit}$ [K]
0.6	0.59	3	0.19	3
0.8	0.07	10	0.037	6
1	0.0033	10	0.0032	10

Table 2.5: Resistivity A coefficient (Eqn. 1.15) determined for $YbNi_4(P_{1-x}As_x)_2$ with $x \geq 0.6$. $T^{\rho}_{\rm fit}$ is the temperature below which the resistivity can be described by $\rho(T) = \rho_0 + AT^2$.

Crystal electrical field and Kondo effect

The position of the maxima $T^{\rho}_{\rm K}$ shown for both current directions in the difference data in the lower row of Fig. 2.16 shifts within the substitution series and is indicated by dashed lines in the figures of the upper row. The appearance of this maximum is not only caused by the Kondo effect but also by the CEF. This well known behaviour has been studied in $CeRu_2Ge_2$ under pressure [146] and was also observed in $CeCu_2Si_2$ [147]. A theoretical description of the resistivity of Ce compounds with and without magnetic order at low temperatures including CEF and Kondo effect was provided by Lassailly *et al.* [148]. In $CeRu_2Ge_2$, a maximum in the magnetic part of the resisitivity occurs. The maximum in $\rho_{\rm mag}(T)$ develops near room temperature for intermediate pressures which is attributed to originate from the Kondo exchange interaction between the conduction electrons and the crystal field split ground state of the Ce^{3+} ions. In the $YbNi_4(P_{1-x}As_x)_2$ series, the negative chemical pressure increases with increasing As content. Or looking the other way round, positive chemical pressure is applied by substituting As in $YbNi_4As_2$ by smaller P atoms. For the pure As compound $x = 1$, a maximum in $\rho_{\rm mag}(T)$ (Fig. 2.16, lower row) occurs at high temperatures and upon increasing P content this maximum broadens and seems to be superposed by a second maximum (Kondo maximum) which shifts to lower T. This leads to the conclusion that also in this system besides Kondo interaction CEF effects are observable in the electrical resistivity. In the $YbNi_4(P_{1-x}As_x)_2$ series, it is not possible to clearly separate both effects.

Anisotropy and shift of the Kondo maximum

The inset of Fig. 2.16 (a) shows a strong anisotropy in the position of the broad maximum $T^{\rho}_{\rm K}$ with respect to the two current directions at low arsenic concentrations. This anisotropy disappears when approaching higher arsenic concentrations. For $j \parallel c$, the Kondo maximum shifts towards lower temperatures upon approaching the quantum-critical arsenic concentration at $x \approx 0.1$.

Fermi-liquid behaviour

FL behaviour is observable in the $YbNi_4(P_{1-x}As_x)_2$ series for $x \geq 0.6$ below a temperature $T^{\rho}_{\rm fit}$. The resistivity can be described by $\rho(T) = \rho_0 + AT^2$ the respective coefficients are summarized in Tab. 2.5. The A coefficient increases in the substitution series for decreasing arsenic content. Since $A \propto (m^*)^2$, we find, as expected, that the correlation effects become stronger for lower arsenic contents.

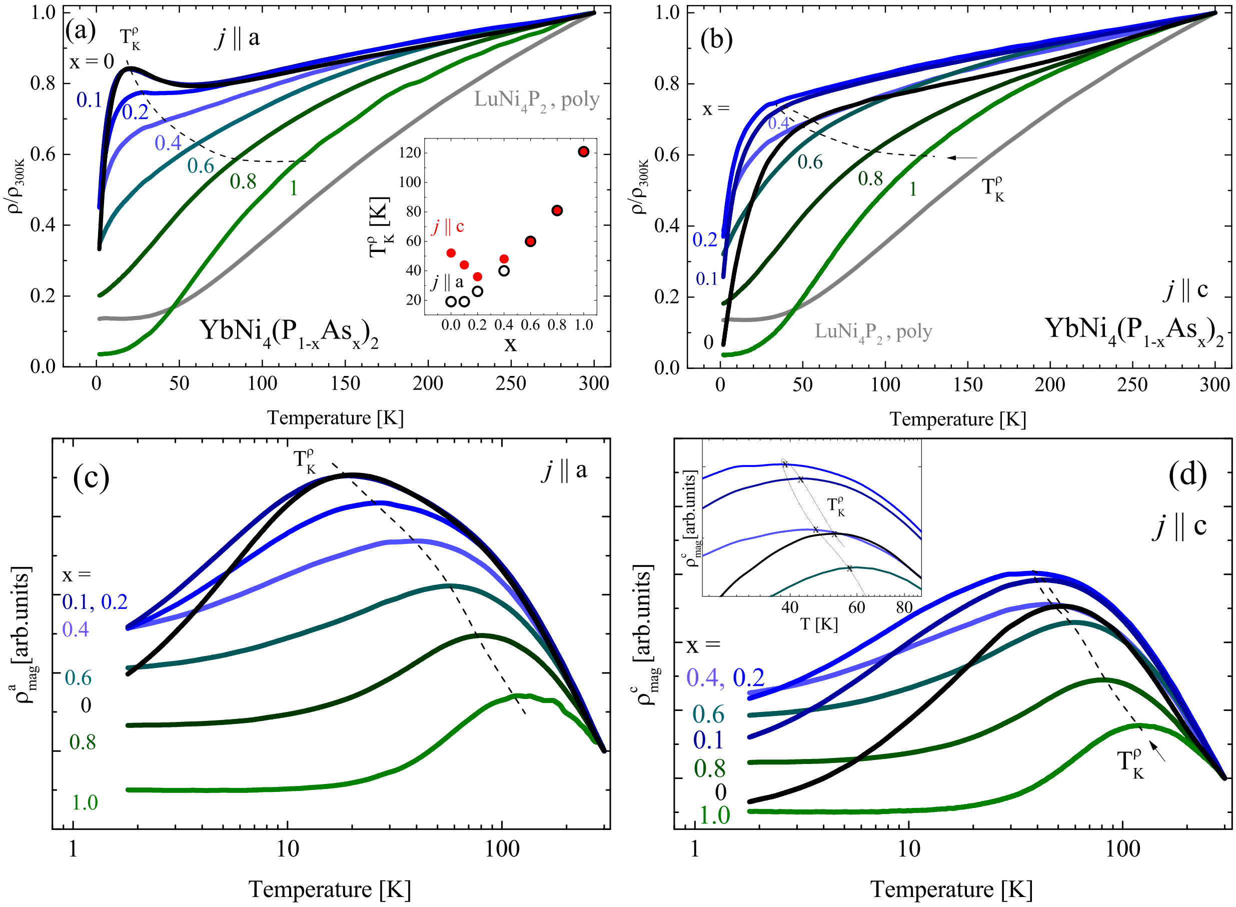

Figure 2.16: Normalized electrical resistivity $\rho/\rho(300\,\mathrm{K})(\mathrm{T})$ from 1.8 K to 300 K measured with current parallel to the crystallographic a-axis, $j \parallel 100$ (a), and parallel to the c-axis, $j \parallel 001$ (b). The grey curve shows the electrical resistivity of the non-magnetic reference LuNi$_4$P$_2$ [48]. The shift of the broad maximum for both current directions in the difference data, $\rho_{\mathrm{mag}}(T)$, is indicated by dashed lines. The inset of Fig. (a) shows the temperatures where the maxima T_{max} in the resistivity occur, evaluated from the data in (c) and (d). The figures in the lower row show $\rho_{\mathrm{mag}}(T)$ obtained by subtraction of the LuNi$_4$P$_2$ reference data (note the logarithmic temperature scale).

Disorder

The resistivity ratio $RR_{1.8\,\mathrm{K}} = \rho(300\,\mathrm{K})/\rho(1.8\,\mathrm{K})$ is regarded as an indicator for the amount of crystal defects and disorder (see Sec. 1.6). In the substition series $\mathrm{YbNi_4(P_{1-x}As_x)_2}$, As (P) atoms act as impurities in the P-rich (As-rich) single crystals and cause disorder. The disorder reaches its maximum for $x = 0.4$ where $RR_{1.8\,\mathrm{K}}$ is minimal as it can be seen in Fig. 2.16, (c) and (d).

2.6.3 $\mathrm{YbNi_4P_2}$: Heat capacity

HC measurements were performed using the commercial measurements options of a Quantum Design PPMS. To determine the magnetic part of the specific heat at high temperatures, it is necessary to subtract the phonon contribution, which is dominant in this temperature range. For this reason, the nonmagnetic reference compound $\mathrm{LuNi_4P_2}$ was synthesized, which is described in section 2.5. The compound $\mathrm{LuNi_4P_2}$ is isostructural to $\mathrm{YbNi_4P_2}$, whereas its f-shell contains an additional electron, therefore is completely filled and nonmagnetic. The phonon spectrum of both compounds can be considered as nearly equal since the masses of Yb and Lu differ only by less than 1%. The specific heat of $\mathrm{LuNi_4P_2}$ was measured as a function of temperature from 1.8 to 200 K and is shown in figure 2.17. The magnetic contribution to the specific heat C^{4f} was obtained by subtracting the specific heat C_{Lu} of the non-magnetic reference compound $\mathrm{LuNi_4P_2}$ from the specific heat C_{Yb} of $\mathrm{YbNi_4P_2}$. Two $\mathrm{YbNi_4P_2}$ samples Yb1 (5.45 mg), Yb2 (9.99 mg) and two $\mathrm{LuNi_4P_2}$ samples Lu1 (10.50 mg), Lu2 (16.63 mg) were measured from $2 - 200\,\mathrm{K}$ as shown in Fig. 2.17. By subtracting the reference data from the sample data in the four possible combinations the reliability of the temperature range of the C^{4f} data becomes appearent. From 2 to 50 K all data sets are equal within the error bars. The accordance gets worse for $50 \leq T \leq 100\,\mathrm{K}$ and for $T > 100\,\mathrm{K}$ the error caused by the long relaxation time in the relaxation method gets large and the obtained data sets differ. For the comparison with the fits done by Zita Hüsges Fig. 2.18, the data set obtained from the two smallest samples were chosen since these data measured by the relaxation method are most reliable in this temperature range. Each transitions to an excited CEF level yields a Schottky contribution to the heat capacity which enables us to estimate the third CEF level which was not detectable by INS.

Determination of the CEF levels from INS and HC

In the solid, an ion is surrounded by neighbouring ions, which cause an electric field at the site of the ion in the center. In the CEF, the $(2J + 1)$-fold degeneracy of the ground state multiplet J splits up as introduced in Sec. 1.4.1. The typical splitting energies are between 10 and 100 meV [72]. Kramers theorem states, that for an odd number of electrons in the outer shell, the degeneracy of the CEF states is at least two, leading to a doublet ground state. The $\mathrm{Yb^{3+}}$ ions in $\mathrm{YbNi_4P_2}$ are located on the same crystallographic position, therefore one expects the same CEF scheme for all $\mathrm{Yb^{3+}}$ ions. The outer $4f$ shell of $\mathrm{Yb^{3+}}$ is filled with 13 electrons, i.e. a single hole. Due to spin-orbit coupling, $J = 7/2$ and $J = 5/2$ are possible total angular momenta of the $4f$ shell and by the third Hund's rule the ground state should be $J = 7/2$ (Tab. 1.2). Therefore, it is $2J + 1 = 8$ fold degenerated. It splits up into doublets under the influence of the CEF which is a pure electrostatic interaction. Hence, at maximum, three CEF transitions should be observed. In preliminary work, the

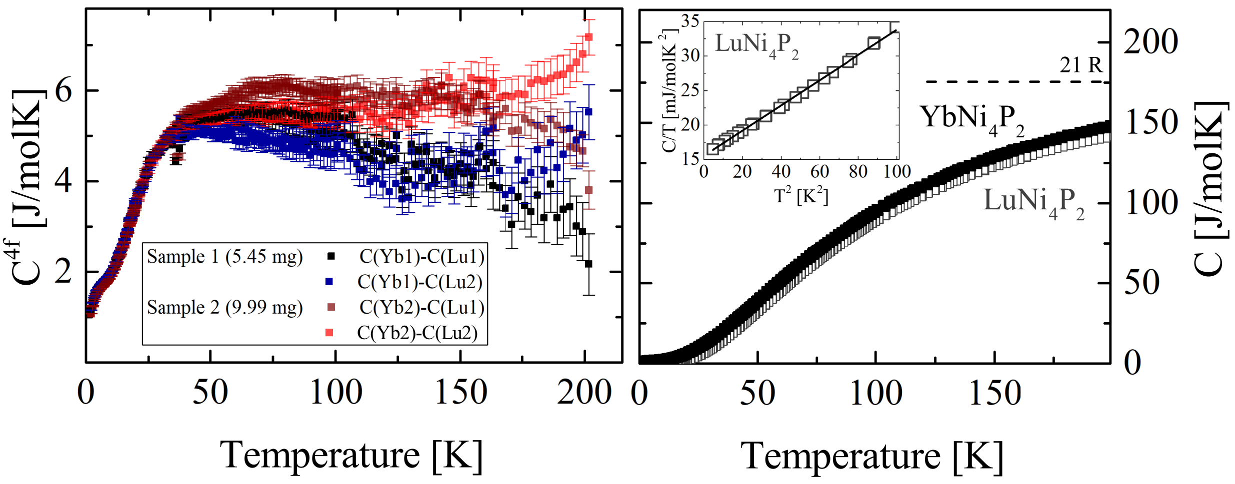

Figure 2.17: *Left:* $YbNi_4P_2$: $C^{4f}(T)$ for different samples; *Right:* HC of $YbNi_4P_2$ and $LuNi_4P_2$ measured from 2 to 200 K. For $T > 200$ K $C(T)$ approaches the classical Dulong-Petit limit of $7 \cdot 3\,R \approx 175$ J/molK. $C(T)/T$ versus T^2 exhibits linear behaviour below 10 K as shown in the inset.

neutron scattering intensity of $YbNi_4P_2$ as a function of energy and wave vector transfer at 1.6 K showed that two main features can be distinguished in the inelastic regime: Intensity maxima due to magnetic excitations ($E \approx 5$ to 15 meV) and intensity maxima due to phonon excitations ($E \approx 12$ to 22 meV) [125]. A two peak fit of the magnetic intensity of $YbNi_4P_2$ at momentum transfer at Q =(2.5 ± 0.5) Å^{-1} and $T = 1.6$ K yield transition energies of (8.5 ± 0.5) meV and (12.5 ± 0.5) meV. At the beginning of this work, no heat capacity data for $T > 10$ K had been published. To identify also the third transition between the CEF levels, heat capacity measurements as part of this work have been performed from 1.8 - 200 K as shown in Fig. 2.17. Since transitions to excited CEF levels yields Schottky contributions to the heat capacity, these data can be compared with the INS results. In the simple case of a four-level scheme with equal degeneracy of all levels, the contribution is given by:

$$\begin{aligned} C_p^{\text{Schottky}} &= \frac{R}{(k_BT)^2}(\Delta_1^2 e^{-\frac{\Delta_1}{k_BT}} + \Delta_2^2 e^{-\frac{\Delta_2}{k_BT}} + \Delta_3^2 e^{-\frac{\Delta_3}{k_BT}} \\ &\quad + (\Delta_2-\Delta_1)^2 e^{-\frac{\Delta_1+\Delta_2}{k_BT}} + (\Delta_3-\Delta_1)^2 e^{-\frac{\Delta_1+\Delta_3}{k_BT}} + (\Delta_3-\Delta_2)^2 e^{-\frac{\Delta_2+\Delta_3}{k_BT}}) \\ &\quad (1 + e^{-\frac{\Delta_1}{k_BT}} + e^{-\frac{\Delta_2}{k_BT}} + e^{-\frac{\Delta_3}{k_BT}})^{-2}. \end{aligned} \tag{2.4}$$

In $YbNi_4P_2$ also the Kondo-broadening of all levels is expected to influence the specific heat and has to be included in this model. A complete theoretical description including all higher levels was not applied. Here, the Kondo broadening of the ground-state doublet was included according to Desgranges [149] together with a further extension proposed by Romero [150] which also accounts for the broadening of the first excited level. For details of the modelling see [129]. In the temperature range above 100 K the magnitude of the phonon contribution is about 30 times larger than the contribution to the specific heat stemming from the transition between excited CEF levels (Fig. 2.17). Additionally the error bars in the data measured by the relaxation method become larger at higher temperature since these are obtained from the subtraction of two quantities which have nearly the same value. As shown in Fig. 2.18, the HC data have been modelled assuming different values for the third CEF level. Good

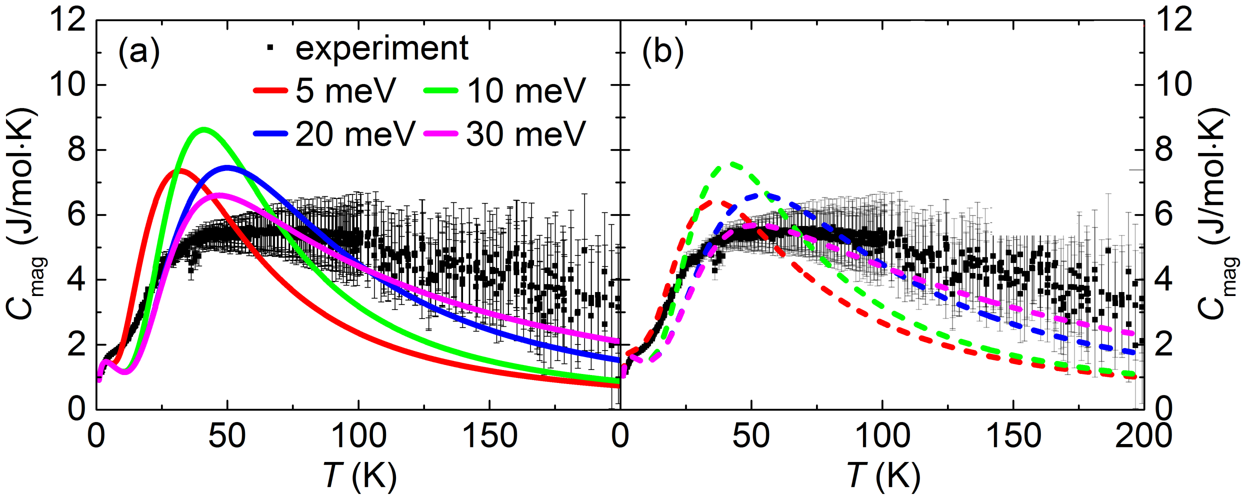

Figure 2.18: Temperature dependence of the heat capacity of $YbNi_4P_2$ measured from 2 - 200 K. Two CEF levels $E_1 = 8.5\,\mathrm{meV}$ and $E_2 = 12.5\,\mathrm{meV}$ have been determined by neutron scattering in preliminary work [126] while the third level was not detectable. The figure shows the comparison of the heat capacity data with a model proposed by Desgranges and Schotte [149] (left frame) and according to Romero *et al.* [150] (right frame) assuming different values for the third level, the modelling was done by Zita Hüsges [129].

accordance in the low temperature range was found for $E = 20\,\mathrm{meV}$ (blue curve), while the height of the maximum in $C_{\mathrm{mag}} = C^{4f}$ is fitted better for $E = 30\,\mathrm{meV}$ (pink curve). Thus, Fig. 2.18 shows that from none of the proposed approaches a clear statement concerning the third CEF level can be made but both models suggest that the third level is at higher energy than the two which have been observed with neutron scattering before. Nevertheless combining the neutron and heat capacity data suggests a level scheme: $E_1 = 8.5\,\mathrm{meV}$, $E_2 = 12.5\,\mathrm{meV}$ and $E_3 \approx 25\,\mathrm{meV}$ which is close to the set of energy eigen values obtained using NMR data (Eqn. 2.6).

2.6.4 $YbNi_4(P_{1-x}As_x)_2$: Heat capacity

Measurements of the specific heat of $YbNi_4(P_{1-x}As_x)_2$ from 5 K down to 350 mK were performed in collaboration with J. Banda (MPI CPfS), for $T > 2\,\mathrm{K}$, the data were partly recorded by P. Ross (Goethe University Frankfurt). The specific heat divided by the temperature C/T is presented in Fig. 2.19. In the substitution series, for $x = 0.8$ (1.0), FL behaviour is observed below 5 K (6 K) with enhanced Sommerfeld coefficients $\gamma_0 = 158\,\mathrm{mJ/molK^2}$ ($96\,\mathrm{mJ/molK^2}$). The Debye temperatures determined from the slope of $C/T = \gamma_0 + \beta T^2$ using Eqn. 1.11 with $s = 7$ are listed in Tab. 2.6. For $x = 0.6$ ($x = 0.4$, $x \leq 0.2$), C/T increases below 10 K up to $C/T(350\,\mathrm{mK}) = 396\,\mathrm{mJ/molK^2}$ ($754, 1120\,\mathrm{mJ/molK^2}$) and no saturation is reached down to 350 mK. The high-temperature part of the specific heat of $YbNi_4P_2$ was used to obtain information on the CEF which is discussed in Sec. 2.6.3.

For $YbNi_4(P_{1-x}As_x)_2$ with $x \geq 0.8$, the Kadowaki-Woods ratio A/γ_0^2 (Eqn. 1.16) does not reach the universal value of $10\,\mu\Omega\mathrm{cmK^2mol^2/J^2}$ for heavy-fermion compounds (Tab. 2.6). While the pure phosphorous compound with $\gamma_0 \approx 2000\,\mathrm{mJ/molK^2}$, $A \approx 52\,\mu\Omega\mathrm{cm/K^2}$ and $A/\gamma_0 = 13\,\mu\Omega\mathrm{cmK^2mol^2/J^2}$ [121] is located on the heavy-fermion line (solid line) in Fig. 2.20,

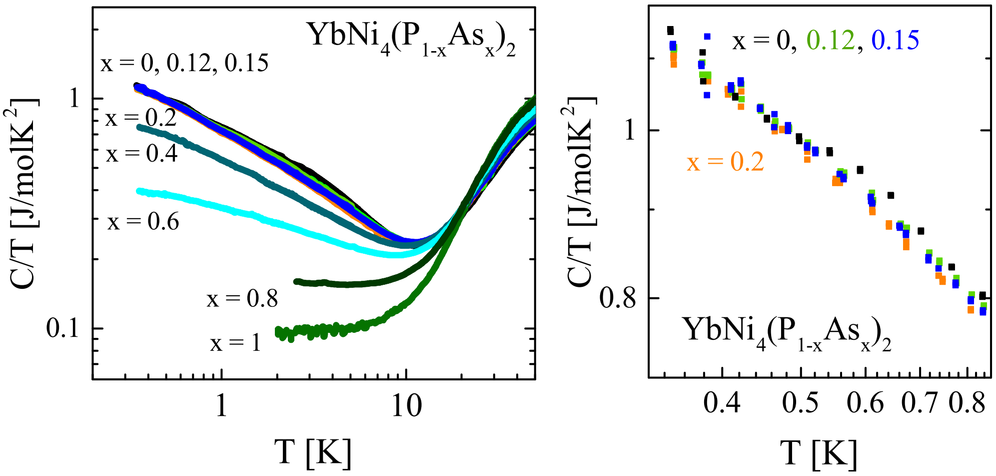

Figure 2.19: *Left:* $C/T(T)$ of YbNi$_4$(P$_{1-x}$As$_x$)$_2$ for $0 \leq x \leq 1$ from 350 mK to 50 K. *Right:* Low temperature part of C/T for $x \leq 0.2$.

x	γ_0 [J/molK^2]	Θ_D [K]	$T_{\mathrm{fit}}^{\mathrm{HC}}$ [K]	$A^{j\parallel a}/\gamma_0^2$ [$\mu\Omega$cmK^{2}mol^2/J^2]	$A^{j\parallel c}/\gamma_0^2$ [$\mu\Omega$cmK^{2}mol^2/J^2]
0.8	0.158	224	5	2.8	1.5
1	0.096	213	6	0.36	0.35

Table 2.6: Sommerfeld coefficients, Debye temperatures (Eqn. 1.11), determined for YbNi$_4$(P$_{1-x}$As$_x$)$_2$ with $x \geq 0.8$. $T_{\mathrm{fit}}^{\mathrm{HC}}$ is the temperature below which C/T saturates and follows $C/T(T) = \gamma_0 + \beta T^2$. The Kadowaki-Woods ratio A/γ_0^2 was evaluated for both current directions.

YbNi$_4$As$_2$ is characterized by this ratio as a transition metal without strong correlations (dashed line). YbNi$_4$(P$_{1-x}$As$_x$)$_2$, $x = 0.8$ is situated inbetween the heavy-fermion and the transition-metal line.

2.6.5 YbNi$_2$P$_2$: Magnetization

Magnetic anisotropy

The anisotropy of the susceptibility of YbNi$_4$P$_2$ was determined using a rotator insert in a MPMS system. The rotator allows for a precise orientation of the sample which is important especially for samples with a high anisotropy. The data, shown in Fig. 2.21, have been recorded by M. Baenitz (MPI CPfS). With the rotator insert it is possible to rotate the sample between $0 \leq \phi \leq 300°$ towards an applied magnetic field during a magnetization measurement. The aim of our investigation was to figure out whether the detection of an anisotropy in the in-plane susceptibility between the [100] and the [110] direction is possible. This anisotropy would cause a 90° periodicity in the in-plane data. For the measurement a well oriented single crystal (040) with $m = 49.63$ mg cut in a cubic shape was used. The comparitively large sample mass was necessary to detect the signal in the background (which

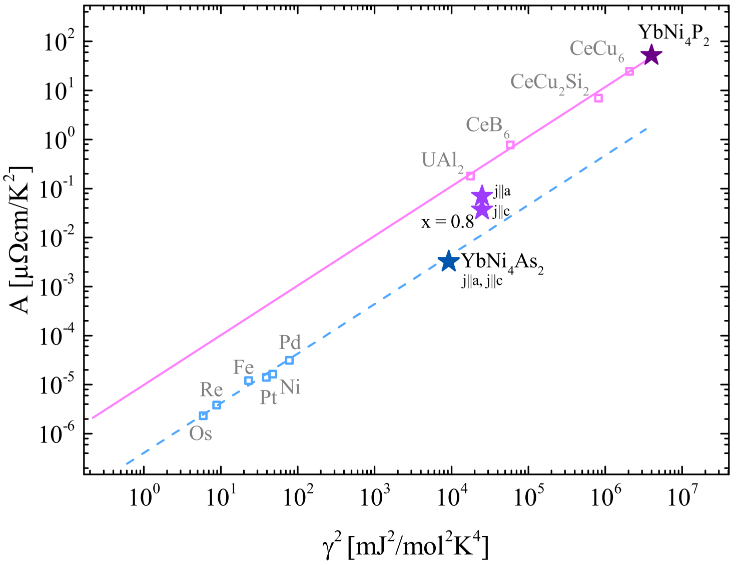

Figure 2.20: The Kadowaki-Woods ratio of some compounds in the $YbNi_4(P_{1-x}As_x)_2$ series, marked by stars, compared to other Kondo-lattice systems and transition metals. After [77].

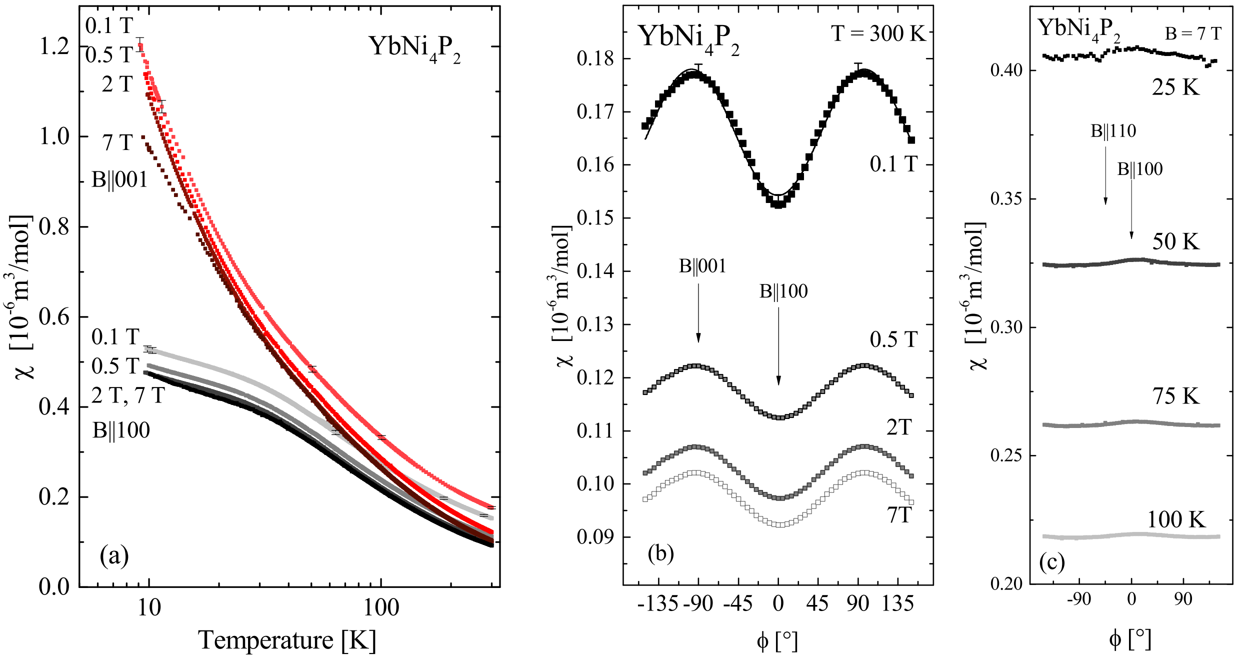

Figure 2.21: $YbNi_4P_2$: (a) Temperature dependence of the susceptibility $\chi(T)$ for field parallel to the two crystallographic main symmetry directions a and c. (b) Angular dependence of the susceptibility $\chi(\phi)$ at $T = 300\,\mathrm{K}$ upon rotation around the (010) axis. The anisotropy $\chi^c/\chi^a = 1.16$ at 300 K, amounts to $\chi^c/\chi^a = 2.2$ at 10 K. The data show a slight assymmetry which is caused by a misalignment of the sample of about 0.5°. (c) The angular dependence of the susceptibility $\chi(\phi)$ at 25, 50, 75 and 100 K for $B = 7\,\mathrm{T}$ upon rotation around the (001) axis shows that there is no detectable anisotropy of the $a - a$ in-plane susceptibility. The data were recorded by M.Baenitz (MPI CPfS).

is large due to the rotator insert). At low temperatures and high fields the measurement was hampered by heating effects upon rotating the sample. In Fig. 2.21 (a), the susceptibility for $B \parallel 100$ and $B \parallel 001$ is shown. The sample was rotated upon the (010) axis and shows an anisotropy between the two main symmetry directions, Fig. 2.21 (b). The anisotropy amounts to $\chi^c/\chi^a = 1.16$ at 300 K, $\chi^c/\chi^a = 2.2$ at 10 K and increases up to $\chi^c/\chi^a = 4.5$ at 1.92 K (determined by VSM) which is in agreement with previously reported data [118]. No detectable anisotropy was found by rotation upon the (001) axis, Fig. 2.21 (c). This is different from e.g. the tetragonal compound Yb$_2$Pt$_2$Pb where a detectable anisotropy at fields below 10 T accessible in the laboratory was reported. Here, different saturation values for field along the [100] and the [110] direction occur [151, 152].

CEF: Comparison with the high field magnetization

YbNi$_4$P$_2$ crystallizes in the ZrFe$_4$Si$_2$-type structure. The occuring symmetries allow for the classification in the space group $P4_2/mnm$. It has to be noted that the environment of the Yb ions in the tetragonal crystal structure is orthorhombic as illustrated in Fig. 2.22. We have studied this compound in high magnetic field to compare our data with the simulation according to the CEF scheme that has been determined in preliminary work [129] and is also discussed in Sec. 2.6.3. YbNi$_4$P$_2$ has a Kondo temperature of about 8 K [121] and it is not possible to reach the saturation magnetization in fields up to 12 T at lowest temperatures. To determine the ground state doublet in the spin bases, the values of the magnetization where saturation is reached is useful. Alternatively, these values could be obtained by measuring the ESR g-factors but so far no ESR signal was detected in YbNi$_4$P$_2$ in the paramagnetic regime.

The magnetization measurements have been performed on YbNi$_4$P$_2$ single crystals which were cut from one large crystal which belongs to a new generation of single crystals grown from a levitating melt by the Czochralski method [133]. The single crystal was oriented using the x-ray Laue backscattering technique. The samples used in the high field measurement had dimensions of only $\approx 1\,\text{mm} \times 1\,\text{mm} \times 0.5\,\text{mm}$ to avoid too large signals and the over bending of the cantilever. They were oriented along the crystallographic main symmetry directions [100] and [001]. Magnetization measurements up to $B = 9$ T were performed using the VSM option of a PPMS. The high-field magnetization measurements have been performed up to 12 T by M. Brando (MPI CPfS) and using the 33 T magnet at the High Field Magnet Laboratory Nijmegen, Netherlands (HFML) in collaboration with O. Young and U. Zeitler. The magnetization was determined in a static field via the torque using a cantilever. Additionally, measurements in pulsed field up to 58 T have been performed by T.Förster at the Helmholtz Zentrum Dresden-Rossendorf (HZDR).

The CEF usually is described in the frame of the Stevens operator formalism [57]. The Hamiltonian of a single Yb^{3+} ion consisting of the CEF term and the Zeeman term takes the form

$$\hat{H} = \hat{C} - \alpha\, g_J\, \mu_B\, \hat{\vec{J}} \cdot \vec{B} \tag{2.5}$$

with $\hat{C} = \sum_{lm} B_l^m O_l^m(\vec{J})$ containing the CEF parameters B_l^m and the Stevens operators $O_l^m(\vec{J})$ with $\vec{J}$ being the total angular momentum. In Eqn. (2.5), the exchange interaction as well as hyperfine coupling are neglected since their energy scales are small compared to the CEF. For the Yb ion in YbNi$_4$P$_2$ nine Stevens operators, O_2^0, O_2^2, O_4^0, O_4^2, O_4^4, O_6^0, O_6^2, O_6^4,

O_6^6 determine the Hamiltonian. The CEF scheme of YbNi$_4$P$_2$ was determined in preliminary work by Z. Hüsges [129, 153] using the energy-level scheme obtained by neutron scattering [126, 154], NMR and susceptibility data [118] as input. The applied fitting procedure yielded the energy eigenvalues

$$E_1 = 8.1\,\mathrm{meV}, \quad E_2 = 12.1\,\mathrm{meV}, \quad E_3 = 29.5\,\mathrm{meV}. \tag{2.6}$$

With the Boltzmann constant $k_B = 0.0861$ meV/K, the corresponding temperatures are

$$E_1/k_B = 94\,\mathrm{K}, \quad E_2/k_B = 140\,\mathrm{K}, \quad E_3/k_B = 342\,\mathrm{K}.$$

From the energy eigenstates

$$\begin{aligned}
\phi_0 &= -0.15\left|\frac{7}{2}\right\rangle + 0.08\left|\frac{3}{2}\right\rangle + 0.33\left|-\frac{1}{2}\right\rangle + \mathbf{0.93}\left|-\frac{5}{2}\right\rangle, \\
\phi_1 &= +0.67\left|\frac{7}{2}\right\rangle + \mathbf{0.69}\left|\frac{3}{2}\right\rangle + 0.27\left|-\frac{1}{2}\right\rangle - 0.05\left|-\frac{5}{2}\right\rangle, \\
\phi_2 &= \mathbf{-0.70}\left|\frac{7}{2}\right\rangle + 0.50\left|\frac{3}{2}\right\rangle + 0.42\left|-\frac{1}{2}\right\rangle - 0.30\left|-\frac{5}{2}\right\rangle, \\
\phi_3 &= +0.20\left|\frac{7}{2}\right\rangle - 0.52\left|\frac{3}{2}\right\rangle + \mathbf{0.80}\left|-\frac{1}{2}\right\rangle - 0.21\left|-\frac{5}{2}\right\rangle
\end{aligned} \tag{2.7}$$

it is obvious that the main contribution to the ground state of YbNi$_4$P$_2$ is $J_z = \pm 5/2$. Starting from this set of energies and eigenstates the magnetization of YbNi$_4$P$_2$ can be predicted to compare it with the high-field data. The calculations leading to the simulations shown in this section have been performed by M. Hofmann-Kliemt, for details see [155]. We performed high-field magnetization measurements to check to which level the proposed CEF scheme is able to predict the field dependence of the magnetization data. In Fig. 2.24, the measured (grey and black curves) and calculated magnetization (red solid line) at 4.2 K up to 58 T is shown. The simulated curve using the proposed CEF scheme only [129, 153] did not match the measured data well. Here, the saturation was reached already at ≈ 5 T in the simulation (not shown). To account for this discrepancy, we have used the values for a Weiss correction determined from the high-temperature part of the inverse susceptibility Fig. 2.23. With $K_\mathrm{W}^c = -6\,\mathrm{T}/\mu_\mathrm{B}$ and $\alpha = 0.94$ the experimental data can be approximated reasonably (Fig. 2.24, dark red solid line). As shown in Fig. 2.24, left frame, the saturation magnetization is reached in the experiment at $B \approx 25$ T with $M_\mathrm{sat} = 2.4\,\mu_\mathrm{B}$ at $T = 4.2$ K. This can also be calculated using Eqns. (2.7) to $M_\mathrm{sat} \approx 2.5\,\mu_\mathrm{B}$ per Yb ion. With this we found that the absolute value of M_sat can be calculated from the CEF scheme as proposed by [129, 153] in good agreement. It has to be mentioned that the simulation does not match the experimental data for low magnetic fields since it does neither account for the Kondo effect nor for the occuring Lifshitz-transitions in YbNi$_4$P$_2$. The Weiss-corrected simulation was applied to higher fields as shown in Fig. 2.24 where multiple steps in the magnetization occur

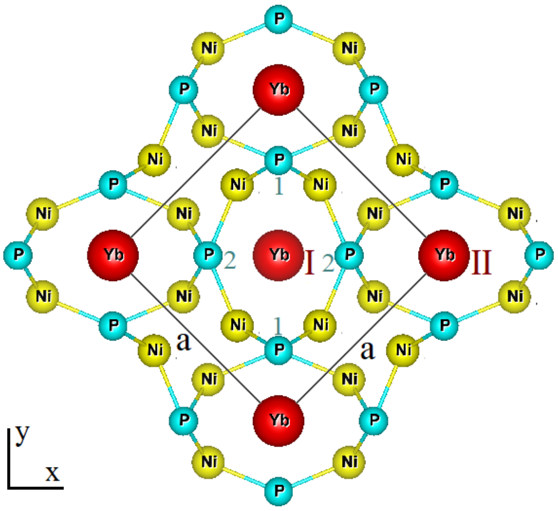

Figure 2.22: View on the tetragonal $a - a$ plane. Each Yb ion (I, II) has an orthorhombic environment which is rotated by 90°. The Yb-ions form chains running along the c-direction. In each chain, the alignment of the orthorhombic environment is the same. The tetragonal unit cell is indicated by the black lines. In NMR measurements different resonance field occur for the two different P sites P_1 and P_2 (see Sec. 2.6.8).

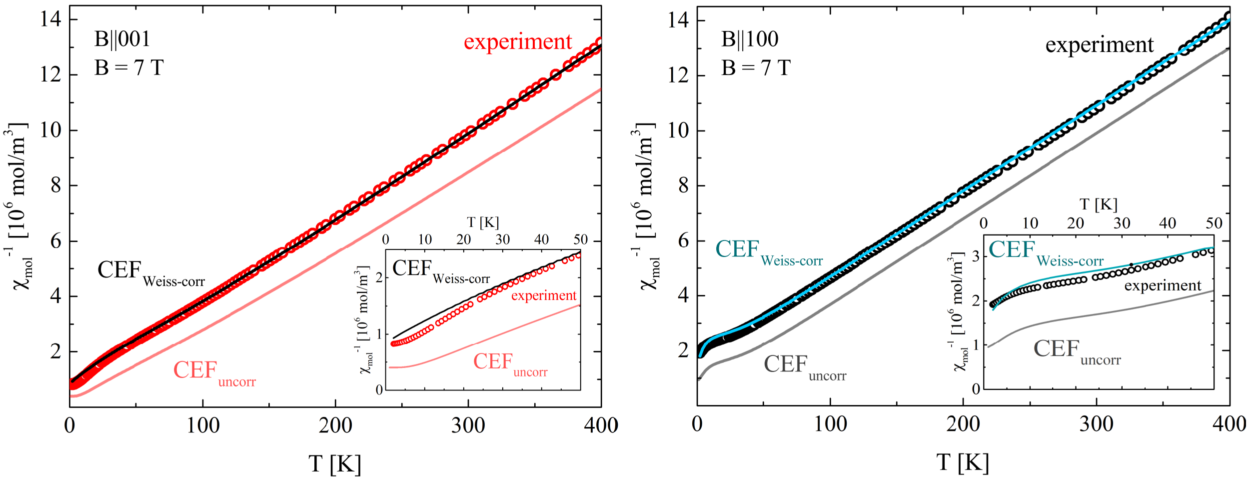

Figure 2.23: χ^{-1}(T) measured in an external field of $B = 7\,\mathrm{T}$; *Left:* Experimental data with $B \parallel 001$ (red circles) are shown together with the simulation according to [129], (light red solid line) and the simulated data using an additional Weiss correction (black solid line).; *Right:* Experimental data with $B \parallel 100$ (black circles) together with the simulation according to [129] (grey solid line) and the simulation including the Weiss shift (blue solid line). In the inset the comparison of the simulation together with the experimental data for $T \leq 50\,\mathrm{K}$ is shown.

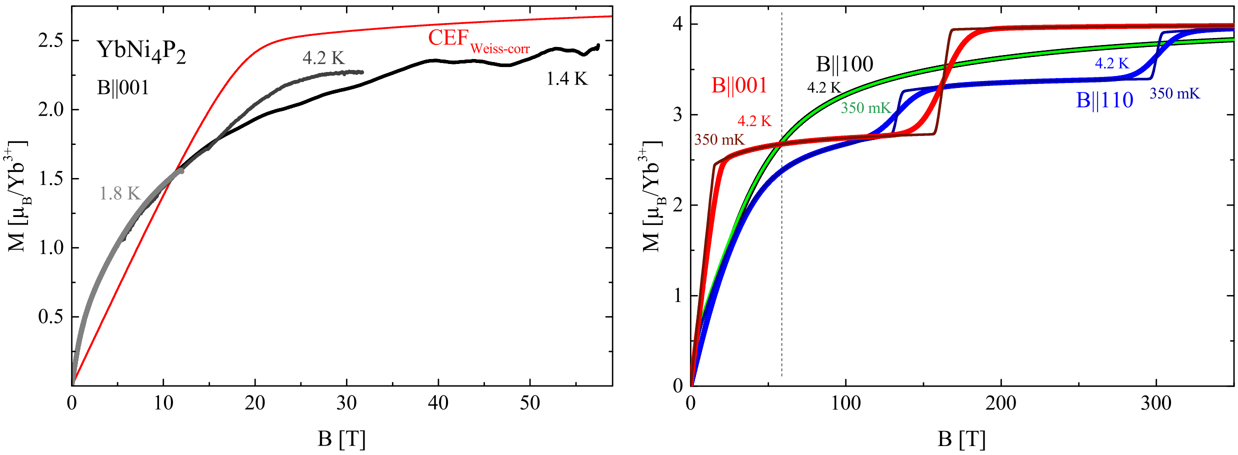

Figure 2.24: $YbNi_4P_2$ *Left:* Magnetization in field up to $B = 9\,\mathrm{T}$ at $T = 2\,\mathrm{K}$ (light grey), up to $B = 32\,\mathrm{T}$ at $T = 4.2\,\mathrm{K}$ (grey) and up to $B = 58\,\mathrm{T}$ at $T = 1.4\,\mathrm{K}$ (black) with external field $B \parallel 001$. The simulated data according to the CEF parameters in [129] using an additional Weiss correction (red solid line) are also shown. *Right:* Simulated high field magnetization for the three crystallographic main symmetry directions at 350 mK (thin lines) and 4.2 K (thick lines). The simulation was done including the Weiss-correction for $B \parallel 100$ (green/black curve), $B \parallel 110$ (dark blue/blue curve), and $B \parallel 001$ (dark red/red curve). The dashed line marks the field which was accessible in our experiments.

as a finger print of the CEF. Especially, the tetragonal in-plane anisotropy is significant in the high-field region.

In summary we found that the saturation magnetization M_{sat} can be calculated from the CEF scheme as proposed by Z.Hüsges [129] in good agreement. The qualitative description of $\chi(T)$ and $M(B)$ was improved by introducing an additional Weiss correction to account for internal fields. The numerically predicted field dependence of the magnetization is strongly anisotropic and shows multiple steps. The calculated curves predict that full saturation will be reached above 200 T for $B \parallel 001$ but above 350 T for the in-plane directions [155].

2.6.6 $YbNi_4(P_{1-x}As_x)_2$: Magnetization

The magnetization of the single crystals in the substitution series $YbNi_4(P_{1-x}As_x)_2$, Fig. 2.25, was investigated between 2 and 400 K. We expect that above $T = 2\,\mathrm{K}$, the susceptibility $\chi(T)$ in the series is dominated by the localized Yb $4f$ moments. Below 50 K, a strong anisotropy in $\chi(T)$ is found for samples with low As content. It turns into a nearly isotropic behaviour for samples with higher As concentrations. This anisotropy of the susceptibility changes within the substitution series as shown in the inset of Fig. 2.25, (a). At $T = 2.3\,\mathrm{K}$, it amounts to a value of $\chi^c/\chi^a = 4.15$ for $x = 0$ while with $\chi^c/\chi^a = 1.01$ it shows only a tiny anisotropy for $x = 1$.

For $B \parallel 100$, a broad hump in $\chi(T)$ can be observed. For $x = 0, 0.12$ and 0.2, the first derivative $d\chi/dT$ of the data, Fig. 2.26, left, shows a maximum at $T_{\mathrm{K}}^{\chi} \approx 20\,\mathrm{K}$. Remarkably, resistivity data for $j \parallel 100$, Fig. 2.16 (a), and inset therein, show maxima near this temperature which are attributed to the Kondo effect. For higher arsenic concentrations, $d\chi/dT$

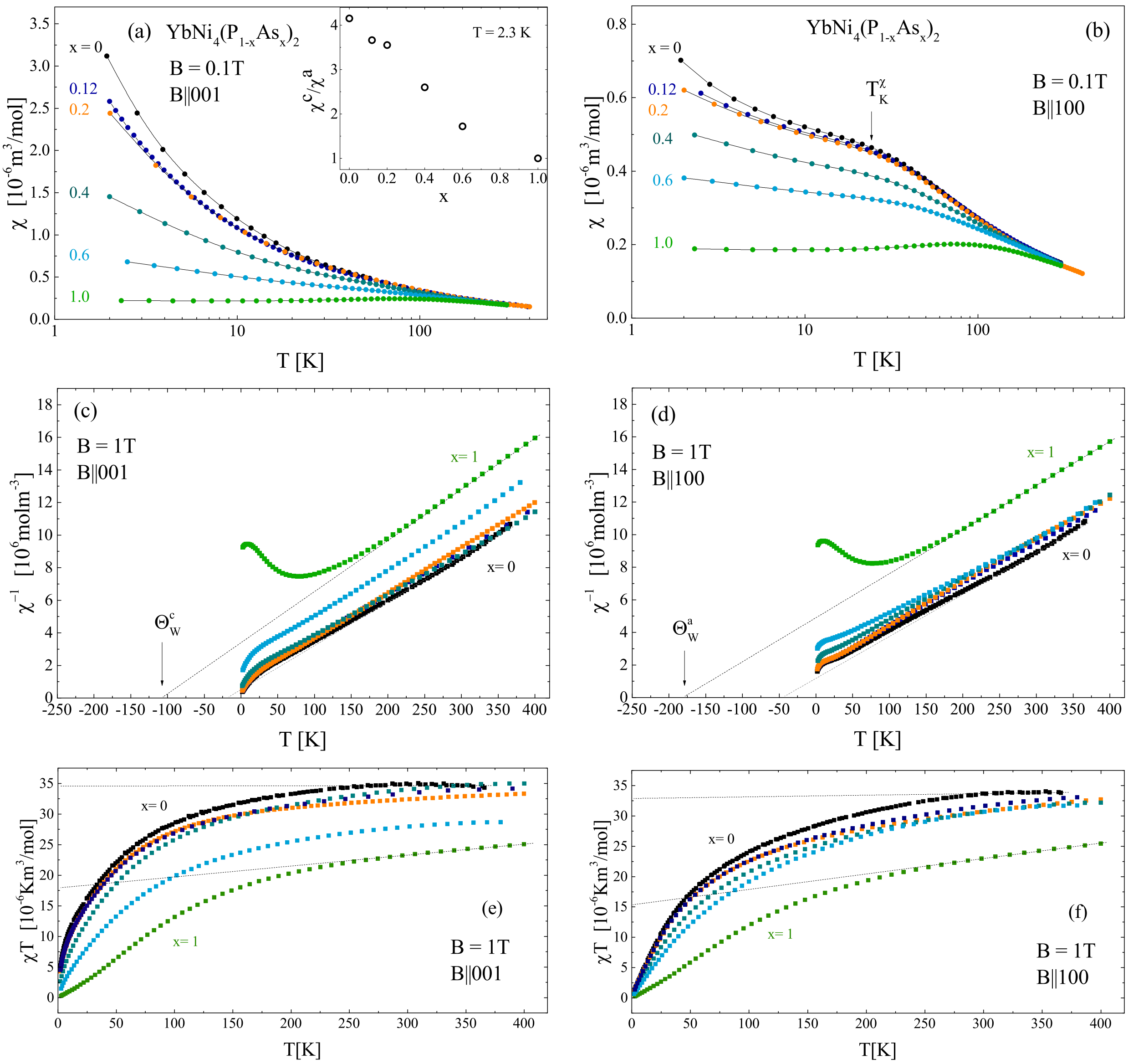

Figure 2.25: YbNi$_4$(P$_{1-x}$As$_x$)$_2$ temperature dependence of the molar susceptibility $\chi(T)$ for $B = \mu_0 H = 0.1\,\mathrm{T}$ (a) $B \parallel 001$ and (b) $B \parallel 100$; Inverse susceptibility $\chi^{-1}(T)$ for $B = 1\,T$ (c) $B \parallel 001$ and (d) $B \parallel 100$; Lower row (e) and (f) show the data of (a) and (b) plotted as χT versus temperature. The inset of (a) shows the anisotropy of $\chi(T)$ for the two field directions at $B = 0.1\,\mathrm{T}$ determined from the data at $T = 2.3\,\mathrm{K}$ in (a) and (b).

changes qualitatively and does not exhibit a clear maximum. For all arsenic concentrations, the hump in $\chi(T)$ extends up to roughly 200 K and is caused mainly by CEF effects. The progress of the analysis of the CEF parameters of the pure phosphorous compound is described in Sec. 2.6.3.

Between 250 and 400 K, $\chi(T)$ exhibits Curie-Weiss behaviour for all As concentrations in both directions. While the effective magnetic moment, μ_{eff}, Fig. 2.25 (c) and (d), changes only slightly, the change in the Weiss temperature, Θ_W, is large. For the pure phosphorous compound, $\mu^c_{\text{eff}} = (4.82 \pm 0.02)\,\mu_B$ and $\mu^a_{\text{eff}} = (4.89 \pm 0.02)\,\mu_B$, are slightly larger than the calculated value $\mu_{\text{eff}}^{calc} = 4.53\,\mu_{\text{B}}$ for the free Yb^{3+} ion. For both crystallographic directions, μ_{eff} decreases down to $\mu_{\text{eff}}^{c} = (4.52 \pm 0.02)\,\mu_{\text{B}}$ and $\mu_{\text{eff}}^{a} = (4.84 \pm 0.02)\,\mu_{\text{B}}$ for the pure arsenic compound. This is a hint for a reduced Yb valence in the arsenic compound. Indications for the reduction of the Yb valence were already found for samples with a low As concentration, $x = 0.13$, in resonant inelastic x-ray scattering (RIXS) [156]. Weiss temperatures of $\Theta_W^c = (-17 \pm 2)\,\text{K}$, $\Theta_W^a = (-37 \pm 3)\,\text{K}$ for $x = 0$ and $\Theta_W^c = (-113 \pm 1)\,\text{K}$, $\Theta_W^a = (-180 \pm 3)\,\text{K}$ for $x = 1$ were determined from the fits in Fig. 2.25 (c) and (d) (dashed lines).

The reason for this large change in the Weiss temperature is unclear. We speculate that this might be caused by the change of the valence of the Yb ion. The effect, illustrated in Fig. 2.25 (e) and (f), can be compensated by subtraction of a small temperature independent contribution from the susceptibility. The Curie-Weiss law, Eqn. (1.21), can be written as

$$\chi(T)T = C_{\text{mol}} + \chi(T)\Theta_W. \tag{2.8}$$

At high temperatures, $T \gg \Theta_W$, the product $\chi(T)T$ is approximately temperature independent. We plotted the data shown in Fig. 2.25 (a) and (b) as $\chi(T)T$ versus temperature in (e) and (f). For $x = 0$, $\chi(T)T$ is constant above 250 K while, as expected, it is temperature dependent for $x = 1$ because Θ_W is large. We find that constant behaviour at high temperatures can be obtained for $x = 1$ by subtracting a small temperature independent Van-Vleck like contribution from the susceptibility data (not shown).

The field dependent magnetization, $M(B)$, for both directions of the applied magnetic field at 2 K is shown in Fig. 2.26, right. For YbNi_4P_2, we observe an identical field dependence as it was determined for Bridgman grown single crystals [118]. For $B \parallel 001$, a polarized moment amounting to $1.24\,\mu_{\text{B}}$ at $B = 7\,\text{T}$ is found while for $B \parallel 100$, the magnetization increases linearly up to $0.53\,\mu_{\text{B}}$ at $B = 7\,\text{T}$. Within the substitution series, also here the anisotropy in $M(B)$ decreases leading to a nearly isotropic field dependence for $x = 1.0$.

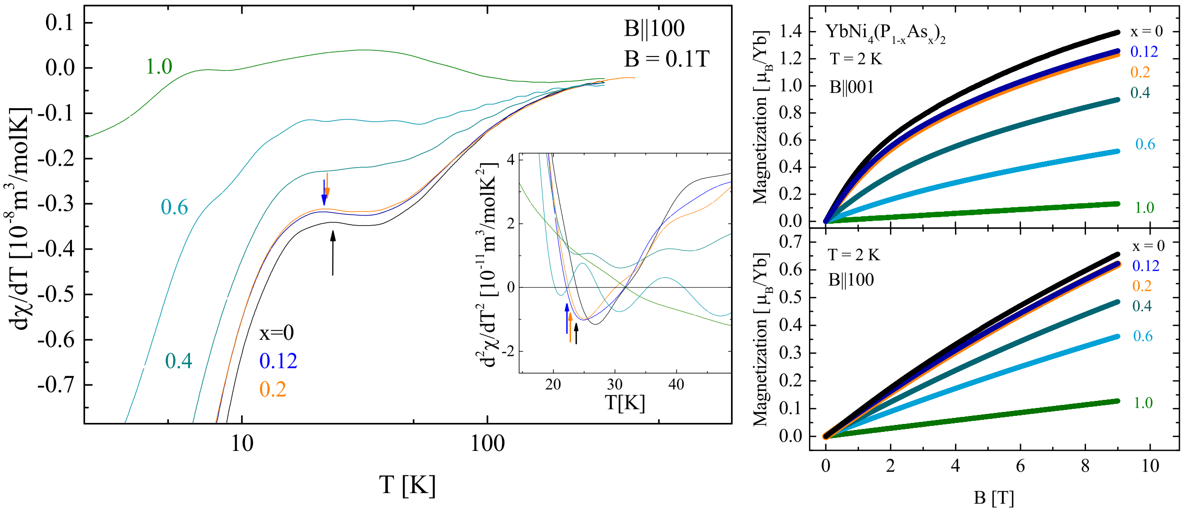

Figure 2.26: $\text{YbNi}_4(\text{P}_{1-x}\text{As}_x)_2$ *Left:* First derivative $d\chi(T)/dT$ of the data shown in Fig. 2.25 (b) for $B \parallel 100$, $B = 0.1\,\text{T}$. The temperatures T_{K}^{χ} where the first derivative exhibits a clear maximum are marked by an arrow. *Right:* Field dependence of the magnetization per Yb ion at $T = 2\,\text{K}$ for the two field directions $B \parallel 001$ and $B \parallel 100$.

2.6.7 Characterization of $YbNi_4As_2$

Electrical resistivity

The temperature dependence of the electrical resistivity $\rho(T)$ of the pure arsenic compound $YbNi_4As_2$, presented in Fig. 2.27, left, is isotropic for both current directions. Below 10 K, $\rho(T)$ shows FL behaviour and is well described by $\rho(T) = \rho_0 + AT^2$, as shown in the inset, with $A = 0.0033\,\mu\Omega\text{cm/K}^2$ and $\rho_0 = 3.05\,\mu\Omega\text{cm}$. The resistivity ratio $RR_{1.8\,\text{K}} = 27$ is found to be isotropic in this compound and higher than that of the pure phosphorous compound.

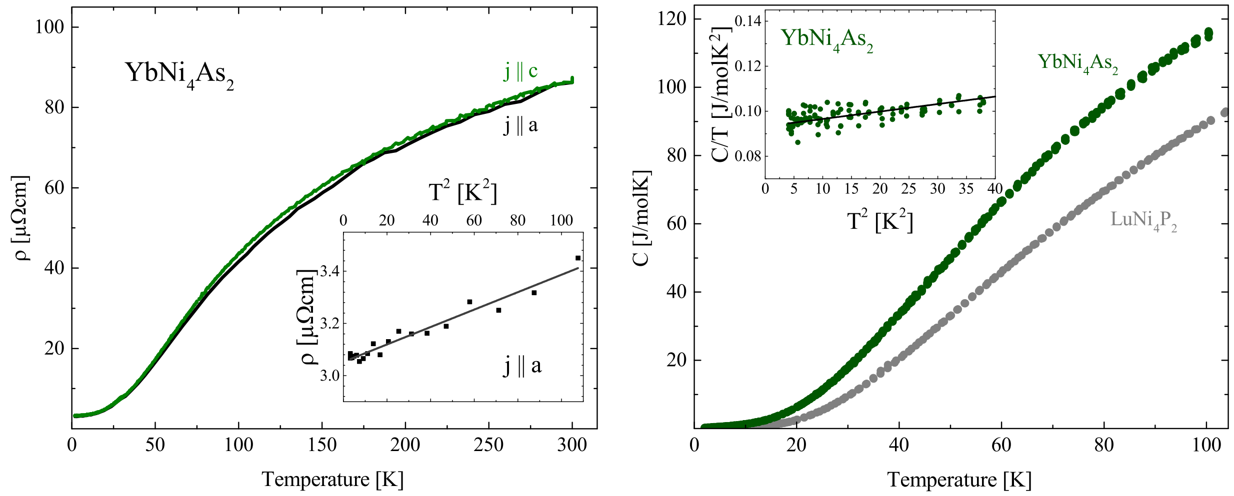

Figure 2.27: *Left:* Electrical resistivity measured on $YbNi_4As_2$ with $j \parallel a$ (black curve) and $j \parallel c$ (red curve). Below 10 K, for both current directions the data can be described by $\rho(T) = \rho_0 + AT^2$ indicating FL behaviour as shown in the inset for $j \parallel a$. *Right:* Heat capacity of $YbNi_4As_2$ (green) and $LuNi_4P_2$ (grey). In the inset, C/T versus T^2 is shown below 6 K.

Heat capacity

The specific heat capacity $C(T)$ of $YbNi_4As_2$ from 2 - 100 K is presented in Fig. 2.27, right, together with the heat capacity of $LuNi_4P_2$ (compare Fig. 2.17). The difference between both data sets is large and it is obvious, that the phosphorous compound cannot be used as a good reference. Below 6 K, heat capacity of $YbNi_4As_2$ can be described by $C/T = \gamma_0 + \beta T^2$ which is shown in the inset of the right figure. The Sommerfeld coefficient is $\gamma_0 = 96\,\text{mJmol}^{-1}\text{K}^{-2}$ and from the slope β of the linear fit a Debye temperature of $\Theta_D = 213\,\text{K}$ was determined.

Magnetization

A first characterization of polycrystalline $YbNi_4As_2$ was reported by Deputier *et al.* [120]. The temperature dependence of the susceptibility of $YbNi_4As_2$ for both directions at an applied magnetic field of $B = 0.1\,\text{T}$ is shown on enlarged scale in Fig. 2.28, left. It is shown in comparison with literature data [120]. The absolute values of the magnetization of this compound are much smaller than of the phosphorous compound which indicates a reduction of the Yb valence. Nearly isotropic Curie-Weiss behaviour with effective magnetic moments $\mu^c_{\mathrm{eff}} = (4.52 \pm 0.02)\,\mu_{\mathrm{B}}$ and $\mu^a_{\mathrm{eff}} = (4.84 \pm 0.02)\,\mu_{\mathrm{B}}$ and the Weiss temperatures $\Theta^c_W = (-113 \pm 1)\,\mathrm{K}$, $\Theta^a_W = (-180 \pm 3)\,\mathrm{K}$ are found and are shown in Fig. 2.28, (a) and (b). The field dependent magnetization of $YbNi_4As_2$ for both directions of the applied magnetic field at 2 K is shown in Fig. 2.28, (c). It is isotropic up to $B = 9\,\mathrm{T}$.

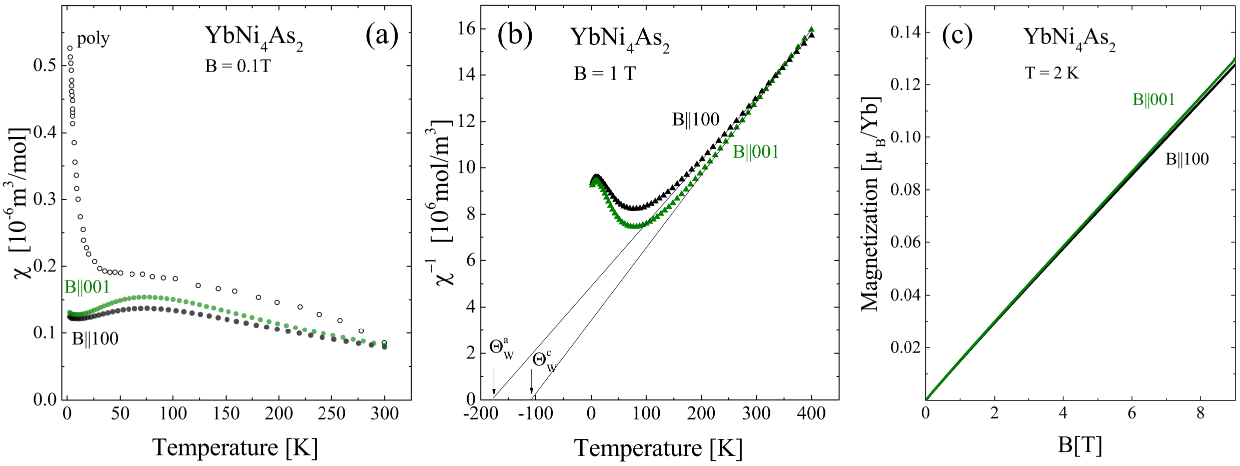

Figure 2.28: $YbNi_4As_2$ (a) Susceptibility with $B = 0.1\,\mathrm{T}$. The data measured on a polycrystalline sample [120] are shown for comparison. (b) Inverse susceptibility for the two field directions $B \parallel 001$ and $B \parallel 100$. (c) Field dependence of the magnetization per Yb ion at $T = 2\,\mathrm{K}$ for the two field directions $B \parallel 001$ and $B \parallel 100$.

2.6.8 Further results

Nuclear magnetic resonance

Nuclear magnetic resonance (NMR) is a widely used technique to study the microscopic properties of molecules and solids. Several Kondo lattice compounds like CeFePO [157] and $YbRh_2Si_2$ [158, 159] have been studied with respect to the type of the magnetic fluctuations. In an NMR experiment, the applied external field influences the movement of the electrons and the resulting inner field acts on the nuclear magnetic moment. The nuclear moments are shielded by the electrons which leads to a shift in the resonance field. A negative shift is expected from the simple conduction electron polarization model for Yb $4f$ ions [160].

$YbNi_4P_2$ contains a very good ^{31}P (relatively high γ_{N}) NMR nucleus with nuclear spin $I = 1/2$ and a natural abundance of 100%. The isotopes of the other elements are much more difficult to detect since they have a much lower natural abundance: ^{171}Yb with $I = 1/2$ (natural abundance 14.31%), ^{173}Yb with $I = 5/2$ (natural abundance 16.13%) and ^{61}Ni with $I = 3/2$ (natural abundance 1.19%). In the past, NMR experiments on $YbNi_4P_2$ powder samples from 300 to 1.8 K have been performed and the ferromagnetic critical fluctuations were investigated [122, 123]. Now, large single crystals are available and facilitate the investigation of the local in-plane anisotropy between the [100] and the [110] direction in this material by NMR down to lowest temperatures. The local probe NMR allows the orthorhombic symmetry of the Yb site to be examined utilizing the fact that in the $a-a$ plane there are two non-equivalent P sites P_1 and P_2 present in the crystal structure as shown in Fig. 2.22. $YbNi_4P_2$ single crystals are presently investigated by Y. Kishimoto (Kobe University) to study the evolution of magnetic fluctuations down to 1.8 K [130]. Further measurements at lowest temperatures and low fields have been started.

Electron spin resonance

The ESR of an $YbNi_4P_2$ single crystal was investigated by Jörg Sichelschmidt (MPI CPfS). The measurement was performed applying microwaves with X-band (9.3 GHz) frequency in magnetic fields up to $B = 1.8\,\mathrm{T}$ at $T = 2.9\,\mathrm{K}$ and $T = 4.6\,\mathrm{K}$. No resonance signal was found for orientations $B \perp c$ and $B \parallel c$ where B is the external field as well as for $b \perp c$ and $b \parallel c$ (b = microwave field). This is an unexpected result since in preliminary research on different other Kondo lattice systems an ESR signal was found if FM fluctuations are present [131].

Millikelvin studies are currently performed by M. Javaheri and M. Scheffler (Universität Stuttgart) to study the ESR of the material near its FM phase transition in a microwave resonator.

Inelastic neutron scattering

The anisotropy and the temperature dependence of spin fluctuations can be studied by INS. Magnetization measurements on $YbNi_4P_2$ single crystals show the unusual effect, that above T_C the c-axis is the magnetically easy direction due to the influence of the CEF, whereas below T_C the magnetic moments order in the basal plane of the tetragonal lattice [14]. This behaviour might be caused by enhanced transverse (in-plane) spin fluctuations arising in the vicinity of the QCP. Previous neutron scattering experiment at ToFToF (cold neutron time-of-flight spectrometer; Maier-Leibnitz Zentrum, Technische Universität München (MLZ)) on $YbNi_4P_2$ powder samples showed an increase of the susceptibility towards low momentum transfer at 1 K, indicating the evolution of ferromagnetic fluctuations [126]. The temperature dependence and the anisotropy of the critical fluctuations is currently investigated with the help of inelastic neutron scattering by S. Lucas, O. Stockert (MPI CPfS) and Z. Hüsges (Helmholtz Zentrum Berlin (HZB)). The single crystal, shown in Fig. 2.29, was mounted on the sample stage such that the use of a horizontal (h 0 l) scattering plane was possible. The critical fluctuations were studied in the vicinity of the weak nuclear reflections (1 0 1) and (2 0 0). First measurements were performed with a low-energy transfer of 0.15 to 0.25 meV at temperatures down to 60 mK at the cold-triple axis spectrometer PANDA (MLZ) and at FLEXX (HZB) and showed the presence of antiferromagnetic fluctuations far above the Curie temperature which was not expected for a FM material. Further studies of the magnetic fluctuations in $YbNi_4P_2$ are in progress.

Angle resolved photoemission spectroscopy

The compound $YbNi_4P_2$ exhibits unusual power-law behaviour of the magnetic susceptibility [14, 121] and the quantum-critical region cannot be described within a local-moment Heisenberg [161] or Ising model [162]. It was proposed that strong transverse spin fluctuations might dominate the magnetic anisotropy at low temperatures [163], but this model implies a first-order phase transition which is not observed in $YbNi_4P_2$. The reason for this unusual behaviour might be the one-dimensional electronic character of $YbNi_4P_2$ and therefore the investigation of the FS of this compound is important. The crystal structure

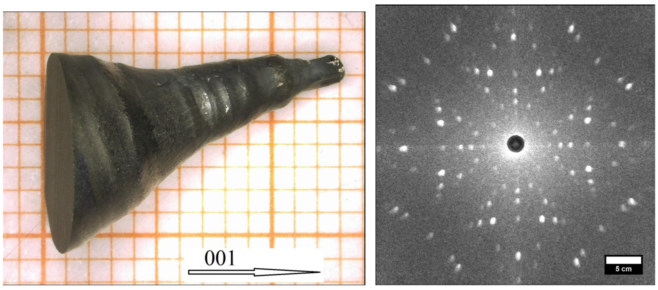

Figure 2.29: *Left:* $YbNi_4P_2$ single crystal (No. 039, $m \approx 1.8\,g$) used for the inelastic neutron scattering experiments; *Right:* Neutron Laue backscattering image taken at the ILL by O. Stockert (MPI CPfS). The beam direction was aligned parallel to the [001] direction of this high-quality single crystal and shows the fourfold symmetry of the tetragonal lattice.

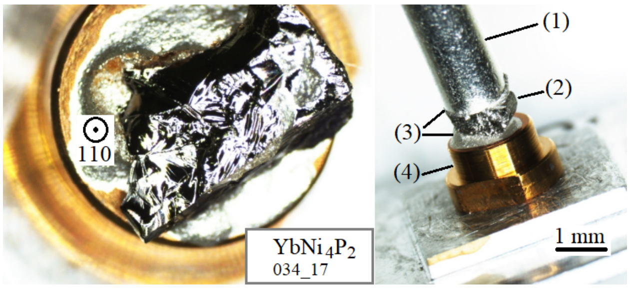

Figure 2.30: The $YbNi_4P_2$ sample No. 034 – 17 was used for the ARPES experiment and glued on an 110 plane. The top-post (1) is attached to the sample (2) with glue (3) on a sample holder (4) in preparation of the measurement. The cleave was done in ultra-high vacuum right before the ARPES measurement performed by D. Vyalikh (San Sebastian).

shows chains of Yb ions running along the crystallographic c-direction which are separated by chains of P and of Ni tetrahedra. Additionally, uncorrelated band structure calculations predict flat FS sheets [121] as shown in the left panel of Fig. 2.31 and the inset therein. Resistivity measurements show a strong anisotropy of a factor of approximately four at low temperatures [14] which indicates the one-dimensional character of this compound. It is expected that ARPES spectra of $YbNi_4P_2$ show a strong Ni-contribution. But also this Ni-dominated FS itself would be of very high interest, as this would be a strong experimental evidence of the quasi 1D character of this material. $YbNi_4P_2$ does not exhibit easy-cleave planes and its investigation by ARPES is therefore hindered. Nevertheless several attempts were undertaken by D. Vyalikh (San Sebastian), Fig. 2.30, and he was able to obtain one spectrum on a cleaved (110) plane. The cleave of samples with (100) or (021) planes was not successful. From the integrated data shown in Fig. 2.31, right panel, it is obvious that these look quite similar to the DOS obtained by uncorrelated band-structure calculations Fig. 2.31, left panel. The calculation shows that one main contribution to the DOS comes from Ni states.

Scanning tunneling microscopy

Low temperature scanning tunneling microscopy (STM) experiments done by L. Jiao from MPI CPfS are currently in progress but also here the investigation is hampered due to

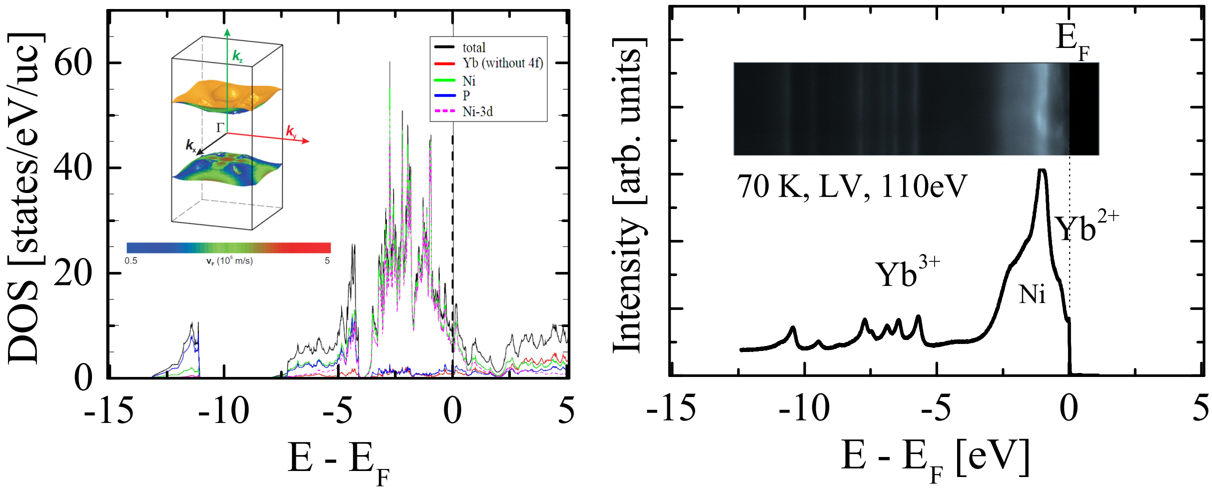

Figure 2.31: Comparison of uncorrelated band structure calculations (left) performed by H. Rosner (MPI CPfS) after [121] with angle-integrated ARPES data (right) obtained by D. Vyalikh (San Sebastian) from a cleaved (110) surface at 70 K using a linear polarized photon beam with an energy of 110 eV.

the occuring difficulties to cleave the samples. The bound distance of several atoms are similar, therefore the crystal possesses no easy-cleave plane. Three types of planes were obtained in first attempts to cleave the single crystals: (100), (331) and (110). The (100) surface is dominant but until now no atomic flat surface could be resolved during the STM measurement.

Lifshitz transitions

Our attempts to determine the FS by ARPES failed so far since the crystals do not exhibit easy-cleave planes as described above. The second standard method would be to determine the zero-field FS via quantum oscillation measurements but this is also not applicable. The reason for that is the occurence of multiple Lifshitz transition (LT) that alter the FS already at fields below 18 T. Which is far below the fields higher than 20 T at which the observation of quantum oscillations is possible. Until now, there is no experimental study on the zero-field FS available. Our recent study of YbNi$_2$P$_2$ in high magnetic fields [105] took advantage on the availability of larger and purer single crystals grown by the Czochralski method. LTs are changes in the FS topology that do not change its symmetry. These transitions offer a new approach to get insight into the FS of YbNi$_4$P$_2$ and its evolution in small fields. LTs occur due to the existence of flat hybridized bands in 4f- and 5f-electron Kondo-lattice systems and have been studied for instance in YbRh$_2$Si$_2$, CeRhIn$_5$ and URu$_2$Si$_2$ [164–166]. In these systems, the Kondo effect creates flat renormalized bands near the Fermi level with a bandwidth of the order of the Kondo temperature $T_K \approx 10\,\text{K} \approx 10\,\text{T}$ and a DOS at the Fermi level which is enhanced by a factor of 1000. This small bandwidth makes it possible to induce LTs at fields below 20 T. By applying a small field on YbNi$_4$P$_2$, its band structure changes and respective signatures in the resistivity and thermopower occur. The analysis of the type of a LT facilitates the determination of the change in the dimension of the involved FS.

3

$\mathbf{YbRh_2Si_2}$

3.1 Introduction to a system close to an antiferromagnetic quantum critical point

The first study of its crystallographic structure was done in 1979 [167] and since then, especially during the last two decades, the low temperature properties of $YbRh_2Si_2$ have been investigated intensively. This is mainly due to the fact that high-quality single crystals became available. In the past years, the crystal growth conditions have been optimized carefully by changing the stoichiometry and the applied temperature profile [168] and now crystal growth experiments with reproducible growth results can be performed. $YbRh_2Si_2$ is a tetragonal compound that crystallizes in the $ThCr_2Si_2$-type structure ($I4/mmm$) with $a = 4.007\,\text{Å}$ and $c = 9.858\,\text{Å}$ [169]. In the past, this Kondo-lattice compound has been studied in great detail due to its proximity to a field induced QCP. $YbRh_2Si_2$ orders antiferromagnetically below $T_\mathrm{N} = 70\,\mathrm{mK}$. A small external field of $B_\mathrm{crit} \approx 60\,\mathrm{mT}$ applied in the tetragonal plane ($B_\mathrm{crit} = 0.66\,\mathrm{T}$ for $B \parallel c$) is sufficient to supress the antiferromagnetic order and shift T_N down to zero at the QCP [20, 97]. The anisotropic magnetization indicates that the Yb^{3+} moments order in an "easy-plane" square lattice perpendicular to the crystallographic c-direction [169]. The application of pressure increases T_N [169] since the ionic volume of the $4f^{13}$ Yb^{3+} configuration is smaller than that of the non-magnetic $4f^{14}$ Yb^{2+} one. Negative chemical pressure can be applied by substituting the smaller Si atoms by larger Ge atoms which tunes the $YbRh_2(Si_{1-x}Ge_x)_2$ through the QCP without altering its electronic properties [97]. In the vicinity of the QCP, unconventional behaviour of the conduction electrons occurs. It shows up, for instance, in the temperature dependence of the electrical resistivity: The well-defined FL behaviour, namely the T^2-temperature dependence of the resistivity observed far away from the QCP at fields higher than B_crit turns into a linear temperature dependence in the vicinity of the QCP. In the $B - T$ phase diagram, an additional temperature scale T^* has been identified in the non FL region. This line has been interpreted as the transition of the FS from a "small Fermi surface" without the $4f$ electrons to a "large Fermi surface" which contains the $4f$ electrons but is still under debate [84, 170, 171].

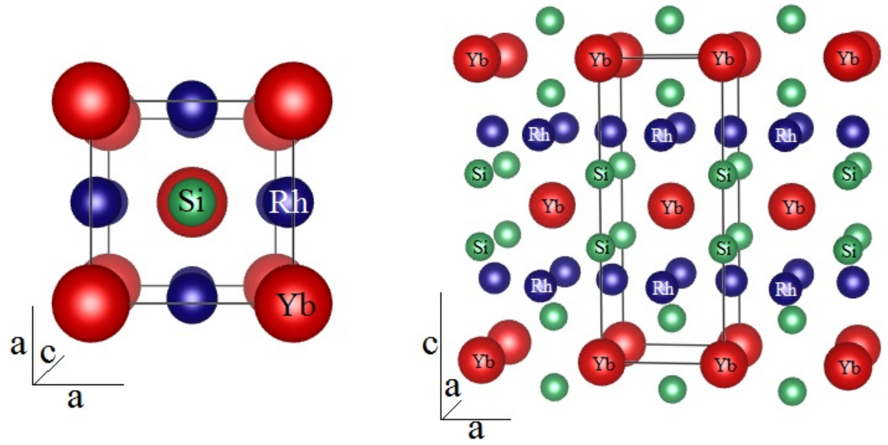

Figure 3.1: Tetragonal crystal structure of $YbRh_2Si_2$. The Yb planes are separated from each other by Si-Rh-Si trilayers.

3.2 Summary of the results and outlook

In the course of this theses, a crystal growth procedure for $YbRh_2Si_2$, which is one of the best studied materials close to an AFM QCP, was established in the Crystal and Material Laboratory Frankfurt. The resulting single crystals are comparable in size and purity to single crystals grown in previous work [168]. Samples of highest purity for ultra-low-temperature investigations were identified by combined magnetization and electrical transport measurements using a PPMS. Our result of $RR_{1.8\mathrm{K}} \approx 32$ for the purest single crystals is slightly higher compared to previous results with $RR_{1.8\mathrm{K}} \approx 27$ [172].

Severals experiments have been started by different collaborations utilizing our new single crystals. J. Saunders and coworkers succeeded in measuring the thermal noise on thin $YbRh_2Si_2$ single crystals and thereby confirmed the superconducting transition at $T_c \approx 2\,\mathrm{mK}$ in $YbRh_2Si_2$ [11, 173]. A new path was opened by M. Brando and coworkers by preparing a meander structure on thin single crystal platelets using the focused ion beam (FIB) technique. The micro-structured samples have an increased current carrying length with increased resistivity. This leads to the reduction of heating effects and to an improved precision of the measurement. The as prepared single crystals will facilitate resistivity measurements in the ultra-low temperature regime [174]. In Kondo systems, a "large" Fermi surface forms due to the hybridization of $4f$ and conduction electrons. In the course of this thesis, the "small" Fermi surface formed exclusively by conduction electrons was detected in a Compton-scattering experiment by D.V. Vyalikh and coworkers at $T = 300\,\mathrm{K}$ [175]. This experiment was performed on large $YbRh_2Si_2$ single crystals. Due to its low lying Néel temperature, its small ordered moment and the absence of single crystals suitable for neutron scattering, the magnetic structure of $YbRh_2Si_2$ is not known until now. Magnetization measurements at low temperatures have been started by M. Brando and coworkers to obtain further information about the ordered phase. In the course of this thesis, new experimental setups were developed by M. Scheffler and coworkers. These allowed to investigate the material by microwave spectroscopy in temperature and field regions that were unaccessible until now [176, 177]. During the past years, the foundation was layed for the investigation of the dynamics of the Kondo state by time-resolved THz studies by C. Wetli, M. Fiebig and H. Kroha. The first material that was studied was $CeCu_{6-x}Au_x$ which exhibits a QCP at $x \approx 0.1$. A terahertz pulse converts heavy fermions in the material into normal light electrons. The heavy-fermion state recovers under emission of a delayed, phase-coherent terahertz reflex. Towards the QCP, the quasiparticle weight collapses while its formation temperature remains almost constant. To validate the conception of the experiment and the experimental method itself with a further heavy-fermion material we contributed to this project by providing large single crystals of $YbRh_2Si_2$ [178].

The application of such new approaches might not only shed light on the still unanswered questions about the magnetic order or the mechanism leading to the heavy-electron superconductivity in $YbRh_2Si_2$ but also address general questions about the dynamics of the Kondo state in quantum critical materials.

3.3 Crystal growth preliminary work

The optimization of the crystal growth of $YbRh_2Si_2$ from indium flux was performed at the MPI CPfS using a two-zone furnace (Xerion) and was described in detail by Krellner *et al.* [168]. In the past, a different attempt using zinc as flux was proposed by Hu *et al.* [179] which yielded large singe crystals but with a low *RRR* value compared to crystals grown from indium flux. This hints to a possible incorporation of zinc into the crystal structure which is not desirable since for low temperature measurements, the crystal quality is an important issue. The single crystal growth of $YbRh_2Si_2$ from indium flux was established in Frankfurt in the course of this thesis. We follow the route presented in [168] due to the high expected purity that can be achieved. The aim was to transfer the process to the high-temperature GERO furnace which was started up at that time in Frankfurt. The first step was to find the suitable growth conditions namely the temperature-time profile and the suitable amount of cooling caused by the argon flow. The influence of the usage of graphite as crucible material on the crystal quality was investigated. Furthermore, experiments were performed to explore the possibilities to implement a seed into the setup. P. Wein and C. Butzke contributed to this project in the course of their Bachelor‘s and Master‘s theses.

3.4 Experimental details

High-purity starting materials Yb ingot (99.99%, Ames Laboratory), Rh powder (99.98% Heraeus), Ir (99,96% Heraeus), Si (99.9999% Wacker) and In (99.9995 N.V. Kawecki-Billiton) were used. Ytterbium is air sensitive and the preparation was done in a glove box filled with purified argon. For the Bridgman growth, the tantalum crucible was put under a flow of argon in a vertical resistive furnace (GERO HTRV70250/18). The crystal structure was characterized by PXRD on crushed single crystals, using Cu-K_α radiation. The chemical composition was measured by EDX. The orientation of the single crystals was determined using a Laue camera with x-ray radiation from a tungsten anode. Four-point resistivity and magnetization measurements were performed using the commercial measurement options of a Quantum Design PPMS.

Growth No.	stoichiometry Yb:Rh:Si	T profile No.	Ref.	d [μm]	m [mg]	$\mathrm{RR}_{1.8\mathrm{K}}$, $j \perp c$
CB101	2:2.2:1.8	Yb01	[168]	200	19.5	32.7

Table 3.1: Parameters of the crystal growth by Bridgman method of $\mathrm{YbRh_2Si_2}$. The thickness d and the mass m are average values of the ten largest single crystals.

T profile No.	furnace	$T_{\max}$ [°C]	t_{hom} [h]	T_1 [°C]	v [mm/h]	T_2 [°C]	duration [h]	Ar flow [ml/min]
Yb01	GERO	1530	1	1480	1	1240	92	155

Table 3.2: Measured temperature-time profile of the crystal growth of $\mathrm{YbRh_2Si_2}$. The crucible was kept at $T_{\max}$ for 1 h to homogenize the melt. All temperatures have been measured in situ at the bottom of the crucible. The temperature of the furnace was measured using a second thermocouple which is included in the furnace. The maximum temperature of the furnace during the growth was $T_{\max}^{\mathrm{furnace}} = 1550$°C.

3.5 Crystal growth from indium flux

The high melting temperature of the transition metal Rh (1963°C) in combination with the low boiling point (1196°C) [180] and high vapour pressure of Yb necessitates the use of a solvent (flux). In preliminary work, it has been found that indium (T_L=157°C) is a suitable solvent [168]. Our setup of the crucible system is shown in Fig. 3.2, b). The elements in a non-stoichiometric composition of Yb : Rh : Si = 2 : 2.2 : 1.8 were weighed in together with indium as flux in a molar elements to flux ratio of 4:96. The total mass of each growth charge was 21 g. The graphite crucible was purified before loading with the initial charge by heating it up to 1600°C under vacuum using a high-frequency furnace. Upon cooling, the porous wall of the graphite crucible was loaded with argon and was transferred into the glove box subsequently. The elements were filled in the graphite crucible with $V = 25$ ml for the Bridgman growth according to the setup shown in Fig. 3.2, b). The inner graphite crucible was put in an outer crucible made of tantalum which was sealed under argon using arc-melting. The parameters for the crystal growth and the temperature-time profiles for the experiments that gave the best results namely the largest crystal size, the smallest amount of indium inclusions and the highest $RR_{1.8\mathrm{K}}$ value can be found in Tabs. 3.1 and 3.2. All experiments have been performed in the high-temperature GERO furnace. A scheme of the temperature-time profile is shown in Fig. 3.2, c). The sealed tantalum crucible was heated up to $T_{\max} = 1530$°C with a rate of 300 K/h. The melt was held at this temperature to ensure homogenization for $t_{\mathrm{hom}} = 1$ h and afterwards the furnace was moved 10 cm upwards. By doing so we got a complete homogenization of the melt and afterwards minimized the time where the melt was exposed to the maximum temperature. At highest temperatures the reactivity of the melt is highest and also the risk of bringing contamination from the crucible into the melt. At $T_1 = 1480$°C the growth started by slow moving of the whole furnace with

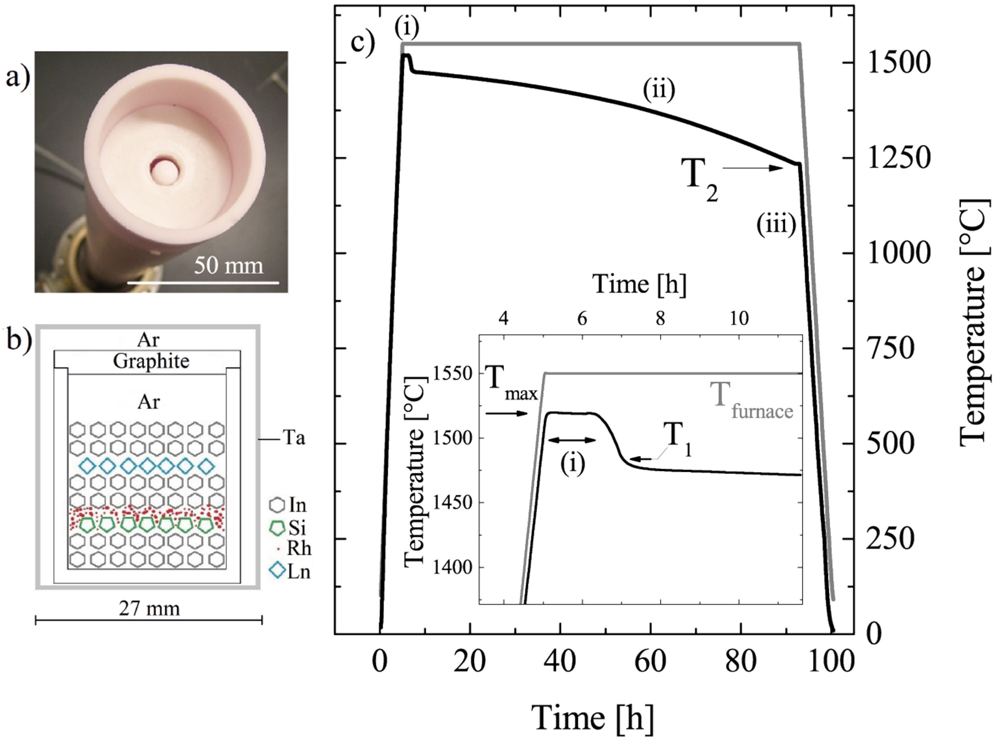

Figure 3.2: Growth of $LnRh_2Si_2$ single crystals by Bridgman method. a) Al_2O_3 crucible holder with thermocouple; b) Setup of the crucible system; c) $LnRh_2Si_2$: Temperature-time-profile.

$v = 1\,\text{mm/h}$ while the position of the crucible stayed fixed. With this setup, we were able to cool the sample without vibrations resulting from the movement which is different from the conventional Bridgman process where the sample is moved from the hotter to the colder zone. Our setup allows for the direct measurement of the temperature at the bottom of the crucible during the growth using a Pt/Rh thermocouple of type B. The platform of the crucible holder made of Al_2O_3 is shown in Fig. 3.2, a). Through the hole in the platform, the tip of the thermocouple is visible. The furnace is moved until the temperature at the sample position has reached $T_2 = 1240°\text{C}$ and a faster cooling period terminated each growth experiment. After the growth, the single crystals were embedded in indium flux. The flux was removed by etching in hydrochloric acid 32%. During this etching process also additional phases that formed during the growth, like e.g. $RhIn_3$, dissolved completely.

3.6 Limitations of the growth method

The aim of the optimization of the crystal growth process in the past [168] was to provide knowledge of the optimal growth conditions which support the formation of crystals that are on the one hand large and on the other hand as pure as possible. In most experiments which were performed in the course of this thesis using the conditions described in [168] crystals were obtained which had a high purity and were also comparable in size to the ones which have been grown in the past. But in some cases the growth completely failed meaning that only small crystals formed or that mainly one large polycrystalline sample formed or

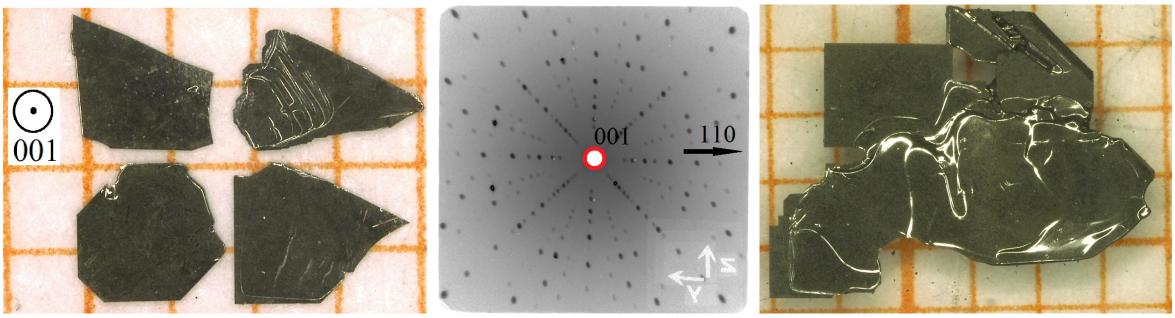

Figure 3.3: $YbRh_2Si_2$ *Left:* Thin single crystal platelets ($d \approx 5 - 8\,\mu$m) used for preparing the meander structure. *Middle:* Laue pattern. *Right:* Large single crystal [181].

that instead of well separated $YbRh_2Si_2$ single crystal platelets a large amount of irregular shaped platelets adherent to each other was obtained. The reason for this is unclear and since the growth is performed in a closed crucible, it is not possible to observe the growth directly. Two main issues impede the full reproducibility of the growth result: The first is that the present setup does not allow to use a seed. The second is that the homogenization might be incomplete due to the poor mixing of the initial melt. The task in future work will be to overcome these issues by developing procedures for the crystal growth which allow for the use of a seed, provide a better mixing of the melt or use a different flux to improve the homogeneity in the substituted crystals.

Nucleation

With the Bridgman-type method presented above, we are able to obtain single crystals with a high purity but their size is limited. Several measurement methods, like neutron scattering on single crystals, require large samples. The first step to increase the sample size is to understand and control the nucleation process. Up to now, the knowledge about the nucleation in our closed system is non-satisfying. Therefore, three types of experiments have been performed to shed light on this problem.

- In experiments of type I, a single crystal was embedded into the bottom of the graphite crucible. This crystal should serve as a seed in order to grow one large single crystal starting from this seed instead of many small pieces. Our observation was that after the growth, the seed crystal could not be identified anymore and seemed to be dissolved by the melt. The resulting crystals in this experiment were of average size. Obviously, in the present setup, it is not possible to obtain a sufficient cooling of the inserted seed.

- In experiments of type II, the graphite crucible had a complete lining of indium such that the direct contact of other elements than indium to the crucible wall was avoided during filling. Three experiments have been performed in this way and in all cases one large polycrystalline sample formed.

- In experiments of type III, the partial contact of other elements than indium with the wall of the crucible was made intentionally. In all cases, a large amount of large and average sized single crystal platelets was obtained after these experiments.

No.	sample	$RR_{1.8\,\mathrm{K}}$	In wt.%
(1)	102-01	29.9	0.00
(2)	101-01	26.2	0.00
(3)	101-03b	25.8	0.00
(4)	102-07	25.3	0.04
(5)	103-04	22.8	0.26
(6)	103-02	25.2	0.63

Table 3.3: Amount of included In and the residual resistivity ratio of samples from different batches.

From the experiments I-III the conclusion can be drawn that a seeding is not possible in the current setup and that the surface roughness of the crucible wall seems to support the nucleation.

Substitution of elements

The quantum critical point can be approached by either applying a small magnetic field or by substituting Rh by Ir. In preliminary work, it was already shown that it is possible to substitute Rh by Ir in $YbRh_2Si_2$ [172]. In the course of this work several attempts have been performed to obtain Ir substituted single crystals. In two experiments where the aim was to substitute 10 and 20% of Rh by Ir we observed that substitution is possible. But while the Ir concentration which was determined by EDX varies strongly between single crystals of the same batch the amount of Ir in one large single crystal is homogeneously incorporated. This observation leads to the conclusion, that in our current setup the homogenization of the melt is not sufficient and Ir is not distributed equally in the melt. The homogenization can be improved in future work by applying different growth methods like e.g. the accelerated crucible rotation technique where the homogenization of the melt can be achieved. The substitution of Si by the larger Ge leads to negative chemical pressure in this compound [97, 182, 183]. Unfortunately it is not possible to achieve Ge concentrations larger than 2% in the crystals in a reproducible way. The reason for this might be the high solubility of Ge in the In flux. To solve this problem the search for a different element or a combination of elements that could be used as flux is necessary.

3.7 Comparison of the growth results

The resulting single crystals, shown in Fig. 3.3, have a platelet-like shape and are as large as $5\,\mathrm{mm} \times 3\,\mathrm{mm} \times 200\,\mu\mathrm{m}$. The thinnest platelets which were used for the meander fabrication have dimensions of $3\,\mathrm{mm} \times 2\,\mathrm{mm} \times 8\,\mu\mathrm{m}$. The c-axis is always perpendicular to the platelets and the largest naturally grown faces besides the {001} faces are {110} faces (85%) or {100} faces (15%). The crystal growth is performed using indium as solvent for the elements. Flux inclusions in the single crystals can be minimized by low growth rates. We found that despite using low cooling rates, the formation of indium inclusions in the single crystals is unavoidable. The amount of these inclusions can be estimated easily utilizing the fact that

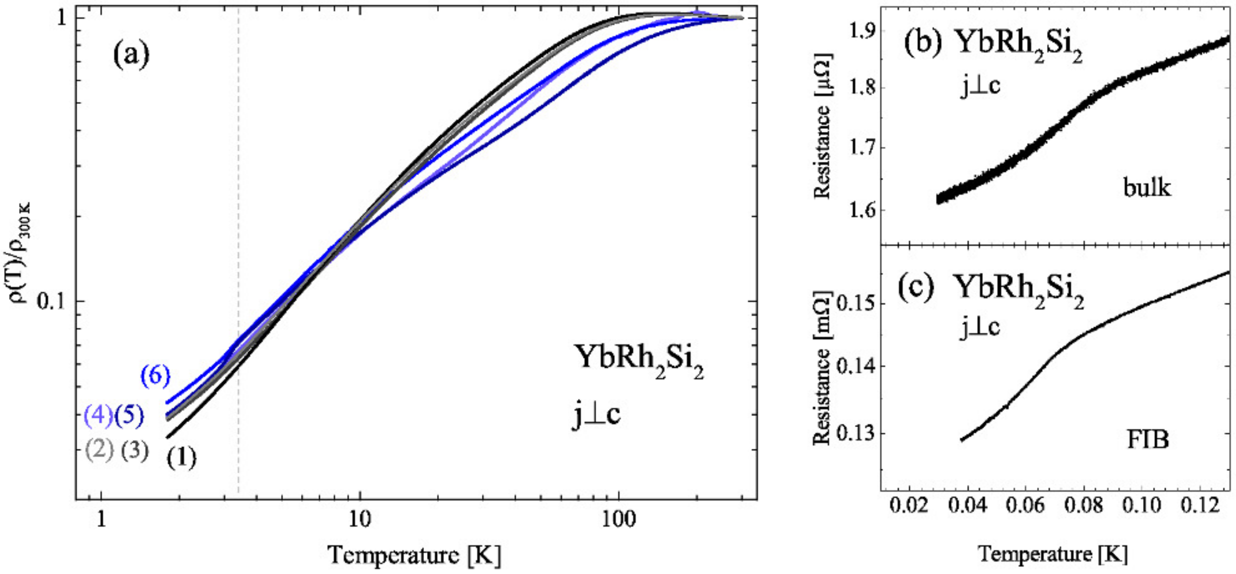

Figure 3.4: (a) Normalized resistivity of $YbRh_2Si_2$ measured with $j \perp c$ from $300 - 1.8$ K. Tab. 3.3 shows the indium amount and the residual resistivity ratio of the samples. The vertical line at 3.4 K marks the temperature where indium becomes superconducting. The data were recorded by C. Butzke [184]. (b) The low-temperature measurement down to $T = 30$ mK was performed on sample CB101-03-kk147 with $j \perp c$ and $B = 0$ T. (c) The micro-structured single crystal (FIB) reproduces the data measured on the not micro-structured bulk single crystal. The low temperature measurements were performed by S. Hamann and A. Steppke (MPI CPfS).

indium becomes a superconductor below $T_c = 3.4$ K [185]. The transition into the superconducting state causes a small jump in the magnetization when cooling below T_c if indium inclusions are present. The sudden decrease in the magnetization occurs since the magnetic volume susceptibility of indium is almost zero $\chi_{\mathrm{In}}^{\mathrm{NC}} = -5.6 \cdot 10^{-7}$ in the normalconducting state [186, 187] whereas it becomes $\chi_{\mathrm{In}}^{\mathrm{SC}} = -1$ in the superconducting state. We found that already for small amounts of included flux the shape of the resistivity curve at temperatures above 1.8 K measured on different samples differs slightly and is influenced by the included indium as shown in Fig. 3.4. We determined the amount of indium in the samples by magnetization measurements and found that the purest samples, No. (1)-(3), show the steepest drop in the resistivity which is attributed to the onset of coherent Kondo scattering. The collected set of reference data enables us to identify and select the purest samples for the low temperature measurements. The samples where the amount of indium was below the detection limit of the magnetization measurement (10^{-9} Am^2) showed a Kondo maximum at $\approx$ 100 K in the resistivity. The resistivity ratio RRR being a measure for the crystal defects can be compared to identify the purest single crystals. In preliminary work, for $j \perp c$ $RRR \approx 35$ [169] corresponding to $RR_{1.8\mathrm{K}} < 15$ [188] and $RR_{1.8\mathrm{K}} \approx 27$ [172] was measured on single crystals. Our result of $RR_{1.8\mathrm{K}} \approx 32$ is slightly higher for the purest single crystals. The electrical resistivity of $YbRh_2Si_2$ single crystals was measured by S. Hamann and A. Steppke (MPI CPfS) down to 30 mK to examine whether the behaviour is similar to that of samples which have been grown in the past at the MPI CPfS. In Fig. 3.4 (b),(c), the occurence of the phase transition is indicated by the kink in the curve at $\approx$ 70 mK and shows

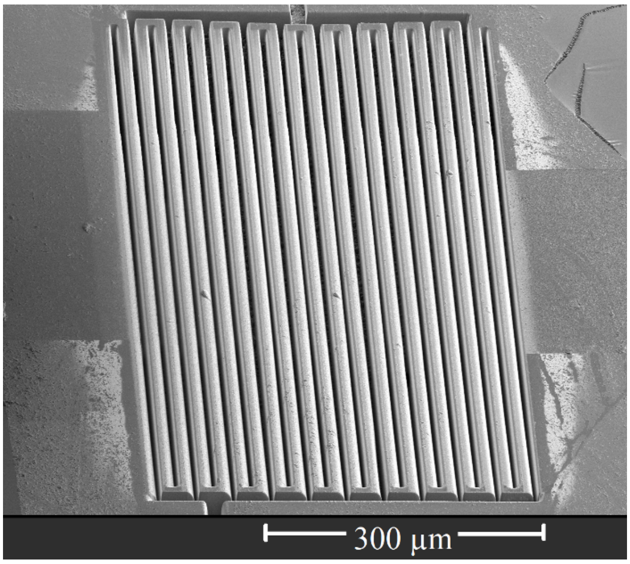

Figure 3.5: $YbRh_2Si_2$: Single crystal of meander shape prepared for transport measurements at ultra-low temperatures. The micro-structuring was applied by M. König and M.Brando (MPI CPfS).

the same characteristics as measured on previous samples [189]. Additionally the influence of the micro-structuring was investigated. It was found that the signal-to-noise ratio of the measurement is increased by using at meander-shaped single crystal, Fig. 3.4 (c).

3.8 Further results from high-quality single crystals

Our high-purity single crystals facilitate further studies of several physical properties of this already well known compound.

Superconductivity in $YbRh_2Si_2$

In $YbRh_2Si_2$, a strong change in the ac susceptibility below 2 mK indicates a superconducting state and recently, bulk superconductivity has been established by data on the Meissner effect for $B < 4\,\mathrm{mT}$ [11, 190]. It has to be noted that in $YbRh_2Si_2$ the nuclear contribution to the specific heat increases by several orders of magnitude below 1 K. This increase is mainly caused by the nuclear moments of the Yb ions [191]. In the proposed Landau-type model [11], the free parameters are tuned such that the onset of the nuclear-electronic order suppresses the $4f$ magnetic order and thus leads to the onset of superconductivity. Since the proposed model deals with a large number of free parameters and the connection to experimentally determined properties of $YbRh_2Si_2$ is relatively weak, it is under strong debate [192]. A different scenario was proposed by C.Geibel [192, 193]. The AFM state ($T_\mathrm{N} = 70\,\mathrm{mK}$) of $YbRh_2Si_2$ exhibits on the one hand an extremly small value of the ordered moment of $m_{4f} \approx 0.002\,\mu_\mathrm{B}$ on the other hand a tiny external field is sufficient to induce a local moment $m_{4f} \approx 0.1\,\mu_\mathrm{B}$ which is much larger. These two properties yield that the AFM state is inherently unstable against the formation of a state with a large magnetic moment which is stabilized by nuclear polarization at $\approx 1\,\mathrm{mK}$. The transition at 2 mK therefore might be a transition from a c-oriented small-ordered-moment to an in-plane oriented large-ordered-moment AFM state. Therefore the superconductivity in $YbRh_2Si_2$ is not connected to the AFM-PM QCP but to a critical point being associated with a change of the magnetic structure.

So far, the superconducting transition was verified by magnetization data but also electrical transport measurements can be used to obtain valuable information about the existence of novel phases. Typical samples cut from single crystals as shown in Fig. 3.3 have dimensions of 2 mm × 1 mm × 0.1 mm, and the bulk resistivity is below $1\,\mu\Omega\text{cm}$. Typically a contact distance of l=1 mm is chosen for the measurement. The resistivity of the sample therefore is

$$R_{\text{sample}} = \rho\frac{l}{A} = 10\,\mu\Omega\text{mm}\,\frac{1\text{mm}}{0.1\text{mm}^2} = 0.1\,\text{m}\Omega.$$

An additional resistance contribution R_{contact} of about 0.1 to $1\,\Omega$ is given by the contacts and dominates the total resistance. The detectable voltage response is

$$U_{\text{sample}} = 0.1\cdot 10^{-9}\,\text{V} = 0.1\,\text{m}\Omega\cdot 10^{-6}\,\text{A}.$$

The use of a current of $I = 10^{-6}$ A causes the total dissipation

$$P_{\text{diss}} = (R_{\text{sample}} + R_{\text{contact}})\cdot I^2 \approx 10^{-13}\,\text{W}.$$

Due to the limitations in the cooling power it is challenging to measure the resistivity below 10 mK [174].

In the course of this work, two groups, S. Bühler-Paschen and coworkers (TU Wien) and a collaboration between J. Saunders and coworkers (RHU London) and M. Brando and coworkers (MPI Dresden) started independently to investigate the transition into the superconducting state by electrical transport and thermal noise measurements using pure $YbRh_2Si_2$ single crystals. In Tab. 3.4 the properties of the samples used by the different groups is summarized.

At the beginning of this work, no data about resistive transitions in the ultra-low-temperature regime where available due to the challenge to measure resistances with minimal dissipation. D. Geiger (TU Wien) investigated the resistivity at ultra-low temperatures on different samples among those also high-quality single crystals of the latest generation. Below 10 mK, a new feature in fields between $50-90$ mT was detected, but a transition into the superconducting state could not be confirmed. The study will be continued after the refinement of the technical details (such as shielding, stray field effects, precision of measurement) and the first results are summarized in [194].

The electrical resistivity was measured indirectly via the Johnson-Nyquist noise by L. Levitin and J. Saunders (RHU London) down to 0.6 mK. Upon cooling the resistivity decreases showing a kink at 12 mK where a steeper linear decrease in the resistivity appears down to 3.7 mK. At this temperature, a distinct drop in the resistivity indicates the transition into the superconducting state [173]. The superconducting state can be suppressed by an external field of 9 mT. The measurements were performed on a single crystal with a thickness of about 8 μm.

In the course of this work, it became possible to increase the sensitivity of the resistivity measurements. Using the flux-growth technique we were able to obtain not only large single crystals as shown in Fig. 3.3, right, but also extremely thin platelets of about 8 μm

YbRh$_2$Si$_2$ Sample/Ref. /Growth No.	exp.	T_C [mK]	ref.	m [mg]	res.ratio $j \perp c$
Krellner [172]	$M(T)$, $C(T)$	2	Schuberth [11]	2.22, 0.75 30.62, 7.1, 5.44	$RRR \approx 150$ $RRR \approx 50$
cb101-01 [184], this work	$\rho(T)$	?	Geiger [194], Paschen [195]	28	$RR_{1.8\mathrm{K}} = 26$
pw101 [181], this work	noise	3.7	Levitin, Saunders [173]	≈ 5	$RR_{1.8\mathrm{K}} = 19$
kkcb108 this work				$\approx 1 - 3$	$RR_{1.8\mathrm{K}} = 24$

Table 3.4: YbRh$_2$Si$_2$ samples used for ultra-low temperature studies

(Fig. 3.3, left). The new approach by the group of M. Brando (MPI CPfS) to fabricate micro-structured samples opens the path to measure the resistivity in the sub-millikelvin temperature range. The meander structure, Fig. 3.5, was produced using the FIB technique. The total length of the meander is about 19 mm and the width per track is about 15 μm. The contacts were made of gold which was deposited on the crystal as well as on the substrate on which the crystal was glued on. The micro-structuring using a gallium FIB (FEI Helios) processing was performed by M. König (MPI CPfS). First tests yielded that the temperature dependence of the measured resistance is almost identical to the temperature dependence of the resistance of not micro-structured single crystals and the phase transition onto the AFM order at 72 mK is clearly visible as shown in Fig. 3.4. That means that the fundamental properties of the material have not been altered by the micro-structuring process. At the same time, the signal-to-noise ratio of the measurement $\Delta R/R$ increased due to the meander structure by one order of magnitude from 0.25% to 0.045% [174] when measured down to 40 mK. The increase of the length of the sample together with the decrease in its cross section due to the meander structure leads to a larger resistivity. The use of lower currents becomes possible and therefore the heating is reduced. This makes measurements in the sub-millikelvin region possible and allows for the further investigation of the superconducting state. To use the high precision of the measurement to its full capacity a high purity of the single crystals is indispensable.

To shed light on the nature of the superconducting transition and the role of the nuclear magnetism, the aim is to perform the measurements also on isotope-pure YbRh$_2$Si$_2$. The single crystals will be grown in future work using for instance the Yb isotopes ^{174}Yb with nuclear spin $I = 0$ or ^{171}Yb with nuclear spin $I = 1/2$. These samples will allow "to switch the nuclear moment on and off" and to directly compare the effect on the physical properties in the sub-millikelvin region.

Temperature dependence of the Fermi surface

In Kondo systems, the interplay between localized 4f spins and itinerant valence electrons leads to an enhanced DOS at the Fermi level. This socalled Kondo resonance [61, 196, 197] arises due to the formation of Kondo singlet states below the single-ion Kondo temperature T_K. In Kondo lattice systems, the magnitude of the DOS as well as the momentum dependence of the quasiparticles are affected by the Kondo effect. At low temperatures, the Fermi surface of a paramagnetic Kondo screened system contains the 4f electrons in the "large Fermi surface". In contrast, the 4f electrons are not part of the "small Fermi surface" when the screening disappears and the system is in an ordered state. This transition from the large to the small FS was confirmed by de Haas-van Alphen measurements in the recent past in Ce-based systems [198] but there is a debate on how this transition takes place with respect to magnetic order [16, 17, 199] and also with respect to the temperature [200, 201]. The temperature dependent change was studied for instance in CeCoIn$_5$ [202] or CeRu$_2$Si$_2$ [203] but experimental evidence is still weak nowadays.

YbRh$_2$Si$_2$ is a Kondo-lattice system with a T_K^* of about 25 K [169]. Below this temperature, the increase of the DOS at the Fermi level with a Sommerfeld coefficient of $\gamma_0 = (1.7 \pm 0.2)\,\mathrm{Jmol^{-1}K^{-2}}$ was confirmed by thermodynamic measurements [20]. This socalled heavy-fermion behaviour occurs in many Ce and Yb compounds and is caused by the interactions between the localized 4f and the itinerant electrons. Upon lowering the temperature, the interaction between both kinds of electrons increases and a controversially discussed issue is how the localized 4f become part of the Fermi surface upon cooling. At the beginning of this work it was observed by ARPES that the large Fermi surface which includes the 4f electrons of YbRh$_2$Si$_2$ does not change into the small Fermi surface without 4f electrons up to 95 K [204]. At that time the question arose if the appropriate temperature range was studied [205]. The change of the Fermi surface with temperature is a widely accepted idea but it is not clear in which temperature range the change happens in Kondo-lattice systems. Our large single crystals enabled us to further investigate this topic since a change to the small Fermi surface is expected for high temperatures. Compton scattering experiments have been performed by Denis Vyalikh (TU Dresden) utilizing a stack of 7 single crystals. The single crystals have been carefully oriented and afterwards glued on top of each other in the same orientation. The experiments yielded that also in YbRh$_2$Si$_2$ the small Fermi surface can be observed at 300 K [175].

Magnetic order

Until now, the magnetic structure of YbRh$_2$Si$_2$ is not known. The compound has a small magnetic moment and a low lying Néel temperature. Additionally neutron scattering experiments on the one hand require larger crystals than that which are available. On the other hand these measurements are hindered due to the large absorption of Rh. Therefore, in the past the magnetic properties of related systems like YbCo$_2$Si$_2$ and of Co substituted YbRh$_2$Si$_2$ have been investigated [67, 69]. YbCo$_2$Si$_2$ orders antiferromagnetically at $T_N = 1.7$ K [206]. In the substitution series Yb(Rh$_{1-x}$Co$_x$)$_2$Si$_2$ the smaller Co stabilizes the magnetism and a second AFM phase appears for low Co concentrations. Samples with $x = 0.27$ become ferromagnetic [68]. Pure YbRh$_2$Si$_2$ and Co substituted YbRh$_2$Si$_2$ is presently further investigated by S. Hamann, M. Brando *et al.* (MPI CPfS) in order to deduce information about the magnetic order in the unsubstituted compound. Pure YbRh$_2$Si$_2$

single crystals (CB101-03-kk147, 102-PW-KK, KK-CB108) used in this study have been grown and were characterized concerning their chemical composition, inclusion content and electrical transport properties down to 1.8 K in the course of this work.

Microwave experiments

In contrast to the high temperature region which is well accessible by spectrocopic techniques, the regime of finite, small magnetic fields at temperatures below 1 K was so far inaccessible: The lowest accessible temperature in ARPES experiments is about 1 K and NMR spectroscopy has been performed at temperatures well below 100 mK, but has been limited in the past to magnetic fields higher than the critical field of $YbRh_2Si_2$ [158, 207]. The spin dynamics in $YbRh_2Si_2$ at temperatures higher than 500 mK has already been investigated by ESR [131, 208, 209]. Recently it became possible to investigate the ESR of $YbRh_2Si_2$ near the QCP [210] and also spectroscopic microwave experiments concerning the electrical conductivity at GHz frequencies, have been performed on $YbRh_2Si_2$ utilizing superconducting stripline resonators. The experiments have been performed by K. Parkkinen and M. Scheffler (Uni Stuttgart) at temperatures and fields close to the QCP [176]. In a temperature range of $40 - 600$ mK and at magnetic fields of up to 140 mT the different electronic phases in a large $YbRh_2Si_2$ which became part of the resonator were probed with a set of different magnetic fields. Signatures of transitions between AFM, non-FL, and FL phases were clearly observed in the microwave response. Recently, angle-dependent measurements have been performed by L. Bondorf and M. Scheffler (Uni Stuttgart)[177] at 1.6 K, as a first step towards the investigation of the anisotropy in the electron-spin resonance in the low temperature region in future experiments.

Time-resolved investigation of the Kondo state using THz radiation

A completely new approach to investigate the time-development of the Kondo state became possible due to the work performed by Christoph Wetli, Manfred Fiebig (ETH Zurich) and Johann Kroha (Uni Bonn). It is known that THz measurements on metallic samples are hindered due to the high reflectivity of metals. Recently, C. Wetli investigated $CeCu_{6-x}Au_x$ (Kondo temperature $T_K \approx 8$ K) using THz radiation and was able to evaluate the extremely weak signal caused by the destruction and recreation of a quasiparticle [211]. First time-resolved measurements were also performed on $YbRh_2Si_2$. Here it turned out to be more difficult to separate the signal from the background: Due to the higher $T_K \approx 25$ K of $YbRh_2Si_2$, the respective signal appears closer to the main signal stemming from the conduction electrons [178]. This work will be continued further to explore the possibilities that open due to the new approach of these time-resolved measurements.

4

Ce($Ru_{1-x}Fe_x$)PO, ($x = 0 - 1.0$)

4.1 Introduction to the series Ce($Ru_{1-x}Fe_x$)PO

In the past during the search for ferromagnetic quantum criticality in a cerium based compound, CeRuPO attracted a lot of attention and was studied intensively [40, 66, 213]. The compound CeRuPO crystallizes in the tetragonal ZrCuSiAs-type structure, shown in Fig. 4.2, with the space group $P4/nmm$. The lattice parameters of the compounds LnTPO (lanthanide Ln = Ce, La; transition metal T = Ru, Fe) are summarized in Tab. 4.1. The layered ZrCuSiAs-type structure has a two dimensional character and is also the structure type of the 1111-iron pnictide superconductors which started to be investigated after the discovery of superconductivity in LaFePO with $T_c = 5\,\mathrm{K}$ in 2006 [214] and in fluorine-doped LaFeAsO with $T_c = 26\,\mathrm{K}$ in 2008 [215]. The compounds CeRuPO and CeFePO were synthezised in a polycrystalline form and their structure was characterized for the first time by Zimmer *et al.* [216]. The tetragonal CeRuPO orders ferromagnetically at $T_C = 15\,\mathrm{K}$ [40, 217] while in CeFePO a possible spin-glass transition at 750 mK found by ac susceptibility measurements and by muon spin experiments was reported by A. Jesche [218]. The Kondo temperature of CeRuPO determined from the entropy is $T_K \approx 10\,\mathrm{K}$ [40] and that of CeFePO is $T_K \approx 10\,\mathrm{K}$ [157] as well. It was shown that the ferromagnetism in CeRuPO turns into antiferromagnetism under pressure at about 2.8 GPa by Kotegawa *et al.* [219]. The existence of a tricritical point was proposed by Lengyel *et al.* [213] since the Néel temperature disappears abruptly around $p_c \approx 3\,\mathrm{GPa}$. The existence of a FM QCP in the substitution series Ce($Ru_{1-x}Fe_x$)PO was proposed by Kitagawa *et al.* [220] who investigated polycrystalline oriented powder samples of the Ce($Ru_{1-x}Fe_x$)PO series by ^{31}P NMR in a field of 0.5 T. They proposed the occurence of a FM QCP at $x_c = 0.86$. This observation is in contrast to the pressure studies on CeRuPO by Kotegawa *et al.* and it might be possible that a magnetic order, if present in the samples, was modified by the applied field during the NMR measurement. Polycrystalline as well as single crystals of the border system have already been investigated in the past by magnetization measurements. Polycrystalline CeRuPO shows Curie-Weiss behaviour at high temperatures with $\Theta_W = 8\,\mathrm{K}$ [217]. The magnetic anisotropy of high-quality single crystals was investigated by Krellner and Geibel [40] and yields the Weiss temperatures for $T \geq 150\,\mathrm{K}$ of $\Theta_W^{ab} \approx 4.2\,\mathrm{K}$, $\Theta_W^{c} \approx -250\,\mathrm{K}$ for $H \parallel c$ and $H \perp c$, respectively, and an effective magnetic moment of $\mu_{\mathrm{eff}} = 2.4\,\mu_{\mathrm{B}}$ for both field directions which is close to the theoretically determined value $\mu_{\mathrm{eff}}^{\mathrm{theo}} = 2.54\,\mu_{\mathrm{B}}$ for a free Ce^{3+} ion. The CEF scheme with a doublet ground state was determined in [172] utilizing

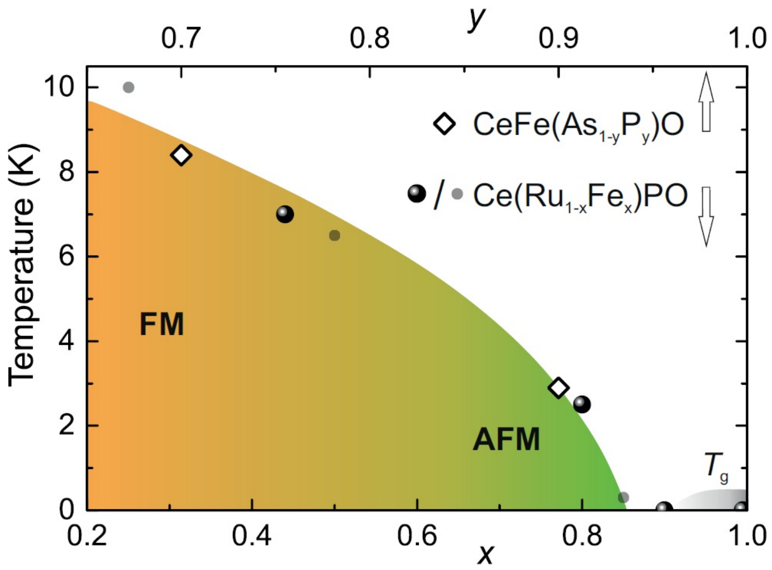

Figure 4.1: Ce(Ru$_{1-x}$Fe$_x$)PO and CeFe(As$_{1-y}$P$_y$)O: Combined $T-x$ phase diagram. In Ce(Ru$_{1-x}$Fe$_x$)PO, an AFM QCP occurs for $x = 0.85$. In the system CeFe(As$_{1-y}$P$_y$)O chemical pressure can be applied by the substitution of As by P. Here, metamagnetic behaviour indicating an AFM state appears for $y = 0.9$ K. Figure taken from [212] by courtesy of John Wiley & Sons, Inc.

the anisotropic magnetic properties as input. The magnetization at 2 K for $H \parallel c$ shows a hysteresis while for $H \perp c$ no hysteresis appears. The magnetization data suggest that below T_C, the magnetic moments align along the crystallographic c-direction [40]. The compound CeRuPO was studied in the past as it was supposed to exhibit a QCP which is a ferromagnetic one upon applying pressure or chemical doping.

4.2 Summary of the results and outlook

It is known that a QCP occurs in the series Ce(Ru$_{1-x}$Fe$_x$)PO for $x \approx 0.86$ but its nature was under debate at the beginning of this thesis. The result of our work was the successful growth and characterization of single crystals in the substitution series Ce(Ru$_{1-x}$Fe$_x$)PO with $x = 0, 0.44, 0.77, 0.86$ and 1.0 to provide high-quality samples for further studies of the putative FM QCP. Our magnetic characterization of the CeRuPO single crystals shows that we were able to reproduce the data reported before for the pure Ru compound [40]. In the case of CeRuPO, reducing the unit cell volume is possible by substituting Ru by the smaller Fe and the ordering temperature can be lowered by this substitution. Single crystals with an area of $\approx 1\,\mathrm{mm}^2$ and a thickness of a few μm of the series Ce(Ru$_{1-x}$Fe$_x$)PO have been grown from tin flux [221]. We optimized the parameters for the single crystal growth and performed a careful characterization of the obtained crystals in the substitution series by PXRD, EDX and magnetization measurements down to $T = 2$ K. Magnetization measurements on CeRuPO revealed ferromagnetic order below $T_C = 15$ K. Samples with $x = 0.44$ show order below $T \approx 8$ K and hysteresis effects in $M(H)$ which are strongly sample dependent. These samples are located in the cross-over region from ferromagnetic to antiferromagnetic order. Clear signatures of antiferromagnetic order below $T_{\mathrm{N}} = 3$ K have been found for samples with $x = 0.77$ while samples with $x = 0.86$ show no magnetic order down to $T = 2\,\mathrm{K}$. In combination with low-temperature measurements by A. Jesche and M. Brando our magnetization data yield that the ferromagnetic order turns into antiferromagnetic order for higher Fe concentrations in $Ce(Ru_{1-x}Fe_x)PO$. The $T - x$ phase diagram can be drawn according to Fig. 4.1 [212]. The data hint to the existence of an AFM QCP in this system at $x = 0.85$ which is consistent with previous pressure studies by Kotegawa *et al.* [219] but is not in accordance with the proposal of a FM QCP by Kitagawa *et al.* [220].

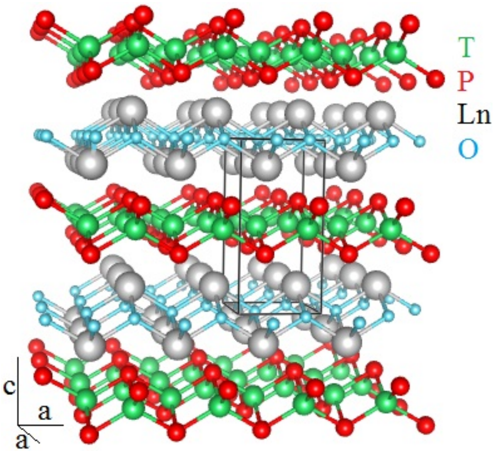

Figure 4.2: LnTPO crystal structure, space group $P4/nmm$

	a [Å]	c [Å]	Ref.
CeRuPO	4.026(1)	8.256(2)	[216]
CeFePO	4.01	8.64	[218]
	3.9176(17)	8.473(5)	this work SC analysis
LaRuPO	4.034(4)	8.356(0)	this work PXRD

Table 4.1: LnTPO: Lattice parameters

4.3 Single crystal growth from tin flux

To grow single crystals in the series $Ce(Ru_{1-x}Fe_x)PO$ the use of a flux consisting of elementary tin was necessary since these compounds contain phosphorous. Besides its high reactivity at low temperatures (sublimation at 416°C) phosphorous exhibits an extremely high vapour pressure (p(650°C)=133 bar) and the flux serves as low melting solvent. The single crystal growth and characterization of the border systems has been performed already successfully in the past - the growth of CeRuPO was described in detail in [40] and that of CeFePO by A. Jesche [218]. The reported growth conditions for the two compounds differ significantly with respect to the growth temperature as well as in the flux to sample ratio

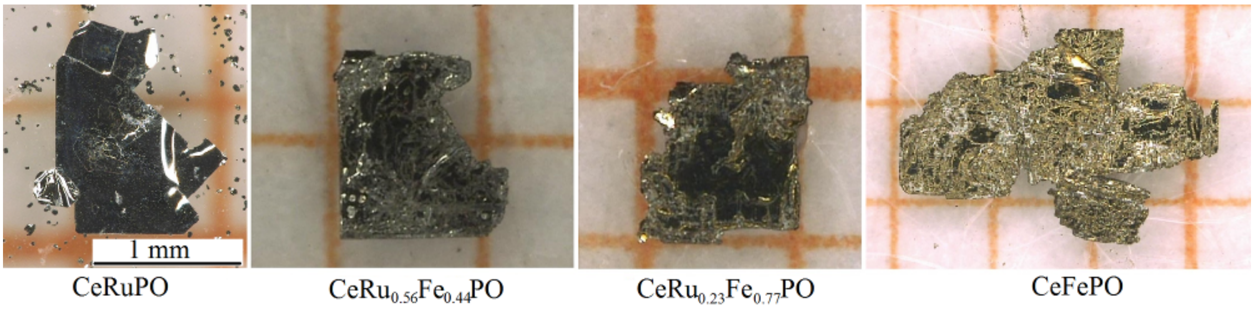

CeRuPO $CeRu_{0.56}Fe_{0.44}PO$ $CeRu_{0.23}Fe_{0.77}PO$ CeFePO

Figure 4.3: Single crystals of the $Ce(Ru_{1-x}Fe_x)PO$ series.

Growth No.	stoichiometry Ce : RuO_2 : P : Fe : SnO_2 : Sn	result	x nominal	x EDX
tb001	8 : 4 : 6 : 0 : 0 : 82	poly	0	0
tb016	2 : 0 : 2 : 1 : 1 : 4	SC, 2 mm × 3 mm	1.0	1.0
tb017	8 : 4 : 6 : 0 : 0 : 82	SC, 1 mm × 1 mm	0	0
tb019	2 : 0.4 : 2 : 0.6 : 0.6 : 4.4	SC, 1 mm × 1 mm	0.60	0.44
tb020	2 : 0.2 : 2 : 0.8 : 0.8 : 4.2	SC, 1 mm × 1.25 mm	0.80	0.77
tb021	2 : 0.15 : 2 : 0.85 : 0.85 : 4.15	SC, 1 mm × 1.25 mm	0.85	0.86

Table 4.2: Parameters of the crystal growth of $CeRu_{1-x}Fe_xPO$ and EDX analysis.

Growth No.	T_{max} [°C]	T_1 [°C]	T_2 [°C]	average cooling rate [K/h]	Ar flow [ml/min]
tb001	1000	-	500	3.6	–
tb016	1488	1425	890	4	150
tb017	1485	1426	920	4	152
tb019	1597	1538	1052	4.1	151
tb020	1591	1538	1061	4.1	150
tb021	1596	1537	1060	4.1	150

Table 4.3: Growth condition for the $CeRu_{1-x}Fe_xPO$ series.

which made an optimization necessary. This optimization of the growth parameters for the single crystal growth in the substitution series $Ce(Ru_{1-x}Fe_x)PO$ was performed by T. Ballé in the course of her Master's thesis [221]. The growth parameters are summarized in Tab. 4.2 and Tab. 4.3. Experiment tb001 has been carried out in a Nabertherm box furnace using a SiO_2 ampoule while for all other experiments a high-temperature GERO furnace (crucible system Al_2O_3 in Nb) was used. During heating with 50 K/h, a holding period of 5 h was included at 450°C to allow for the slow reaction of phosphorous with the tin flux. The maximum temperature T_{max} was held for $t_{hom} = 1$ h to ensure the complete homogenization of the melt followed by a fast lowering of the temperature to T_1. Between T_1 and T_2 the temperature was lowered slowly. The growth was terminated by a fast cooling step with ≈ 200 K/h. After the growth the tin flux was removed by etching in hydrochloric acid. In some experiments foreign phases like Ru_3Sn_7, RuP_2, $Ce_2Fe_{12}P_7$ or SnO_2 appeared which did not dissolve in HCl. The successful optimization yielded thin single crystal platelets for $x = 0, 0.44, 0.77, 0.86$ and 1.0 shown in Fig. 4.3 of an area up to several mm^2 and a thickness of a few micrometers.

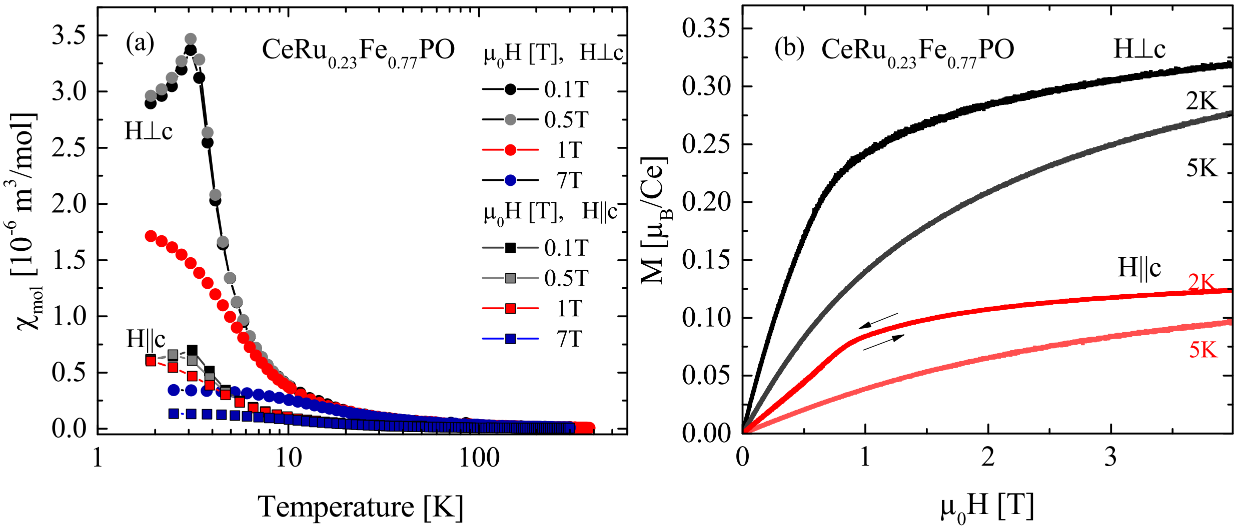

Figure 4.4: Ce(Ru$_{0.23}$Fe$_{0.77}$)PO single crystal (a) Molar susceptibility $\chi(T)$ at different fields. (b) Field dependence of the magnetization $M(B)$ at temperatures below and above the AFM phase transition at $T_\mathrm{N} = 3\,\mathrm{K}$.

4.4 Magnetization

The magnetization of the single crystals was measured using the VSM option of the PPMS. The field dependence of the magnetization of several Ce(Ru$_{1-x}$Fe$_x$)PO, $x = 0.44$ single crystals was investigated and strong sample dependencies were found, Fig. 4.5 (a). The samples of this batch order magnetically below $T \approx 8\,\mathrm{K}$ and show the cross-over from ferromagnetism close to the border system CeRuPO to an AFM order for higher Fe concentrations. Four samples with $x = 0.77$ that were investigated show AFM order. For $H \perp c$, the magnetic susceptibility, Fig. 4.4, (a), increases upon cooling down to the Néel temperature of $T_\mathrm{N} = 3\,\mathrm{K}$, and afterwards decreases rapidly for $\mu_0 H = 0.1\,\mathrm{T}$ and $0.5\,\mathrm{T}$. The magnetic transition is not as pronounced as for $H \perp c$ but also visible for $H \parallel c$. For both field directions, the magnetic transition is shifts to lower temperatures for higher fields which is a characteristic property of an antiferromagnet. Above $1\,\mathrm{T}$, no magnetic order is found down to $2\,\mathrm{K}$. The field dependence of the magnetization at $2\,\mathrm{K}$, depicted in Fig. 4.4, (b), shows a weak metamagnetic transition for $H \parallel c$ while for $H \perp c$ the increase is linear. The magnetization clearly shows the absence of FM order in the sample with $x = 0.77$ and a transition into the AFM state at $T_\mathrm{N} = 3\,\mathrm{K}$. Three samples with $x = 0.86$ were examined and show no order down to $T = 2\,\mathrm{K}$. The field dependence of the magnetization of one of the single crystals is shown in Fig. 4.5, (b).

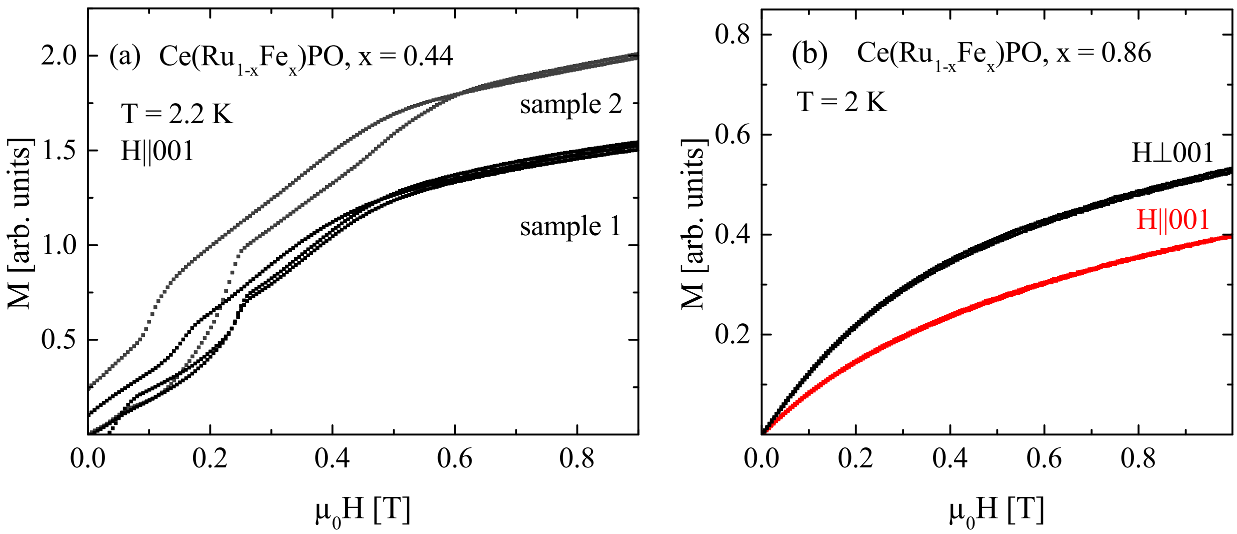

Figure 4.5: (a) Field dependence of the magnetization measured on two different $Ce(Ru_{0.56}Fe_{0.44})PO$ samples with $H \parallel 001$ at $T = 2.2\,K$. (b) Field dependence of the magnetization of a paramagnetic $Ce(Ru_{0.14}Fe_{0.86})PO$ single crystal for $H \parallel 001$ and $H \perp 001$ at 2 K. Due to the extremely low weight of the samples, no reliable absolute value of the magnetization can be given.

Growth No.	stoichiometry La : RuO_2 : P : Sn	result	duration h	T_{max} [$°C$]	T_2 [$°C$]	Ref.
1001	7 : 3.5 : 5.25 : 84.25	poly, SC 0.1 mm × 0.1 mm	130	985	500	[172]

Table 4.4: Parameters of the synthesis of LaRuPO in a quartz ampoule using a Nabertherm box furnace. While the main part of the synthezised material was polycrystalline some small single crystals (SC) were also found after removing the flux by etching with hydrochloric acid.

4.5 Synthesis and characterization of LaRuPO

To further investigate the pure compound CeRuPO concerning the magnetic (spin wave) and crystal-field excitations by INS several grams of polycrystalline material have been synthesized. Additionally, the non-magnetic LaRuPO as a phonon reference has been prepared. The parameters for the synthesis are summarized in Tab. 4.4. The elements were weight in non-stoichiometrically 4.4 and sealed in an evacuated quartz ampoule. The synthesis was performed in a Nabertherm box furnace. The furnace was heated up to $T_{max} = 985°C$ and cooled down slowly with a rate of 4 K/h to $T_2 = 500°C$. Afterwards the furnace was switched off leading to a cooling rate of $\approx 200\,K/h$. The flux was removed by etching in hydrochlorid acid.

5

LnT_2Si_2 ($Ln = Sm$, Gd, Ho; $T = Rh$, Ir)

5.1 Bulk and surface properties of materials with $ThCr_2Si_2$-type structure

In the following sections, the single crystal growth and characterization of tetragonal antiferromagnetic materials is described. In particular their surface related magnetic properties are subject of interest. In the first step, we characterize their bulk properties to provide a firm basis for the interpretation of the subsequent ARPES measurements. The materials with $ThCr_2Si_2$-type structure contain Ln ions and show local-moment magnetism due to the spatially localized character of the $4f$-wave functions. The magnetic moments of the Ln ions polarize the spins of the conduction electrons which mediate the magnetic exchange (RKKY interaction). Unlike cerium and ytterbium compounds, in which the Ln-$4f$ shell contains one electron or one electron hole with a non-magnetic configuration (Ce^{4+}/Yb^{2+}) close in energy to a magnetic one (Ce^{3+}/Yb^{3+}) and therefore can show the Kondo effect, the materials presented in this section show local-moment magnetism and no Kondo effect. In Tab. 5.1, an overview about the magnetic structures of related compounds containing Pr, Nd, Tb, Dy and Er is provided. For these compounds, the magnetic structures were determined by neutron diffraction which is hindered in the cases of Sm, Gd and Ho compounds due to their large absorption cross sections for neutrons. Consequently, the magnetic structures of the latter are usually not available in the literature. Accept for $HoRh_2Si_2$ [222], the physical properties of the compounds LnT_2Si_2 (Ln=Sm, Gd, Ho; T=Rh, Ir) were poorly documented and we therefore characterized them from the ground up in preparation of the ARPES studies. In materials where electronic surface states, like Dirac or Shockley states [108, 109, 111, 112], arise these states can be investigated by spectroscopic techniques like ARPES at the surface of the single crystals. The aim is to find materials which possess electronic surface states and to identify control parameters by which these could be manipulated to open a path for future application. In Sec. 5.3 and Sec. 5.4, the growth of the single crystals and their characterization by PXRD, EDX and Laue method is described. The results of the electrical transport, heat capacity and magnetization measurements are shown in Sec. 5.5 to Sec. 5.9 separately for each compound.

5.2 Summary of the results and outlook

We have grown single crystals of materials containing different lanthanide ions where the occurrence of electronic surface states was predicted by band structure calculations. To perform ARPES experiments the requirements on the purity of the single crystals are high since only samples with a low amount of crystal defects allow for a high resolution of the measured data. Another criterion besides the purity is the sample size. The single crystals should have a thickness of about $200\,\mu$m and a minimum area of 2×2 mm. We therefore optimized the growth parameters with respect to the largest single crystal size and the highest possible purity in our crystal growth experiments. Finally, we obtained large single crystal platelets with an area of up to $12\,\mathrm{mm}^2$ and a thickness of $50-300\,\mu$m. The growth procedure which was originally developed for the growth of $YbRh_2Si_2$ from indium flux turned out to be quite robust and could be adapted for the growth of the related compounds by small variation of the growth parameters. We have successfully grown single crystals of these compounds from indium flux for the first time. Their purity was characterized by determining the residual resistivity ratio $RR_{1.8\,\mathrm{K}}$ for each compound. We obtained for all compounds, except for $HoRh_2Si_2$, $RR_{1.8\,\mathrm{K}} \geq 25$ with $j \perp c$. Their thermodynamic and anisotropic electrical transport and magnetic properties, which were not known before, have been studied in this work [223]. A summary of some physical properties can be found in Tab. 5.2. In contrast to Pr, Nd, Tb, Dy and Er compounds, the study of compounds containing Sm, Gd or Ho by neutron scattering experiments is hindered due to the high absorption cross section of the Ln ion [224]. We therefore obtained information on their magnetic properties through bulk magnetization measurements. Additionally, in the case of $GdRh_2Si_2$ RIXS was used to investigate its magnetic structure in collaboration with K. Kummer [225].

The paramagnetic resonance was studied in collaboration with J. Sichelschmidt [226] and as a follow up, it was found that in the ordered regime the rotation of the AFM order parameter driven by an external rotating field can be traced by ESR [227].

ARPES revealed two-dimensional electron states at the Si-terminated surface of $GdRh_2Si_2$. These Dirac and Shockley surface states exhibit itinerant magnetism and their spin splitting arises from a strong exchange interaction with the ordered Gd 4f moments [115]. The surface states in $HoRh_2Si_2$ are affected by the electromagnetic exchange interaction (RKKY) as well as by the spin-orbit coupling. The study revealed that the temperature can be used as a tuning parameter for the surface magnetism since the temperature dependent changes in the moment orientation in the bulk reflect in the surface properties [116]. ARPES studies revealed that for Sm ions in $SmRh_2Si_2$, the electronic properties of bulk and surface are rather similar and the Sm ions behave in both cases slightly mixed valent. Their mean valence was estimated to be about 2.94 at $T = 10\,\mathrm{K}$ [114]. Such a reduction of the valence of the Sm ion might be caused by a Kondo screening but our characterization of the bulk properties of this compound did not show any signatures of the Kondo effect in $SmRh_2Si_2$. The electronic states of the compounds were investigated by ARPES in collaboration with D.V. Vyalikh and coworkers.

	T_N [K]	$\vec{k}$ $T_\mathrm{N2} < T < T_\mathrm{N}$	T_N2 [K]	$\vec{k}$ $T < T_\mathrm{N2}$	moment orientation	ref.
$PrRh_2Si_2$	68	(0 0 1)	–	–	$\parallel c$	[228]
$PrIr_2Si_2$	45.5	(0 0 5/6)	23.7	(001)	–	[229]
$NdRh_2Si_2$	56	(0 0 1)	–	–	$\parallel c$	[230]
$NdIr_2Si_2$	33		18	(0 0 1)	$\parallel c$	[231]
$TbRh_2Si_2$	98 ± 2	(0 0 1)	–	–	$\parallel c$	[232]
$TbIr_2Si_2$	72 ± 3	(0 0 1)	–	–	$\parallel c$	[232]
$DyRh_2Si_2$	52 ± 2	(0 0 1)	18	(0 0 1)	$\parallel c$ canted $\approx 19°$ below T_N2	[233]
$DyIr_2Si_2$	40 ± 3	(0 0 1)	–	–	$\parallel c$	[234]
$ErRh_2Si_2$	12.8 ± 2	(0 0 1)	–	–	$\perp c$	[230]
$ErIr_2Si_2$	10 ± 3	(0 0 1)	–	–	$\perp c$	[233]

Table 5.1: $LnRh_2Si_2$ and $LnIr_2Si_2$ ($I4/mmm$): Magnetic order below T_N with magnetic propagation vector $\vec{k}$ determined by neutron diffraction. In some compounds, a second magnetic ordered phase was found below T_N2.

	T_N [K]	T_N2 [K]	γ_0 $[\frac{\mathrm{mJ}}{\mathrm{molK}^2}]$	$\mu_\mathrm{eff}^\mathrm{exp}$ $[\mu_\mathrm{B}]$	$\mu_\mathrm{eff}^\mathrm{theo}$ $[\mu_\mathrm{B}]$	$RR_{1.8\mathrm{K}}^{j\parallel c}$ $RR_{1.8\mathrm{K}}^{j\perp c}$	a/c	reference
$GdRh_2Si_2$	107	-	3	8.28	7.94	6 23	0.405	[223], this work
$SmRh_2Si_2$	64	-	8	-	0.85	10 25	0.404	this work
$HoRh_2Si_2$	29	11.8	39	11.1	10.6	8.3 14.5	0.406	[235], this work
$GdIr_2Si_2$	86	-	27	8.26 ($B \parallel 001$)	7.94	18 30	0.409	this work
$HoIr_2Si_2$	22	-	37	10.64 ($B \parallel 001$)	10.6	12 29	0.410	this work

Table 5.2: Summary of some properties of the compounds LnT_2Si_2 with the space group $I4/mmm$.

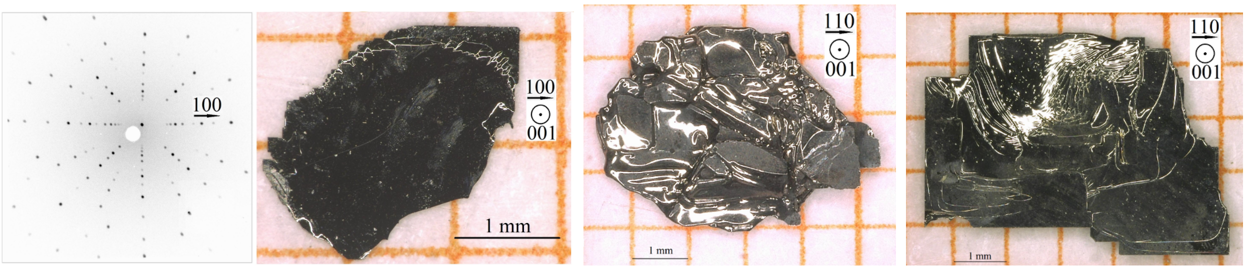

Figure 5.1: $LnRh_2Si_2$ single crystals. *Left:* $SmRh_2Si_2$ with Laue pattern. The pattern shows the fourfold symmetry of the tetragonal lattice. Sharp reflections indicate the high crystallinity of the single crystal. *Middle:* $GdRh_2Si_2$. *Right:* $HoRh_2Si_2$.

5.3 Single crystal growth from indium flux

No successful single crystal growth of $SmRh_2Si_2$, $GdRh_2Si_2$, $GdIr_2Si_2$ and $HoIr_2Si_2$ had been reported in the literature at the beginning of this work. The single crystal growth of $HoRh_2Si_2$ by applying the Czochralski method without specifying the parameters in detail was reported by Shigeoka *et al.* [235]. We have grown $LnRh_2Si_2$ (Ln = Sm, Gd, Ho) single crystals from In flux as described in [168, 223]. The ideal initial stoichiometry for a crystal growth experiment is influenced by the solubility of the starting materials in the flux. For $YbRh_2Si_2$ the careful optimization of the stoichiometry was described in [168], but since the solubility of Yb and Sm (Gd, Ho) in In is different we did not use the composition that was found to be ideal for the growth of the Yb compound. Instead, the initial weight of Sm (Gd, Ho), Rh (Ir) and Si was chosen to be stoichiometric for the first experiments together with 96 at% In. This elements-flux ratio was used in analogy to that reported for $YbRh_2Si_2$ [168]. We found that this indium-flux method is quite robust. It can be adapted to grow many related compounds by using only slightly changed growth parameters. These parameters of the crystal growth and the temperature-time profiles for the experiments can be found in Tab. 5.3 and Tab. 5.4 for the rhodium compounds, and in Tab. 5.6 and Tab. 5.5 for the iridium compounds. The temperature profile was chosen in analogy to that reported for $YbRh_2Si_2$ and optimized accordingly. For the growth of some compounds, not only the temperature-time profile has been optimized but also the stoichiometry of the initial weight. All experiments have been performed in the high-temperature GERO furnace. The furnace was heated up to the maximum furnace temperature of $T_{\mathrm{max}} = 1550°\mathrm{C}$ with a rate of 300 K/h. After a homogenization period of 1 h the furnace was moved upwards applying a fast-move period ($v = 100\,\mathrm{mm/h}$) in the first and a slow-move period ($v = 1\,\mathrm{mm/h}$) in the second step. The first step was done to lower the temperature quickly to T_1 after the homogenization of the melt and to avoid the long exposure at a high temperature which might lead to an enhanced pollution of the melt with crucible material graphite. During the slow-move period, the crystal growth took place. This step was terminated at T_2. Afterwards, the furnace was cooled down with 200 K/h to room temperature. For the iridium compounds, the cooling was performed with a lower cooling rate ($\Delta T = 50\,\mathrm{K/h}$) than for the rhodium compounds ($\Delta T = 200\,\mathrm{K/h}$). The idea was to include an annealing period and to obtain crystals in the low-temperature $ThCr_2Si_2$-type crystal structure $I4/mmm$. The indium flux was removed from the single crystals by etching with 32% hydrochloric acid. The investigation of the resulting crystals (PXRD, EDX) revealed the formation of $SmRh_2Si_2$, $GdRh_2Si_2$ and $HoRh_2Si_2$ besides a binary RhIn compound. The analysis of the PXRD pattern of the iridium compounds yielded that we obtained $GdIr_2Si_2$ and $HoIr_2Si_2$ in the $ThCr_2Si_2$-type crystal structure. The single crystals had a platelet-like habitus. Their dimensions can be found in Tab. 5.7.

- The $SmRh_2Si_2$ growth experiments yielded thin single crystal platelets. These platelets have been partly covered by a crystalline layer of a secondary phase. The EDX analysis showed that this layer consists of Rh and Si. Besides these thin single crystal platelets, in some experiments also a polycrystalline part formed at the bottom of the crucible from which some larger single crystal grains could be extracted. Growth 801 yielded several single crystal grains with $d = 0.8\,\mathrm{mm}$ and $m = 9\,\mathrm{mg}$ and growth 804 with $d = 0.9\,\mathrm{mm}$ and $m = 20\,\mathrm{mg}$.

- The $GdRh_2Si_2$ single crystals had a platelet-like habitus and an $\mathrm{RR}_{1.8\mathrm{K}} = 25$. The first crystals had an average thickness of $d = 15\,\mu\mathrm{m}$ which is much thinner compared to $YbRh_2Si_2$ single crystals grown with the same method. To approach the required sample thickness of about $200\,\mu\mathrm{m}$, the crystal growth was optimized and the optimization of the temperature-time profile yields single crystals with an up to 60 times larger mass compared to the starting experiment.

- Single crystals of $HoRh_2Si_2$ could be grown with a high yield after extension of the slow-move period towards a higher ($T_1 = 1530°\mathrm{C}$) as well as a lower temperature ($T_2 = 1065°\mathrm{C}$).

- The first growth experiment of $GdIr_2Si_2$, where the initial charge was composed stoichiometrically, yielded phase pure polycrystalline material as well as a few small single crystals of $\approx 3\,\mathrm{mg}$. The change of the initial stoichiometry to the ratio Gd : Ir : Si = 11 : 9 : 9 increased the weight of the single crystals to $\approx 7\,\mathrm{mg}$ but the increase of the Gd content in the initial melt led to the formation of single crystals which crystallized partially in the high-temperature phase (HTP), $P4/nmm$. It was not possible to transform these single crystals into the low-temperature phase (LTP) during one week of annealing in an evacuated quartz ampoule at $T = 1000°\mathrm{C}$, in contrast to the successful transformation of $CeIr_2Si_2$ by Niepmann *et al.* [236]. Although the PXRD patterns prove the absence of the HTP in the single crystals, the obtained ARPES spectra do not show sharp electronic bands. The reason might be that the transformation from the HTP to the LTP in the single crystals is not finished and traces of the HTP are still present. The complete avoidance of conditions where the HTP forms seems to be key to provide crystals for spectroscopic studies. This will be a task for future growth experiments.

- The first growth experiments of $HoIr_2Si_2$ yielded phase pure polycrystalline material in the LTP and only a few small single crystals. Here, a significant enlargement of the single crystal sizes was obtained by the optimization of the temperature-time profile and an upscaling of the initial weight.

$SmRh_2Si_2$ Growth No.	stoichiometry Sm:Rh:Si	T profile No.	remarks	d [μm]	m [mg]	$RR_{1.8K}$ $j \perp c$
801*	1:2:2	Sm01	Rh_3In_7	20	0.4	25
802	1:2:2	Sm02	Rh_3In_7 + layer	< 15	< 0.4	-
803	1:2:2	Sm01	Rh_3In_7 + layer	60 - 70	1	-
804	1:2:2	Sm03	Rh_3In_7 + Rh-Si layer	20 - 30	0.5	-
$GdRh_2Si_2$ Growth No.	stoichiometry Gd:Rh:Si					
301	1:2:2	Gd01	-	15	0.45	25
302	1:2:2	Gd02	-	650	9.1	21
303*	1:2:2	Gd03	initial charge doubled	575	26.5	24
304*	1:2:2	Gd03	same charge as 303	610	25	-
305*	1:2:2	Gd03	same charge as 303	635	24.3	-
$HoRh_2Si_2$ Growth No.	stoichiometry Ho:Rh:Si					
501	1:2:2	Ho01	-	28	2.8	–
502*	1:2:2	Ho02	initial charge doubled	295	10.8	14.5

Table 5.3: Parameters of the crystal growth of the $LnRh_2Si_2$ compounds. d is the shortest dimension of the platelets and m is the average mass. Both were determined by taking the average over 10 single crystals. The parameters of the T profiles can be found in Tab. 5.4. The experiments which gave the best result with respect to the crystal size and purity are marked by an asterisk.

T profile No.	furnace	$T_{\max}$ [°C]	T_1 [°C]	v [mm/h]	T_2 [°C]	duration [h]
Sm01*	GERO	1550	1505	1	1270	88
Sm02	GERO	1550	1535	1	1075	160
Sm03	GERO	1550	1505	1	1075	121
Gd01	GERO	1550	1475	1	1230	85
Gd02	GERO	1550	1500	1	1010	157
Gd03*	GERO	1550	1520	1	1070	157
Ho01	GERO	1550	1515	1	1340	72
Ho02*	GERO	1550	1530	1	1065	157

Table 5.4: Measured parameters of the temperature-time profiles of the crystal growth for the $LnRh_2Si_2$ compounds.

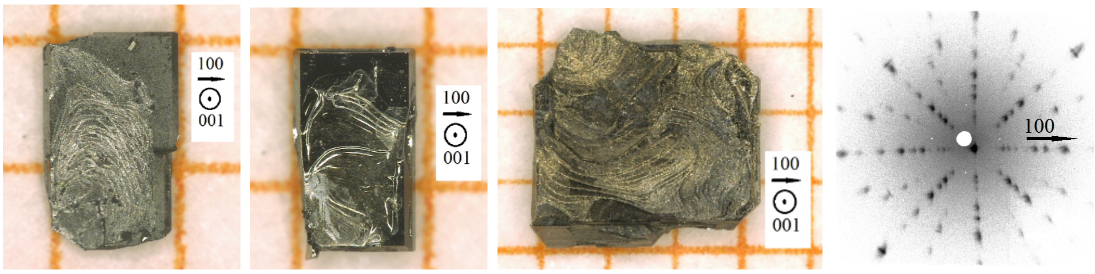

Figure 5.2: *Left:* $GdIr_2Si_2$ single crystal ($I4/mmm$). *Middle:* $GdIr_2Si_2$ single crystal from growth 1103. The crystals from this batch crystallized partially in the high-temperature phase ($P4/nmm$). Right: $HoIr_2Si_2$ single crystal ($I4/mmm$) and Laue pattern showing the fourfold symmetry of the tetragonal lattice. The Laue patterns of the Ir compounds show less sharp spots than of the Rh compounds, compare Fig. 5.1, indicating their poorer crystallinity.

T profile No.	furnace	$T_{\max}$ [°C]	T_1 [°C]	v [mm/h]	T_2 [°C]	duration [h]
GdIr01	GERO	1550	1520	1	1010	160
GdIr02*	GERO	1550	1530	1	1070	160
GdIr03	GERO	1550	1535	1	1080	160
HoIr01	GERO	1600	1564	1	1400	99
HoIr02	GERO	1550	1525	1	1050	160
HoIr03	GERO	1550	1515	1	1380	160
HoIr04*	GERO	1550	1535	1	1090	160

Table 5.5: Measured parameters of the temperature-time profiles of the crystal growth for the $LnIr_2Si_2$ compounds.

$GdIr_2Si_2$ Growth No.	stoichiometry Gd:Ir:Si	T profile No.	remarks	d [μm]	m [mg]	$RR_{1.8K}$ $j \perp c$
1101	1:2:2	GdIr01	polycrystalline, few crystals $I4/mmm$	250 - 400	3.0 - 3.5	–
1102*	1:1:1	GdIr02	single crystals 2×2 mm^2 $I4/mmm$	180 - 200	10 - 20	30
1103	11:9:9	GdIr03	single crystals 1.5×1 mm^2 $P4/nmm$ (62%) $I4/mmm$ (38%)	300	5 - 7	–
$HoIr_2Si_2$ Growth No.	stoichiometry Ho:Ir:Si					
901	1:2:2	HoIr01	polycrystalline, few platelets	100 - 150	0.3	–
902	1:2:2	HoIr02	polycrystalline, few platelets	120 - 160	0.6	–
903	1:2:2	HoIr03	polycrystalline, platelets 1×1 mm^2	120 - 150	1.5 - 2	–
904*	1:2:2	HoIr04	upscaled, platelets 2×3 mm^2	400 - 650	32	29

Table 5.6: Parameters of the crystal growth of the $LnIr_2Si_2$ compounds. d is the shortest dimension of the platelets and m is the average mass. Both were determined by taking the average over 10 single crystals. The parameters of the T profiles can be found in Tab. 5.5. The experiments which gave the best result with respect to the crystal size and purity are marked by an asterisk.

5.4 Structural and chemical characterization

$LnRh_2Si_2$

The compounds $LnRh_2Si_2$ crystallize in the tetragonal body-centered $ThCr_2Si_2$-type structure ($I4/mmm$) which consist of layers of edge sharing RhSi tetrahedra alternating with Ln atoms. The structure type is quite common among compounds with the chemical notation AT_2X_2 (A = alkaline metal, lanthanide or actinide, T = transition metal, X = element with metallic and/or non-metallic properties). Silicides in this structure type show a large variety of physical properties such as superconductivity ($CeCu_2Si_2$ [9], $YbRh_2Si_2$ [11]), hidden-order (URu_2Si_2 [237]) or quantum critical behaviour ($YbRh_2Si_2$ [169]).

$LnIr_2Si_2$ polymorphism

The compounds $LnIr_2Si_2$ crystallize in two structure types, namely the tetragonal body-centered $ThCr_2Si_2$-type structure ($I4/mmm$) and the primitive $CaBe_2Ge_2$-type structure ($P4/nmm$). Both structure-types can be deduced from the $BaAl_4$ structure, but in the HTP the order of two layers of Ir and Si is changed which leads to a reduced symmetry in the structure. The $ThCr_2Si_2$-type structure is the LTP and the $CaBe_2Ge_2$-type structure is the HTP. The HTP can be transformed into the LTP by annealing, as reported for $CeIr_2Si_2$ by Niepmann and Pöttgen [236]. Here, annealing at $T = 870\,\mathrm{K}$ enclosed in evacuated silica tubes for two weeks led to the complete transformation of β-$CeIr_2Si_2$ (HTP) into α-$CeIr_2Si_2$ (LTP). Polymorphism in AIr_2Si_2 (A = lanthanide) was also already found and is well documented for a large number of compounds, among them for instance $YbIr_2Si_2$, $LaIr_2Si_2$, $GdIr_2Si_2$ and $HoIr_2Si_2$ [238, 239]. In the past, the cleavability of Ir-compounds like $YbIr_2Si_2$ was not as good as that of the respective Rh compound. The reason for that might be the existence of the high-temperature phase for the Ir compounds which might hinder the cleavability, if the transformation to the low temperature phase is incomplete. We therefore carefully checked the crystal structure by PXRD to ensure the complete transformation of the single crystals into the low-temperature structure.

PXRD

Powder x-ray diffraction measurements on the $LnRh_2Si_2$ and the $LnIr_2Si_2$ compounds confirmed the $I4/mmm$ tetragonal structure. The lattice constants of $SmRh_2Si_2$, $GdIr_2Si_2$ and $HoIr_2Si_2$ which show a large spread in the documented values or are poorly characterized in the literature were determined and can be found in Tabs. 5.8, 5.9 and 5.12, respectively. A single crystal structural analysis was performed on $GdIr_2Si_2$ and $HoIr_2Si_2$ to determine the Si z-position in the structure. The result is shown in Tab. 5.10 and Tab. 5.13.

W. Bazela analyzed the crystal and magnetic structure parameters in LnT_2X_2 compounds and found that for the ratio of the lattice constants $a/c < 0.415$ collinear magnetic structures occure while above this value modulated structures are observed [240] . In Tab. 5.2 the a/c ratios for the Rh and Ir compounds are summarized and in all cases $a/c < 0.415$ which hints to collinear magnetic structures in these compounds.

LnT_2Si_2	d/l [mm/mm]	face 1	face 2	face 3
$SmRh_2Si_2$	0.02/3	{001}	{100}	{110}
$GdRh_2Si_2$	0.6/3.5	{001}	{110} 80%, {100} 20%	{100} 80%, {110} 20%
$HoRh_2Si_2$	0.25/4	{001}	{110}	{100}
$YbRh_2Si_2$	0.2/3	{001}	{110} 80%, {100} 20%	{100} 80%, {110} 20%
$GdIr_2Si_2$	0.35/1.1	{001}	{100}	{110}
$HoIr_2Si_2$	0.65/2.8	{001}	{100}	{110}

Table 5.7: LnT_2Si_2 ($I4/mmm$): Naturally grown faces; face 1 is the largest and face 3 is the smallest face. d is the thickness in mm averaged over ten single crystals and l is the largest extension in mm perpendicular to d of the single crystals.

EDX

The chemical composition determined by EDX microprobe analysis revealed (20±1)at.% Ln, (40±1)at.% Rh and (40±2)at.% Si. We cannot exclude some Rh-Si site exchange within these error bars; however, for the related compound $YbRh_2Si_2$ a detailed structural and chemical analysis was conducted by highly accurate X-ray diffraction and wavelength dispersive X-ray spectroscopy measurements [241]. There, it turned out that the structure accepts some Rh-Si site exchange, with a rather small homogeneity range for Rh, which was found to be $40.0 - 40.2$ at.%.

X-ray Laue

In preparation of the single crystals for the physical characterization their orientation was determined using the Laue method. The Laue pattern of a tetragonal single crystal shows a symmetric pattern of reflections. The symmetry of the Laue pattern reflects the symmetry of the crystal structure. Although no quantitative statement about the crystallinity can be made from the comparison of different Laue patterns, qualitative observations give useful information. Sharp Laue reflections indicate a high crystallinity of the investigated sample. The Laue pattern of flux-grown single crystals usually show extremely sharp Laue spots since the single crystals grew freely in the flux without any force acting on them. In the course of this work it turned out, that Laue pattern from $LnRh_2Si_2$ show sharp reflections as expected. In contrast, the reflections in the Laue pattern of $LnIr_2Si_2$ ($I4/mmm$) crystals were much broader and washed out for all investigated single crystals. This is probably due to the fact that a transformation from the HTP to the LTP took place during the growth which led to a distorted lattice.

All single crystals grown from indium flux exhibit naturally grown faces. The existence of faces leads to conclusions about the growth velocity of the respective faces of a single crystal [28]. This is due to the fact that the fast growing faces disappear and the slow growing persist. For the different LnT_2Si_2 compounds we summarize the occuring faces and also determined the frequency of the occurence of the in-plane faces in Tab. 5.7. In the course of this work, more than 350 single crystals have been oriented. Most of them in preparation of the spectroscopic measurements.

a[Å]	c[Å]	V[Å^3]	Reference
4.05(4)	10.0(3)	164.8	[247], [248]
4.042	10.01	163.5	[251]
4.051(2)	10.020(7)	164.5	[249],[250]
4.055(5)	10.040(2)	165.1	this work

Table 5.8: Lattice parameters of SmRh$_2$Si$_2$ ($I4/mmm$).

5.5 SmRh$_2$Si$_2$

Sm-based compounds have been studied rarely in the past compared to compounds containing lanthanide ions like Ce, Eu, Gd, Ho or Yb, but the recent discovery of topologically insulating behaviour in SmB$_6$ [242–244] renewed the interest in the community in Sm-based compounds in general. Some Sm compounds exhibiting strongly correlated electron behaviour like the heavy-fermion compounds SmOs$_4$Sb$_{12}$ [245] or SmT$_2$Al$_{20}$ [246] have a complex crystallographic structure and the characterization of systems with lower complexity is highly desired. At the beginning of this work, the crystal structure of SmRh$_2$Si$_2$ was already known [247, 248] and an isothermal section ($T = 870\,$K) of the ternary Sm-Rh-Si phase diagram had been explored by Morozkin *et al.* [249, 250]. Susceptibility measurements as well as electrical resistivity measurements on polycrystalline samples had been reported by different authors: Signatures of magnetic transitions in the susceptibility at 62, 35 and 10 K and a kink in the resistivity at 60.5 K were observed by Kochetkov *et al.* [251]. Felner and Nowik reported about peaks in the susceptibility at $8 \pm 2\,$K and $46 \pm 2\,$K [248]. From these reported data, the determination of the precise value of the Néel temperature was not possible.

Heat capacity and entropy

In Fig. 5.3 specific-heat data are shown for the two related materials SmRh$_2$Si$_2$ and LuRh$_2$Si$_2$. The latter serves as a non-magnetic reference system with a completely filled $4f-$shell. The LuRh$_2$Si$_2$ data were taken from Ref. [252]. For SmRh$_2$Si$_2$ a pronounced and sharp λ-type anomaly is observed at $T_{\mathrm{N}} = 64\,$K, establishing a second order phase transition into the AFM ordered phase. For $T < 6\,$K the specific heat of SmRh$_2$Si$_2$ fits to $C/T = \gamma_0 + \beta T^2$ (cf. inset (b) of Fig. 5.3) with the Sommerfeld coefficient $\gamma_0 \approx 8$mJ/(molK^2). A Debye temperature of $\Theta_D \approx 460\,$K can be calculated from the slope β according to $\beta = 12 \cdot 5\pi^4 R/(5\Theta_D^3)$ but β certainly is not only influenced by the phonon contribution to the specific heat but also by a magnon contribution since it was determined in the ordered phase. The phonon and a possible magnon contribution to the specific heat can not be separated since their temperature dependence is the same in this 3D AFM material. The determined Debye temperature therefore is too large and not reliable.

Fig. 5.3 shows that the magnetic part of the entropy of the system increases up to the phase transition and increases further towards higher temperature. The Sm ion with $J = 5/2$ has 6 possible states and without the presence of CEF effects the entropy would amount to $S^{4\mathrm{f}} = R\ln 6$ at the phase transition. By subtracting the heat capacity of the non-magnetic

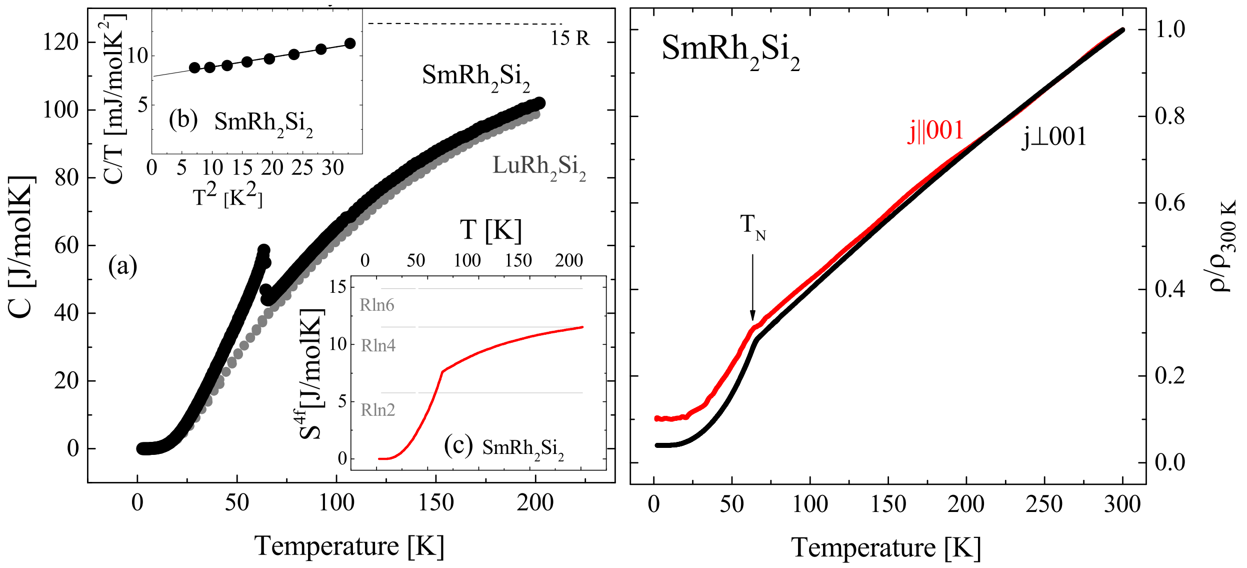

Figure 5.3: *Left:* (a) Specific-heat data as function of temperature for a single crystal of SmRh$_2$Si$_2$ and polycrystalline LuRh$_2$Si$_2$ (from Ref. [252]). Inset (b) enlarges the low-temperature part of the specific heat of SmRh$_2$Si$_2$, plotted as C/T versus T^2. From a linear fit below $T = 6\,\mathrm{K}$, the Sommerfeld coefficient and the Debye temperature was extracted. Inset (c) shows the magnetic entropy. *Right:* Temperature dependence of the normalized resistivity $\rho(T)/\rho(300\,\mathrm{K})$ for $j \parallel c$ and $j \perp c$. At $\mathrm{T_N} = 65\,\mathrm{K}$ the onset of antiferromagnetic order is indicated by kinks in the curves for both current directions.

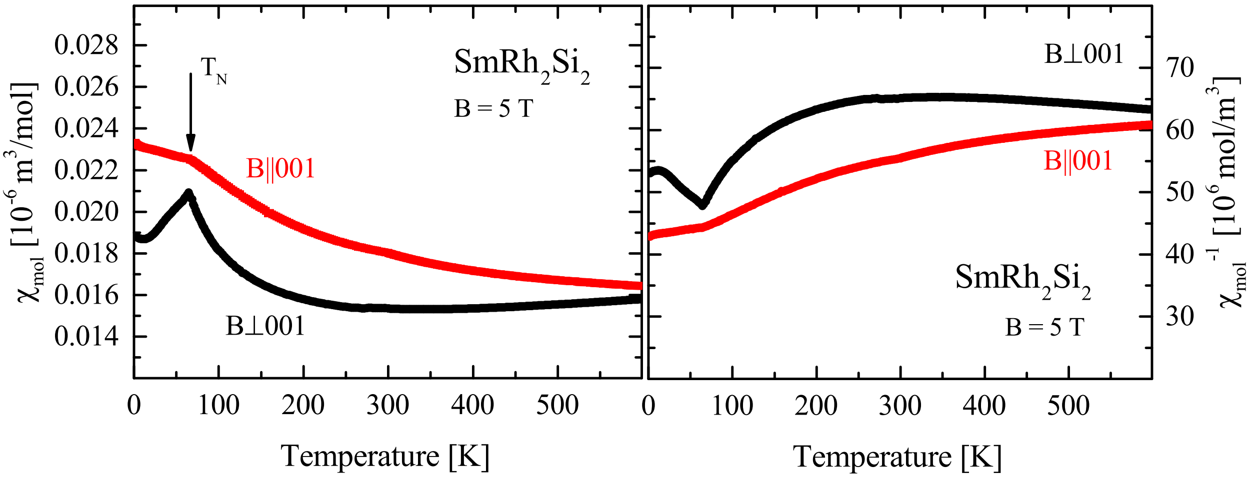

Figure 5.4: SmRh$_2$Si$_2$ *Left:* Susceptibility $\chi(T)$ as a function of temperature for $B \parallel 001$ and $B \perp 001$. *Right:* The inverse susceptibility $\chi^{-1}(T)$, does not show Curie-Weiss behaviour at high temperatures.

reference compound $LuRh_2Si_2$ [252] we obtained the magnetic part of the specific heat C^{4f} and by integrating C^{4f}/T the entropy which is connected to the magnetic part of the heat capacity. We find that the entropy is larger than $R\ln 2$ at the phase transition which shows that besides the ground state doublet also the occupation of higher levels contributes to the entropy. At the Néel temperature only half of the expected value of $R\ln 6$ is reached, Fig. 5.3 left panel, inset (c).

Electrical resistivity

Electrical transport data, Fig. 5.3, right panel, show anisotropic behaviour for current flow parallel and perpendicular to the [001]-direction below T_N. We determined $RR^{j\|c}_{1.8\,\mathrm{K}} = 10$ and $RR^{j\perp c}_{1.8\,\mathrm{K}} = 25$. The absolute value of $\rho(T)$ at room temperature for the in-plane resistivity was about $80\,\mu\Omega$cm. For better comparison of the data with $j \parallel c$ and $j \perp c$, we present the normalized resistivity $\rho(T)/\rho_{300\,\mathrm{K}}$. For both directions, the resistivity shows a linear-in-T behaviour from 300 K to the AFM phase transition. Upon cooling, at T_N a change of the slope of the resistivity curves occurs and the decrease of the resistivity becomes stronger. In previous work, $\mathrm{RRR} = \rho_{200\mathrm{K}}/\rho_0 \sim 5$ was determined for polycrystalline material [251]. The residual resistivity ratios $\mathrm{RRR} = \rho_{300\mathrm{K}}/\rho_0 \sim 25$ (corresponding to $\mathrm{RRR} = \rho_{200\mathrm{K}}/\rho_0 \sim 17.5$) determined on our samples for $j \perp c$ shows that we succeeded in growing high-quality crystals using an indium flux.

Temperature dependence of the magnetization

The magnetic moment of the Sm ions in $SmRh_2Si_2$ is small and the signal often is dominated by the background contribution. We therefore studied this material by using large single crystals with a mass of about 30 mg. The temperature dependent magnetization measurements up to 600 K have been carried out by J. Banda and M. Brando (MPI CPfS). In Fig. 5.4, the temperature dependence of the susceptibility for a field of $B = 5\,\mathrm{T}$ along two main symmetry directions is shown. Upon cooling, the transition into the AFM-ordered state appears at the Néel temperature $T_\mathrm{N} = 65\,\mathrm{K}$. For $B \perp c$, the susceptibility decreases strongly below T_N and shows a small increase at lowest temperatures. This feature varies from sample to sample and is probably caused by a paramagnetic defect contribution. The comparison of the susceptibility curves for both field directions yield that below T_N the magnetic moments are ordered within the basal plane of the tetragonal lattice. Additionally, our data shows the absence of further magnetic transitions which were proposed by [247] and [251] in previous works. The inverse susceptibility as shown in the right panel of Fig. 5.4 up to $T = 600\,\mathrm{K}$ does not exhibit Curie-Weiss behaviour and it is a well known fact, that for Sm compounds often Van-Vleck-like paramagnetic contributions to the magnetization occur [55].

Sm has the electronic configuration [Xe] $4\mathrm{f}^6\ 6\mathrm{s}^2$ and according to Hund‘s rules a Sm^{3+} ion ($4f^5$ configuration) has $L = 5$, $S = 5/2$, $J = L - S = 5/2$. In contrast, a Sm^{2+} ion ($4f^6$ configuration) has $L = 3, S = 3, J = L - S = 0$. For Sm^{2+} ions the ground state with $J = 0$ would not cause any paramagnetic effect. In this case Van Vleck contributions from higher levels would be the only contribution to the susceptibility [54]. In our case, ARPES experiments led to the conclusion that the deviation from the 3+ valence of the Sm ions in the bulk and at the surface is small. The mean valence was estimated to be about 2.94 at 10 K [114]. Hund‘s rules allow for the prediction of the ground state of a Sm^{3+} ion but give

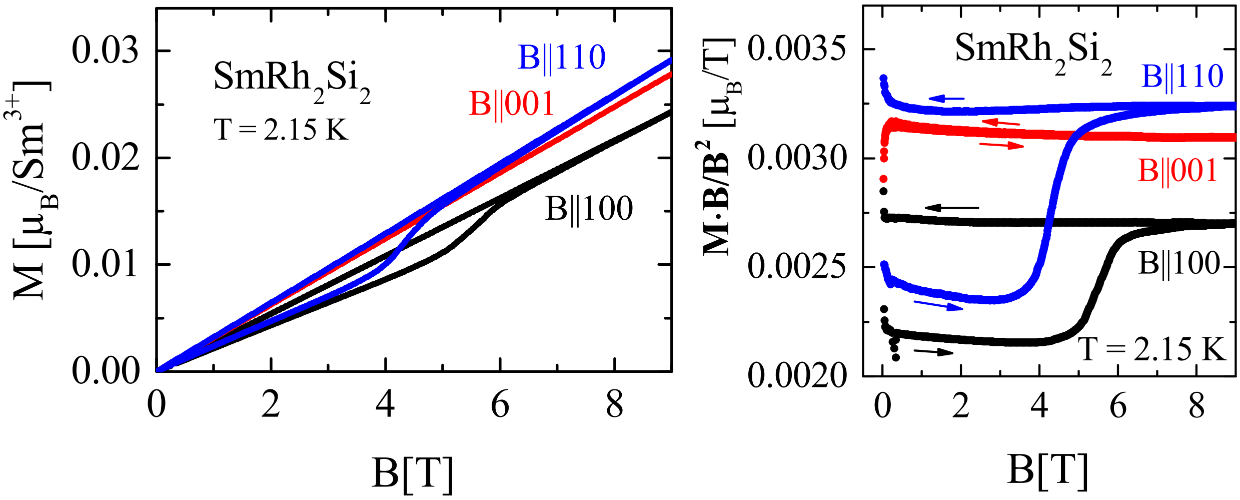

Figure 5.5: SmRh$_2$Si$_2$ *Left:* Field dependence of the magnetization $M = \vec{M} \cdot \vec{B}/B$ at $T = 2.15\,\mathrm{K}$ for field applied along the three main symmetry directions. *Right:* The figure shows the data of the left panel plotted as $\vec{M} \cdot \vec{B}/B^2$.

no information about excited states or how close in energy they are from the ground state. It is well known, that in Sm compounds not only the ground state multiplet is populated but also low-lying excited states which have different J than the ground state. Those excited states which exhibit a close proximity in energy to the ground state are also significantly populated which leads to a shift in the effective magnetic moment μ_{eff} compared to the value predicted for a system where only the ground state is populated. The determination of the effective magnetic moment from the slope of a linear fit to the inverse susceptibility $\chi^{-1}(T)$ according to Eqn. 1.22 is therefore not possible since this is applicable for systems where only the ground state is populated and where the inverse susceptiblity shows a linear behaviour at high temperatures [54]. To conclude, we found that in SmRh$_2$Si$_2$ the occupation of excited levels close to the ground state leads to a Van-Vleck like paramagnetic contribution to the susceptibility. Consequently, no information about the valence of the Sm ions in SmRh$_2$Si$_2$ can be obtained by this method.

Field dependence of the magnetization

The field dependence of the magnetization was investigated using the VSM option of a Quantum Design PPMS at $T = 2.15\,\mathrm{K}$ in fields up to $B = 9\,\mathrm{T}$. In Fig. 5.5, the magnetization for fields applied along the main symmetry directions is shown. Here, the magnetization shows anisotropic hystereses effects. While the slope of M is constant for field B along the [001] direction, for $B \perp 001$, it is smaller and shows hysteresis effects. This field dependent behaviour is consistent with a moment orientation in the basal plane of the tetragonal lattice. The occurence and size of the hystereses effects is strongly sample dependent.

ARPES

The valence of the Sm ions in our SmRh$_2$Si$_2$ single crystals was studied by ARPES and contributions from the bulk as well as from the surface to the photoemission spectrum have been determined. Divalent Sm $4f$ contributions to the photoemission spectrum are expected close to the Fermi level and have been observed experimentally in the past for Sm metal [253] and a number of Sm compounds [254, 255]. Such emissions from divalent Sm were mostly identified as surface valence transitions in the trivalent systems. Our study revealed that for Sm ions in $SmRh_2Si_2$, the electronic properties of bulk and surface are rather similar and the Sm ions behave in both cases only slightly mixed valent. The mean valence of the Sm ions in $SmRh_2Si_2$ was estimated to be about 2.94 at $T = 10\,\mathrm{K}$ [114]. Such deviations from the 3+ valence usually occur in Ce or Yb compounds which show the Kondo effect. Until now, we did not observe in electrical transport or specific heat measurements any signatures of a Kondo screening of the Sm ions in $SmRh_2Si_2$.

Summary and outlook

We have grown $SmRh_2Si_2$ single crystals for the first time which enables us not only to determine the phase transition temperature but also to study the anisotropic behaviour of this compound via electrical transport and magnetization measurements. In this work, single crystals of $SmRh_2Si_2$ have been grown by a modified Bridgman method from indium flux. After an optimization of the temperature-time profile of the growth experiment, we obtained millimetre-sized single crystals with a platelet habitus with the c axis perpendicular to the platelet. PXRD measurements on crushed single crystals confirmed the $I4/mmm$ tetragonal structure. The lattice parameters are in agreement with the data published for polycrystalline samples and are summarized in Tab. 5.8. The specific heat of $SmRh_2Si_2$ shows a sharp λ-type anomaly at $T_\mathrm{N} = 64\,\mathrm{K}$, establishing a second order phase transition into the AFM ordered phase. The data can be described by $C/T = \gamma_0 + \beta T^2$ with the Sommerfeld coefficient $\gamma_0 \approx 8\mathrm{mJ/(molK^2)}$ for $T < 6\,\mathrm{K}$. Magnetic measurements on the single crystals show the ordering of the Sm^{3+} moments at $T_\mathrm{N} = 65\,\mathrm{K}$ and the reorientation of magnetic domains for an external field applied in the $a-a$ plane of the tetragonal lattice. The inverse susceptibility does not exhibit Curie-Weiss behaviour at high temperatures and we found that in $SmRh_2Si_2$ the occupation of excited levels close to the ground state leads to a Van-Vleck-like paramagnetic contribution to the susceptibility. Due to the small magnetic moment, the contribution of the background to the measured signal in magnetization measurements is large. In future growth experiments, an optimization towards a higher single crystal mass will be performed to enable a further study of the magnetic properties of this compound. Below $T_\mathrm{N} = 65\,\mathrm{K}$, electrical transport data show an anisotropy for current flow parallel to the different main symmetry directions. The residual resistivity ratio $\mathrm{RRR} = \rho_{300\mathrm{K}}/\rho_0 \sim 25$ shows that we suceeded in growing high-quality single crystals from a high-temperature In flux. The single crystals enabled the investigation of their bulk and surface properties by ARPES. It turned out that at $T = 10\,\mathrm{K}$ the valence of the Sm ions is smaller than three at the surface as well as in the bulk [114]. This hints to a possible Kondo screening of the Sm^{3+} ions which could not be confirmed so far by our investigation of the bulk properties of this compound.

5.6 $GdRh_2Si_2$

Studies of Gd-compounds are of special interest since the $4f$ shell of Gd is half filled and therefore its ground state with $S = 7/2$ and $L = 0$ is insensitive to crystal-electric-field (CEF) effects. In the past, polycrystalline $GdRh_2Si_2$ was subject to several investigations. Magnetization and Mössbauer studies were performed by Felner and Nowik [247, 248] examining the series RRh_2Si_2 and by Czjzek *et al.* [256] with focus on the properties of the transition metal T in the compounds GdT_2Si_2. From Mössbauer spectra of ^{155}Gd in $GdRh_2Si_2$ it was deduced that the rare earth local moments order antiferromagnetically with the ordering in the basal plane perpendicular to the fourfold symmetry axis of the tetragonal lattice [247, 248]. It is known from neutron diffraction experiments, that the antiferromagnetic (AFM) properties in the series $LnRh_2Si_2$ arise due to a stacking of ferromagnetic layers [232]. Pressure studies by Szytuła *et al.* [257] revealed that the Néel temperature of $GdRh_2Si_2$ decreases with increasing applied pressure. An ESR study was performed by Kwapulinska *et al.* [258] and they found that the g-factor is temperature independent from T_N to 300 K with $g = 1.995 \pm 0.010$. Recently, the magnetic properties of $GdRh_2Si_2$ were investigated by hyperfine interactions and magnetization measurements [259]. All measurements up to now were carried out on polycrystalline material since single crystals were not available.

Summary and outlook

In this work, we report on the successful single crystal growth and the characterization of $GdRh_2Si_2$. We presented a detailed study of the bulk properties, namely heat capacity, magnetization and electrical transport of $GdRh_2Si_2$ single crystals in [223, 225] to provide a firm basis for the interpretation of the spectroscopic measurements [115]. PXRD measurements on crushed single crystals confirmed the $I4/mmm$ tetragonal structure with lattice parameters $a = 4.042(2)$ Å and $c = 9.986(4)$ Å, which is in agreement with the data published for polycrystalline samples [247, 257, 259]. The specific heat of $GdRh_2Si_2$, shown in Fig. 5.6 (left panel), exhibits a sharp λ-type anomaly at $T = 107\,\mathrm{K}$, establishing a second order phase transition into the AFM ordered phase. The data can be described by $C/T = \gamma_0 + \beta T^2$ with the Sommerfeld coefficient $\gamma_0 \approx 3\mathrm{mJ/(molK^2)}$ for $T < 7\,\mathrm{K}$ and the slope $\beta = (0.58 \pm 0.03)\,\mathrm{mJ/molK^4}$ of the linear fit. An accurate value for the Debye temperature cannot be determined since the magnon and phonon contributions to the specific heat, which both exhibit a T^3 temperature dependence, cannot be separated. Electrical transport data, Fig. 5.6 (right panel), show a large anisotropy for current flow parallel and perpendicular to the [001]-direction below T_N. The residual resistivity ratio $\mathrm{RRR} = \rho_{300\mathrm{K}}/\rho_0 \sim 23$ shows that we succeeded in growing high-quality crystals from a high-temperature indium flux. Magnetic measurements on the single crystals, Fig. 5.7 and Fig. 5.8 (left panel), show the ordering of the Gd^{3+} moments at $T_N = 107\,\mathrm{K}$ and a spin-flop transition at $B_{sf} \approx 1\,\mathrm{T}$ with an external field applied along the [100]-direction. The effective magnetic moment $\mu_{\mathrm{eff}} = (8.28 \pm 0.10)\,\mu_B$ agrees well with values from literature, and is larger than the theoretically predicted value of $\mu_{\mathrm{eff}}^{\mathrm{theo}} = 7.94\,\mu_B$. The determined Weiss temperature, $\Theta_{\mathrm{W}} = (8 \pm 5)\,\mathrm{K}$, is much smaller than T_N, indicating a pronounced competition between antiferromagnetic and ferromagnetic interactions.

$GdRh_2Si_2$ single crystals have been investigated in more detail by VSM, x-ray magnetic circular dichroism (XMCD) and RIXS [225]. Our low temperature investigation yielded that this compound represents an exemplary case for a simple antiferromagnetic order with in-plane ordered moments and weak in-plane anisotropy. Applying the field parallel to the tetragonal plane, M/B is isotropic in the limit $B = 0$. When increasing the field, strong anisotropic effects arise (Fig. 5.8, right panel). For field parallel to the [100]-direction,

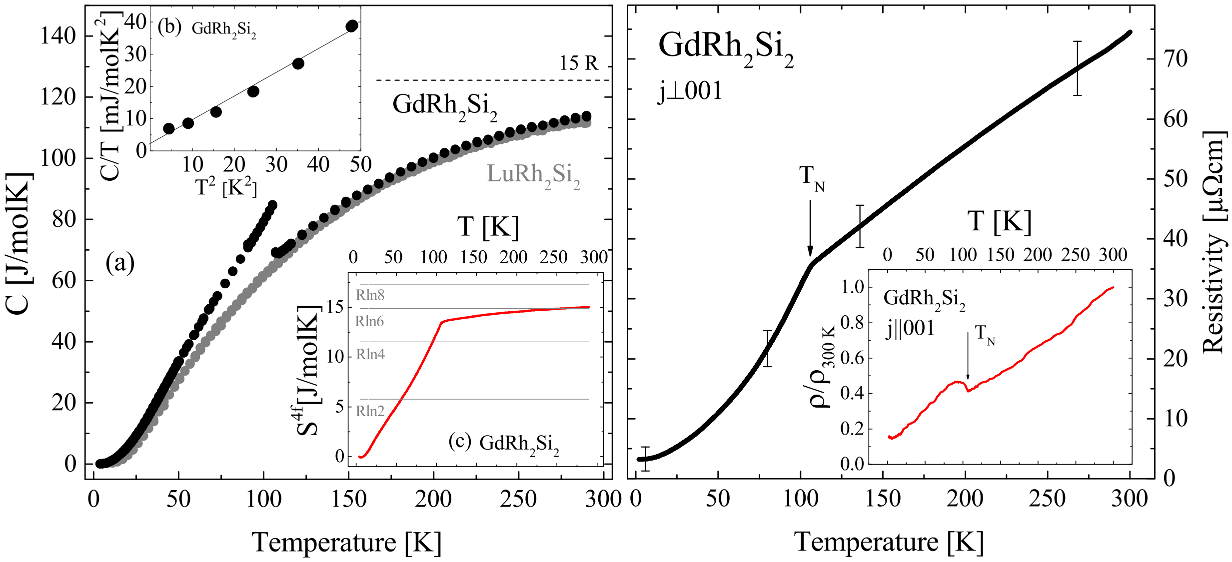

Figure 5.6: *Left:* GdRh$_2$Si$_2$, temperature dependence of the heat capacity. *Right:* GdRh$_2$Si$_2$, temperature dependence of the electrical resistivity.

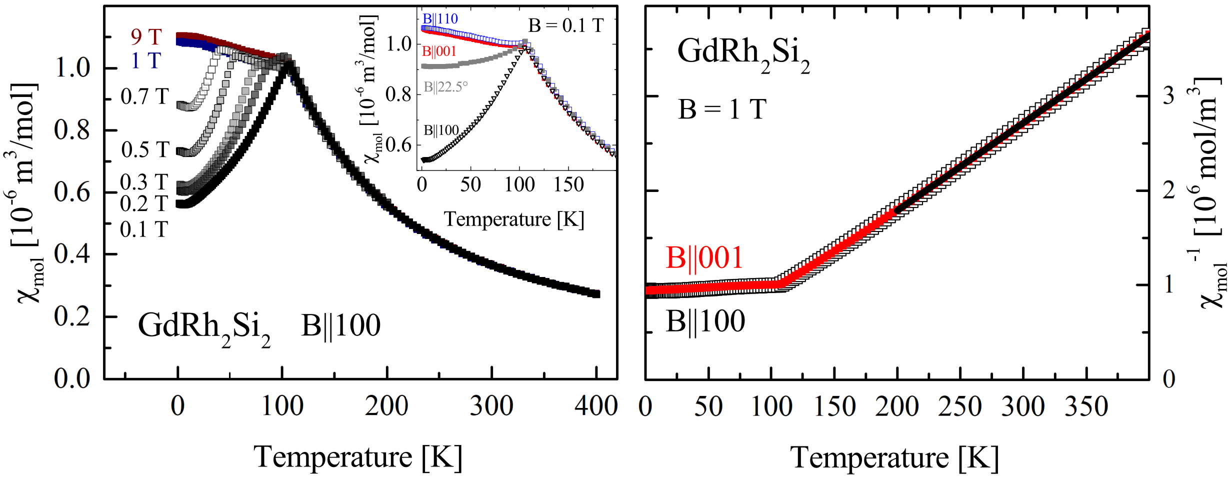

Figure 5.7: *Left:* GdRh$_2$Si$_2$, temperature dependence of the susceptibility. The inset shows the data for $B = 0.1$ T aligned along different crystallographic orientations. 22.5° is the angle between the field and the crystallographic [110] direction. *Right:* Inverse susceptibility.

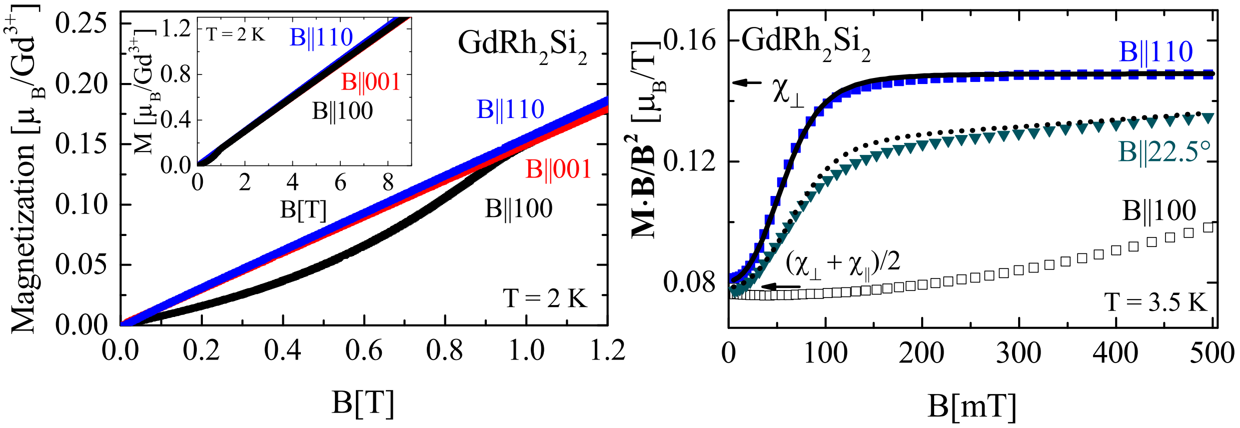

Figure 5.8: GdRh$_2$Si$_2$ *Left:* Magnetization M versus the applied external field B up to 9 T. *Right:* Field dependence of M/B in the low-field region.

we observed a spin-flop transition which is the rotation of local spin directions [260]. In contrast, we explain the sudden increase of the susceptibility in [110]-direction at low fields by domain effects. Since the low field regime yields a magnetic behaviour of a unique simplicity, we set up a magnetic mean field model combined with an Ising chain model (for details see [225]). With the assumption that the magnetic moments are aligned parallel to the [110]-direction, the experimental data were perfectly reproduced. We therefore conclude that the magnetic moments are aligned along the [110]-direction in the tetragonal lattice at low temperatures. Additional magnetic scattering experiments confirm the arrangement of the magnetic moments in staggered ferromagnetic layers along the [001]-direction. The magnetization of these layers have opposite directions forming the antiferromagnetic bulk with the magnetic propagation vector $\vec{k} = (0,0,1)$. Furthermore an XMCD study rules out a Rh contribution to the magnetization, proposed in Ref. [248]. The ESR of the single crystals has been investigated in the paramagnetic state [226]. Furthermore, it turned out that an ESR signal can also be detected in the magnetically ordered regime which enabled the investigation of the weak in-plane anisotropy in this system by magnetic resonance [227]. A detailed ARPES study of the single crystals revealed the presence of two-dimensional electron states at the Si-terminated surface of GdRh$_2$Si$_2$ [115]. The surface states exhibit itinerant magnetism and their spin splitting arises from a strong exchange interaction with the ordered Gd 4f moments.

5.7 HoRh$_2$Si$_2$

The antiferromagnetic compound HoRh$_2$Si$_2$ has been investigated in the past by neutron diffraction [232, 235, 261] and different magnetically ordered phases have been identified upon cooling. In total, three magnetic transitions one at $\mathrm{T_N} = 29$ K, and two others at $T_{\mathrm{N1}} = 27$ K and $T_{\mathrm{N2}} = 11$ K occur when lowering the temperature. Between 29 K and 27 K an incommensurate structure (Phase I) occurs. Between 27 K and 11 K the magnetic moments are ordered along the c direction (Phase II) and diffuse scattering, indicating a paramagnetic ab-component, appears. Below 11 K (Phase III), a simple AFM structure with propagation vector $\vec{k} = (0,0,1)$ is observed where the magnetic moments tilt away from the c-axis upon cooling. The tilt angle reaches 32.5° at 1.5 K [261]. Specific heat and magnetization measurements confirmed the magnetic order at $T_{N2} = 11\,K$ and $T_{N1} = 27\,K$ [262]. The crystal-field parameters of the material were determined by Takano *et al.* [263].

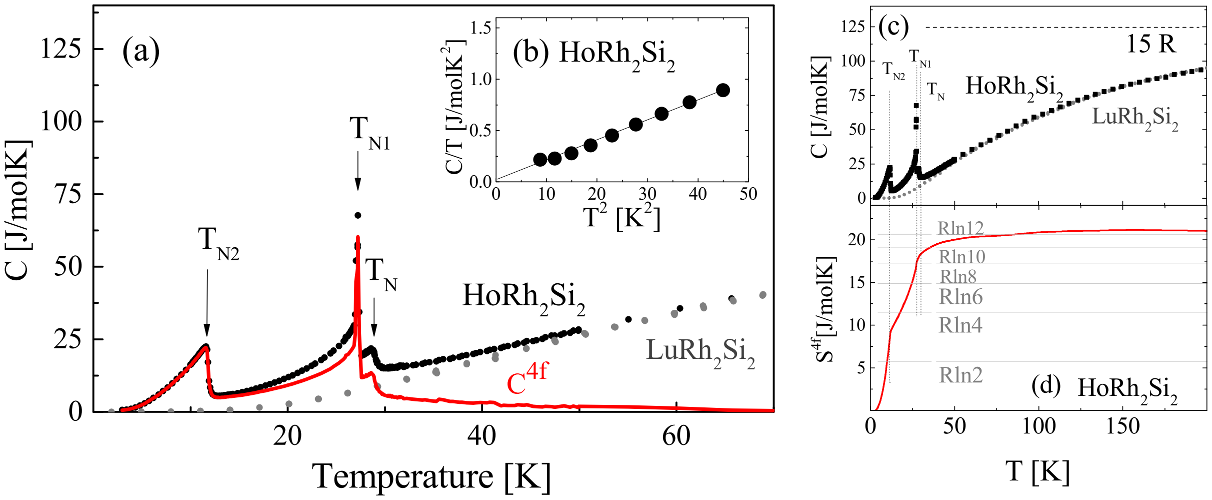

Figure 5.9: *Left:* (a) $HoRh_2Si_2$, temperature dependence of the heat capacity (black symbols). The magnetic part of the heat capacity C^{4f} (red symbols) was obtained by subtracting the heat capacity of the non-magnetic reference compound $LuRh_2Si_2$ (data taken from J. Ferstl [252]) which is shown for comparison (grey symbols). (b) Determination of the Sommerfeld coefficient γ_0 from a linear fit of C/T versus T^2. *Right:* (c) Heat capacity of $HoRh_2Si_2$ and $LuRh_2Si_2$ measured up to $T = 200\,K$ approaching the high-temperature Dulong-Petit value of $15\,R$. (d) Magnetic entropy of $HoRh_2Si_2$ obtained by integration of C^{4f}/T vs. T.

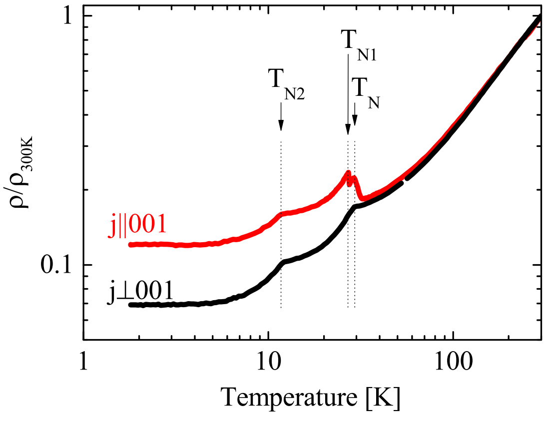

Figure 5.10: $HoRh_2Si_2$, temperature dependence of the electrical resistivity measured with $j \parallel 001$ (red symbols) and $j \perp 001$ (black symbols).

Heat capacity, electrical transport and magnetization, T $\geq$ 1.8 K

PXRD measurements on crushed single crystals confirmed the $I4/mmm$ tetragonal structure with lattice parameters $a = 4.018(6)$ Å and $c = 9.908(1)$ Å, which is in agreement with the data published for polycrystalline samples [248]. Specific heat measurements on the single

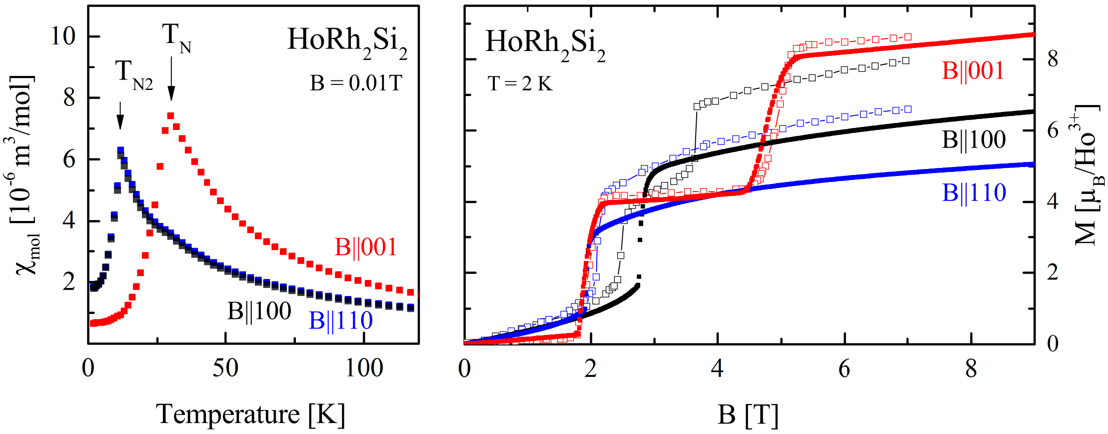

Figure 5.11: *Left:* $\chi(T)$ at $B = 0.01\,\mathrm{T}$, *Right:* $M(B)$ at $T = 2\,\mathrm{K}$; Note that the magnetization measured with field aligned in the $a - a$ plane differs from the curves shown with open symbols reported by Shigeoka *et al.* [222].

crystals grown from indium flux, Fig. 5.9, (a), perfectly reproduced the data obtained from Czochralski grown single crystals which were published by Shigeoka *et al.* [235]. The first transition $T_\mathrm{N} = 29.1\,\mathrm{K}$ and the third transition at $T_\mathrm{N2} = 11.8\,\mathrm{K}$ that occur upon cooling are second order phase transitions while the transitions at $T_\mathrm{N1} = 27\,\mathrm{K}$ is a first order phase transition. The Sommerfeld coefficient $\gamma_0 \approx 39\,\mathrm{mJ/(molK^2)}$ obtained from a linear fit of C/T versus T^2 below $T = 7\,\mathrm{K}$, Fig. 5.9 (b), is slightly enhanced. The magnetic part of the entropy Fig. 5.9 (c) reaches $S^{4f} \approx R\ln 10$ at T_N which is much smaller than the expected $R\ln(2J+1) = R\ln 17$ for the Ho^{3+} ion indicating that the overall splitting of the CEF levels is larger than T_N. The entropy saturates at about $R\ln 12$ which is far below $R\ln 17$. This discrepancy is probably caused by the large uncertainty in the measured heat capacity data for $T > 50\,\mathrm{K}$ as demonstrated above for YbNi$_4$P$_2$ in Fig. 2.17. Our electrical transport measurements, Fig. 5.10, show an anisotropy between the two current directions $j \parallel c$ and $j \perp c$. For $j \perp c$, the resistivity shows two anomalies at $T_\mathrm{N} = 29.1\,\mathrm{K}$ and $T_\mathrm{N2} = 11.8\,\mathrm{K}$ and decreases monotonically upon cooling. For $j \parallel c$, the resistivity increases at T_N which indicates a larger magnetic unit cell compared to the structural unit cell along the [001]-direction when entering the ordered phase. An additional anomaly at $T_\mathrm{N1} = 27\,\mathrm{K}$ occurs for $j \parallel c$. At this temperature, the ordering of the magnetic moments along the [001]-direction was observed by Shigeoka *et al.*. This anomaly at $T_\mathrm{N1} = 27\,\mathrm{K}$ is absent for $j \perp c$. The residual resistivity ratio determined for both current directions is also highly anisotropic: $RR^{j\perp c}_{1.8\,\mathrm{K}} = \rho_{300\,\mathrm{K}}/\rho_{1.8\,\mathrm{K}} \sim 14.5$ and $RR^{j\parallel c}_{1.8\,\mathrm{K}} = \rho_{300\mathrm{K}}/\rho_{1.8\,\mathrm{K}} \sim 8.3$. The magnetization of the system had already been investigated by Shigeoka *et al.* [235]. We were able to reproduce the temperature dependent susceptibility data, the respective measurements are shown in Fig. 5.11, left frame, but got different results for the field dependence of the magnetization for $B \parallel 100$ and $B \parallel 110$, Fig. 5.11, right frame. Connected to the CEF effects in this compound, the magnetization shows an anisotropic step-like behaviour. In the investigated field range, the magnetization does not reach the saturation value of $M_\mathrm{sat} = g_J J\,\mu_B = 10\,\mu_B$ per Ho^{3+} ion with $S = 2$, $L = 6$, $J = L + S = 8$ and $g_J = 5/4$. The magnetization upon increasing field, $B \parallel 001$ (red, closed symbols) shows two steps at $B \approx 2\,\mathrm{T}$ and $5\,\mathrm{T}$ which is consistent with the previously reported data (red, open symbols). For field $B \parallel 100$ we found only one step in the magnetization at $B \approx 2.7\,\mathrm{T}$ (black, closed symbols) with $M(7\,\mathrm{T}) \approx 6\,\mu_\mathrm{B}$

per Ho^{3+} ion while two-step behaviour with $M(7\,\mathrm{T}) \approx 8\,\mu_\mathrm{B}$ per Ho^{3+} ion was reported by Shigeoka *et al.* (black, open symbols). For $B \parallel 110$ (blue, closed symbols), we found one-step behaviour as reported by Shigeoka *et al.* (blue, open symbols) but with $M(7\,\mathrm{T}) \approx 4.9\,\mu_\mathrm{B}$ per Ho^{3+} ion instead of $M(7\,\mathrm{T}) \approx 6.8\,\mu_\mathrm{B}$ per Ho^{3+} ion.

ESR

A $HoRh_2Si_2$ single crystal has been investigated by ESR from 20 to 300 K with $H \parallel c$ and $H \perp c$ by J. Sichelschmidt (MPI CPfS). No ESR resonance was observable in the X-band (9.4 GHz). The reason for the absence of the ESR line might be that the relaxation process in $HoRh_2Si_2$ is fast due to the large orbital angular momentum of Ho in this compound and an ESR line might be observable at much higher fields [264].

ARPES

Our ARPES study [116] of $HoRh_2Si_2$ gave the following result: It is known from bulk magnetization measurements that the $4f$ moments exhibit a kind of magnetic frustration since their projections parallel and perpendicular to the $a-a$ surface plane order at different temperatures. The surface state is affected by the electromagnetic exchange interaction as well as by the spin-orbit coupling (Rashba effect). The study revealed that the temperature dependent changes in the moment orientation in the bulk reflect in the surface properties. Thus the temperature can be used as a tuning parameter for the surface magnetism. In particular it is of interest how the inclination of the $4f$ moments and the resulting tilt of effective magnetic fields at the surface act on the two-dimensional surface electrons, which might have important implications for possible applications in spintronic devices. When the temperature is tuned across the respective transitions, the spins of the two-dimensional surface electrons may be either locked within the surface by means of Rashba spin-orbit interactions or they might reorientate along the direction of the ordered $4f$ moments leading to an orientation perpendicular or inclined at a certain angle with respect to the c-axis.

Summary and outlook

In this work, we have grown $HoRh_2Si_2$ single crystals from indium flux using a Bridgman-type method. While the heat capacity measured on Czochralski grown single crystals reported by Shigeoka *et al.* [235] was reproduced perfectly by our data, differences have been found in the field dependence of the magnetization reflecting the properties of the CEF. Our electrical transport measurements shows that the first order as well as the two second order phase transitions are visible in the electrical resistivity. ARPES experiments were performed on the magnetically active, silicon-terminated surface of $HoRh_2Si_2$ single crystals [116]. It was found that the spin-dependent properties of the electrons can be manipulated by using the temperature as the tuning parameter. The temperature-dependent competition between spin-orbit and magnetic exchange interaction was studied and yielded that upon changing the temperature, the inclination of the $4f$ moments changes and the resulting tilt of the effective magnetic fields at the surface act on the two-dimensional electrons.

a [Å]	c [Å]	space group	sample	ref.
4.0561	9.9560	$I4/mmm$	PC	[266]
4.063	9.952	$I4/mmm$	PC	[167]
4.058	9.963	$I4/mmm$	PC	[267]
4.052	9.943	$I4/mmm$	PC	[268]
4.057(0)	9.971(3)	$I4/mmm$	PC	this work
4.0600(12)	9.930(4)	$I4/mmm$	SC	this work
4.111	9.733	$I4/mm$	PC	[268]
4.111	9.733	$P4/nmm$	PC	[268]

Table 5.9: $GdIr_2Si_2$: Lattice parameters determined by PXRD from polycrystalline samples (PC) or by single crystal analysis (SC).

atom	Wyckoff position	x	y	z	U(eq) [Å^2]
Gd	2a	0	0	0	0.032
Ir	4d	0	0.5	0.25	0.0314
Si	4e	0	0	0.3761	0.033

Table 5.10: Atomic coordinates and equivalent isotropic displacement parameters for $GdIr_2Si_2$ ($I4/mmm$) determined by single crystal analysis at $T = 173\,\mathrm{K}$. U(eq) is defined as one third of the trace of the orthogonalized U^{ij} tensor.

5.8 $GdIr_2Si_2$

In the past, polycrystalline $GdIr_2Si_2$ has been synthesized, see Tab. 5.9, and two polymorphous phases were found with this stoichiometry namely a LTP ($I4/mmm$) and a HTP ($P4/nmm$). A first characterization of the magnetic properties of the LTP was reported by Czjzek *et al.* [256] and Tung *et al.* [265]. No characterization of the anisotropic properties of this compound was reported so far.

Heat capacity, magnetization and electrical transport, $T \geq 1.8\,\mathrm{K}$

The specific heat of $GdIr_2Si_2$, shown in Fig. 5.13 (left panel, (a)), exhibits a λ-type anomaly at $T = 86\,\mathrm{K}$, establishing a second order phase transition into the AFM ordered phase. The data can be described by $C/T = \gamma_0 + \beta T^2$ with the Sommerfeld coefficient $\gamma_0 \approx 27\,\mathrm{mJ/(molK^2)}$ for $T < 5\,\mathrm{K}$, (left panel, inset (b)) and a slope $\beta = 0.0016\,\mathrm{J/(molK^4)}$ of the linear fit. A reliable value of the Debye temperature cannot be determined here since the phonon and a possible magnon contribution exhibit the same T^3 temperature dependence and cannot be separated. The magnetic part of the entropy S^{4f} reaches $\approx 80\%$ of the expected value $R\,\ln 8$ at the Néel temperature (left panel, inset (c)) indicating that the overall splitting of the CEF levels is larger than T_N. In Fig. 5.14, a broad hump is visible at $T/T_\mathrm{N} = 0.25$ in C^{4f} of $GdRh_2Si_2$ and $GdIr_2Si_2$. This behaviour is observed also for other Gd-compounds, like e.g. $GdCu_2Si_2$ [269–272]. Electrical transport data, Fig. 5.13 (right panel), show an anisotropy for current flow parallel and perpendicular to the [001] direction. The measurement with current parallel to

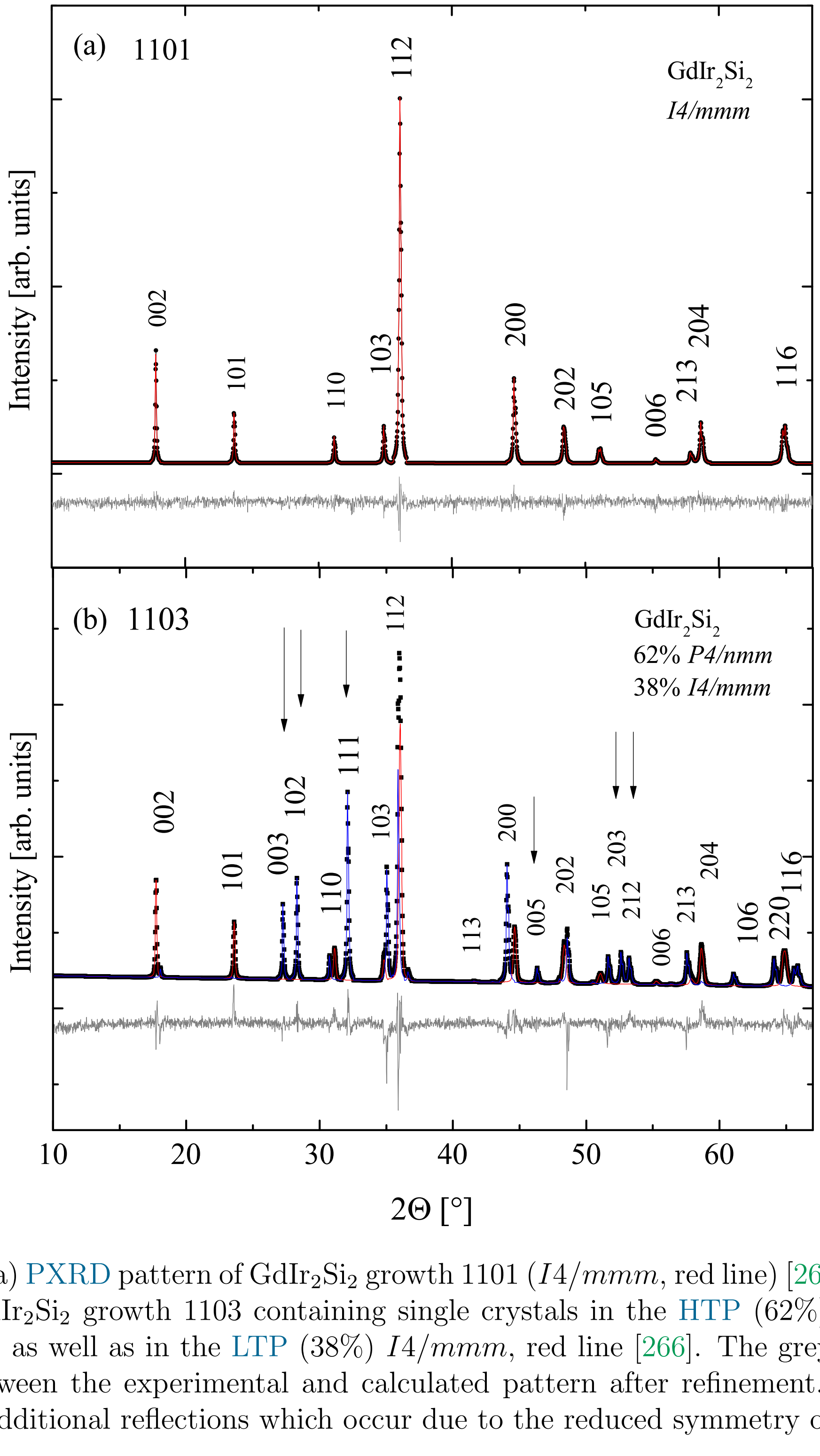

Figure 5.12: (a) PXRD pattern of $GdIr_2Si_2$ growth 1101 ($I4/mmm$, red line) [266]; (b) PXRD pattern of $GdIr_2Si_2$ growth 1103 containing single crystals in the HTP (62%) $P4/nmmZ$, blue line [268] as well as in the LTP (38%) $I4/mmm$, red line [266]. The grey curve is the difference between the experimental and calculated pattern after refinement. The arrows indicate the additional reflections which occur due to the reduced symmetry of the HTP.

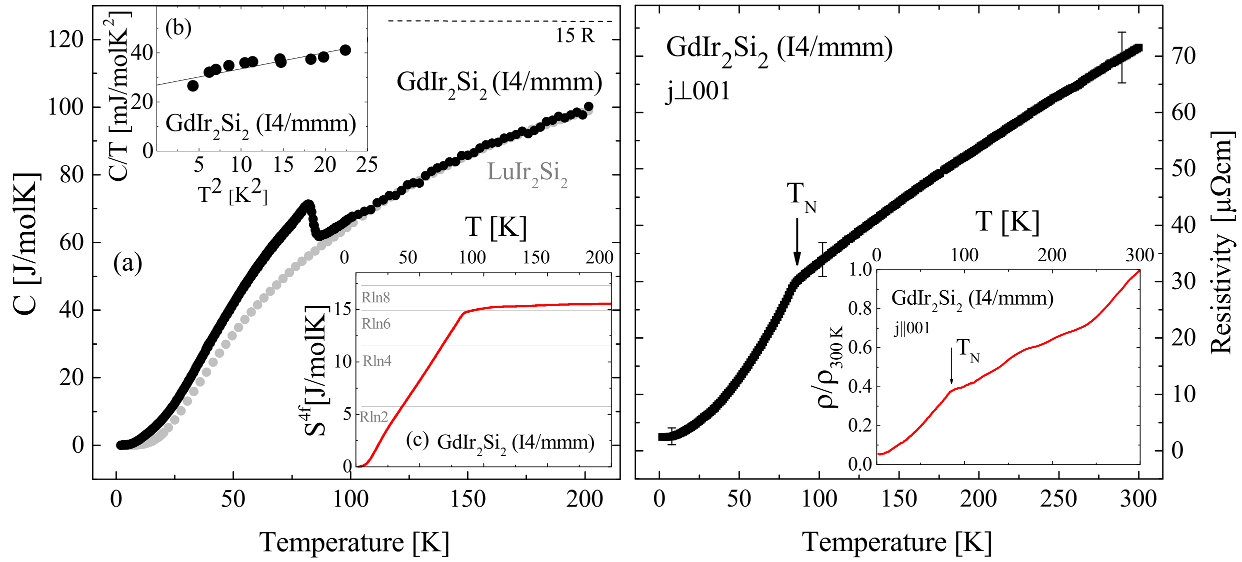

Figure 5.13: $GdIr_2Si_2$ *Left:* (a) Temperature dependence of the specific heat capacity. $LuIr_2Si_2$ data from [172], (b) Determination of the Debye temperature Θ_D and the Sommerfeld coefficient γ_0, (c) Magnetic contribution to the entropy; *Right:* $GdIr_2Si_2$, temperature dependence of the electrical resistivity.

the [001] direction was difficult to realize due to the small sample size with $d < 400\,\mu$m. For both current directions the resistivity decreases below the Néel temperature $T_\mathrm{N} = 86\,$K which deviates from the behaviour observed for $j \parallel c$ in $GdRh_2Si_2$ (compare Fig. 5.6, right panel). In contrast in $GdRh_2Si_2$, an increase of the resistivity below T_N appears and was attributed to the enlargement of the (magnetic) unit cell when entering the ordered phase. This is obviously not the case for $GdIr_2Si_2$. The residual resistivity ratio is RRR $= \rho_{300\mathrm{K}}/\rho_0 \sim 30$ for $j \perp c$ and RRR $= \rho_{300\mathrm{K}}/\rho_0 \sim 18$ for $j \parallel c$, which is slightly higher than that of the respective Rh compound.

The temperature dependent magnetization, Fig. 5.15, inset of the left panel, shows a strong anisotropy for $B \parallel 001$ and $B \perp 001$ with $B = 0.01\,$T and hints to a moment orientation in the basal plane of the tetragonal lattice. The ordering of the Gd^{3+} moments at $T_N = 87\,$K is indicated for all field directions by a kink in the susceptibility curve. The field dependence of the magnetization at 3.5 K is shown in Fig. 5.16, left panel, and the same data are depicted as $\vec{M} \cdot \vec{B}/B^2$ in the right panel. In contrast to $GdRh_2Si_2$ where the moments are aligned along one of the in-plane main symmetry directions, this is not the case in $GdIr_2Si_2$ at 3.5 K. The susceptibility $\vec{M} \cdot \vec{B}/B^2$ is constant for $B \parallel 001$ which is consistent with moments ordered in the $a - a$ plane. A constant susceptibility is also reached at $B \approx 2\,$T for $B \parallel 110$ and at $B \approx 2.5\,$T for $B \parallel 100$. At lower fields, the susceptibility changes strongly with field for both in-plane directions. These observations and the comparison with $GdRh_2Si_2$ hint to a moment orientation between the [100] and the [110] direction in the $a - a$ plane at $T = 3.5\,$K. From the slope of the inverse susceptibility $\chi^{-1}(T)$ from 200to 400 K, the effective magnetic moments and the Weiss temperatures were determined according to Eqns. 1.22. The obtained values of the effective magnetic moments for the different field directions are summarized in Tab. 5.11 and are close to the effective magnetic moment, $\mu_{\mathrm{eff}}^{\mathrm{theo}} = 7.94\,\mu_B$, of a free Gd^{3+} ion. The determined Weiss temperatures,

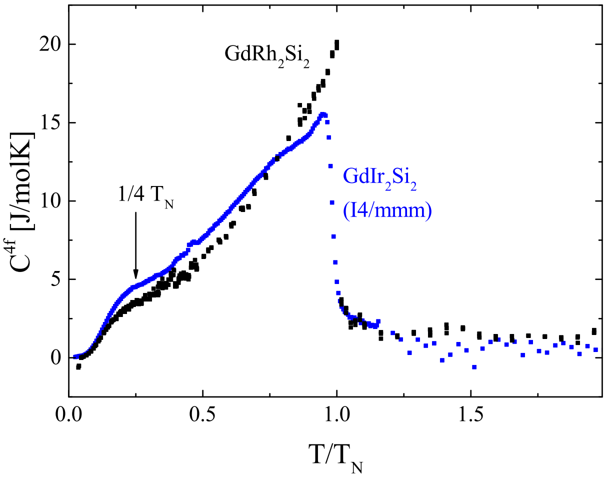

Figure 5.14: The magnetic part of the specific heat capacity C^{4f} of $GdIr_2Si_2$ and $GdRh_2Si_2$ was obtained by subtraction of the heat capacity of the non-magnetic references $LuRh_2Si_2$ [252] and $LuIr_2Si_2$ [172] from the measured data. A broad hump is visible at $T/T_N = 0.25$ in both Gd compounds.

take values close to $\Theta_W = 0$ and thus are much smaller than T_N. This behaviour is, similar to that observed in $GdRh_2Si_2$.

Summary and outlook

In this work, single crystals of $GdIr_2Si_2$ have been grown by a modified Bridgman method from indium flux. After an optimization of the temperature-time profile of the growth experiment, we obtained millimetre-sized single crystals with a platelet habitus with the c-axis perpendicular to the platelet in the $I4/mmm$ tetragonal structure which is the LTP. Our PXRD measurements on crushed single crystals confirmed this $I4/mmm$ tetragonal structure with lattice parameters which are in agreement with the data published for polycrystalline samples as summarized in Tab. 5.9. We excluded the presence of crystals in the high temperature phase ($P4/nmm$) by PXRD as demonstrated in Fig. 5.12 (a). We determined the Si z-position in the crystal structure by single-crystal structure analysis, Tab. 5.10. In the past, it turned out that this value is often close, but not exactly 0.375 and this deviation has a huge impact on the calculated band structure [273]. While a Néel temperature of $T_N = 81\,K$ [256] and $T_N = 82.4\,K$ [265] determined from powder samples was reported, our heat capacity measurements on single crystals revealed $T_N = 86\,K$ and a Sommerfeld coefficient of $\gamma_0 \approx 27 mJ/(molK^2)$. At the Néel temperature, a second order phase transition into the AFM ordered phase occurs. Electrical transport measurements yielded a residual resistivity ratio of $RRR = \rho_{300K}/\rho_0 \sim 30$ for $j \perp c$ and of $RRR = \rho_{300K}/\rho_0 \sim 18$ for $j \parallel c$. The temperature and field dependence of the magnetization hints to a moment orientation in the basal plane of the tetragonal lattice, Fig. 5.15 and Fig. 5.16. The effective magnetic moments for the different field directions $\mu_{eff}^{001} = 8.26\,\mu_B$ and $\mu_{eff}^{100} = 8.11\,\mu_B$ are close to the effective magnetic moment, $\mu_{eff}^{theo} = 7.94\,\mu_B$, of a free Gd^{3+} ion. The Weiss temperatures, take values close to $\Theta_W = (0 \pm 5)\,K$ and thus are much smaller than T_N. The investigation of the ESR of $GdIr_2Si_2$ was started by J.Sichelschmidt (MPI CPfS). A resonance is detectable in this material in the paramagnetic regime but not in the ordered phase [264]. First experiments

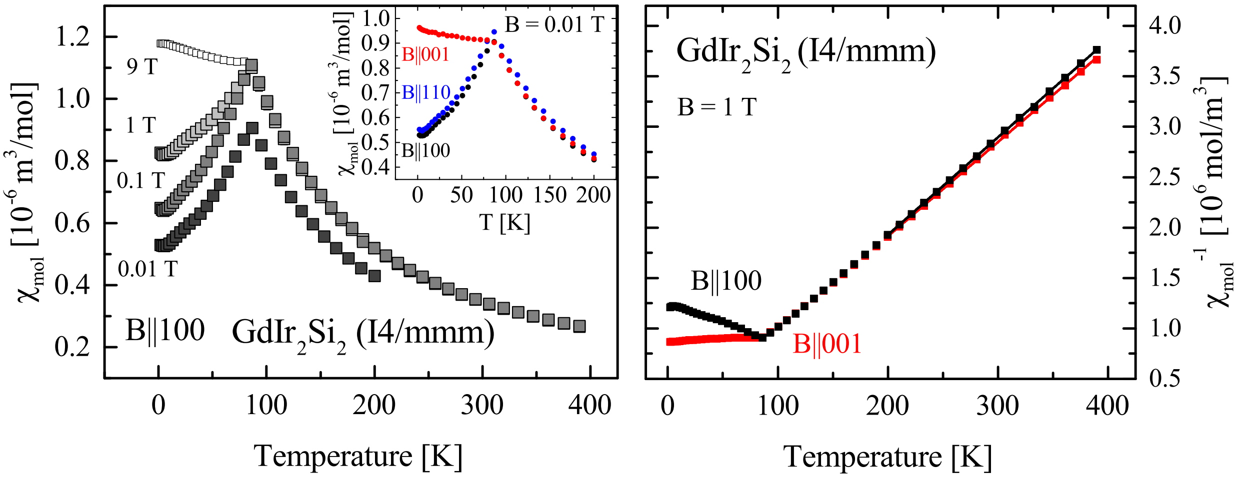

Figure 5.15: $GdIr_2Si_2$ *Left:* Temperature dependence of the magnetic susceptibility for $B \parallel 100$, The temperature dependence of the magnetic susceptibility for $B = 0.01\,\mathrm{T}$ along the different crystallographic orientations is shown in the inset; *Right:* Inverse susceptibility for $B = 1\,\mathrm{T}$. The effective magnetic moments μ_{eff} and Weiss temperatures Θ_W have been determined for $B \parallel 001$ and $B \parallel 100$ from the linear fit to the data above $T = 200\,\mathrm{K}$ and are summarized in Tab. 5.11.

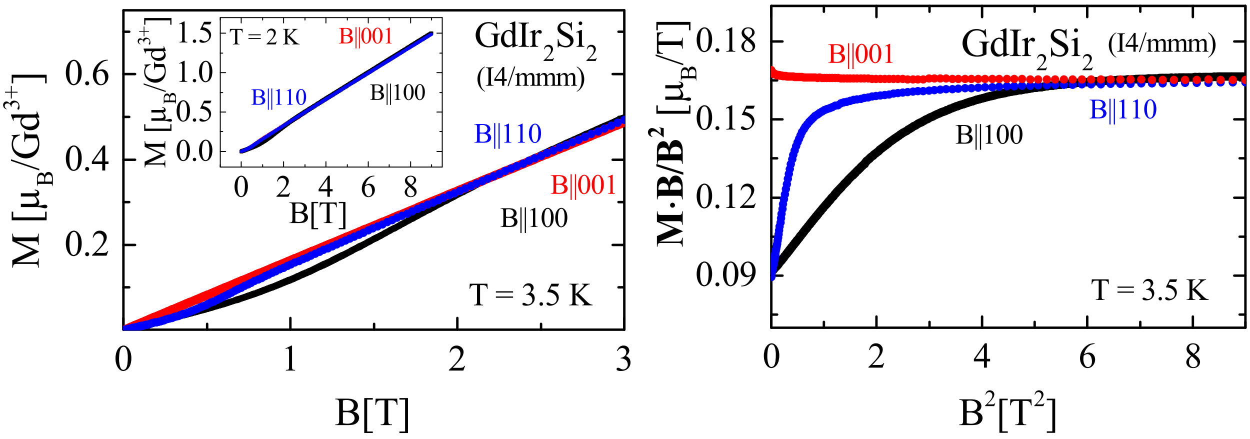

Figure 5.16: $GdIr_2Si_2$ *Left:* Field dependence of the magnetization for different crystallographic orientations at $T = 3.5\,\mathrm{K}$; *Right:* Data of the left panel depicted as M/B versus B^2 for $T = 3.5\,\mathrm{K}$

sample	μ_{eff} $[\mu_B]$	Θ_{W} [K]	T_{N} [K]	method	ref.
poly	8.05	-12 ± 3	81	magnetization	[256]
poly	7.94	-6.4	82.4	dc susceptibility	[265]
SC, $B \parallel 100$	8.11	0 ± 5	87	magnetization	this work
SC, $B \parallel 110$	8.15	-3 ± 1	87	magnetization	this work
SC, $B \parallel 001$	8.26	5 ± 5	87	magnetization	this work
SC	–	–	86	ac transport	this work
SC	–	–	86	heat capacity	this work

Table 5.11: GdIr$_2$Si$_2$: Comparison of the reported physical properties with those found in this work. The effective magnetic moments μ_{eff} and Weiss temperatures Θ_{W} were determined from the slope of the inverse magnetic susceptibility for $B = 1\,\mathrm{T}$. The Néel temperature was determined from different physical quantities.

a [Å]	c [Å]	space group	sample	ref.
4.042	9.707	$I4/mmm$	PC	[268]
4.0371	9.8769	$I4/mmm$	PC	this work
4.0476(6)	9.884(2)	$I4/mmm$	SC	this work
4.085	9.572	$P4/nmmZ$	PC	[268]

Table 5.12: HoIr$_2$Si$_2$: Lattice parameters

showed, that the obtained crystal quality was not sufficient for ARPES studies since it was not possible to resolve the band-splitting in the ordered phase. In the past, it was already observed, for instance, in the case of YbRh$_2$Si$_2$ and YbIr$_2$Si$_2$ that the crystallinity of the Rh compound was better than that of the Ir compound. This fact might be due to the existence of polymorphism in the Ir compounds. In future growth experiments, the temperature-time profile for the growth of GdIr$_2$Si$_2$ has to be optimized further to avoid the formation of the HTP completely.

5.9 HoIr$_2$Si$_2$

In the case of HoIr$_2$Si$_2$, besides the existence of polymorphism in the space groups $I4/mmm$ (LTP) and $P4/nmm$ (HTP) [268], no characterization of its physical properties was reported in the past. We therefore characterized the LTP of this material from the ground up.

Heat capacity, electrical transport and magnetization, T$\geq$ 1.8 K

The specific heat of HoIr$_2$Si$_2$, shown in Fig. 5.17 (a), exhibits an anomaly at $T_{\mathrm{N}} = 22\,\mathrm{K}$, establishing a second order phase transition into the AFM ordered phase. The data can

atom	Wyckoff position	x	y	z	U(eq) [Å^2]
Ho	2a	0	0	0	0.0283
Ir	4d	0	0.5	0.25	0.0275667
Si	4e	0	0	0.3777	0.0286667

Table 5.13: Atomic coordinates and equivalent isotropic displacement parameters for $HoIr_2Si_2$ ($I4/mmm$) determined by single crystal analysis at $T = 173\,\mathrm{K}$. U(eq) is defined as one third of the trace of the orthogonalized U^{ij} tensor.

be described by $C/T = \gamma_0 + \beta T^2$ with a slightly enhanced Sommerfeld coefficient $\gamma_0 \approx 37\,\mathrm{mJ/(molK^2)}$ for $T < 5\,\mathrm{K}$, (left panel, inset (b)). The magnetic part of the entropy, S^{4f}, Fig. 5.17 (c) reaches $R\ln 4$ at T_N which is much smaller than the expected $R\ln(2J+1) = R\ln 17$ for the Ho^{3+} ion indicating that the overall splitting of the CEF levels is much larger than T_N. The entropy saturates at about $R\ln 12$ which is far below $R\ln 17$. The increase from $R\ln 4$ to $R\ln 12$ above the Néel temperature to about 100 K can be attributed to CEF effects. This discrepancy is probably caused by the large uncertainty in the measured heat capacity data for $T > 50\,\mathrm{K}$ as demonstrated above in Fig. 2.17 for $YbNi_4P_2$. The same behaviour was already observed for $HoRh_2Si_2$. Electrical transport data, Fig. 5.17 (right panel), show a kink at $T_N \approx 21\,\mathrm{K}$ and an anisotropy for current flow parallel and perpendicular to the [001]-direction. The residual resistivity ratio $\mathrm{RRR} = \rho_{300\mathrm{K}}/\rho_0 \sim 29$ for $j \perp c$ ($\mathrm{RRR} = \rho_{300\mathrm{K}}/\rho_0 \sim 12$ for $j \parallel c$) is slightly higher than that of the respective Rh compound. In the cases of $GdRh_2Si_2$ and $HoRh_2Si_2$, an increase of the resistivity for $j \parallel c$ is observed upon cooling when entering the AFM phase which hints to the sudden enlargement of the (magnetic) unit cell volume at the Néel temperature, Figs. 5.6 and 5.10. For $HoIr_2Si_2$, a drop of the resistivity upon cooling below the Néel temperature is observed for both current directions and no signs for an enlargement of the (magnetic) unit cell occur. The field dependent magnetization, Fig. 5.18, right panel, shows a strong anisotropy for $B \parallel 001$ and $B \perp 001$. While for both in-plane directions, the magnetization increases linearly, the susceptibility is nearly zero for $B \parallel 001$ in low fields. This field dependence hints to the ordering of the magnetic moments along the c direction. For higher fields, the influence of the CEF becomes visible and a step-like magnetization occurs which is similar to the behaviour of $HoRh_2Si_2$ in field. Temperature dependent magnetic measurements on the single crystals, Fig. 5.18, left panel, show the ordering of the Ho^{3+} moments at $T_N = 22\,\mathrm{K}$. The data can be well understood with the assumption of the moments ordered along the c direction. Upon increasing the temperature up to the Néel temperature, the moments fluctuate between the up and the down state which leads to an increase of the susceptibility. The effective magnetic moments and Weiss temperatures, determined from the experimental data from 200 to 400 K according to Eqns. 1.22, are summarized in Tab. 5.14. The effective magnetic moments agree well with the predicted value of $\mu_\mathrm{eff}^\mathrm{theo} = 10.6\,\mu_\mathrm{B}$ for the free Ho^{3+}. The determined Weiss temperature for the different crystallographic directions, is isotropic for field in the $a - a$ plane. A strong anisotropy occurs for field parallel and perpendicular to the c-direction. While Θ_W hints to the presence of FM fluctuation for field along the [001] direction, AFM fluctuations are present for field perpendicular to this direction. The magnetization and susceptibility data, Fig. 5.18, strongly suggest that the magnetic moments order along the c direction. The in-plane susceptibility does not provide evidence for the

	$\mu_{\mathrm{eff}}\,[\mu_B]$	$\theta_{\mathrm{W}}\,[\mathrm{K}]$
$B \parallel 100$	10.53	-26.1
$B \parallel 110$	10.52	-26.3
$B \parallel 001$	10.64	25.9

Table 5.14: $HoIr_2Si_2$: Effective magnetic moments μ_{eff} and Weiss temperatures θ_{W} determined from the slope of the inverse magnetic susceptibility for $B = 1\,\mathrm{T}$ for different crystallographic directions.

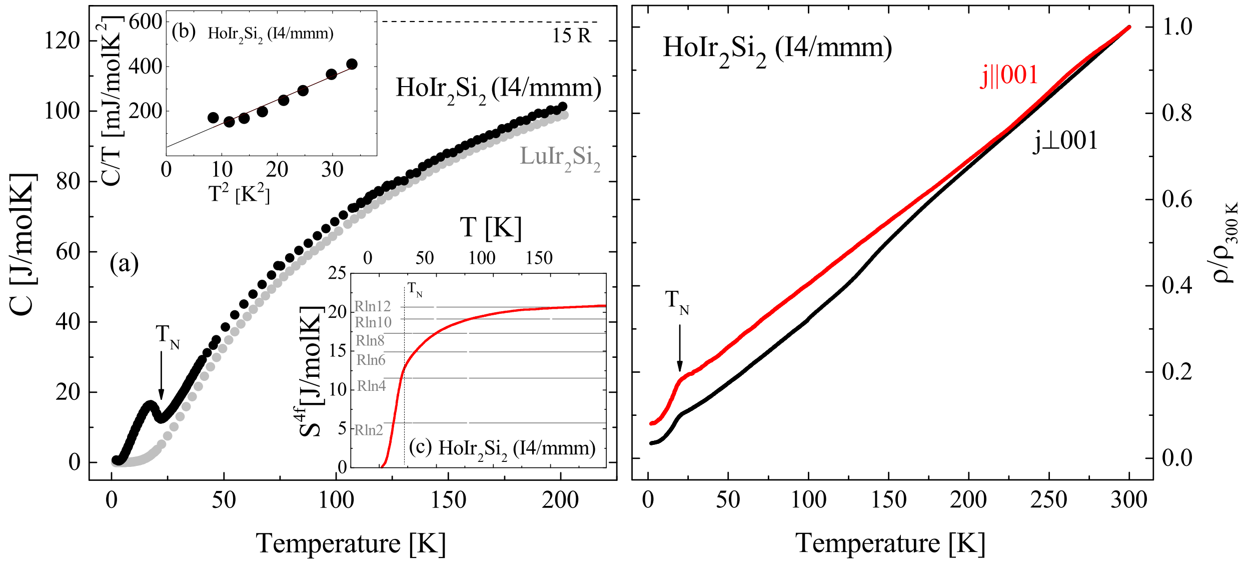

Figure 5.17: $HoIr_2Si_2$ *Left:* (a) Temperature dependence of the specific heat capacity. $LuIr_2Si_2$ data from [172], (b) Determination of the Debye temperature Θ_D and the Sommerfeld coefficient γ_0, (c) Magnetic contribution to the entropy; *Right:* $HoIr_2Si_2$, temperature dependence of the electrical resistivity. A kink in the curves for both current directions occurs at the Néel temperature $T_{\mathrm{N}} = 20\,\mathrm{K}$.

onset of the order of an in-plane component at a transition at lower T like it is observed in $HoRh_2Si_2$. Such an additional transition is connected to higher order CEF terms which probably are different for Rh and Ir compounds. Weaker higher order terms would also be in accordance with the more Ising type behaviour of the Ir compound [274].

ESR

Neither in the paramagnetic nor in the ordered phase an ESR resonance was detectable [264] between 300 K and 4 K for X-band frequency.

Summary and outlook

In this work, single crystals of $HoIr_2Si_2$ have been grown by a modified Bridgman method from indium flux. After an optimization of the temperature-time profile of the growth experiment, we obtained millimetre-sized single crystals. They had a platelet habitus, with the c-axis perpendicular to this platelet and formed in the $I4/mmm$ tetragonal structure, which

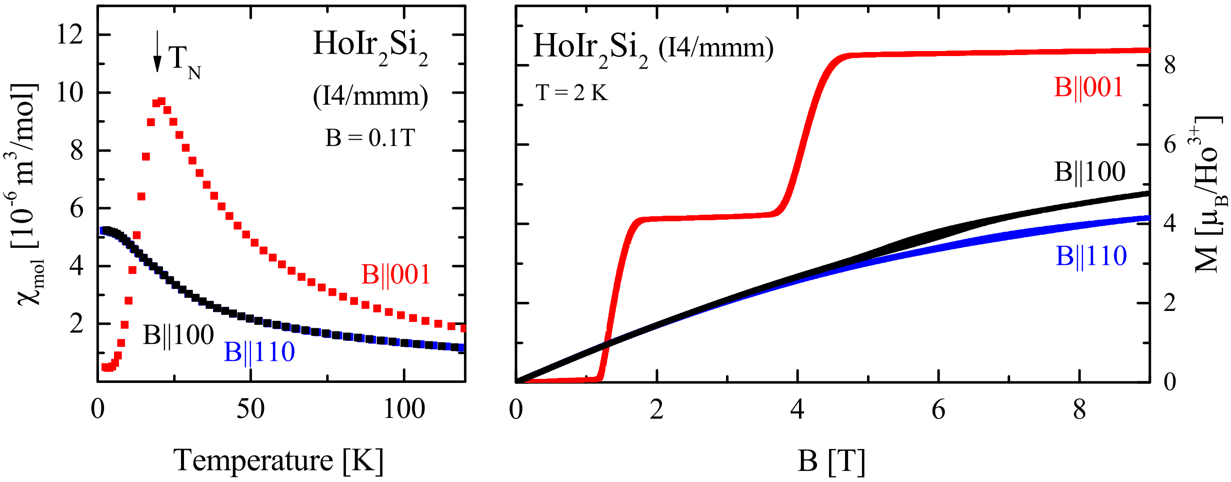

Figure 5.18: $\mathrm{HoIr_2Si_2}$: *Left:* Temperature dependence of the susceptibility at $B = 0.1\,\mathrm{T}$, *Right:* Magnetization M versus the applied external field B at $T = 2\,\mathrm{K}$ up to 9 T.

is the LTP. Our PXRD measurements on crushed single crystals confirmed this $I4/mmm$ tetragonal structure with lattice parameters which are in agreement with the data published for polycrystalline samples as summarized in Tab. 5.12. The PXRD pattern did not show any additional reflections belonging to the $P4/nmm$ structure. We additionally performed a single crystal structure analysis to exactly determine the Si z-position in $\mathrm{HoIr_2Si_2}$, Tab. 5.13 to give reliable input for the band structure calculations. We present a detailed study of the bulk properties, namely heat capacity, magnetization and electrical transport of $\mathrm{HoIr_2Si_2}$ single crystals. Our heat capacity measurements confirm the occurence of a second order phase transition at the Néel temperature $T_{\mathrm{N}} = 22\,\mathrm{K}$. The Sommerfeld coefficient $\gamma_0 \approx 37\mathrm{mJ/(molK^2)}$ determined from the specific heat data is enhanced. The temperature and field dependence of the magnetization hints to the ordering of the magnetic moments along the c direction. In the inverse magnetic susceptibility a strong anisotropy with $\Theta_W^{001} = 26\,\mathrm{K}$ and $\Theta_W^{100} = -26\,\mathrm{K}$ occurs for field parallel and perpendicular to the c-direction. The effective magnetic moment $\mu_{\mathrm{eff}}^{001} = 10.64\mu_B$ and $\mu_{\mathrm{eff}}^{100} = 10.53\mu_B$ is close to the expected value for a free $\mathrm{Ho^{3+}}$ ion ($\mu_{\mathrm{eff}}^{theo} = 10.6\mu_B$). The residual resistivity ratio $\mathrm{RRR} = \rho_{300\mathrm{K}}/\rho_0 \sim 29$ for $j \perp c$ and $\mathrm{RRR} = \rho_{300\mathrm{K}}/\rho_0 \sim 12$ for $j \parallel c$ is anisotropic and slightly higher than that of the respective Rh compound.

6

Summary

Today, superconductivity, magnetism and quantum criticality are main research fields in solid-state physics. Quantum criticality and quantum phase transitions can be investigated in systems for which a control parameter exists that can be used to suppress for instance a magnetic order until the phase transition occurs at zero temperature. This point is called a quantum critical point (QCP). Preferably, quantum critical behaviour is studied on single crystals. In comparison with polycrystalline material, single crystals can be grown with a high purity such that the measured physical properties stem from the material of interest and are not superposed by impurity effects. Additionally, anisotropic behaviour can be studied. The focus in this thesis was on the single crystal growth and characterization of materials which can be tuned to a QCP by a non-thermal control parameter. The investigated compounds are the series $YbNi_4(P_{1-x}As_x)_2$ exhibiting a ferromagnetic QCP at $x \approx 0.1$, the compound $YbRh_2Si_2$ exhibiting a field induced QCP for $B_{crit} \approx 60\,\mathrm{mT}$ ($B \perp c$) and the series $Ce(Ru_{1-x}Fe_x)PO$ with a QCP at $x \approx 0.86$. At first, the crystal growth procedure was developed for all compounds; afterwards, the single crystals have been grown and were characterized. Elements of highest possible purity served as the starting point in all crystal growth experiments. On the one hand, the single crystal growth was performed by the Bridgman method and on the other hand by the Czochralski method. While nowadays the Czochralski method is used for the industrial production of silicon single crystals, it is seldom used for the growth of single crystals for fundamental research in solid state physics. This might be mainly caused by the fact that the adaption of this method to a specific material is comparably elaborate. Besides the structural and chemical characterization of the single crystals, by powder x-ray diffraction (PXRD), Laue method and energy-dispersive x-ray spectroscopy (EDX), the physical properties as specific heat capacity, electrical resistivity and magnetization have been investigated between $1.8 - 300\,\mathrm{K}$. In addition, the single crystals have been further investigated within different collaborations down to low temperatures ($20\,\mathrm{mK}$) and in the case of $YbRh_2Si_2$ down to sub-millikelvin temperatures. Furthermore, single crystals of antiferromagnetic compounds LnT_2Si_2 (Ln = Sm, Gd, Ho; T = Rh, Ir) have been grown in the scope of this thesis. These compounds have comparably high Néel temperatures and therefore are not suitable for studies of quantum criticality. Instead, the focus on these compounds was the investigation of electronic surface states by angle resolved photoemission spectroscopy (ARPES).

The tetragonal $\mathbf{YbNi_4P_2}$ single crystals have been grown with two different methods [133]. The Bridgman method yielded single crystals with a mass of 10 mg at maximum.

The single crystals which were obtained by the Czochralski method grew up to a mass of 1800 mg. Several obstacles were passed when the process for the growth of large $\mathrm{YbNi_4P_2}$ single crystals was developed. The compound contains elements of high vapour pressure at high temperature, namely ytterbium and phosphorous, and the high melting element nickel. Initially, the high reactivity of the melt with the tendency to attack the crucible material impeded the prereaction. The following conditions were found to be suitable: (i) the crucible setup consisting of a boron nitride inner and a niobium outer crucible, (ii) a Yb-P-Ni stacking of the elements in the crucible, and (iii) a maximum temperature of 900°C. Furthermore, a homogenization and cleaning of the obtained precursor is necessary. The application of an argon pressure of 20 bar in the growth chamber was key to slow down the evaporation of P and Yb and to achieve stable growth conditions. A seed holder with an appropriate heat diffusion rate was designed and a well oriented crystal was used for the single crystal growth by the Czochralski method from a levitating melt utilizing a Ni-rich flux.We have demonstrated that the high-temperature metal-flux technique can be used to grow large single crystals of materials with volatile elements. Furthermore, the Czochralski method was applied to grow single crystals in the substitution series $\mathbf{YbNi_4(P_{1-\mathit{x}}As_{\mathit{x}})_2}$ for $x = 0.1, 0.12, 0.15, 0.2, 0.4, 0.6, 0.8$ and 1.0. By analyzing the chemical composition of the samples using EDX we found that the arsenic distribution in the samples is homogeneous [48]. The characterization of their structure by PXRD showed that the increase of the arsenic content in the substitution series caused the unit cell to enlarge as expected. The crystallinity of the samples was investigated by Laue-Method using two different radiations, namely x-rays and neutrons. While x-rays penetrate only several micrometers into the sample, the neutron-penetration depth is several centimeter. Therefore, x-ray Laue is sensitive to the surface and neutron Laue probes the bulk. During single crystal growth, the formation of small angle grain boundaries might occur. By combining both techniques, single crystals where the misalignment in the lattice is below the detection limits of about 0.5 degree were identified. These single crystals were cut and prepared to further characterize their physical properties down to lowest temperatures. Our single crystals of pure and arsenic substituted $\mathrm{YbNi_4P_2}$ have been further characterized by electrical transport, heat capacity and magnetization measurements. Electrical transport measurements down to lowest temperatures (20 mK) were performed in collaboration with M. Brando and coworkers and S. Friedemann and coworkers and showed a sharp transition into the ferromagnetic state at $T_C = 150\,\mathrm{mK}$. Additionally, the resistivity ratio, the best indicator for the high sample purity, was improved from previous $RRR = 16$ to $RRR = 60$ for $j \parallel c$. The resistivity as well as the magnetization exhibit a strong anisotropy parallel and perpendicular to the crystallographic c-direction, which is consistent with previous results and supports the assumption of a one-dimensional electronic structure. Due to the high sample purity, the anomalies observed in transport measurements appear much more pronounced in comparison to measurements on previous samples. This enabled H. Pfau and coworkers to investigate the Lifshitz transitions that occur in this compound [105]. In particular, their cummulated occurrence at low fields is extraordinary. Upon these transitions, the topology of the Fermi surface changes, which yields signatures in electrical transport and thermodynamic data. Through their analysis, information on the topology of the Fermi surface can be obtained. Our large single crystals facilitate ultrasound studies which are currently performed by Y.Tsui and coworkers in the group of M. Lang in Frankfurt. The first analysis of the data yielded that the Lifshitz transitions in $\mathrm{YbNi_4P_2}$ can also be detected by ultrasound.

We studied the arsenic substituted samples in more detail to localize the region of occuring non-Fermi liquid behaviour in the phase diagram. Electrical transport measurements on single crystals of the $YbNi_4(P_{1-x}As_x)_2$ series show that the pronounced anisotropy in the electrical resistivity of $YbNi_4P_2$ turns into an almost isotropic behaviour in the case of $YbNi_4As_2$. For arsenic concentrations up to $x = 0.4$, the Kondo scattering causes a pronounced drop in the resistivity below $T = 50\,\mathrm{K}$. Additionally, crystal electric field effects occur at high temperatures. Low temperature electrical transport measurements on single crystals near the quantum critical arsenic content $x \approx 0.1$ as well as pressure studies on a single crystal with $x = 0.12$ have been started by S. Friedemann and coworkers to further investigate the physics around the ferromagnetic QCP. The heat capacity was measured down to $T = 350\,\mathrm{mK}$ in collaboration with J. Banda at the MPI CPfS in Dresden: for low arsenic concentrations, the specific heat capacity divided by temperature C/T increases heavily at low temperatures indicating the presence of strong electronic correlations. Down to $T = 350\,\mathrm{mK}$, the heat capacity data shows critical behaviour on the non-magnetic side of the QCP up to $x = 0.2$ identical to that of $YbNi_4P_2$. For samples with $x \leq 0.2$, this leads to strongly enhanced Sommerfeld coefficients of $\gamma_0 > 1000\,\mathrm{mJmol^{-1}K^{-2}}$. For high arsenic concentrations, C/T becomes constant with enhanced Sommerfeld coefficients $\gamma_0 = 158\,\mathrm{mJmol^{-1}K^{-2}}$ for $x = 0.8$ and $\gamma_0 = 96\,\mathrm{mJmol^{-1}K^{-2}}$ for $x = 1.0$ showing Fermi-liquid behaviour below $T \approx 5\,\mathrm{K}$. Measurements of the magnetization showed that the effective magnetic moment decreases from $\mu_{\mathrm{eff}}^c = (4.82 \pm 0.02)\,\mu_\mathrm{B}$ at the phosphorous side to $\mu_{\mathrm{eff}}^c = (4.52 \pm 0.02)\,\mu_\mathrm{B}$ at the arsenic side, which hints a reduction of the Yb valence. The angular dependence of the susceptibility $\chi(\phi)$ of $YbNi_4P_2$ above 2 K in different external fields was studied in collaboration with M. Baenitz (MPI CPfS Dresden). While the anisotropy upon rotation about the (001) axis was below the detection limit, an anisotropy in $\chi(\phi)$ was found when rotating about the (100) axis.

Phase pure samples of $LuNi_4P_2$ have been synthesized and were characterized in the frame of this work. These samples have been used as a non-magnetic reference compound in specific heat capacity measurements.

In collaboration with different groups, several experiments have been started using our new single crystals. Determining the magnetic specific heat of $YbNi_4P_2$ at high temperatures made it possible to estimate the missing third crystal electric field (CEF) level E_3. The combination of the neutron and heat capacity data suggests a level scheme of $E_1 = 8.5\,\mathrm{meV}$, $E_2 = 12.5\,\mathrm{meV}$ and $E_3 \approx 25\,\mathrm{meV}$ which was worked out in collaboration with Z. Hüsges [153]. The determined CEF scheme was obtained by an elaborate fitting procedure and is connected to large error bars. Therefore, a further refinement is appreciated. Additional experimental input can be obtained by single crystal nuclear magnetic resonance (NMR). In the tetragonal compound $YbNi_4P_2$, the environment of the Yb atoms is orthorhombic and NMR is a method by which the local anisotropy of the Yb atoms in their orthorhombic environment can be studied. NMR experiments on large single crystals have been started by H. Yasuoka, H. Tou and coworkers. Good agreement was already found by comparing the calculated magnetization according to the estimated CEF scheme with high-field magnetization data in collaboration with T. Förster and M. Brando. In collaboration with Z. Hüsges, S. Lucas and O. Stockert using samples with masses up to 1800 mg, antiferromagnetic (AFM) fluctuations far above the Curie temperature could be detected by inelastic neutron scattering, which is in good agreement with the non-occurrence of an electron spin resonance (ESR) in earlier measurements ($T_{\mathrm{min}} = 2.9\,\mathrm{K}$, X-band (9.4 GHz)) by J. Sichelschmidt. In

contrast to the expectation that the observation of an ESR resonance is possible in Kondo lattice systems if ferromagnetic fluctuations are present, surprisingly no ESR resonance was detectable in $YbNi_4P_2$.
First ARPES experiments on $YbNi_4P_2$ performed in collaboration with D.V. Vyalikh and coworkers showed that mainly nickel states contribute to the density of states (DOS) near the Fermi level. Further ARPES studies have been started to get more insight into its electronic structure.

With the new generation of single crystals, it now becomes possible to investigate the physics of the ferromagnetic QCP in arsenic substituted $YbNi_4P_2$ in more detail. This will provide experimental data which might enable us to improve the understanding of ferromagnetic quantum criticality in Kondo-lattice systems.

The best studied material close to an AFM QCP **$YbRh_2Si_2$**, was grown from indium flux by a modified Bridgman method. A large number of the tetragonal single crystals have been grown, which vary in shape and size and are suitable for variable demands. These platelet shaped single crystals with their area of several mm^2, a thickness of up to $200\,\mu m$ and a resistivity ratio $RR_{1.8\,K} \approx 33$ are comparable in size and purity to single crystals grown in previous work. Samples of highest purity for ultra-low-temperature investigations were identified by combined magnetization and electrical transport measurements using a physical property measurement system (PPMS). Severals experiments have been started by different collaborations utilizing our new single crystals. In the course of this theses, J. Saunders and coworkers succeeded in measuring the thermal noise on thin $YbRh_2Si_2$ single crystals and thereby confirmed the superconducting transition at $T_c \approx 2\,mK$ in $YbRh_2Si_2$. New possibilities arose through M. Brando and coworkers by preparing a meander structure on thin single crystal platelets using the focused ion beam technique (FIB). The micro-structured samples have an increased current carrying length which increases their resistivity, leads to the reduction of heating effects and to an improved precision of the measurement. The as prepared single crystals will facilitate resistivity measurements at sub-millikelvin temperatures. In Kondo systems, a "large" Fermi surface forms due to the hybridization of $4f$ and conduction electrons. In the course of this thesis, the "small" Fermi surface formed exclusively by conduction electrons was detected in a Compton-scattering experiment by D.V. Vyalikh and coworkers at $T = 300\,K$. This experiment was performed on large $YbRh_2Si_2$ single crystals [175]. Due to its low-lying Néel temperature, its small ordered moment and the absence of single crystals suitable for neutron scattering, the magnetic structure of $YbRh_2Si_2$ is not known until now. Magnetization measurements at low temperatures have been started by M. Brando and coworkers to obtain further information about the ordered phase. In the course of this thesis, new experimental setups were developed by M. Scheffler and coworkers. These allowed to investigate the material by microwave spectroscopy at millikelvin temperatures and low fields that were unaccessible until now [176, 177]. During the past years, the foundation was layed for the investigation of the dynamics of the Kondo state by time-resolved THz studies by C. Wetli, M. Fiebig and H. Kroha. The first materials that were studied were $CeCu_{6-x}Au_x$ which exhibits a quantum critical point at $x \approx 0.1$ and $YbRh_2Si_2$. A terahertz pulse converts heavy fermions in the material into normal light electrons. The heavy-fermion state recovers under emission of a delayed, phase-coherent terahertz reflex. Towards the QCP, the quasiparticle weight collapses, while its formation temperature remains almost constant [211]. To validate the conception of the experiment and the experimental method itself with a further heavy-fermion material, we contributed to this project by providing large single crystals of $\mathrm{YbRh_2Si_2}$.

The application of such new experimental approaches might not only shed light on the still unanswered questions about the magnetic order or the mechanism leading to the heavy-electron superconductivity in $\mathrm{YbRh_2Si_2}$, but also address general questions about the dynamics of the Kondo state in quantum critical materials.

It is known that a QCP occurs in the series $\mathbf{Ce(Ru_{1-x}Fe_x)PO}$ for $x \approx 0.86$, but its nature was under debate at the beginning of this thesis. The result of our work was the successful growth and characterization of single crystals in the substitution series $\mathrm{Ce(Ru_{1-x}Fe_x)PO}$ with $x = 0, 0.44, 0.77, 0.86$ and 1.0 to provide high-quality samples for further studies of the putative ferromagnetic QCP. Our magnetic characterization of the CeRuPO single crystals shows that we were able to reproduce the data reported before for the pure Ru compound. In the case of CeRuPO, reducing the unit cell volume is possible by substituting Ru by the smaller Fe and the ordering temperature can be lowered by this substitution. Single crystals with an area of $\approx 1\,\mathrm{mm}^2$ and a thickness of a few μm of the series $\mathrm{Ce(Ru_{1-x}Fe_x)PO}$ have been grown from tin flux. We optimized the parameters for the single crystal growth and performed a careful characterization of the obtained crystals in the substitution series by PXRD, EDX and magnetization measurements down to $T = 2\,\mathrm{K}$. Magnetization measurements on CeRuPO revealed ferromagnetic order below $T_C = 15\,\mathrm{K}$. Samples with $x = 0.44$ show order below $T \approx 8\,\mathrm{K}$ and hysteresis effects in $M(H)$ which are strongly sample dependent. These samples are located in the cross-over region from ferromagnetic to antiferromagnetic order. Clear signatures of antiferromagnetic order below $T_{\mathrm{N}} = 3\,\mathrm{K}$ have been found for samples with $x = 0.77$, while samples with $x = 0.86$ show no magnetic order down to $T = 2\,\mathrm{K}$. In combination with low-temperature measurements by A. Jesche and M. Brando, our magnetization data yield that the ferromagnetic order turns into antiferromagnetic order for higher Fe concentrations in $\mathrm{Ce(Ru_{1-x}Fe_x)PO}$. The data hint to the existence of an antiferromagnetic QCP in this system at $x = 0.85$ [212] which is consistent with previous pressure studies by Kotegawa *et al.* but is not in accordance with the proposal of a ferromagnetic QCP by Kitagawa *et al.*.

Furthermore, we have grown single crystals of antiferromagnetic materials with $\mathrm{ThCr_2Si_2}$-type structure containing different lanthanide ions where electronic surface states were predicted by band structure calculations to occur. ARPES experiments require high purity single crystals. Only samples with a low amount of crystal defects yield a high resolution in the measured data. Besides the purity, another criterion is the sample size. We therefore performed crystal growth experiments aiming to optimize the growth parameters with respect to the largest single crystal size and the highest possible purity. The platelet shaped single crystals have an area of up to $12\,\mathrm{mm}^2$ and a thickness of $50 - 300\,\mu$m. We have successfully grown single crystals of $\mathbf{SmRh_2Si_2}$, $\mathbf{GdRh_2Si_2}$, $\mathbf{GdIr_2Si_2}$, $\mathbf{HoRh_2Si_2}$ **and** $\mathbf{HoIr_2Si_2}$ using a Bridgman-type growth method [223]. This growth procedure which was originally developed for the growth of $\mathrm{YbRh_2Si_2}$ from indium flux turned out to be quite robust and could be adapted for the growth of the related compounds by small variation of the growth parameters. Thermodynamic and anisotropic electrical transport and magnetic properties of these compounds, which were not known before, have been studied from the ground up. Their purity was characterized by determining the residual resistivity ratio and was larger than $RR_{1.8\,\mathrm{K}} = 25$ for $j \perp c$. The investigation of the magnetic structure by neutron scattering of compounds containing elements like Sm, Gd and Ho is hindered due to their large absorption cross-section for neutrons. Nevertheless, the detailed study of the bulk magnetization of $\mathrm{GdRh_2Si_2}$ enabled us to determine its magnetic structure by combining resonant inelastic x-ray scattering (RIXS) and magnetization measurements and comparing the latter with the data predicted by a mean-field model. We discovered that in $\mathrm{GdRh_2Si_2}$, the magnetic moments are aligned along the [110]-direction in the basal plane of the tetragonal lattice. In the structure, ferromagnetic planes are stacked along the [001] direction which yields the AFM order of this compound [225]. The ESR of the single crystals has been investigated in the paramagnetic state [226]. Furthermore, it turned out that an ESR signal can also be detected in the magnetically ordered regime which enabled the investigation of the weak in-plane anisotropy in this system by magnetic resonance [227]. The electronic states arising at the surface of the single crystals were investigated by ARPES in collaboration with D.V. Vyalikh and coworkers. A detailed ARPES study of the $\mathrm{GdRh_2Si_2}$ single crystals revealed the presence of two-dimensional electron states at the Si-terminated surface [115]. The surface states exhibit itinerant magnetism and their spin splitting arises from a strong exchange interaction with the ordered Gd $4f$ moments. ARPES experiments were performed on the magnetically active, silicon-terminated surface of $\mathrm{HoRh_2Si_2}$ single crystals [116]. It was adjudged that the spin-dependent properties of the electrons can be manipulated by using the temperature as the tuning parameter. The temperature-dependent competition between spin-orbit and magnetic exchange interaction was studied and yielded that upon changing the temperature, the inclination of the $4f$ moments changes and the resulting tilt of the effective magnetic fields at the surface act on the two-dimensional electrons. Our ARPES studies revealed that for Sm ions in $\mathrm{SmRh_2Si_2}$, the electronic properties of bulk and surface are rather similar and the Sm ions behave in both cases slightly mixed valent. Their mean valence was estimated to be about 2.94 at $T = 10\,\mathrm{K}$ [114]. Such a reduction of the valence of the Sm ion might be caused by a Kondo screening, but our characterization of the bulk properties of this compound did not show any signatures of the Kondo effect in $\mathrm{SmRh_2Si_2}$.

In the course of this thesis, many single crystals with highest purity of various materials have been grown and were characterized. These will contribute to improve the understanding of the physics in the field of strongly correlated electron systems.

Bibliography

[1] L. Schultz, J. Wecker, and E. Hellstern. *J.Appl.Phys.*, 61:3583, 1987.

[2] Y. Wang, Y. Li, C. Rong, and J. P. Liu. *Nanotechnology*, 18:465701, 2007.

[3] J. P. Franck, F. D. Manchester, and D. L. Martin. *Proc.Roy.Soc.A*, 263:494, 1961.

[4] C. D. Bredl, S. Horn, F. Steglich, B. Lüthi, and R. M. Martin. *Phys.Rev.Lett.*, 52:1982, 1984.

[5] T. E. Mason, G. Aeppli, A. P. Ramirez, K. N. Clausen, C. Broholm, N. Stücheli, E. Bucher, and T. T. M. Palstra. *Phys.Rev.Lett.*, 69:490, 1992.

[6] M. Dzero, K. Sun, V. Galitski, and P. Coleman. *Phys.Rev.Lett.*, 104:106408, 2010.

[7] C. M. Varma. *Rev.Mod.Phys.*, 48:219, 1976.

[8] V. K. Pecharsky, K. A. Gschneidner Jr., and L. L. Miller. *Phys.Rev.B*, 43:10906, 1991.

[9] F. Steglich, J. Aarts, C. D. Bredl, W. Lieke, D. Meschede, W. Franz, and H. Schäfer. *Phys.Rev.Lett.*, 43:1892, 1979.

[10] C. Petrovic, P. G. Pagliuso, M. F. Hundley, R. Movshovich, J. L. Sarrao, J. D. Thompson, Z. Fisk, and P. Monthoux. *J.Phys.Condens.Matter*, 13:L337, 2001.

[11] E. Schuberth, M. Tippmann, L. Steinke, S. Lausberg, A. Steppke, M. Brando, C. Krellner, C. Geibel, R. Yu, Q. Si, and F. Steglich. *Science*, 351:485, 2016.

[12] H. v. Löhneysen. *J.Phys.Condens.Matter*, 8:9689, 1996.

[13] P. Carretta, M. Giovannini, M. Horvatić, N. Papinutto, and A. Rigamonti. *Phys.Rev.B*, 68:220404, 2003.

[14] A. Steppke, R. Küchler, S. Lausberg, E. Lengyel, L. Steinke, R. Borth, T. Lühmann, C. Krellner, M. Nicklas, C. Geibel, F. Steglich, and M. Brando. *Science*, 339:933, 2013.

[15] L. Zhu, M. Garst, A. Rosch, and Q. Si. *Phys.Rev.Lett.*, 91:066404, 2003.

[16] P. Coleman, C. Pépin, Q. Si, and R. Ramazashvili. *J.Phys.Condens.Matter*, 13:R723, 2001.

[17] K. Q. Si, S. Rabello, and J. L. Smith. *Nature*, 413:804, 2001.

[18] S. Sachdev. *Quantum phase transitions.* New York: Cambridge Univ. Press, 1999.

[19] A. Schröder, G. Aeppli, R. Coldea, M. Adams, O. Stockert, H. v. Löhneysen, E. Bucher, R. Ramazashvili, and P. Coleman. *Nature*, 407:351, 2000.

[20] P. Gegenwart, J. Custers, C. Geibel, K. Neumaier, T. Tayama, K. Tenya, O. Trovarelli, and F. Steglich. *Phys.Rev.Lett.*, 89:056402, 2002.

[21] G. Sparn, O. Stockert, F. M. Grosche, H. Q. Yuan, E. Faulhaber, C. Geibel, M. Deppe, H. S. Jeevan, M. Loewenhaupt, G. Zwicknagl, and F. Steglich. *J.Phys.Chem.Solids*, 67:529, 2006.

[22] G. Knebel, D. Braithwaite, P. C. Canfield, G. Lapertot, and J. Flouquet. *High Pressure Research*, 22:167, 2002.

[23] T. Fukuhara, I. Okuno, K. Maezawa, and Y. Ônuki. *J.Magn.Magn.Mater.*, 310:e18, 2007.

[24] B. Wolf, U. Tutsch, S. Dörschug, C. Krellner, F. Ritter, W. Assmus, and M. Lang. *J.Appl.Phys.*, 120:142112, 2016.

[25] M. Imada, T. Misawa, and Y. Yamaji. *J.Phys.Condens.Matter*, 22:164206, 2010.

[26] M. Brando, D. Belitz, F. M. Grosche, and T. R. Kirkpatrick. *Rev.Mod.Phys.*, 88:025006, 2016.

[27] S. Fujimori. *J.of Phys.Condens.Matter*, 28:153002, 2016.

[28] K. T. Wilke and J. Bohm. *Kristallzüchtung.* VEB Deutscher Verlag der Wissenschaften, Berlin, 1988.

[29] T. B. Massalski, H. Okamoto, P. R. Subramanian, and L. Kacprzak. *Binary alloy phase diagrams.* ASM International, Ohio, 1990.

[30] A. N. Nesmeyanov. *Vapor pressure of the Chemical Elements.* Elsevier Publishing Company, 1963.

[31] W. Kossel. *Zur Theorie des Kristallwachstums.* Nachr. Akad. Wiss. Göttingen, 1927.

[32] I. N. Stranski. *Z. phys. Chemie*, 136:259, 1928.

[33] Y. B. Kuz'ma, S. I. Chykhrij, and S. L. Budnyk. *J.Alloy.Compd.*, 298:190, 2000.

[34] Q. S. Huang, L. Liu, J. F. Li, F. Lin, and Y. H. Zhou. *J. Phase Equilibr. Diff.*, 31:532, 2010.

[35] P. C. Canfield and Z. Fisk. *Philos.Mag.B*, 65:1117, 1992.

[36] P. C. Canfield and I. R. Fisher. *J.Cryst.Growth*, 225:155, 2001.

[37] M. G. Kanatzidis, R. Pöttgen, and W. Jeitschko. *Angew.Chem.Int.Edit.*, 44:6996, 2005.

[38] Y. Ônuki, R. Settai, K. Sugiyama, Y. Inada, T. Takeuchi, Y. Haga, E. Yamamoto, H. Harima, and H. Yamagami. *J.Phys.Condens.Matter*, 19:125203, 2007.

[39] S. Seiro and C. Geibel. *J.Phys.Condens.Mat.*, 26:046002, 2014.

[40] C. Krellner and C. Geibel. *J. Cryst. Growth*, 310:1875, 2008.

[41] A. Jesche and P. C. Canfield. *Philos.Mag.*, 94:2372, 2014.

[42] K. J. Bachmann, E. Buehler, J. L. Shay, and A. R. Strnad. *J.Electron.Mater.*, 4:389, 1975.

[43] N. F. Sun, X. W. Wu, X. Wu, Y. W. Zhao, L. X. Cao, Q. Zhao, W. L. Guo, J. Zhang, Z. P. Zhao, K. Y. Bi, and T. N. Sun. *Solid-state and integrated-circuit technology*, 1:267, 2001.

[44] Ch. Kloc, M. Ch. Lux-Steiner, M. Keil, J. R. Baumann, G. Döll, and E. Bucher. *J. Cryst. Growth*, 106:635, 1990.

[45] C. H. Lee, H. Kitô, H. Ihara, K. Akita, N. Yanase, C. Sekine, and I. Shirotani. *J. Cryst. Growth*, 263:358, 2004.

[46] T. Fujiwara, K. Kanto, K. Matsubayashi, Y. Uwatoko, and T. Shigeoka. *J.Phys.Conf.Ser.*, 273:012112, 2011.

[47] G. Zhang, X. Tao, S. Wang, G. Liu, Q. Shi, and M. Jiang. *J.Cryst. Growth*, 318:717, 2011.

[48] K. Kliemt and C. Krellner. Characterization of $\mathrm{YbNi_4(P_{1x}As_x)_2}$, $x = 0, 0.2$ single crystals grown by Czochralski method. *J.Phys.Conf.Ser.*, 807:032005, 2017. http://stacks.iop.org/1742-6596/807/i=3/a=032005.

[49] A. C. Larson and R. B. Von Dreele. *Los Alamos National Laboratory Report LAUR*, page 86, 2000.

[50] J. Laugier. *Crystal orientation by Laue method.* OrientExpress 3.4, 2013.

[51] M. A. Ruderman and C. Kittel. *Phys.Rev.*, 96:99, 1954.

[52] T. Kasuya. *Prog.Theo.Phys.*, 16:45, 1956.
[53] K. Yosida. *Phys.Rev.*, 106:893, 1957.
[54] S. Blundell. *Magnetism in Condensed Matter*. Oxford University Press, Oxford, 2011.
[55] K. H. J. Buschow and F. R. de Boer. *Physics of Magnetism and Magnetic Materials*. Kluwer Academic Publishers, New York, 2003.
[56] U. Walter. *Z.Phys.B - Condens.Matter*, 62:299, 1986.
[57] M. Hutchings. *Solid State Phys. Adv. Res. Appl.*, 16:227, 1964.
[58] J. Kondo. *Prog.Theo.Phys.*, 32:37, 1964.
[59] K. D. Schotte and U. Schotte. *Phys.Lett.*, 55A:38, 1975.
[60] N. B. Brandt and V. V. Moshchalkov. *Adv.Phys.*, 33:373, 1984.
[61] K. Andres, J. E. Graebner, and H. R. Ott. *Phys.Rev.Lett.*, 35:1779, 1975.
[62] H. R. Ott, O. Marti, and F. Hullinger. *Solid State Commun.*, 49:1129, 1984.
[63] A. Sumiyama, Y. Oda, H. Nagano, Y. Ônuki, K. Shibutani, and T. Komatsubara. *J.Phys.Soc.Jpn.*, 55:1294, 1986.
[64] C. Lacroix. *J.Appl.Phys.*, 53:2131, 1982.
[65] S. Doniach. *Physica*, 91:231, 1977.
[66] M. E. Macovei, M. Nicklas, C. Krellner, C. Geibel, and F. Steglich. *J.Phys.Cond.Matter*, 20:505205, 2008.
[67] S. Mederle, R. Borth, C. Geibel, F. M. Grosche, G. Sparn, O. Trovarelli, and F. Steglich. *J.Phys.Condens.Matter*, 14:10731, 2002.
[68] S. Lausberg, A. Hannaske, A. Steppke, L. Steinke, T. Gruner, L. Pedrero, C. Krellner, C. Klingner, M. Brando, C. Geibel, and F. Steglich. *Phys.Rev.Lett.*, 110:256402, 2013.
[69] C. Klingner, C. Krellner, M. Brando, C. Geibel, F. Steglich, D. V. Vyalikh, K. Kummer, S. Danzenbächer, S. L. Molodtsov, C. Laubschat, T. Kinoshita, Y. Kato, and T. Muro. *Phys.Rev.B*, 83:144405, 2011.
[70] C. Kittel. *Einführung in die Festkörperphysik*. Oldenbourg Verlag München, 1991.
[71] C. Enss and S. Hunklinger. *Tieftemperaturphysik*. Springer Verlag Berlin, 2000.
[72] P. Fulde. *Correlated Electrons in Quantum Matter*. World Scientific Publishing, 2012.
[73] G. Czycholl. *Theoretische Festkörperphysik*. Springer Verlag Berlin Heidelberg, 2008.
[74] L. Landau. *Sov.Phys.JETP*, 3:920, 1957.
[75] A. Tari. *The specific heat of matter at low temperatures*. Imperial College Press, London, 2003.
[76] K. Kadowaki and S. B. Woods. *Solid State Commun.*, 58:507, 1986.
[77] A. C. Jacko, J. O. Fjaerestad, and B. J. Powell. *Nat.Phys.*, 5:422, 2009.
[78] N. W. Ashcroft and D. N. Mermin. *Festkörperphysik*. Oldenbourg Verlag München, 2013.
[79] P. Coleman. *Heavy Fermions: Electrons at the Edge of Magnetism*. John Wiley and Sons, 2007.
[80] L. D. Landau. *Zh.Eksp.Teor.Fiz.*, 7:19, 1937.
[81] J. A. Hertz. *Phys.Rev.B*, 14:1165, 1976.
[82] Kenneth G. Wilson. *Rev.Mod.Phys.*, 47:773, 1975.
[83] V. S. Dotsenko and V. S. Dotsenko. *Adv.Phys.*, 32:129, 1983.
[84] H. v. Löhneysen, A. Rosch, M. Vojta, and P. Wölfle. *Rev.Mod.Phys.*, 79:1015, 2007.
[85] M. Vojta. *Rep.Prog.Phys.*, 66:2069, 2003.
[86] G. R. Stewart. *Rev.Mod.Phys.*, 73:797, 2001.

[87] R. E. Baumbach, J. J. Hamlin, L. Shu, D. A. Zocco, J. R. O‘Brien, P. C. Ho, and M. B. Maple. *Phys.Rev.Lett.*, 105:106403, 2010.

[88] A. J. Millis. *Phys.Rev.B*, 48:7183, 1993.

[89] T. Moriya. *Spin fluctuations in itinerant electron magnetism.* Springer, Berlin, 1985.

[90] R. Kuechler, N. Oeschler, P. Gegenwart, T. Cichorek, K. Neumaier, O. Tegus, C. Geibel, J. A. Mydosh, F. Steglich, L. Zhu, and Q. Si. *Phys.Rev.Lett.*, 91:066405, 2003.

[91] T. Moriya and T. Takimoto. Anormalous properties around magnetic instability in heavy electron systems. *J.Phys.Soc.Jpn.*, 64:960, 1995.

[92] G. Sparn, L. Donnevert, P. Hellmann, R. Horn, F. Laube, A. Link, S. Thomas, P. Gegenwart, B. Buschinger, C. Geibel, and F. Steglich. *Rev. High Pressure Sci. Technol.*, 7:431, 1998.

[93] H. Q. Yuan, F. M. Grosche, M. Deppe, G. Sparn, C. Geibel, and F. Steglich. *Phys.Rev.Lett.*, 96:047008, 2006.

[94] S. Kambe, S. Raymond, L.-P. Regnault, J. Flouquet, P. Lejay, and P. Haen. *J.Phys.Soc.Jpn.*, 65:3294, 1996.

[95] R. Kuechler, P. Gegenwart, C. Geibel, and F. Steglich. *Sci.Techn.Adv.Mat.*, 8:428, 2007.

[96] O. Stockert and F. Steglich. *Annu. Rev. Condens. Matter Phys.*, 2:79, 2011.

[97] J. Custers, P. Gegenwart, H. Wilhelm, K. Neumaier, Y. Tokiwa, O. Trovarelli, C. Geibel, F. Steglich, C. Pepin, and P. Coleman. *Nature*, 424:524, 2003.

[98] Q. Si, J. Pixley, E. Nica, S. J. Yamamoto, P. Goswami, R. Yu, and S. Kirchner. *J.Phys.Soc.Jpn.*, 83:061005, 2014.

[99] F. Steglich, H. Pfau, S. Lausberg, S. Hamann, P. Sun, U. Stockert, M. Brando, S. Friedemann, C. Krellner, C. Geibel, S. Wirth, S. Kirchner, E. Abrahams, and Q. Si. *J.Phys.Soc.Jpn.*, 83:061001, 2014.

[100] S. Friedemann, N. Oeschler, S. Wirth, C. Krellner, C. Geibel, F. Steglich, S. Paschen, S. Kirchner, and Q. Si. *Proc. Natl. Acad. Sci. USA*, 107:14547, 2010.

[101] T. Senthil, M. Vojta, and S. Sachdev. *Phys.Rev.B*, 69:035111, 2004.

[102] P. Wölfle and E. Abrahams. *Phys.Rev.B*, 84:041101, 2011.

[103] E. Abrahams, J. Schmalian, and P. Wölfle. *Phys.Rev.B*, 90:045105, 2014.

[104] P. Wölfle and E. Abrahams. *Phys.Rev.B*, 93:075128, 2016.

[105] H. Pfau, R. Daou, S. Friedemann, S. Karbassi, S. Ghannadzadeh, R. Kuechler, S. Hamann, A. Steppke, D. Sun, M. Koenig, A. P. Mackenzie, K. Kliemt, C. Krellner, and M. Brando. *Phys.Rev.Lett.*, 119:126402, 2017.

[106] D. Belitz, T. R. Kirkpatrick, and T. Vojta. *Phys.Rev.Lett.*, 82:4707, 1999.

[107] *VSM Option User‘s manual.* Physical Property Measurement System, Quantum Design, 2011.

[108] P. O. Gartland and B. J. Slagsvold. *Phys.Rev.B*, 12:4047, 1975.

[109] S. Danzenbächer, D. V. Vyalikh, K. Kummer, C. Krellner, M. Holder, M. Höppner, Yu. Kucherenko, C. Geibel, M. Shi, L. Patthey, S. L. Molodtsov, and C. Laubschat. *Phys.Rev.Lett.*, 107:267601, 2011.

[110] M. Güttler, K. Kummer, S. Patil, M. Höppner, A. Hannaske, S. Danzenbächer, M. Shi, M. Radovic, E. Rienks, C. Laubschat, C. Geibel, and D. V. Vyalikh. *Phys.Rev.B*, 90:195138, 2014.

[111] A. H. Castro Neto, F. Guinea, N. M. R. Peres, K. S. Novoselov, and A. K. Geim. *Rev.Mod.Phys.*, 81:109, 2009.

[112] A. Chikina, M. Höppner, S. Seiro, K. Kummer, S. Danzenbächer, S. Patil, A. Generalov, M. Güttler, Yu. Kucherenko, E. V. Chulkov, Yu. M. Koroteev, M. Köpernik, C. Geibel, M. Shi, M. Radovic, C. Laubschat, and D. V. Vyalikh. *Nat.Commun.*, 95, 2014.

[113] A. F. Santander-Syro, M. Klein, F. L. Boariu, A. Nuber, P. Lejay, and F. Reinert. *Nat.Phys.*, 5:637, 2009.

[114] A. Chikina, A. Generalov, K. Kummer, M. Güttler, V. N. Antonov, Yu. Kucherenko, K. Kliemt, C. Krellner, S. Danzenbächer, T. Kim, P. Dudin, C. Geibel, C. Laubschat, and D. V. Vyalikh. *Phys.Rev.B*, 95:155127, 2017.

[115] M. Güttler, A. Generalov, M. M. Otrokov, K. Kummer, K. Kliemt, A. Fedorov, A. Chikina, S. Danzenbächer, S. Schulz, E. V. Chulkov, Yu. M. Koroteev, N. Caroca-Canales, M. Shi, M. Radovic, C. Geibel, C. Laubschat, P. Dudin, T. K. Kim, M. Hoesch, C. Krellner, and D. V. Vyalikh. *Sci.Rep.*, 6:24254, 2016.

[116] A. Generalov, M. M. Otrokov, A. Chikina, K. Kliemt, K. Kummer, M. Höppner, M. Güttler, S. Seiro, A. Fedorov, S. Schulz, S. Danzenbächer, E. V. Chulkov, C. Geibel, C. Laubschat, P. Dudin, M. Hoesch, T. Kim, M. Radovic, M. Shi, N. C. Plumb, C. Krellner, and D. V. Vyalikh. *Nano Letters*, 17:811, 2017.

[117] S. I. Chikhrij, S. V. Orishchin, and Y. B. Kuz′ma. *Dopov.Akad.Nauk.*, 2:78, 1986.

[118] C. Krellner and C. Geibel. *J.Phys.Conf.Ser.*, 391:012032, 2012.

[119] S. I. Chikhrij, Y. K. Gorelenko, S. V. Orishchin, R. V. Skolozdra, and Y. B. Kuz′ma. *Sov. Phys. Solid State*, 33:1556, 1991.

[120] S. Deputier, O. Peña, T. Le Bihan, J. Y. Pivan, and R. Guerin. *Physica B: Condens.Matter*, 233:26, 1997.

[121] C. Krellner, S. Lausberg, A. Steppke, M. Brando, L. Pedrero, H. Pfau, S. Tencé, H. Rosner, F. Steglich, and C. Geibel. *New J. Phys.*, 13:103014, 2011.

[122] R. Sarkar, P. Khuntia, C. Krellner, C. Geibel, F. Steglich, and M. Baenitz. *Phys.Rev.B*, 85:140409, 2012.

[123] R. Sarkar, P. Khuntia, J. Spehling, C. Krellner, C. Geibel, H.-H. Klauss, and M. Baenitz. *Phys. Status Solidi B*, 250:519, 2013.

[124] J. Spehling, M. Günther, C. Krellner, N. Yèche, H. Luetkens, C. Geibel, and H.-H. Klauss. *Phys.Rev.B*, 85:140406(R), 2012.

[125] Z. Huesges, O. Stockert, M. M. Koza, C. Krellner, C. Geibel, and F. Steglich. *Phys. Status Solidi B*, 250:522, 2013.

[126] Z. Huesges, M. M. Koza, J. P. Embs, T. Fennell, G. Simeoni, C. Geibel, C. Krellner, and O. Stockert. *J.Phys.Conf.Ser.*, 592:01208, 2015.

[127] P. Gegenwart, F. Steglich, C.Geibel, and M.Brando. *Eur.Phys.J. Special Topics*, 224:975, 2015.

[128] R. Sarkar, J. Spehling, P. Materne, H. Luetkens, C. Baines, M. Brando, C. Krellner, and H.-H. Klauss. *Phys.Rev.B*, 95:121111(R), 2017.

[129] Z. Huesges. *Probing magnetic fluctuations close to quantum critical points by neutron scattering.* PhD thesis, TU Dresden, 2015.

[130] Y. Kishimoto, H. Yasuoka, T. Kubo, K. Kliemt, C. Krellner, H. Kotegawa, H. Tou, C. Geibel, and M. Baenitz. *to be published.*

[131] C. Krellner, T. Förster, H. Jeevan, C. Geibel, and J. Sichelschmidt. *Phys.Rev.Lett.*, 100:066401, 2008.

[132] K. Kliemt. *Crystal Growth and Characterization of* $YbNi_4P_2$. Master's Thesis, Goethe University, Frankfurt, 2014.

[133] K. Kliemt and C. Krellner. *J. Cryst. Growth*, 449:129, 2016.

[134] H. Okamoto. *J. Phase Equilibr. Diff.*, 31:200, 2010.

[135] S. Nuettgens, F. Buellesfeld, S. Reutzel, D. Finsterbusch, and W. Assmus. *Cryst.Res.Technol.*, 32:1073, 1997.

[136] R. Takke and W. Assmus. *J.Cryst.Growth*, 49:97, 1980.

[137] S. Nuettgens, G. Keyser, F. Ritter, and W. Assmus. *Physica B*, 281,282:979, 2000.

[138] J. R. Gambino, T. R. McGuire, and Y. Nakamura. *J.Appl.Phys.*, 38:1253, 1967.

[139] S. Friedemann et al. *to be published.*

[140] B. H. Toby. *J.Appl.Crystallogr.*, 34:210, 2001.

[141] J. Y. Pivan, R. Guerin, E. H. Ghadraoui, and M. Rafiq. *J. Less Common Met.*, 153:125, 1989.

[142] S. I. Chikhrij, S. V. Orishchin, and Y. B. Kuz′ma. *Dopov.Akad.Nauk.A*, 7:79, 1986.

[143] W. Jeitschko, F. Terbüchte, E. J. Reinbold, P. G. Pollmeier, and T. Vomhof. *J. Less. Common Met.*, 161:125, 1990.

[144] QuantumDesign. *Electro-transport Application note, Physical Property Measurement System*, 2016.

[145] S. Friedemann. *private communication*, 2017.

[146] H. Wilhelm, D. Jaccard, V. Zlatić, R. Monnier, B. Delley, and B. Coqblin. *J.Phys.Condens.Matter*, 17:S823, 2005.

[147] W. Franz, F. Steglich, and D. Wohlleben. *J.Phys.Colloques*, 40:C5, 1979.

[148] Y. Lassailly, A. K. Bhattacharjee, and B. Coqblin. *Phys.Rev.B*, 31:7424, 1985.

[149] H.-U. Desgranges and K. Schotte. *Phys.Lett.A*, 91:240, 1982.

[150] M.A. Romero, A.A. Aligia, J.G. Sereni, and G. Nieva. *J.Phys.Condens.Matter*, 26:025602, 2014.

[151] W. Miiller, L. S. Wu, M. S. Kim, T. Orvis, J. W. Simonson, M. Gamża, D. M. McNally, C. S. Nelson, G. Ehlers, A. Podlesnyak, J. S. Helton, Y. Zhao, Y. Qiu, J. R. D. Copley, J. W. Lynn, I. Zaliznyak, and M. C. Aronson. *Phys.Rev.B*, 93:104419, 2016.

[152] A. Ochiai, S. Matsuda, Y. Ikeda, Y. Shimizu, S. Toyoshima, H. Aoki, and K. Katoh. *J.Phys.Soc.Jpn.*, 80:123705, 2011.

[153] Z. Huesges, K. Kliemt, C. Krellner, M. Rotter, P. Novák, J.Kuneš, C. Geibel, and O. Stockert. Analysis of the crystal electric field parameters of $\mathrm{YbNi_4P_2}$. preprint, 2018.

[154] M. Rotter, D. M. Le, J. Keller, L. G. Pascut, T. Hoffmann, M. Doerr, R. Schedler, P. Fabi, S. Rotter, M. Banks, and N. Klüver. McPhase Users Manual. 2013.

[155] K. Kliemt, M. Brando, M. Hofmann-Kliemt, T. Förster, O. Young, U. Zeitler, C. Geibel, and C. Krellner. preprint, 2018.

[156] K. Kummer, C. Geibel, C. Krellner, G. Zwicknagl, C. Laubschat, N. B. Brookes, and D. V. Vyalikh. *arXiv:1612.02169v1*, 2016.

[157] E. M. Brüning, C. Krellner, M. Baenitz, A. Jesche, F. Steglich, and C. Geibel. *Phys.Rev.Lett.*, 101:117206, 2008.

[158] K. Ishida, K. Okamoto, Y. Kawasaki, Y. Kitaoka, O. Trovarelli, C. Geibel, and F. Steglich. *Phys.Rev.Lett.*, 89:107202, 2002.

[159] M. Baenitz, R. Sarkar, P. Khuntia, C. Krellner, C. Geibel, and F. Steglich. *Phys.Stat.Sol.C*, 10:540, 2013.

[160] G. C. Carter, L. H. Bennett, and D. J. Kahan. *Metallic Shifts in NMR I.* Pergamon, Oxford, 1977.

[161] E. C. Andrade, M. Brando, C. Geibel, and M. Vojta. *Phys.Rev.B*, 90:075138, 2014.

[162] E. Ising. *Z. Phys.*, 31:253, 1925.

[163] F. Krüger, C. J. Pedder, and A. G. Green. *Phys.Rev.Lett.*, 113:147001, 2014.

[164] H. Pfau, R. Daou, S. Lausberg, H. R. Naren, M. Brando, S. Friedemann, S. Wirth, T. Westerkamp, U. Stockert, P. Gegenwart, C. Krellner, C. Geibel, G. Zwicknagl, and F. Steglich. *Phys.Rev.Lett.*, 110:256403, 2013.

[165] D. Aoki, G. Seyfarth, A. Pourret, A. Gourgout, A. Mc-Collam, J. A. N. Bruin, Y. Krupko, and I. Sheikin. *Phys.Rev.Lett.*, 116:037202, 2016.

[166] M. M. Altarawneh, N. Harrison, S. E. Sebastian, L. Balicas, P. H. Tobash, J. D. Thompson, F. Ronning, and E. D. Bauer. *Phys.Rev.Lett.*, 106:146403, 2011.

[167] D. Rossi, R. Marazza, and R. Ferro. *J. Less Common Met.*, 66:17, 1979.

[168] C. Krellner, S. Taube, T. Westerkamp, Z. Hossain, and C. Geibel. *Philos.Mag.*, 92:2508, 2012.

[169] O. Trovarelli, C. Geibel, S. Mederle, C. Langhammer, F. M. Grosche, P. Gegenwart, M. Lang, G. Sparn, and F. Steglich. *Phys.Rev.Lett.*, 85:626, 2000.

[170] S. Paschen, T. Luehmann, S. Wirth, P. Gegenwart, O. Trovarelli, C. Geibel, F. Steglich, P. Coleman, and Q. Si. *Nature*, 432:881, 2004.

[171] P. Gegenwart, T. Westerkamp, C. Krellner, Y. Tokiwa, S. Paschen, C. Geibel, F. Steglich, E. Abrahams, and Q. Si. *Science*, 315:969, 2007.

[172] C. Krellner. *Ferromagnetische Korrelationen in Kondo-Gittern:* YbT_2Si_2 *und CeTPO (T = Übergangsmetall).* PhD thesis, TU Dresden, 2009.

[173] J. Saunders. *The resistive transition into superconductivity.* International conference on strongly correlated electron systems, Symposium: Heading for new shores with $\mathrm{YbRh_2Si_2}$, Prague, 2017.

[174] A. Steppke and M. Brando. *private communication.* Quantum Criticality and Novel Phases 2017, Berlin, 2017.

[175] M. Güttler, K. Kummer, K. Kliemt, C. Krellner, S. Seiro, C. Geibel, C. Laubschat, Y. Sakurai, D. V. Vyalikh, and A. Koizumi. *preprint*, 2018.

[176] K. Parkkinen, M. Dressel, K. Kliemt, C. Krellner, C. Geibel, F. Steglich, and M. Scheffler. *Phys.Proc.*, 75:340, 2015.

[177] L. Bondorf, M. Beutel, M. Thiemann, M. Dressel, D. Bothner, J. Sichelschmidt, K. Kliemt, C. Krellner, and M. Scheffler. *Physica B: Condens. Matter*, 536:331, 2018.

[178] C. Wetli. *Time-Resolved Collapse And Revival Of The Kondo State Near A Quantum Phase Transition.* PhD thesis, ETH Zürich, 2017.

[179] R. Hu, J. Hudis, C. Stock, C. L. Broholm, and C. Petrovic. *J. of Cryst. Growth*, 304:114, 2007.

[180] D. R. Lide. *CRC Handbook of Chemistry and Physics.* CRC Press, Boca Raton, 2005.

[181] Philipp Wein. *Kristallzüchtung von* $YbRh_2Si_2$. Bachelor's thesis, Goethe University Frankfurt, 2014.

[182] O. Trovarelli, J. Custers, P. Gegenwart, C. Geibel, P. Hinze, S. Mederle, G. Sparn, and F. Steglich. *Physica B*, 312:401, 2002.

[183] J. Custers, P. Gegenwart, C. Geibel, F. Steglich, P. Coleman, and S. Paschen. *Phys.Rev.Lett.*, 104:186402, 2010.

[184] C. Butzke. *Kristallzüchtung und Charakterisierung von Yb(Rh$_{1-x}$Ir$_x$)$_2$Si$_2$ ($x = 0.00 - 0.17$).* Master's thesis, Goethe University Frankfurt, 2015.

[185] B. Matthias, T. H. Geballe, and V. B. Compton. *Rev.Mod.Phys.*, 35:1, 1963.

[186] J. Verhaeghe, G. Vandermeerssche, and G. Le Compte. *Phys.Rev.*, 80:758, 1950.

[187] B. N. Aleksandrov, B. I. Verkin, and I. V. Svechkarev. *J.Exp.Theor.Phys.*, 12:25, 1961.

[188] S. Friedemann. *Elektrischer Transport und Quantenkritikalität in reinem und substituiertem YbRh$_2$Si$_2$.* PhD thesis, TU Dresden, 2009.

[189] T. Westerkamp. *Quantenphasenübergänge in den Schwere-Fermionen-Systemen Yb(Rh$_{1-x}$M$_x$)$_2$Si$_2$ und CePd$_{1-x}$Rh$_x$.* PhD thesis, TU Dresden, 2009.

[190] E. Schuberth, M. Tippmann, M. Kath, C. Krellner, C. Geibel, T. Westerkamp, C. Klingner, and F. Steglich. *J.Phys.Conf.Ser.*, 150:042178, 2009.

[191] A. Steppke, M. Brando, N. Oeschler, C. Krellner, C. Geibel, and F. Steglich. *Phys.Stat.Sol.B*, 247:737, 2010.

[192] Focus session: Superconductivity in the Vicinity of a Quantum Critical Point. *DPG Frühjahrstagung, Dresden*, 2017.

[193] C. Geibel. *private communication.* Quantum Criticality and Novel Phases 2017, Berlin, 2017.

[194] D. Geiger. *Investigations of quantum critical materials at low energies.* PhD thesis, TU Wien, 2016.

[195] S. Paschen. *The resistive transition into superconductivity.* International conference on strongly correlated electron systems, Symposium: Heading for new shores with YbRh$_2$Si$_2$, Prague, 2017.

[196] A. A. Abrikosov. *Physics*, 2:5, 1965.

[197] J. W. Allen, S.-J. Oh, M. B. Maple, and M. S. Torikachvili. *Phys.Rev.B*, 28:5347, 1983.

[198] Y. Ônuki and R. Settai. *Low Temp. Phys.*, 38:89, 2012.

[199] P. Gegenwart, Q.Si, and F. Steglich. *Nat.Phys.*, 4:186, 2008.

[200] G. Zwicknagl. *Phys.Scr.*, T49A:34, 1993.

[201] S. Burdin, A. Georges, and D. R. Grempel. *Phys.Rev.Lett.*, 85:1048, 2000.

[202] A. Koitzsch, S. V. Borisenko, D. Inosov, J. Geck, V. B. Zabolotnyy, H. Shiozawa, M. Knupfer, J. Fink, B. Bchner, E. D. Bauer, J. L. Sarrao, and R. Follath. *Phys.Rev.B*, 77:155128, 2008.

[203] A. Koizumi, G. Motoyama, Y. Kubo, T. Tanaka, M. Itou, and Y. Sakurai. *Phys.Rev.Lett.*, 106:136401, 2011.

[204] K. Kummer, S. Patil, A. Chikina, M. Guettler, M. Hoeppner, A. Generalov, S. Danzenbaecher, S. Seiro, A. Hannaske, and C. Krellner. *Phys.Rev.X*, 5:011028, 2015.

[205] *Conference on strongly correlated electron systems, Hangzhou, China*, 2016.

[206] N. Mufti, K. Kaneko, A. Hoser, M. Gutmann, C. Geibel, C. Krellner, and O. Stockert. *Phys.Rev.B*, 94:045116, 2016.

[207] S. Kambe, H. Sakai, Y. Tokunaga, G. Lapertot, T. D. Matsuda, G. Knebel, J. Flouquet, and R. E. Walstedt. *Nat.Phys.*, 10:840, 2014.

[208] J. Sichelschmidt, V. A. Ivanshin, J. Ferstl, C. Geibel, and F. Steglich. *Phys.Rev.Lett.*, 91:156401, 2003.

[209] J. Sichelschmidt, T. Kambe, I. Fazlishanov, D. Zakharov, H.-A. Krug von Nidda, J. Wykhoff, A. Skvortsova, S. Belov, A. Kutuzov, and B.I. Kochelaev. *Phys. Status*

Solidi B, 247:747, 2010.

[210] M. Scheffler, K. Schlegel, C. Clauss, D. Hafner, C. Fella, M. Dressel, M. Jourdan, J. Sichelschmidt, C. Krellner, C. Geibel, and F. Steglich. *Phys. Status Solidi B*, 250:439, 2013.

[211] Ch. Wetli, J. Kroha, K. Kliemt, C. Krellner, O. Stockert, H. von Löhneysen, and M. Fiebig. *arXiv:1703.04443v1*, 2017.

[212] A. Jesche, T. Ballé, K. Kliemt, C. Geibel, M. Brando, and C. Krellner. *Phys. Status Solidi B*, 254:1600169, 2017.

[213] E. Lengyel, M. E. Macovei, A. Jesche, C. Krellner, C. Geibel, and M. Nicklas. *Phys.Rev.B*, 91:035130, 2015.

[214] Y. Kamihara, H. Hiramatsu, M. Hirano, R. Kawamura, H. Yanagi, T. Kamiya, and H. Hosono. *J.Am.Chem.Soc.*, 128:10012, 2006.

[215] Y. Kamihara, T. Watanabe, M. Hirano, and H. Hosono. *J.Am.Chem.Soc.*, 130:3296, 2008.

[216] B. I. Zimmer, W. Jeitschko, J. H. Albering, R. Glaum, and M. Reehuis. *J.Alloy.Compd.*, 229:238, 1995.

[217] C. Krellner, N. S. Kini, E. M. Brüning, K. Koch, H. Rosner, M. Nicklas, M. Baenitz, and C. Geibel. *Phys.Rev.B*, 76:104418, 2007.

[218] A. Jesche. *3d- und 4f-Korrelationen in quaternären Eisenpniktiden: der Sonderfall* $CeFeAs_{1-x}P_xO$. PhD thesis, TU Dresden, 2011.

[219] H. Kotegawa, T. Toyama, S. Kitagawa, H. Tou, E. Matsuoka R. Yamauchi, and H. Sugawara. *J.Phys.Soc.Jpn.*, 82:123711, 2013.

[220] S. Kitagawa, K. Ishida, T. Nakamura, M. Matoba, and Y. Kamihara. *J.Phys.Soc.Jpn.*, 82:033704, 2013.

[221] T. Ballé. *Synthese, Kristallzüchtung und Charakterisierung von* $CeRu_{1-x}Fe_xPO$. Master's thesis, Goethe University Frankfurt, 2016.

[222] T. Shigeoka, T. Fujiwara, K. Matsubayashi, and Y. Uwatoko. *J.Phys.Conf.Ser.*, 391:012063, 2012.

[223] K. Kliemt and C. Krellner. *J. Cryst. Growth*, 419:37, 2015.

[224] O. Stockert. private communication, 2016.

[225] K. Kliemt, M. Hofmann-Kliemt, K. Kummer, F. Yakhou-Harris, C. Krellner, and C. Geibel. *Phys.Rev.B*, 95:134403, 2017.

[226] J. Sichelschmidt, K. Kliemt, C. Krellner, and C. Geibel. *J.Phys.Conf.Ser.*, 807:012007, 2017.

[227] J. Sichelschmidt, K. Kliemt, M. Hofmann-Kliemt, and C. Krellner. *arXiv:1710.03079*, 2017.

[228] A. Szytuła, D Kaczorowski, Ł. Gondek, A. Arulraj, S. Baran, and B.Penc. *Solid State Commun.*, 146:61, 2008.

[229] M. Mihalik, M. Divis, and V. Sechovský. *Phys.Rev.B*, 81:174431, 2010.

[230] J. Leciejewicz, H. Ptasiewicz-Bak, A. Szytula, and M. Slaski. *Physica B + C*, 130:382, 1985.

[231] R. Welter, K. Halich, and B. Malaman. *J.Alloy.Compd.*, 353:48, 2003.

[232] M. Slaski, J. Leciejewicz, and A. Szytuła. *J.Magn.Magn.Mater.*, 39:268, 1983.

[233] J. P. Sanchez, A. Blaise, E. Ressouche, B. Malaman, G. Venturini, K. Tomala, and R. Kmieć. *J.Magn.Magn.Mater.*, 128:295, 1993.

[234] M. Melamud, H. Pinto, I. Felner, and H. Shaked. *J.Appl.Phys.*, 55:2034, 1984.

[235] T. Shigeoka, T. Fujiwara, K. Munakata, K. Matsubayashi, and Y. Uwatoko. *J.Phys.Conf.Ser.*, 273:012127, 2011.

[236] D. Niepmann and R. Pöttgen. *Intermetallics*, 9:313, 2001.

[237] T. T. M. Palstra, A. A. Menovsky, J. van den Berg, A. J. Dirkmaat, P. H. Kes, G. J. Nieuwenhuys, and J. A. Mydosh. *Phys.Rev.Lett.*, 55:2727, 1985.

[238] P. Villars and L. D. Calvert. *Pearson‘s handbook of crystallographic data for intermetallic compounds*, volume 2nd ed. Material Park (OH): American Society for Metals, 1991.

[239] E. Parthé and B. Chabot. *Handbook on the chemistry and physics of rare earths.* Amsterdam: Elsevier Science Publishers, 1984.

[240] W. Bazela. *J.Alloy.Compd.*, 442:132, 2007.

[241] S. Wirth, S. Ernst, R. Cardoso-Gil, H. Borrmann, S. Seiro, C. Krellner, C. Geibel, S. Kirchner, U. Burkhardt, Y. Grin, and F. Steglich. *J.Phys.Condens.Matter*, 24:294203, 2012.

[242] T. Takimoto. *J.Phys.Soc.Jpn.*, 80:123710, 2011.

[243] F. Lu, J. Zhao, H. Weng, Z. Fang, and X. Dai. *Phys.Rev.Lett.*, 110:096401, 2013.

[244] D. J. Kim, J. Xia, and Z. Fisk. *Nat.Mater.*, 13:466, 2014.

[245] S. Sanada, Y. Aoki, H. Aoki, A. Tsuchiya, D. Kikuchi, H. Sugawara, and H. Sato. *J.Phys.Soc.Jpn.*, 74:246, 2005.

[246] R. Higashinaka, T. Maruyama, A. Nakama, R. Miyazaki, Y. Aoki, and H. Sato. *J.Phys.Soc.Jpn.*, 80:093703, 2011.

[247] I. Felner and I. Nowik. *Solid State Commun.*, 47:831, 1983.

[248] I. Felner and I. Nowik. *J.Phys.Chem.Solids*, 45:419, 1984.

[249] A. V. Morozkin, Yu. D. Seropegin, and O. I. Bodak. *J.Alloy.Compd.*, 234:143, 1996.

[250] A. V. Morozkin and Yu. D. Seropegin. *J.Alloy.Compd.*, 237:124, 1996.

[251] Yu. V. Kochetkov, V. N. Nikiforov, S. A. Klestov, and A. V. Morozkin. *J.Magn.Magn.Mater.*, 157:665, 1997.

[252] J. Ferstl. *New Yb-based systems: From an intermediate-valent to a magnetically ordered state.* PhD thesis, TU Dresden, Cuvillier Göttingen, 2007.

[253] G. K. Wertheim and G. Crecelius. *Phys.Rev.Lett.*, 40:813, 1978.

[254] J. W. Allen, L. I. Johansson, I. Lindau, and S. B. Hagstrom. *Phys.Rev.B*, 21:1335, 1980.

[255] H. Yamaoka, P. Thunström, I. Jarrige, K. Shimada, N. Tsujii, M. Arita, H. Iwasawa, H. Hayashi, J. Jiang, T. Habuchi, D. Hirayama, H. Namatame, M. Taniguchi, U. Murao, S. Hosoya, A. Tamaki, and H. Kitazawa. *Phys.Rev.B*, 85:115120, 2012.

[256] G. Czjzek, V. Oestreich, H. Schmidt, K. Łatka, and K. Tomala. *J.Magn.Magn.Mater.*, 79:42, 1989.

[257] A. Szytuła, A. Budkowski, M. Slaski, and R. Zach. *Solid State Commun.*, 57:813, 1986.

[258] E. Kwapulinska, K. Kaczmarska, and A. Szytuła. *J.Magn.Magn.Mater.*, 73:65, 1988.

[259] G. A. Cabrera-Pasca, A. W. Carbonari, R. N. Saxena, B. Bosch-Santos, J. A. H. Coaquira, and J. A. Filho. *J.Alloy.Compd.*, 515:44, 2012.

[260] E. Stryjewski and N. Giordano. *Adv.Phys.*, 26:487, 1977.

[261] T. Jaworska-Gołab, Ł. Gondek, A. Szytuła, A. Zygmunt, B. Penc, J. Leciejewicz, S. Baran, and N. Stüsser. *J.Phys.Condens.Matter*, 14:5315, 2002.

[262] K. Sekizawa, Y. Takano, H. Takigami, and Y. Takahashi. *J. Less Common Met.*, 127:99, 1987.

[263] Y. Takano, K. Ohhata, and K. Sekizawa. *J.Magn.Magn.Mater.*, 66:187, 1987.

[264] J. Sichelschmidt. *private communication*, 2017.

[265] L. D. Tung, J. J. M. Franse, K. H. J. Buschow, P. E. Brommer, and N. P. Thuy. *J. Alloys Comp.*, 260:35, 1997.

[266] K. H. J. Buschow and D. B. de Mooij. *Philips J. Res.*, 41:55, 1986.

[267] M. Slaski and A. Szytuła. *J. Less Common Met.*, 87:1, 1982.

[268] W. X. Zhong, B. Lloret, W. L. Ng, B. Chevalier, J. Etourneau, and P. Hagenmuller. *Rev.Chim.Miner.*, 22:711, 1985.

[269] R. S. Fishman and S. H. Liu. *Phys.Rev.B*, 40:11028, 1989.

[270] M. Bouvier, P. Lethuillier, and D. Schmitt. *Phys.Rev.B*, 43:13137, 1991.

[271] J. A. Blanco, D. Gignoux, P. Morin, and D. Schmitt. *Europhys.Lett.*, 15:671, 1991.

[272] J. A. Blanco, D. Gignoux, and D. Schmitt. *Phys.Rev.B*, 43:13145, 1991.

[273] P. Reiss, P. M. C. Rourke, G. Zwicknagl, F. M. Grosche, and S. Friedemann. *Phys. Status Solidi B*, 250:498, 2013.

[274] C. Geibel. *private communication*, 2017.

Acknowledgments

Many people contributed in various ways to the results presented in this thesis. I enjoyed the good cooperation and their support and want to thank them hereby.

Firstly, I want to thank Prof. Dr. Cornelius Krellner who provided the opportunity to work in the field of strongly correlated electron systems. During the past years I enjoyed your support not only during daily work but also in joining numerous collaborations within the community. I took profit on your experience and always enjoyed the discussions on our projects.

Furthermore, I thank Prof. Dr. Michael Lang for writing the second evaluation of my doctoral thesis.

The single crystal growth of $YbNi_4P_2$ was a long-standing project which was initialised by Cornelius Krellner. At the beginning, my knowledge about the Czochralski growth method was boosted enormously during a stay at Prof. Dr. Peter Gilles laboratory at the LMU in Munich. He is a world leading expert in this field and I'm grateful for the experiences that I got during this visit. I thank Prof. Dr. Peter Gille for writing the third evaluation of my doctoral thesis.

A special thank goes to Judith Schwerin that I was allowed to look over her shoulder during her experiment in Prof. Gilles laboratory. I got insight into the work at low temperatures during a stay at the MPI CPfS Dresden in the group of Manuel Brando. Here, the first characterization of the low-temperature properties of the quantum-critical materials was done by Sandra Hamann, Alexander Steppke and Jacintha Banda. Thank you for the pleasant days in your group! I acknowledge the collaboration with different groups concerning $YbNi_4P_2$:
The neutron scattering group consisting of Zita Hüsges (HZB Berlin), Stefan Lucas and PD Dr. Oliver Stockert (MPI CPfS Dresden) started to study the magnetic fluctuations on large single crystalline $YbNi_4P_2$ and I learned about their experimental work during the visits at FRM II in Munich and at FLEXX at the HZB in Berlin. I also thank Astrid Schneidewind for her support at FRM II. The characterization of the single crystals by Oliver Stockert using neutron Laue backscattering was a great help. The delicate analysis of the Lifshitz transitions in this material was carried out by Heike Pfau from Stanford and supported experimentally by Sven Friedemann (University of Bristol), Sandra Hamann, Alexander Steppke, Dan Sun, Markus König and Manuel Brando (MPI CPfS Dresden). The ESR was investigated by Jörg Sichelschmidt (MPI CPfS Dresden) and Marc Scheffler (Universität Stuttgart). The NMR was studied by Tetsuro Kubo, Yasuki Kishimoto, Prof. Dr. Hideki Tou (Kobe University),

Prof. Dr. Hiroshi Yasuoka (Los Alamos), Michael Baenitz (MPI CPfS Dresden) and was strongly influenced by the ideas of PD Dr. Christoph Geibel (MPI CPfS Dresden).

The material was investigated by STM by Lin Jiao and PD Dr. Steffen Wirth (MPI CPfS Dresden). First ARPES studies were performed by Prof. Dr. Denis V. Vyalikh (San Sebastian). I enjoyed the stay at the HFML Nijmegen supported by Olga Young where I got insights in the experimental difficulties of high-field magnetization measurements, in italien cooking thanks to Manuel Brando and in Fourier analysis of the data thanks to Tobias Förster (HZDR Dresden). Additionally, I thank Matthias Hofmann-Kliemt for the simulation of the high-field magnetization data. First ultra-sound measurements on $YbNi_4P_2$ performed by Yeekin Tsui, PD Dr. Bernd Wolf and Prof. Dr. Michael Lang (Goethe University Frankfurt) are in progress.

There is a strong interest in the canonical quantum critical material $YbRh_2Si_2$ in the community and several projects were started in the frame of this work:
Microwave spectroscopy was done by Wolfgang Voesch, Linda Bondorf, Desiree Rausch, Markus Thiemann and Marc Scheffler (Universität Stuttgart). In their work they extended the accessible field and temperature range for this method using new coplanar resonators. THz spectroscopy was used by Christoph Wetli, Shovon Pal and Prof. Dr. Manfred Fiebig (ETH Zürich) and got theoretical support by Prof. Dr. Johann Kroha (Uni Bonn) to investigate the nature of the Kondo state. Low temperature electrical transport measurement were started by Diana Geiger and Prof. Dr. Silke Bühler-Paschen (TU Wien). Prof. Dr. Marie-Aude Measson (CNRS, Paris) started to investigate the material by Raman spectroscopy. Lev Levitin and Prof. Dr. John Saunders (Royal Holloway University of London) performed thermal noise measurements at ultra-low temperatures to study the transition into the superconducting state. Furthermore, $1/f$ noise spectroscopy on this material was started by Martin Lonski and Prof. Dr. Jens Müller (Goethe University Frankfurt).

The compounds $LnRh_2Si_2$ turned out to show remarkable surface states in ARPES studies. I enjoyed the fruitful collaboration with Alla Chikina, Monika Güttler, Susanne Schulz, PD Dr. Steffen Danzenbächer, Prof. Dr. Clemens Laubschat (TU Dresden), Alexander Generalov (Lund University), Mikhail M. Otrokov and Prof. Dr. Denis V. Vyalikh (San Sebastian). During joining beamtimes at PSI (Villigen) and at ESRF (Grenoble), I got insight into the ARPES experiments and I learned about RIXS from Kurt Kummer.

I have benefited a lot from dicussions with PD Dr. Christoph Geibel in the course of the various projects. Thank you, Christoph, for the detailed replies to all my questions! I acknowledge discussions with Prof. Dr. Frank Steglich and Prof. Dr. Roser Valenti and thank for highlighting the importance of pure single crystals for solid state research. I took profit from stimulating discussions with Prof. Dr. Paul Canfield during his stay in Frankfurt. I enjoyed the collaboration with Prof. Dr. Hanoh Lee and thank Wu Xie and Prof. Dr. Huiqui Yuan (Zhejiang University Hangzhou, China) for providing insights into the chinese scientific life and culture.

I acknowledge the detailed constructive comments on the manuscript from Prof. Dr. Wolf Aßmus. I thank Prof. Dr. Martin Schmidt for technical discussions especially about reasonable attempts concerning substitutions and for his comments on parts of the manuscript.

Special thanks goes to my colleagues in the lab, Franz Ritter and Klaus-Dieter Luther, for indispensable scientific and technical support which I really enjoyed over the past years. I acknowledge the support from Antonia Morherr through solving technical problems with the PPMS. Additionally, I thank Pascal Puphal for increasing my knowledge about spin liquids. I thank my Bachelor and Master students Philipp Wein, Constantin Butzke, Tanita Ballé, Philipp Ross, Fabian Feldmann, Paul Denck, Marius Peters for their interest and support in the various projects. I‘m greatly indebted to Sebastian, Marius, Matthias, Fabian and Christine for proofreading the manuscript.

Furthermore, I thank Florian Hohmann, Knut Pfeiffer, Michael Röder and Corinna Banditt from the metal and glas blower workshops (Goethe University, Frankfurt) for technical support, Michael Bolte (Chemistry department, Goethe University, Frankfurt) for single crystal structure determination, Gudrun Auffermann for the sample analysis by carrier gas hot extraction and Christoph Klausnitzer (MPI CPfS Dresden) for technical support during the heat capacity measurements. Administrative matters were professionally and carefully handled by Hannah Döring and I acknowledge a lot her irreplacable support.

I'm grateful to my husband Matthias for his tremendous encouragement during the past years and also for pulling me out of the lab in the evenings.

This thesis was supported by the Deutsche Forschungsgemeinschaft via the projects ”Ferromagnetische Quantenkritikalität und Supraleitung in Yb-basierten Schwere-Fermion-Systemen”, ”Topologie von Fermi-Flächen und neuartige elektronische Zustände in Systemen mit stark korrelierten Elektronen”, ”Exotischer Magnetismus und Korrelationsphänomene an der Oberfläche und im Volumen von Seltenerd-basierten Materialien” and SFB/TRR49.

Publications

Parts of this PhD thesis have already been published in the following peer reviewed articles:

1. K. Kliemt and C. Krellner, *Single crystal growth and characterization of GdRh$_2$Si$_2$*, J. Cryst. Growth **419**, 37 (2015), [arXiv:1612.00781]
2. K. Parkkinen, M. Dressel, K. Kliemt, C. Krellner, C. Geibel, F. Steglich and M. Scheffler, *Signatures of Phase Transitions in the Microwave Response of YbRh$_2$Si$_2$*, Phys. Proc. **75**, 340 (2015), [arXiv:1604.00331]
3. M. Güttler, A. Generalov, M. M. Otrokov, K. Kummer, K. Kliemt, A. Fedorov, A. Chikina, S. Danzenbächer, S. Schulz, E. V. Chulkov, Yu. M. Koroteev, N. Caroca-Canales, M. Shi, M. Radovic, C. Geibel, C. Laubschat, P. Dudin, T. K. Kim, M. Hoesch, C. Krellner and D. V. Vyalikh, *Robust and tunable itinerant ferromagnetism at the silicon surface of the antiferromagnet GdRh$_2$Si$_2$*, Sci. Rep. **6**, 24254 (2016)
4. K. Kliemt and C. Krellner, *Crystal growth by Bridgman and Czochralski method of the ferromagnetic quantum critical material YbNi$_4$P$_2$* J. Cryst. Growth, **449**, 129 (2016), [arXiv:1606.05517]
5. A. Jesche, T. Ballé, K. Kliemt, C. Geibel, M. Brando and C. Krellner *Avoided ferromagnetic quantum critical point: Antiferromagnetic ground state in substituted CeFePO*, Phys. Status Solidi B **254**, 1600169 (2017), Special Issue "Iron-Based High Temperature Superconductors" DFG-SPP 1458, [arXiv:1605.03515]
6. A. Generalov, M. M. Otrokov, A. Chikina, K. Kliemt, K. Kummer, M. Höppner, M. Güttler, S. Seiro, A. Fedorov, S. Schulz, S. Danzenbächer, E. V. Chulkov, C. Geibel, C. Laubschat, P. Dudin, M. Hoesch, T. Kim, M. Radovic, M. Shi, N. C. Plumb, C. Krellner and D. V. Vyalikh, *Spin Orientation of Two-Dimensional Electrons Driven by Temperature-Tunable Competition of Spin-Orbit and Exchange-Magnetic Interactions*, Nano Letters **17**, 811-820 (2017)
7. J. Sichelschmidt, K. Kliemt, C. Krellner, C. Geibel, *Paramagnetic Resonance in GdRh$_2$Si$_2$*, J. Phys. Conf. Ser. **807**, 012007 (2017)
8. K. Kliemt and C. Krellner, *Characterization of YbNi$_4$(P$_{1-x}$As$_x$)$_2$, $x = 0; 0.2$ single crystals grown by Czochralski method*, J. Phys. Conf. Ser. **807**, 032005 (2017), [arXiv:1612.00753]
9. K. Kliemt, M. Hofmann-Kliemt, K. Kummer, F. Yakhou-Harris, C. Krellner and C. Geibel, *GdRh$_2$Si$_2$: An exemplary tetragonal system for antiferromagnetic order with weak in-plane anisotropy*, Phys. Rev. B **95**, 134403 (2017), [arXiv:1703.04114]
10. A. Chikina, A. Generalov, K. Kummer, M. Güttler, V. N. Antonov, Yu. Kucherenko, K. Kliemt, C. Krellner, S. Danzenbächer, T. Kim, P. Dudin, C. Geibel, C. Laubschat and D. V. Vyalikh, *Valence instability in the bulk and at the surface of the antiferromagnet SmRh$_2$Si$_2$*, Phys. Rev. B **95**, 155127 (2017)
11. P. Puphal, M. Bolte, D. Sheptyakov, A. Pustogow, K. Kliemt, M. Dressel, M. Baenitz, C. Krellner, *Strong magnetic frustration in $Y_3Cu_9(OH)_{19}Cl_8$: a distorted kagome antiferromagnet*, J.Mater.Chem.C (2017), [arXiv:1702.01036]
12. H. Pfau, R. Daou, S. Friedemann, S. Karbassi, S. Ghannadzadeh, R. Kuechler, S. Hamann, A. Steppke, D. Sun, M. König, A. P. Mackenzie, K. Kliemt, C. Krellner

and M. Brando, *Cascade of magnetic field induced Lifshitz transitions in the ferromagnetic Kondo lattice material* $YbNi_4P_2$, Phys. Rev. Lett. **119**, 126402 (2017), [arXiv:1612.06273]

13. L. Bondorf, M. Beutel, M. Thiemann, M. Dressel, D. Bothner, J. Sichelschmidt, K. Kliemt, C. Krellner, M. Scheffler, *Angle-dependent electron spin resonance of* $YbRh_2Si_2$ *measured with planar microwave resonators and in-situ rotation*, Physica B: Condens. Matter **536**, 331 (2018), [arXiv:1711.05759]

Preprints

1. J. Sichelschmidt, K. Kliemt, M. Hofmann-Kliemt, C. Krellner, *Weak magnetic anisotropy in* $GdRh_2Si_2$ *studied by magnetic resonance*, under review 2018, [arXiv:1710.03079]
2. Ch. Wetli, J. Kroha, K. Kliemt, C. Krellner, O. Stockert, H. v. Löhneysen, M. Fiebig, *Time-resolved collapse and revival of the Kondo state near a quantum phase transition*, under review 2018, [arXiv:1703.04443v1]
3. Z. Huesges, K. Kliemt, C. Krellner, M. Rotter, P. Novák, J. Kuneš, C. Geibel and O. Stockert, *Analysis of the crystal electric field parameters of* $YbNi_4P_2$, under review 2018
4. Y. Kishimoto, H. Yasuoka, T. Kubo, K. Kliemt, C. Krellner, H. Kotegawa, H. Tou, C. Geibel and M. Baenitz, *Evolution of Ising-like magnetic fluctuations in a quasi one-dimensional heavy-fermion compound* $YbNi_4P_2$ *probed by* ^{31}P *nuclear magnetic resonance*, preprint, 2018
5. K. Kliemt, M. Brando, M. Hofmann-Kliemt, T. Förster, O. Young, U. Zeitler and C. Krellner $YbNi_4P_2$ *in high magnetic fields*, preprint, 2018
6. M. Güttler and K. Kummer and K. Kliemt and C. Krellner and S. Seiro and C. Geibel and C. Laubschat and Y. Sakurai and D.V. Vyalikh and A. Koizumi, *Visualizing the Kondo lattice crossover in* $YbRh_2Si_2$ *by Compton scattering*, preprint, 2018
7. A. Generalov, J. Falke, I. A. Nechaev, M. Otrokov, M. Güttler, A. Chikina, K. Kliemt, K. Kummer, S. Danzenbächer, D. Usachov, T. Kim, P. Dudin, E. V. Chulkov, C. Laubschat, C. Geibel, C. Krellner, and D. V. Vyalikh, *Strong spin-orbit coupling in a two dimensional Kondo lattice*, preprint, 2018

Patent

M. U. Schmidt, K. Kliemt, *Einfärben von Glas mit organischen Pigmenten (Coloration of glass with organic pigments),* DE Application No. 10 2013 114 793 A1, filed 23-12-2013, published 25-06-2015.

Versicherung

Ich erkläre hiermit, dass ich die vorgelegte Dissertation selbständig angefertigt und mich anderer Hilfsmittel als der in ihr angegebenen nicht bedient habe, insbesondere, dass alle Entlehnungen aus anderen Schriften mit Angabe der betreffenden Schrift gekennzeichnet sind. Ich versichere, die Grundsätze der guten wissenschaftlichen Praxis beachtet, und nicht die Hilfe einer kommerziellen Promotionsvermittlung in Anspruch genommen zu haben.

Frankfurt am Main, den 30.01.2018 Kristin Kliemt